ABSTRACT

Title of Dissertation: INDIUM PHOSPHIDE BASED OPTICAL WAVEGUIDE MEMS FOR COMMUNICATIONS AND SENSING

Marcel Werner Pruessner,
Doctor of Philosophy, 2005

Dissertation Directed By: Professor Reza Ghodssi,
Department of Electrical and Computer Engineering

Indium phosphide (InP) is extensively used for integrated waveguide and photonic devices due to its suitability as a substrate for direct bandgap materials (e.g. $In_{1-X}Ga_XAs_YP_{1-Y}$) operating at the $\lambda$=1550 nm communications wavelength. However, little work has been reported on InP optical waveguide micro-electro-mechanical systems (MEMS).

In this work, InP cantilever and doubly-clamped beams were micromachined on an $In_{0.53}Ga_{0.47}As$ "sacrificial layer" on (100) InP substrates. Young's modulus was measured using nanoindentation and microbeam-bending. Intrinsic stress and material uniformity (stress gradient) were obtained by measuring the profile of doubly-clamped

and cantilever beams using confocal microscopy. The study resulted in a Young's modulus of 80.4–106.5 GPa (crystal orientation-dependent). Although InP was grown lattice-matched to the substrate, arsenic from the underlying $In_{0.53}Ga_{0.47}As$ sacrificial layer resulted in intrinsic compressive stress. Adding trace amounts of gallium to the InP layer during epitaxial growth induced tensile stress to offset the effect of arsenic.

The materials characterization was extended to develop optical waveguide switches and sensors. In the first device, two parallel waveguides were actuated to vary the spacing between them. By modulating the gap using electrostatic pull-in actuation, the optical coupling strength was controlled via the evanescent field. Low voltage switching (<10 V), high speed (4 μs), low crosstalk (–47 dB), and low-loss (<10 %) were achieved. Variable coupling over a 17.4 dB dynamic range was also demonstrated.

The second device utilized a single movable input waveguide, which was actuated via electrostatic comb-drives to end-couple with one of several output waveguides. Low voltage switching (<7 V), 140 μs switching speed (2 ms settling time), low crosstalk (–26 dB), and low-loss (<3.2 dB) were demonstrated.

Sensing techniques based on mass-loading were developed using end-coupled cantilever waveguides. Here, the mechanical resonance frequency was measured by actuating the cantilever and measuring the end-coupled optical power at the output waveguide. A proof-of-concept experiment utilized a focused-ion-beam to mill the cantilever tip and resulted in a measurable resonance shift with mass-sensitivity $\Delta m/\Delta f$=5.1 fg/Hz. The cantilever waveguide devices and measurement techniques enable accurate resonance detection in mass-based cantilever sensors and also enable single-chip sensors with on-chip optical detection to be realized.

# INDIUM PHOSPHIDE BASED OPTICAL WAVEGUIDE MEMS FOR COMMUNICATIONS AND SENSING

By

Marcel Werner Pruessner

Dissertation submitted to the Faculty of the Graduate School of the
University of Maryland, College Park, in partial fulfillment
of the requirements for the degree of
Doctor of Philosophy
2005

Advisory Committee:
Professor Reza Ghodssi, Chair
Professor Bongtae Han
Professor Ping-Tong Ho
Professor John Melngailis
Professor Jon Orloff

# Dedication

*To Paula.*

*And to Manfred Pruessner.*

# Acknowledgements

None of this work would have been possible without the help of many individuals.

I wish to thank my advisor, Prof. Reza Ghodssi (ECE), for guiding me in this research for the last five years. It's been fun. I also wish to thank the committee members, Prof. Bongtae Han (ENME), Prof. Ping-Tong Ho (ECE), Prof. John Melngailis (ECE), and Prof. Jon Orloff (ECE) for useful feedback. Prof. Chia-Hung Yang (ECE) served on the original research proposal committee.

My family provided love, support, and a roof over my head during my formative years. Paula Simon provided everything else that makes life worthwhile, especially during the course of this research.

Many colleagues assisted in various aspects of this work. The Laboratory for Physical Sciences (LPS) cleanroom staff, especially Mr. Laurence C. ("Toby") Olver, was most helpful with device fabrication. Dr. S. Kanakaraju ("Raju") and Mr. Lynn C. Calhoun (both of LPS) performed all the MBE wafer growths. Dr. Madhumita Datta and Mr. Daniel P. Kelly were part of the original InP MEMS group at the MEMS Sensors and Actuators Lab (MSAL) and provided useful feedback. I thank Mr. Kuldeep Amarnath (ECE and LPS) for providing the optical testing setup and for helping me with some of the experiments. Dr. Todd King (Materials Branch, NASA-GSFC) gave me access to most of the equipment needed for my M.S. research and spent countless hours assisting me with the materials characterization and measurements. Dr. Rohit Grover (LPS) taught me how to fabricate InP optical waveguides. Dr. Wen-Hsien Chuang (MSAL) performed the FIB processing. Mr. Jonathan McGee and Mr. Nathan Siwak are the new members of the InP MEMS group at MSAL and have provided useful questions and comments. All the other members of MSAL provided help in many different ways. I especially thank Mr. Alireza Modafe (my office mate during the last five years) for critical and useful comments and discussions (and occasional arguments) and Mr. Brian Morgan for detailed reading and editing of my work.

Prof. Martin Reiser (ECE) and Prof. Patrick G. O'Shea (ECE) encouraged my pursuit of engineering and first exposed me to experimental research with the University of Maryland Electron Ring (UMER) group. Prof. John Melngailis was the first to tell me about MEMS when I was taking his undergraduate course on microfabrication.

None of this work would have been possible without generous funding from various agencies and foundations: the National Science Foundation CAREER award (Prof. Ghodssi), the Laboratory for Physical Sciences (LPS), and the ARCS Foundation (Washington, D.C. Chapter).

To friends, family, and all those who helped out along the way: Thanks.

Marcel Pruessner
July 28, 2005

# Table of Contents

Dedication ..... ii
Acknowledgements ..... iii
Table of Contents ..... iv
List of Tables ..... ix
List of Figures ..... x

CHAPTER 1 ..... 1
INTRODUCTION ..... 1
1.1 Introduction ..... 1
1.2 Research Accomplishments ..... 2
1.3 All-Optical Switching ..... 4
1.3.1 Literature Review: "Traditional" Optical Switches ..... 4
1.3.2 Limitations of Traditional Optical Switching Technology ..... 9
1.3.3 Advantages of MEMS ..... 10
1.3.4 Literature Review: *MEMS* Optical Switches ..... 12
1.3.4.1 Free-space Optical MEMS Switches ..... 13
1.3.4.2 Guided Wave Optical MEMS Switches ..... 14
1.4 Indium Phosphide Based Optical Devices ..... 15
1.4.1 Why Indium Phosphide? ..... 15
1.4.2 InP-Based Optical MEMS ..... 18
1.5 Approach: InP-Based MEMS Integrated Waveguide Devices ..... 19
1.5.1 Monolithic Integration ..... 19
1.5.2 Suspended Waveguide Technology ..... 20
1.5.3 Electrostatically-Actuated Waveguides ..... 21
1.5.4 Optical Switching: Coupling Mechanisms ..... 23
1.6 Research Objectives and Organization ..... 25

CHAPTER 2 ..... 27
InP AS A MICROMECHANICAL MATERIAL ..... 27
2.1 Introduction ..... 27
2.2 Mechanical Characterization of InP ..... 27
2.2.1 Stress Measurements: Intrinsic and Gradient Stresses ..... 28
2.2.2 Nanoindentation ..... 30
2.2.3 Beam Bending ..... 32
2.2.4 Electrostatic Testing ..... 36
2.3 Stress Engineering ..... 38
2.4 Summary ..... 40

CHAPTER 3 ..... 41
SUSPENDED WAVEGUIDES ..... 41
3.1 Introduction ..... 41
3.2 InP MEMS Epiwafer Design ..... 42
3.2.1 InGaAsP Material System and Epilayer Design ..... 43

3.2.2 Possible Waveguide Designs ..... 50
3.3 Suspended Waveguides ..... 53
3.3.1 Approach ..... 53
3.3.2 Design ..... 55
3.4 Experimental Characterization ..... 56
3.5 Active Waveguides ..... 59
3.6 Summary ..... 59

CHAPTER 4 ..... 61
FABRICATION ..... 61
4.1 Introduction ..... 61
4.2 Epiwafer and Layer Structure ..... 61
4.3 Processing ..... 63
4.3.1 Standard Clean ..... 64
4.3.2 Lithography: Stepper ..... 64
4.3.3 Dry Etching ..... 66
4.3.4 Metallization ..... 69
4.3.5 Thinning and Cleaving ..... 70
4.3.6 Sacrificial Wet Etching ..... 72
4.3.7 Supercritical Drying ..... 73
4.4 Mounting ..... 74
4.5 Summary ..... 76

CHAPTER 5 ..... 77
MEMS EVANESCENT COUPLERS ..... 77
5.1 Introduction ..... 77
5.2 Theory: Evanescent Coupling ..... 77
5.2.1 Coupling Between Identical Single-Mode Waveguides ..... 79
5.2.2 Coupling: General Case ..... 82
5.2.3 Optical Switching via Evanescent Coupling ..... 82
5.3 Literature Review ..... 83
5.4 MEMS Evanescent Coupler ..... 85
5.4.1 MEMS Actuator Design ..... 88
5.4.2 Optical Design ..... 91
5.4.3 Design Summary ..... 95
5.5 Experimental Results ..... 96
5.5.1 Electro-Thermally Actuated MEMS Couplers ..... 99
5.5.2 Electrostatically Actuated MEMS Couplers ..... 102
5.6 Discussion ..... 115
5.7 Improved Designs ..... 117
5.7.1 Comb-Drive Couplers, Third Electrode Couplers, and Surface Coatings ..... 117
5.7.2 Experimental: Comb-Drive and Third Electrode Couplers ..... 118
5.7.3 Single-Mode Devices ..... 121
5.8 Summary ..... 123

CHAPTER 6 ..... 125
END-COUPLED OPTICAL WAVEGUIDE SWITCHES ..... 125
6.1 Introduction ..... 125
6.2 Theory: End-Coupling between Optical Waveguides ..... 125
6.3 Literature Review ..... 127
6.3.1 Prior MEMS End-Coupled Optical Waveguide Switches ..... 127
6.3.2 Novelty ..... 130
6.4 Approach ..... 132
6.5 Design Considerations ..... 133
6.5.1 Actuator Design ..... 133
6.5.2 Optical Design ..... 139
6.6 Experimental Results ..... 151
6.6.1 Sacrificial Release and Strain Relaxation ..... 151
6.6.2 Optical Coupling Efficiency and Crosstalk ..... 154
6.6.3 Temporal and Frequency Response ..... 157
6.7 Discussion ..... 158
6.8 Alternative Designs ..... 161
6.8.1 Doubly-Clamped Pull-In Actuator Switches ..... 161
6.8.2 Cantilever Pull-In Actuator Switches ..... 165
6.9 Summary ..... 167

CHAPTER 7 ..... 169
MICROMECHANICAL RESONATOR SENSORS ..... 169
7.1 Introduction ..... 169
7.2 Resonant Sensors ..... 169
7.2.1 Background: MEMS Resonant Sensors ..... 169
7.2.2 Literature Review ..... 172
7.2.3 Limitations of Current MEMS Resonant Sensors ..... 175
7.2.4 MEMS Cantilever Waveguide Resonant Sensors ..... 176
7.3 Device Design ..... 179
7.3.1 Mechanical Design ..... 180
7.3.2 Optical Design ..... 183
7.4 Experimental Results ..... 186
7.4.1 Technique 1: Frequency Sweep ..... 186
7.4.2 Technique 2: Unit Step and Impulse Response ..... 189
7.4.3 Proof-of-Concept Experiment: Mass Sensing ..... 193
7.4.4 Electrostatic Tuning ..... 196
7.4.5 Frequency Doubling ..... 199
7.4.6 Repeatability ..... 203
7.5 Discussion: Sensitivity Limits ..... 205
7.5.1 Displacement Sensitivity of Optical Response ..... 206
7.5.2 High Optical Q Cavities: Tunable Filters ..... 208
7.5.3 Fundamental Detection Limits ..... 209
7.5.4 Damping ..... 210
7.5.5 Higher-Order Vibrational Modes ..... 212
7.6 Future Work ..... 214

7.6.1 Functionalization: Cantilever Waveguide Sensors ..... 214
7.6.2 Single-Chip Sensors ..... 216
7.7 Summary ..... 217

CHAPTER 8 ..... 219
CONCLUSION ..... 219
8.1 Introduction ..... 219
8.2 Summary of Accomplishments ..... 219
8.3 Other MEMS-Actuated Waveguide Device Applications ..... 222
8.3.1 In-Plane MEMS-Tunable Fabry-Perot Filters ..... 222
8.3.2 Micro-Ring and Micro-Disk Resonator Filters ..... 223
8.3.3 WDM Transmitters and Receivers ..... 225
8.4 Comments and Future Work ..... 226
8.5 Summary ..... 228

APPENDIX A ..... 229
MATLAB SCRIPT FOR CALCULATION OF InGaAsP PROPERTIES ..... 229
A.1 Introduction ..... 229
A.2 MATLAB Source Code ..... 229
A.3 Typical Output Window ..... 233
A.4 Summary ..... 233

APPENDIX B ..... 235
BASIC THEORY OF DIELECTRIC OPTICAL WAVEGUIDES ..... 235
B.1 Introduction ..... 235
B.2 Theory: Mirror Waveguides ..... 235
B.2 Theory: Planar Integrated Dielectric Waveguides ..... 239
B.3 Multimode Waveguides and the Cutoff Condition ..... 242
B.4 Summary ..... 244

APPENDIX C ..... 245
EVANESCENT COUPLING BETWEEN NON-IDENTICAL WAVEGUIDES AND MULTI-MODE WAVEGUIDES ..... 245
C.1 Introduction ..... 245
C.2 Coupling Between Non-Identical Waveguides ..... 245
C.3 Coupling Between Multi-Mode Waveguides ..... 248
C.4 Comments ..... 251
C.4 Summary ..... 252

APPENDIX D ..... 255
DERIVATION OF CLASSICAL PULL-IN LIMIT AND PULL-IN VOLTAGE ..... 255
D.1 Introduction ..... 255
D.2 Pull-In Limit ..... 256
D.3 Pull-In Voltage ..... 258
D.4 Comments and Summary ..... 258

APPENDIX E ..... 261
DERIVATION OF ELECTROSTATIC COMB-DRIVE FORCE ..... 261
E.1 Introduction ..... 261
E.2 Comb-Drive Force ..... 261
E.3 Comments and Summary ..... 264

APPENDIX F ..... 267
MATLAB SCRIPT FOR CALCULATION OF FAST FOURIER TRANSFORM ..... 267
F.1 Introduction ..... 267
F.2 MATLAB Source Code ..... 268
F.3 Summary ..... 269

BIBLIOGRAPHY ..... 271
LIST OF PUBLICATIONS ..... 285
Journal Papers ..... 285
Conference Paper & Poster Presentations ..... 285
Other Meetings ..... 287
Thesis/Dissertation ..... 287

# List of Tables

Table 1. 1: Comparison of various non-MEMS optical switching technologies [28].....10
Table 1. 2: Summary of InP material properties along with those of GaAs (reference [58] unless noted) and Si (reference [59] unless noted). InP and GaAs are direct bandgap semiconductors.....17

Table 2. 1: Nanoindentation Results.....32

Table 3. 1: Summary of different waveguide designs and their challenges. Waveguide: WG, sacrificial layer: SL.....51

Table 5. 1: Summary of variable optical coupling ($\lambda$ = 1550 nm, TE-polarization).....111

Table 6. 1: Summary of Gaussian waist for TE- and TM-modes ($\lambda$=1550 nm).....141
Table 6. 2: Summary of expected optical losses in end-coupled switch.....150

Table 7. 1: Length scaling of cantilever sensors.....182
Table 7. 2: Calculated sensitivity ($\Delta m/\Delta f$) for three cantilever waveguide sensors.....183
Table 7. 3: Summary of Femlab mode simulation ($m$ = 0): a) 0.6 μm wide (top), b) 0.8 μm wide (bottom). For both waveguides: height=1.5 μm, $n_{Core}$ = 3.173.....184
Table 7. 4: Resonance frequencies for three cantilever waveguide sensors.....194
Table 7. 5: Summary of FALL cycle resonance frequency for CB-3.....204
Table 7. 6: Example of four sensor detector.....216

# List of Figures

Figure 1. 1: a) Optical-electrical-optical (OEO), and b) all-optical data link. ..... 2
Figure 1. 2: Fiber attenuation vs. wavelength. [56]. ..... 16
Figure 1. 3: Parallel-plate actuators: a) *normal* force, b) *tangential* force. The direction of the force and movement of the plates is such that the total capacitance is increased. ..... 22
Figure 1. 4: Lateral (evanescent) coupling (top view schematic). ..... 23
Figure 1. 5: End–coupling (top view schematic). ..... 24
Figure 1. 6: Resonating cantilever waveguide for environmental sensing. ..... 25

Figure 2. 1: Intrinsic strain: a) cantilevers, b) measured cantilever curvature, c) doubly-clamped beams, and d) measured doubly-clamped beam buckling. ..... 30
Figure 2. 2: Nanoindentation setup: a) schematic of nanoindenter with capacitive actuation and sensing (left), b) AFM with nanoindentation setup added on (right). ..... 32
Figure 2. 3: Beam bending schematic with point load applied to a doubly-clamped beam. ..... 33
Figure 2. 4: Beam bending of a doubly clamped beam showing clearly the linear and nonlinear regions of displacement. The experiments were carried out in the linear region (dy < 500 nm). ..... 34
Figure 2. 5: Young's modulus measurement using beam bending: a) neglecting intrinsic compressive stress (left), and b) including the effects of intrinsic stress (right). In (a) the curve fit is a polynomial, while in (b) the fit is linear. ..... 36
Figure 2. 6: Electrostatic testing: beam bending with applied electrostatic pressure load. ..... 37
Figure 2. 7: Electrostatic beam bending: a) 0V (top), b) 8.8V (bottom). ..... 38
Figure 2. 8: Tensile stress engineering: trace amounts of gallium (Ga) counter the effects of arsenic (As) contamination during MBE growth. Doubly-clamped beams are flat, while cantilevers are curled due to an intrinsic strain gradient. ..... 39

Figure 3. 1: Various III-V compound semiconductor systems, including the InGaAsP system. The dashed horizontal line indicates materials that can be grown lattice-matched to InP substrates (adapted from reference [62]). ..... 44
Figure 3. 2: InP-based waveguide: a) InP top/bottom cladding, b) air cladding. ..... 48
Figure 3. 3: Typical MATLAB output window for a set of core and cladding layers for an InP-based MEMS waveguide: a) refractive index, $n$, vs. wavelength, b) summary of output parameters. The input parameters are $x_{Ga}$ and $y_{As}$. ..... 50
Figure 3. 4: Top view diagram of suspended waveguide indicating Gaussian expansion of beam waist in the tether region [76]. ..... 54
Figure 3. 5: Released InP waveguide with tethers [9]. ..... 54
Figure 3. 6: Waveguide propagation loss as a function of number of tethers [9]. ..... 57
Figure 3. 7: Waveguide loss as a function of tether width for 15 tethers [9]. The inset shows the effects of lithography and rounding of corners on the effective tether width. ..... 58

Figure 4. 1: Layer structure 1 with InP-based 2 μm core and 1 μm top and bottom cladding ("InP cladding" design). ..... 62
Figure 4. 2: Layer structure 2 with InP-based 1.5 μm core and air top and bottom cladding ("air cladding" design). ..... 63
Figure 4. 3: General process flow for InP-based optical waveguide MEMS devices fabricated on a semi-insulating (SI) substrate. ..... 64
Figure 4. 4: InP waveguide sidewall after RIE in methane-hydrogen chemistry. ..... 68
Figure 4. 5: Cleaved cross-section of InP waveguide (before sacrificial etch). ..... 68
Figure 4. 6: Island formation due to "balling up" of the AuGe alloy after annealing (RTA). ..... 70
Figure 4. 7: Cleaved waveguide facets after thinning of the chip. ..... 71
Figure 4. 8: Sacrificial etch bars with varying widths of 2 – 18 μm. The etch bars of width smaller than 10 μm have been sacrificially etched and lifted off. ..... 73
Figure 4. 9: Released cantilever test structures after supercritical drying. ..... 74
Figure 4. 10: Aluminum mount (26 mm × 7 mm × 3 mm). The dark region is the chip. ..... 75
Figure 4. 11: Side view of aluminum sample holder with mounted chip. This view shows the 1 mm notch (depression) in the holder for mounting the 200 μm thick chip. ..... 75

Figure 5. 1: Guided TE-modes in a two-dimensional slab dielectric waveguide for modes $m$=0, 1, 2, 3, and 8; $n_2 < n_1$. (adapted from [86]). ..... 78
Figure 5. 2: a) Waveguide with mode 1 and propagation constant $\beta_1$, b) waveguide with mode 2 and $\beta_2$, c) superposition of modes 1 and 2 (adapted from [86]). ..... 79
Figure 5. 3: Coupling between two slab waveguides (core refractive indices $n_1$ and $n_2$ and cladding index $n$). Mode $m$ = 0 is initially in waveguide 1 ($z = z_1$), but eventually couples to waveguide 2 ($z = z_2$). It resides completely in waveguide 2 after traveling length $L_C$ ($z = z_3$) (adapted from [86]). ..... 80
Figure 5. 4: MEMS evanescent coupler: a) top view schematic at $V$=0, b) schematic of coupled *power* ($P$) with actuated waveguides at $V$=$V_{PI}$ (pull-in) and coupling length $L_C$, c) optical coupling of *fields* (field amplitude, $A$) via mode interference ($V$=$V_{PI}$), d) coupled power along z-axis ($V$=$V_{PI}$). ..... 86
Figure 5. 5: Pull-in actuator with movable top electrode and fixed bottom electrode separated by initial gap $g_0$. ..... 88
Figure 5. 6: Half-structure model: a) two movable waveguides with applied actuation voltage, $V_0$, b) equivalent model with electrically-neutral axis (dashed line), c) single movable waveguide at $V_0/2$ and fixed ground plane (dashed line). ..... 89
Figure 5. 7: Calculated pull-in voltage for various MEMS coupler designs. ..... 90
Figure 5. 8: Typical OWMS simulation of two coupled waveguides (cross-section view). The image on the right shows the simulated optical power in the waveguide. ..... 91
Figure 5. 9: a) coupling length, $L_C$, and coupling coefficient, $\kappa$, vs. waveguide *gap*, b) polarization dependence, $\kappa_{S\text{-polarization}}/\kappa_{P\text{-polarization}}$ (TE vs. TM). ..... 93
Figure 5. 10: BeamPROP simulation (mode of $m$=0, $\lambda$=1550 nm, TE-polarization) for *gap* = 60 nm: a) top view of power distribution, b) variation in coupled power. ..... 94

Figure 5. 11: BeamPROP simulation for modes $m = 0$, 1, 2. The $m = 0$ mode exhibits the longest coupling length, $L_C$ and contains most of the optical coupled power, while the $m = 1$, 2 modes only represent 1 % or less of the power in the $m = 0$ mode. Parameters: waveguide $w = 2$ μm, *gap* = 60 nm, $\lambda = 1550$ nm (TE). .....95
Figure 5. 12: MEMS coupler: a) top view, b) detail of suspended waveguides in the coupling region (*gap* = 1 μm, before actuation), c) detail of sidewall roughness. .....97
Figure 5. 13: Optical test setup schematic. .....98
Figure 5. 14: Optical test setup: a) monitor view of lensed fiber and waveguide (top left), b) complete setup (right), c) detail of chip and probes (bottom left). .....98
Figure 5. 15: Substrate leakage current via a 4500 Å thick InP buffer layer. .....99
Figure 5. 16: a) I-V measurements for $R_{13}$ and $R_{23}$, b) calculated Joule heating. .....101
Figure 5. 17: Electro-thermally actuated coupler: a) actuation, b) *BAR* output, c) *CROSS* waveguide optical output. .....101
Figure 5. 18: Measured pull-in voltage for various coupler test structures along with the calculated pull-in voltage from Figure 5. 7. Inset: pull-in test structure. .....103
Figure 5. 19: Coupling length during pull-in for an $L = 500$ μm device (*coupler 1a*). .....105
Figure 5. 20: Stiction in an $L = 1000$ μm coupler (*coupler 2b*) at $V = 0$ after initial pull-in: a) top view of complete coupler, b) magnified view of stiction region. .....106
Figure 5. 21: Switching in *coupler 2b*: a) actuation, b) $P_{BAR}$, c) $P_{CROSS}$, d) loss. .....107
Figure 5. 22: Switching speed: a) risetime for coupler 1a, b) falltime for coupler 1a, c) risetime for coupler 2a, d) falltime for coupler 2a, e) risetime for coupler 2b (gap << 2 μm), e) falltime for coupler 2b (gap << 2 μm). .....108
Figure 5. 23: Variable optical coupling in *coupler 2b*. .....111
Figure 5. 24: Variable optical coupling in *coupler 3b*. .....112
Figure 5. 25: Polarization dependence: a) TE-, b) TM-polarization ($\lambda = 1550$ nm). .....113
Figure 5. 26: a) Comb-drive coupler (OFF), b) comb-drive coupler (ON, V > 0), c) third-electrode coupler (OFF), d) third-electrode coupler (ON, V > 0). .....118
Figure 5. 27: Measured optical power in the comb-drive coupler. .....119
Figure 5. 28: Third-electrode coupler: a) actuation; b)-f): $P_{CROSS}$; b) $V_{Sine}$=5.029 V, c) 6.226 V, d) 6.601 V, e) 6.820 V. Grey line: data; black line: 20 point average. .....121
Figure 5. 29: Air cladding couplers with 1.0 μm thick core (n=3.173): a) characteristic coupling length, $L_C$, for S-polarization, b) $\kappa_{S\text{-}pol}/\kappa_{P\text{-}pol}$. .....122

Figure 6. 1: End-coupling between waveguides with $\phi_1(x,y,z)$ and $\phi_2(x,y,z)$. .....126
Figure 6. 2: Schematic of 1×2 end-coupled waveguide switch. .....133
Figure 6. 3: Comb-drive actuator: a) rest state ($V = 0$), b) actuated state ($V > 0$). .....134
Figure 6. 4: Capacitive actuation via the normal and tangential electrostatic forces between two electrodes. .....134
Figure 6. 5: Calculated comb-drive force for $N = 80$ comb-pairs ($h = 4$ μm). .....135
Figure 6. 6: a) fixed-fixed beam (FB) suspension, b) Y-suspension (Y-S), c) double-serpentine suspension (2-SS), d) Y-serpentine suspension (Y-SS). .....137
Figure 6. 7: Simulated switching force for various suspensions, assuming 2 μm displacement. Parameters: 400 μm wide comb-drive ($N = 80$ comb-pairs). .....138

Figure 6. 8: Calculated switching voltage: double-serpentine suspension (2-SS). .....138
Figure 6. 9: a) End-separation, b) axial offset, and c) angular misalignment. .....140
Figure 6. 10: a) Simulated Gaussian mode, b) 1/e beam waist, $w_X$, c) 1/e waist, $w_Y$. .....141
Figure 6. 11: Calculated end-separation coupling loss due to beam divergence (gray box: 1.55 μm air gap). .....142
Figure 6. 12: Calculated coupling loss due to end-separation. .....144
Figure 6. 13: Calculated Fabry-Perot loss vs. wavelength for fixed gap=1.55 μm. .....145
Figure 6. 14: Crosstalk: a) 2.0 μm maximum offset, b) detail, showing only 0.5 μm maximum offset. Offset = 0 μm is the $V$ = 0 rest position of the input waveguide. At offset = –2 μm the input and output waveguides are fully aligned. .....147
Figure 6. 15: Coupling loss due to angular misalignment in $x$- and $y$-direction. .....148
Figure 6. 16: Scattering loss per facet as a function of RMS surface roughness. .....150
Figure 6. 17: Strain relaxation in various 1×2 end-coupled switches after release. The L = 1600 μm exhibit strain relaxation and displacement of the comb-fingers. .....152
Figure 6. 18: a) Complete 2-SS type end-coupled switch, b) detail of movable input and fixed output waveguides, c) detail of comb-drive actuator. .....153
Figure 6. 19: Optical end-coupled power vs. DC actuation voltage. .....154
Figure 6. 20: Comparison of the experiment (Figure 6. 19) with the optical model. .....156
Figure 6. 21: Temporal response of optical switch (square actuation voltage). .....158
Figure 6. 22: Resonance behavior of the optical switch (sinusoidal actuation). .....158
Figure 6. 23: Asymmetric structure with regard to input and output cross-sectional area for a Y-suspension (Y-S) type device: a) before sacrificial release etch, b) after release etch and strain relaxation. .....160
Figure 6. 24: Pull-in type switch. As shown, the input will align with output 2. .....162
Figure 6. 25: SEM of pull-in type end-coupled switch. .....162
Figure 6. 26: Out-of-plane deflection of cantilever tip after sacrificial release for $W$ = 1.0 and 1.5 μm wide waveguides. Note: $W$ = 1.0 μm has a uniform measurement error. .....163
Figure 6. 27: Temporal response: a) actuation signal, b) optical coupled output. .....165
Figure 6. 28: Schematic of pull-in type cantilever switch. .....166
Figure 6. 29: SEM of cantilever waveguide switch. .....166

Figure 7. 1: Basic measurement approach of environmental (chemical/biological) sensors using MEMS transducers [36]. .....170
Figure 7. 2: Environmental sensors: resonant (left) and static (right) [36]. .....171
Figure 7. 3: Micro- and nanoscale structures have energies and resonant frequencies approaching the vibrational modes of single molecules [36]. .....172
Figure 7. 4: Cantilever position measurement using an optical detection technique commonly used in atomic force microscopes (AFM's) [36]. .....175
Figure 7. 5: Electrostatically-actuated cantilever waveguide sensor. .....177
Figure 7. 6: Calculated resonance frequencies for cantilever sensors. .....180
Figure 7. 7: Calculated optical power vs. cantilever waveguide displacement, assuming zero gap between waveguide facets. .....185
Figure 7. 8: Frequency sweep with sinusoidal actuation voltage. .....187
Figure 7. 9: Frequency sweep with Lorentzian curve fit ($V_{Sine}$ = 6 Vp-p). .....187

Figure 7. 10: Cantilever phase shift (vertical dashed lines): a) $f < f_0$, 180° phase shift, $\Delta\phi$, between actuation and optical power, b) $f \approx f_0$, $\Delta\phi$=90°, C) $f > f_0$, $\Delta\phi$=0°.....188
Figure 7. 11: 'Ringing' measurement with square wave actuation voltage.....190
Figure 7. 12: a) Square wave actuation signal, b) optical output 'ringing,' c) ringing period, *T*, and decay time constant, $\tau$ (RISE cycle). .....190
Figure 7. 13: a) Magnitude FFT, b) Magnitude $j\omega\cdot$FFT and Lorentzian curve fit. Data taken from FALL cycle (CB-3, $V_{DC}$ = 10 Vp-p), Lorentzian curve fit for f = 146 – 220 kHz to obtain resonant frequency, $f_0$ (Rsq. = 0.998).....192
Figure 7. 14: Measured resonance frequencies for three cantilever sensors from ringing technique and extracted *T* and $\tau$ and eqn. (7.9).....194
Figure 7. 15: Detail of FIB milled cantilever sensor. .....196
Figure 7. 16: Measured resonance frequency shift after FIB milling of cantilever.....196
Figure 7. 17: Electrostatic tuning: a) $j\omega\cdot$FFT magnitude, b) resonant frequency.....199
Figure 7. 18: a) Mechanical oscillation of input cantilever waveguide (one period), b) optical coupled output power (two high-low cycles).....201
Figure 7. 19: Frequency doubling: a) actuation, b) optical ringing, c) electrostatic tuning (RISE cycle, left) and frequency doubling (FALL cycle, right).....201
Figure 7. 20: a) FALL cycle resonance curves for FALL cycle for different $V_{DC}$, b) extracted resonance frequencies as a function of actuation voltage.....203
Figure 7. 21: Repeatability measurements for $V_{DC}$ = 9.6 V (FALL cycle). .....205
Figure 7. 22: a) Calculated output power vs. input cantilever displacement, b) sensitivity dP/dx (normalized). Beam waist $w_X$ = 0.631 μm, $\lambda$ = 1550 nm (TE).....206
Figure 7. 23: Measured optical power vs. DC actuation (static measurement). The voltage squared gives the electrostatic force and, roughly, the displacement. .....208

Figure 8. 1: InP-based in-plane MEMS-tunable Fabry-Perot filter [179]. .....223
Figure 8. 2: Measured filter spectral response (adapted from [179]). .....223
Figure 8. 3: Micro-ring resonator optical filter with bus input and output waveguides coupled evanescently to the ring (adapted from [27]). .....224
Figure A. 1: Output window: a) core and cladding refractive index vs. Wavelength, b) summary of core and cladding properties. .....234

Figure B. 1: Waveguide with confinement in the y-direction using perfect mirrors and wave propagation in the z-direction: a) ray-optics, b) TEM plane waves, c) interference pattern of TEM plane waves is invariant along the *z*-direction, d) electric field distribution for modes *m* = 1, 2, 3, and 6 (adapted from [86]). .....237
Figure B. 2: Dielectric slab waveguide (adapted from [86]). .....239
Figure B. 3: Plot of transcendental eqn. (B.10) for extracting the bounce angle $\theta_m$ for a mode *m* (adapted from [86]).....241
Figure B. 4: Graphical illustration of the maximum modes in a slab waveguide [86].....243
Figure B. 5: Modes *m* = 1, 2, and 3 in a multi-mode waveguide [56].....243

Figure C. 1: Coupling between two slab waveguides. Mode *m* = 0 is initially in the *BAR* waveguide ($z = z_1$), but eventually couples to the *CROSS* waveguide

($z = z_2$). It resides completely in the *CROSS* waveguide after traveling length $L_C$ ($z = z_3$) (adapted from [86]).....246
Figure C. 2: Even ($m$ =0) and odd ($l$ = 1) modes (left), b) mode overlap resulting in zero overlap integral (right).....249
Figure C. 3: Dielectric slab waveguide with guided ray (lower-order mode) and unguided mode (extreme case of higher-order mode).....250
Figure C. 4: BeamPROP simulation of coupled power for modes $m$ = 0, 1, 2. The $m$ = 0 mode exhibits the longest characteristic coupling length, $L_C$. However, it also contains most of the coupled power, with the $m$ = 1, 2 modes only representing 1 % or less of the power in the $m$ = 0 mode. Parameters: waveguide refractive index $n$ = 3.17, width $w$ = 2 μm, $gap$ = 60 nm, λ = 1550 nm, TE-polarization.....252

Figure D. 1: Schematic of pull-in actuator with movable ($k_{Mechanical}$) and fixed electrode.....256

Figure E. 1: Comb-drive actuator: a) V=0 (rest), b) V > 0 (actuation).....262
Figure E. 2: Simplified schematic using two parallel-plate electrodes: a) normal force (left), b) tangential force (right). Comb-drive actuators take advantage of tangential forces.....262
Figure E. 3: Comb-drive actuator schematic illustrating zero net normal force and non-zero net tangential force.....264

Figure F. 1: Ringing Data: a) actuation, b) optical rining, c) detail of RISE data.....267
Figure F. 2: a) Extracted FFT data, b) jω·FFT data.....268

# CHAPTER 1

# INTRODUCTION

## 1.1 Introduction

There is great interest in creating so-called optical integrated circuits (OIC's) or photonic integrated circuits (PIC's) that are capable of switching *optical* rather than *electrical* signal [1]. The fundamental difference between existing optical networks and future *all-optical* networks is illustrated in Figure 1. 1. Current data networks typically handle several signal formats by transmitting optical signals over long distances via single-mode fibers and performing data manipulation, such as switching and filtering, on electrical signals. Therefore, current networks require an optical-electrical-optical (OEO) signal conversion step, one that is costly in terms of network speed, bandwidth, power consumption, hardware complexity, and signal integrity (noise). It is expected that future networks will avoid the OEO signal conversion step by performing all data manipulation directly on optical signals, thereby greatly increasing network performance. The field that will enable all-optical data manipulation is referred to as integrated optics. It is envisioned that integrated optical circuits will eventually reach a complexity similar to that of very large-scale integrated (VLSI) electronic circuits.

This dissertation presents research combining micro-electro-mechanical systems (MEMS) and 'traditional' indium phosphide (InP) waveguide technology for all-optical switching applications. MEMS are promising for wavelength-division multiplexed communications due to their potential for wavelength and polarization independence, low power, and low crosstalk [2-5]. Indium phosphide (InP), a III-V compound

semiconductor, is a desirable material from an integrated optics point of view since InP and InP-based materials (indium-gallium-arsenide-phosphide, or InGaAsP) enable optical gain at 1550 nm, the wavelength at which standard optical fiber exhibits minimal attenuation.

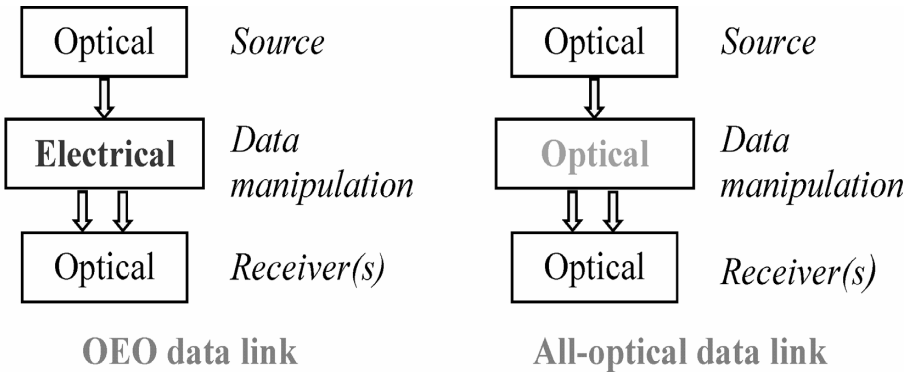


**Figure 1. 1: a) Optical-electrical-optical (OEO), and b) all-optical data link.**

## 1.2 Research Accomplishments

The specific research accomplishments in this dissertation research are as follows:

- **Mechanical characterization of thin-film InP-based micromechanical films and structures:** The merging of InP-based waveguide technology with MEMS is not a trivial endeavor. For one, InP is not a traditional MEMS material and is known to be less robust compared to silicon or gallium arsenide in terms of hardness and fracture strength [6]. Consequently, initial work focused on developing a suitable layer structure and fabrication platform for InP-based optical waveguide MEMS. The micro-mechanical properties of thin-film InP grown by molecular beam epitaxy (MBE) were then measured to ascertain its

applicability as a MEMS material [7]; this work was performed for my Master's thesis [8].

- **Platform technology for MEMS-actuated InP optical waveguides:** The 'suspended waveguide technology' [9] was developed to enable *movable* InP-based waveguides that can be electrostatically actuated. Testing and characterization of static waveguides was performed by Mr. Daniel Kelly [9], although the concept and idea are my own. I extended the initial work on suspended waveguides to incorporate MEMS-*actuated* waveguides.

Once these basic building blocks for InP-based MEMS optical waveguide technology were developed, several InP-based electrostatically-actuated optical waveguide devices were designed, fabricated, and experimentally characterized:

- **MEMS-actuated evanescent coupler:** In this device, two parallel movable waveguides are optically coupled. By varying the spacing between the two movable waveguides via electrostatic pull-in actuation, the amount of power transfer between the waveguides is controlled. Both optical switches and variable optical couplers are demonstrated.
- **MEMS-actuated end-coupled switch:** Rather than using two parallel waveguides, a single movable input waveguide is actuated to align axially with one of two fixed output waveguides. Coupling proceeds via end-coupling (also referred to as butt- or end-fire coupling). Instead of pull-in actuation, comb-drive actuators and serpentine suspensions are used to ensure low-voltage operation.

- **Cantilever waveguide resonant sensor:** The end-coupled switches are modified for environmental sensing applications. A single movable cantilever input waveguide is end-coupled to a single fixed output waveguide. The cantilever can be made to resonate at its natural frequency via electrostatic actuation. By measuring the modulated coupled optical power at the output, the resonance frequency is obtained. Changes in the resonant frequency reflect changes in the environment due to chemical or biological agents.

## 1.3 All-Optical Switching

All-optical switching refers to the direct manipulation and routing of optical signals without the need for an intermediate conversion to electrical signals before switching takes place. In this section, current approaches for all-optical switching are reviewed. Both 'traditional' and MEMS-based switches are covered using representative examples from the literature. However, the reader should be aware that this discussion is by no means complete as new devices are constantly being reported. Additional literature is presented in Chapters 5-6, and a review of resonator sensors is given in Chapter 7.

### 1.3.1 Literature Review: "Traditional" Optical Switches

'Traditional' all-optical integrated waveguide switches, defined here as devices that do not involve MEMS and have no moving parts, generally make use of one or a combination of several mechanisms: a) thermal effects, b) electro-optic effects, c) acousto-optic effects, or d) non-linear optical effects. Some representative examples from the literature are now reviewed.

*a) Thermal effects*

Localized heating of a semiconductor or dielectric waveguide causes a slight volume expansion and a corresponding change in the refractive index. This in turn results in an optical path difference and hence an optical phase shift that can be used for switching [10]. For example, a Mach-Zehnder Interferometer (MZI) has been combined with a micro-heater in one of the two $SiO_X$-$SiO_2$ waveguides comprising the MZI [11]. This type of configuration has resulted in a 2×2 switch with rise- and fall-times of 150 μs and 180 μs, respectively, and power consumption of 110 mW (2.9 V and 37.8 mA) at 1550 nm wavelength operation. A 16×16 switch using silica-on-silicon technology has also been reported requiring 17 W total switching power [12]. This technology is relatively mature, with a fully-packaged 2x2 thermo-optic polymer waveguide switch already reported [13].

Although thermo-optic switches are simple and effective as switches, they do have a significant shortcoming. For example, thermal switches are typically slow with switching times in the 1 ms range. Also, they require significant power in the mW range or greater. This can become prohibitive in large-scale switch networks.

*b) Electro-optic effects*

Electro-optic devices make use of either 1) the linear electro-optic effect (Pockels effect), 2) the non-linear electro-optic effect (Kerr effect), or 3) electro-absorption (via the Franz-Keldysh effect or the Quantum Confirmed Stark Effect [14]) [15]. The linear and non-linear electro-optic effects cause a change in the refractive index of a waveguide if an electric field is applied. This change in the refractive index causes a phase shift that

can be exploited for switching applications. The electro-optic effect has been applied to GaAs/AlGaAs Y-junction waveguides and has resulted in low-voltage (6 V) switching with −12 dB crosstalk at 1.06 μm wavelength [16]. A similar device utilizing InGaAsP Y-junction waveguides has also been demonstrated with 10 dB modulation depth (7 V applied reverse bias) at 1530-1570 nm wavelength [17].

The Franz-Keldysh electro-absorption effect refers to the shift in the absorption or bandgap edge (band bending) in a semiconductor with the application of an electric field [15]. For example, consider a waveguide that is (just barely) transparent at wavelength $\lambda_1 > \lambda_{g1}$, where $\lambda_{g1}$ is the bandgap wavelength. The application of an electric field will cause the absorption band edge to shift to a longer wavelength $\lambda_{g2} > \lambda_{g1}$ so that the waveguide is no longer transparent at $\lambda_1 < \lambda_{g2}$. Electro-absorption modulators were used in a 2×2 InGaAsP switch resulting in 30 dB modulation depth (2.5V applied reverse bias) at 1570 nm wavelength [18].

Electro-optic switches are attractive due to their high-speed and low-power requirements. However, they require materials that exhibit these types of effects and are often expensive and thus not suitable for large-scale deployment. Furthermore, they often require complex fabrication processes, which limits integration with electronics and other components.

*c) Acousto-optic effects*

The acousto-optic effect, or scattering from sound waves, is called Brillouin scattering. It can be thought of as "scattering of light from acoustic phonons" [19]. Most acousto-optic devices fall into one of two types: 1) *Bragg* scattering, in which the

interaction length is long so that phase matching becomes important, and 2) *Raman-Nath* scattering, in which the interaction length is short so that phase matching is not an issue [19]. In essence, acoustic waves will create a density variation in the material of interest. This density variation results in a grating-like variation in the refractive index which will scatter light. It is this scattering, together with phase matching considerations, that can be utilized to create optical modulators and switches.

A 3×3 fused-fiber acousto-optic switch requiring 4 mW of power at 1550 nm wavelength has been demonstrated with switching times of 100 μs [20]. Polarization-independent switching has also been reported using fused-fiber couplers with non-uniform cross-sections [21]. The use of surface acoustic waves (SAW) for efficient acousto-optic modulation at low drive powers has also been proposed [22].

Acousto-optic switches have several limitations. For one, acousto-optic effects typically lead to large channel crosstalk and may increase the cost and complexity of optical switches due to the difficulty of large-scale integration, although 8x8 acousto-optic switches with 26 dB crosstalk have recently been demonstrated [23]. Another limitation of acousto-optic switches is the significant energy requirement for inducing strain via mechanical energy (acoustic waves). Typically, mW of power (or more) is therefore required for switching.

*d) Non-linear optical effects*

Non-linear optical effects include all those effects in which light guiding materials respond in a non-linear manner to a driving effect (and thus may include some of the effects already described above). In general, this driving effect is light itself.

Consequently, only lasers are typically used to study non-linear optics because non-linear optical effects only become significant for the high light intensities possible with lasers [19]. Although the study of non-linear optics can include electro-optic and acousto-optic effects, only those effects not discussed in previous sections are now presented. For example, optical bistability (switching) was recently demonstrated in a ring-resonator filter by exploiting the thermo-optic effect of silicon [24] – but this thermo-optic effect was induced via an optical signal and thus is considered a non-linear optical effect.

Modulation of the transmittance in an amorphous silicon/silicon oxide photonic crystal using the optical Kerr non-linearity has been demonstrated [25]. This optical Kerr non-linearity is similar to the electro-optic Kerr effect, except that a high intensity *optical* signal is used in place of an applied *electric* field. In the experiment an optical pump signal at 1.71 μm wavelength and high intensity (18 GW/cm$^2$) was used to modulate the refractive index of the photonic crystal. A probe signal (the information carrying signal) at 1.51 μm wavelength was then modulated as it passed through the crystal. Simulation of an all-optical switch relying on modification of the refractive index via optical pumping and electron-hole generation has also been reported [26]. Recently, a similar approach for all-optical switching has been experimentally demonstrated using optical pumping (carrier injection, electron-hole generation) of a GaAs-AlGaAs micro-ring resonator [27].

Non-linear optics is still in the research stage, with few products – if any – available at present. Among the possible reasons are that non-linear optical effects are only significant in certain materials and may require high intensity light sources before

the nonlinear optical effects become useful. This limits the possibility of integrating the devices with existing optical networks.

### 1.3.2 Limitations of Traditional Optical Switching Technology

The preceding section (section 1.3.1) has presented a number of 'traditional' (i.e. *non-MEMS*) approaches for all-optical switching. However, all of these approaches have some limitation, as indicated in Table 1. 1 (based on reference [28]). For example, thermal switches are typically slow and require significant power. Electro-optic switches require materials that exhibit these types of effects and are often expensive and/or require complex fabrication processes. Acousto-optic devices typically exhibit relatively large channel crosstalk and may increase the cost and complexity of optical switches due to the difficulty of large-scale integration. Finally, non-linear optical effects are only significant in certain materials and may require high intensity light sources before the nonlinear optical effects become useful.

Clearly, an optical switching technology must be developed that is large bandwidth, inexpensive, requires only simple processing, can be fabricated in any number of material systems (i.e. the switching mechanism is not material dependent), consumes little power, and can be operated at reasonably fast switching speeds. It turns out that MEMS enables all of these constraints to be met. The only possible concerns are reliability and speed – which are not prohibitive, as will be shown.

MEMS can be made extremely reliable, as is evident by the numerous MEMS products currently available. For example, MEMS accelerometers are now standard in automobiles [29], and the Digital Mirror Display (DMD) is now commonly used in

projector and display technology [30]. Furthermore, MEMS/NEMS (nano-electro-mechanical systems) resonators have been demonstrated with up to 1 GHz frequency [31] so that extremely high-speed MEMS devices appear possible in the near future.

**Table 1. 1: Comparison of various non-MEMS optical switching technologies [28].**

| **Technology** | **Advantages** | **Limitations** |
|---|---|---|
| Thermal | 1) Simple fabrication,<br>2) inexpensive materials | 1) Switch power (> 100 mW)<br>2) Slow speed (~ ms) |
| Electro-optic | 1) High-speed (ns),<br>2) Low-voltage (< 10 V) | 1) Expensive,<br>2) Integration issues |
| Acousto-optic | 1) High speed (μs)<br>2) Broad tuning range for filter | 1) Large-scale integration<br>2) Require piezo-materials or external actuators |
| Non-linear optic | 1) High-speed (< ns),<br>2) light source for switching | 1) Expensive,<br>2) Integration issues |
| MEMS | 1) Low-loss, low crosstalk<br>2) Wavelength and/or polarization independent | 1) Require new process technology<br>2) Long-term reliability<br>3) Speed (?) |

### 1.3.3 Advantages of MEMS

Recently, there has been considerable interest in using MEMS technology for all-optical switching applications [3, 5]. Micro-electro-mechanical systems (MEMS) are fabricated in a manner similar to integrated circuits and have dimensions in the micron range (occasionally, nanometers or millimeters). However, since MEMS often comprise

moving parts, two types of fabrication processes are employed to create free-standing stuctures: bulk- and surface micromachining. In bulk micromachining [32], material is removed from the bulk substrate. This enables the realization of free-standing structures formed from overlying thin films. Surface micromachining [33] does not remove substrate material. Rather, several thin films are deposited on the substrate, and the top most layer remains, while an underlying layer is selectively removed, thereby creating free-standing structures.

Free-standing or movable MEMS devices created by bulk- or surface micromachining generally comprise *sensors* or *actuators*. Examples of MEMS sensors include accelerometers used for airbag deployment in automobiles [29], pressure sensors [34, 35], and chemical sensors [36]. Actuators include micro-motors [37] (electrostatic [38] and magnetic [39]) for precision movements, micro-heaters [40] for biological and chemical applications, and miniaturized speakers [41] for communications. While MEMS often employ moving parts, this is not a strict requirement: for example, microfluidic devices [42] often only comprise miniature fluidic channels and no moving parts. Similarly, micro-heaters or imagers contain no moving parts. Therefore, MEMS must be viewed as a broad field encompassing many different technologies. The unifying trend in MEMS, however, is the ability to sense or act upon the environment (in a broad context) – that is, MEMS comprises *sensors* and *actuators*.

Now, why employ MEMS for all-optical switching (i.e. optical MEMS or MOEMS)? For one, the optical path difference in optical switching is of the order of a wavelength (a few hundred nm to around one micron). Therefore, low power MEMS actuators [3] are ideally suited for providing the small required optical phase shifts.

MEMS also have the potential for low crosstalk, insensitivity to both wavelength and polarization, and enable large-scale switch networks with a large number of ports [43]. Most importantly, few other approaches offer both low power consumption and low loss. For this reason, MEMS is a promising technology that may provide a low cost approach for developing very large scale integrated optical (optical-VLSI) switching networks.

Some of the potential drawbacks of MEMS, as indicated in Table 1. 1, include the relatively slow switching speed as well as the long-term device reliability. This research, however, will show that waveguide MEMS optical switches enable speeds approaching 1 μs and possibly faster, which is competitive with non-MEMS approaches such as acousto-optic devices. Furthermore, the long-term performance of MEMS can be very reliable, as demonstrated by the success of products by Texas instruments [30, 44] and Analog Devices [29]. Finally, while the devices in this work are made of InP-based materials and are thus suitable for providing *active* optical gain, *passive* devices can be readily fabricated from inexpensive materials (such as silicon-on-insulator, SOI) without change in the basic design. Therefore, the present MEMS approach is both flexible and inexpensive while at the same time providing excellent performance in terms of loss, size, scalability, and speed.

### 1.3.4 Literature Review: *MEMS* Optical Switches

A number of optical MEMS switches have already been demonstrated. These generally comprise: 1) free-space optical switches, and 2) guided wave optical switches. Some representative examples from the literature are now reviewed.

#### 1.3.4.1 Free-space Optical MEMS Switches

Free-space devices generally refer to those devices in which light is not confined but propagates through free-space (i.e. air). Switching is usually accomplished by using small, movable mirrors to redirect the beam of light to a desired output port.

Texas Instruments, for example, developed a digital micromirror device (DMD), which utilizes micromirrors and electrostatic actuation to produce a projection display technology [30, 44]. This type of optical MEMS device is now prevalent in overhead projectors. Lin et al. used a similar technology to develop a free-space optical switch for optical networks [45]. The experimentally demonstrated 8×8 port switch utilized poly-silicon mirrors coated with gold and exhibited sub-millisecond switching times at ±100 V square wave actuation signal. Using movable mirrors, 256×256 [46, 47] and 512×512 matrix [48] switches have also been demonstrated and are currently being deployed in systems. Thermal actuation has also been used to actuate micro-mirrors in switching applications [49]. A 2×2 switch with poly-silicon/CrAu resistive heating actuator exhibited switching times of 400–600 μs and losses of 0.55–0.7 dB.

While free-space optical MEMS devices have been the most successful so far – as demonstrated by the numerous products already available today – there are some serious limitations. For one, the size of individual mirrors is typically large: 500 μm diameter for the Lucent LambdaRouter matrix switch [48]. Second, mirrors limit the ability for monolithically integrating active optical devices on-chip. Free-space switches therefore require a hybrid approach in which the mirrors are passive and any active optoelectronics (laser sources, semiconductor optical amplifiers, etc.) are located on a separate chip. Third, due to the relatively large mass of the moving mirrors, the switching speed is

limited to around 500 μs to 1 ms. Clearly, in order for high-speed, densely-integrated optical MEMS devices to be realized, a different technology must therefore be utilized.

#### 1.3.4.2 Guided Wave Optical MEMS Switches

An alternate approach to free-space optical MEMS switching utilizes actuated moving waveguides. Waveguide optics means that light is confined and thus does not suffer from diffraction losses as free-space optics does. Furthermore, guided-wave optics devices can be made very small and enable a large number of devices on a single chip.

*Ollier et al.* demonstrated a 1×2 opto-electro-mechanical switch as early as 1995 by fabricating movable silica waveguides on a silicon-based MEMS platform [43, 50]. The initial switch demonstration required 270 V for actuation and exhibited 3.5 dB loss [50]. Continued development of these switches has improved their performance to <70 V actuation with losses of 0.3 dB or better and switching times of < 1 ms [43]. Gallium arsenide (GaAs) based moving waveguide switches with actuation voltages as low as 3.3 V and switching speeds of 32 μs have already been demonstrated [51].

A 4×4 matrix of optical switches has recently been demonstrated that uses a bi-stable actuation mechanism by inserting a micro-mirror between two waveguides [52]. In this manner, power is only consumed when switching from state 1 to state 2. Stable operation in any one of the two states does not consume any power.

A different approach replaces the micro-mirrors in free-space switches with small "bubbles" of index matching oil as a switching mechanism between planar waveguides [53]. Here, a micro-heater causes expansion of a dielectric fluid in a cavity between two waveguides. In the off-state, light is reflected by 90 degrees from the facet of one

waveguide into another. When the heater is switched on, the dielectric fluid expands into a cavity and light can now pass through the cavity unhindered. Switching times of 100 ms with 0.1 W power and < 3 dB loss have been demonstrated.

Recently, silicon-on-insulator (SOI) optical waveguide MEMS have been demonstrated. Here, silicon optical waveguides and movable mirrors were fabricated monolithically on an SOI substrate. A Mach-Zehnder interferometer (MZI) was combined with movable mirrors, thereby enabling a variable phase shift between the MZI arms. This phase shift enabled optical switching (at 70 V) with 150 μs response time [54]. While the mirrors imply free-space operation, light is mainly confined in the waveguides and the free-space portion between waveguide and mirrors is 7.5 μm. Therefore, this modulator/switch is essentially a guided-wave MEMS device.

Silicon-on-insulator (SOI) has also been utilized for wavelength-selective switching by combining MEMS-acutated silicon waveguides with micro-disk resonator filters [55]. A similar approach has also been taken using micro-ring resonators made of $SiN_X/SiO_2$ in combination with a MEMS-actuated membrane [47].

## 1.4 Indium Phosphide Based Optical Devices

### 1.4.1 Why Indium Phosphide?

Most optical MEMS devices discussed above are either silicon-based or polymer-based and are thus passive. III-V semiconductors, however, have several advantages over silicon. They are direct bandgap materials and are therefore capable of producing active optoelectronic devices such as lasers and semiconductor optical amplifiers (SOAs). III-V semiconductor active optoelectronics can be operated at the 1550 nm wavelength

(for indium gallium arsenide phosphide – InGaAsP – devices). This is significant because optical fibers exhibit minimal losses at the 1550 nm wavelength, as shown in Figure 1. 2 [56]. Extremely high-speed electronics can also be developed with III-V's due to their higher electron mobility [57]. Finally, III-V semiconductors enable precise fabrication by surface micromachining, due to the ability to epitaxially grow very thin layers with abrupt transitions from one material to the next. The epitaxially grown materials can exhibit high selectivity during (wet) etching and hence facilitate the fabrication process. It is also possible to grow epitaxial layers with intrinsic stress, a useful tool for mechanical design of MEMS devices. While III-V semiconductors are by no means mainstream materials, they have been studied for many years, and relatively mature fabrication technologies exist. Therefore, these materials are at the forefront of next-generation optoelectronic devices. The mechanical characterization of InP for MEMS applications was the focus of my M.S. research [8] and is reviewed in Chapter 2. Some properties of InP are summarized in Table 1. 2.

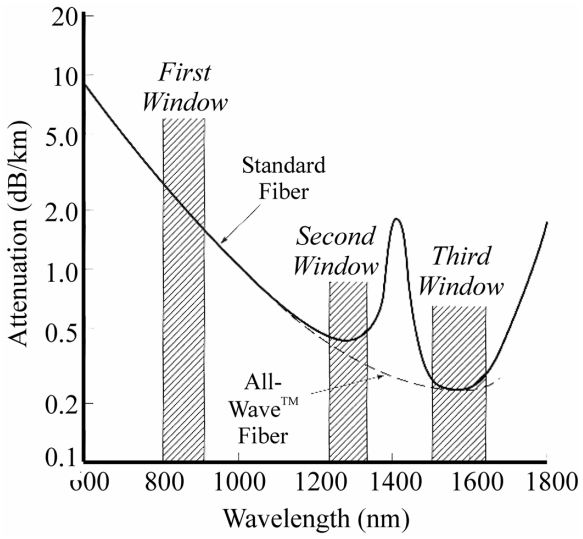


**Figure 1. 2: Fiber attenuation vs. wavelength. [56].**

**Table 1. 2: Summary of InP material properties along with those of GaAs (reference [58] unless noted) and Si (reference [59] unless noted). InP and GaAs are direct bandgap semiconductors.**

| **Property** | **InP** | **GaAs** | **Si** |
|---|---|---|---|
| Crystal structure | Zinc blend [60] | Zinc blend | Diamond |
| Crystal density ($g/cm^3$) | 4.791 [60] | 5.3176 | 2.33 [61] |
| Lattice constant (Å) | 5.8688 [60] | 5.65325 | 5.43 |
| Bandgap, Eg (eV) | 1.34 [62] | 1.42 [59] | 1.12 (Indirect) |
| Bandgap, $\lambda g$ (nm) | 920 [62] | 873 [59] | 1100 (Indirect) |
| Dielectric constant $\varepsilon$ | 12.60 [60] | 12.846 (300 K) | 11.9 |
| Refractive index | 3.41 [60] | 3.30 (300 K) | 3.45 (1550nm) [63] |
| $\mu_{electron}$ ($cm^2/V{\cdot}s$) | 5370 (300 K) [58] | 9200 (300 K) | 1450 |
| $\mu_{hole}$ ($cm^2/V{\cdot}s$) | 150 (300 K) [58] | 400 (300 K) | 450 |
| $n_{intrinsic}$ ($cm^{-3}$); *as-grown* may be higher | $1.2\times10^8$ [58] | $2.1\times10^6$ | $1.45\times10^{10}$ |
| Melting Point, $T_M$ (K) | 1335 [58] | 1513 | 1740 [6] |
| Specific heat ($J/g{\cdot}K$) | 0.322 [6] | 0.327 [6] | 0.712 [61] |
| Therm. Resist. ($K{\cdot}cm/W$) | 1.47 [6] | 2.27 [6] | 0.675 |
| Therm. Exp. ($10^{-6}/°C$) | 4.56 [6] | 5.6 | 2.6 [6] |
| Young's Modulus (GPa) | [011]: 80.4 [7] | [011]: 99.1 [60] | 136 [64] |
| Poisson's ratio | [010]-[001]: 0.357 [60] | [010]-[001]: 0.33 [60] | 0.2 (poly-Si) [61] |
| Hardness (GPa) | 6.2 [7] | 6 [65] | 12.6 [64] |

### 1.4.2 InP-Based Optical MEMS

InP-based optical MEMS have been reported in the literature in the past. Review papers on micromachining and sacrificial etching of III-V semiconductor compounds for MEMS applications appeared in 1996 (*Hjort* [66] and *Seassal et al.*[67]), and in 2000 (*Leclerq et al.*) [68].

The first demonstration of InP MEMS cantilever beams was reported in 1997 by *Greek et al.* [6], although InGaAs bridges and beams were already reported in 1996 [67]. In the work by *Greek et al.*, the strength of InP beams was evaluated using micro-beam bending, resulting in a fracture strength of 3.1 GPa.

A MEMS tunable vertical cavity Fabry-Perot filter made of InP-air Bragg reflectors was reported by *Spisser et al.* in 1998 [69, 70]. This device exhibited a total tuning range of 62 nm over 1488-1550 nm wavelengths for an actuation voltage of 14 V. A similar tunable filter was reported in 2001 by *Bondavalli et al.* [71, 72] with 100 nm tuning range at 11 V. Better filters have been reported over the years with tuning ranges of 112 nm at 5 V (*Daleiden et al.* [73]) and 140 nm at 3.2 V and 0.2 mA (*Irmer et al.* [74]). Recently, a record tuning range of 160 nm has been obtained in a tunable vertical cavity filter with high mirror reflectivity over an 1100 nm spectral range [75].

Most InP-based MEMS have concentrated on free-space optical devices with vertical cavities, i.e. tunable Fabry-Perot filters. The research in this dissertation differs in two respects from previous work: 1) optical waveguides are used instead of free-space mirrors, and 2) the devices require *in-plane* motion rather than *vertical* motion and vertical cavities. Both aspects of this work will enable high-density optical integration

rather than the hybrid integration inherent in vertical motion devices and sets the present work apart from previous research.

An important aspect of this work concerns the mechanical properties of InP for MEMS applications. Clearly, InP is not as robust as silicon: both Young's modulus and hardness are significantly lower than those of single-crystal silicon. However, as long as MEMS devices in which the displacements are fairly small are developed – of the order of one wavelength (i.e. around 1 μm) – then InP is a suitable micro-*mechanical* material [6-8]. Furthermore, the optoelectronic properties of InP, including the ability of InP-based materials to provide optical gain at 1550 nm wavelength, make it an attractive material for all-optical integrated devices.

## 1.5 Approach: InP-Based MEMS Integrated Waveguide Devices

The approach taken in this research is the monolithic integration of InP-based waveguides with MEMS electrostatic actuators. The basic idea behind this approach including layer structure design, the suspended waveguide approach, and electrostatic actuation are now briefly reviewed. Finally, two types of switches and their coupling mechanisms are introduced. The extension of this technology to other devices including environmental sensing is also presented.

### 1.5.1 Monolithic Integration

Monolithic integration enables both passive as well as active components to be realized on the same chip (e.g. passive waveguides and active laser sources or semiconductor optical amplifiers). While the present work only focuses on passive

devices (no optical gain medium), this work can be extended to enable active devices made of InGaAsP, such as lasers, to be integrated on-chip. Therefore, this research enables complex integration of optical components in a compact platform and enables both active and passive devices to be integrated monolithically.

In the present approach, passive InP-based optical waveguide MEMS are developed by monolithically integrating both waveguide and MEMS actuator in the same semiconductor layers. This approach implies that the waveguides not only serve to guide light, but also act as mechanical structures. These mechanical structures must be conducting so that they can be electrostatically actuated. Therefore, design of an appropriate layer structure is a challenging task. Several properties must be controlled simultaneously: a) optical (refractive index, bandgap), b) electrical (bandgap), c) mechanical (control intrinsic stress), and d) chemical (require complete selectivity during wet etching). These issues will be addressed in Chapters 3–4, which deal with waveguide design and device fabrication, respectively.

### 1.5.2 Suspended Waveguide Technology

In order to create freely movable optical devices, suspended waveguides were developed [9, 76]. These essentially consist of waveguides that are freely suspended in air by supporting tethers spaced every 1000–1500 μm or so along the length of the waveguides. The material underneath the waveguides is completely removed using wet chemical etching. A small optical loss is incurred at each tether, but this loss is fairly small and does not deteriorate device performance significantly, as will be shown in Chapter 3. Furthermore, having suspended waveguides has the benefits of a) enabling

movable waveguides, and b) reducing optical losses to the substrate via substrate radiation modes.

### 1.5.3 Electrostatically-Actuated Waveguides

Once suspended waveguides are realized, we can develop actuated devices. For macro-scale devices magnetic actuation (such as in electric motors) is generally preferred due to the large force available. However, as we scale device dimensions down in size to the micron level, electrostatic actuation becomes the preferred force generating mechanism. The reason for this shift is due to force scaling; the energy density for electrostatic and magnetic actuators is given by [37]:

$$W_{Electrostatic} = \frac{\varepsilon E^2}{2}, \text{ and} \tag{1.1a}$$

$$W_{Magnetic} = \frac{B^2}{2\mu}, \tag{1.1b}$$

respectively, where ε is the permittivity, $E$ is the electric field strength, μ is the magnetic permeability, and $B$ is the magnetic flux density. For most devices, the magnetic flux does not increase substantially for smaller feature sizes. However, the electric field strength generally increases as $1/gap$ (if we consider a parallel plate capacitor, for example) and the electrostatic energy density thus increases as $1/gap^2$. Consequently, electrostatic actuators are often preferred over magnetic actuators in micro-systems. Another advantage of electrostatic actuators is their power consumption: while magnetic motors require significant current and power, electrostatic motors only require applied

voltages with little current consumed. Finally, magnetic actuators typically require difficult fabrication steps compared to electrostatic devices. Additional details of energy density scaling in electrostatic micro-motors are reviewed by *Trimmer and Gabriel* [77].

The waveguides in this research are conducting and can therefore be electrostatically actuated. Both *normal* electrostatic forces, as experienced between two parallel plates, as well as *tangential* electrostatic forces, as experienced due to fringe fields between two parallel plates can be utilized for actuation. These two actuation mechanisms (Figure 1. 3) are discussed in greater detail in Chapters 5 and 6, respectively, when the design of evanescent-coupled and end-coupled switches are presented. Derivation of the electrostatic force and fundamental properties are reviewed in Appendix D and Appendix E.

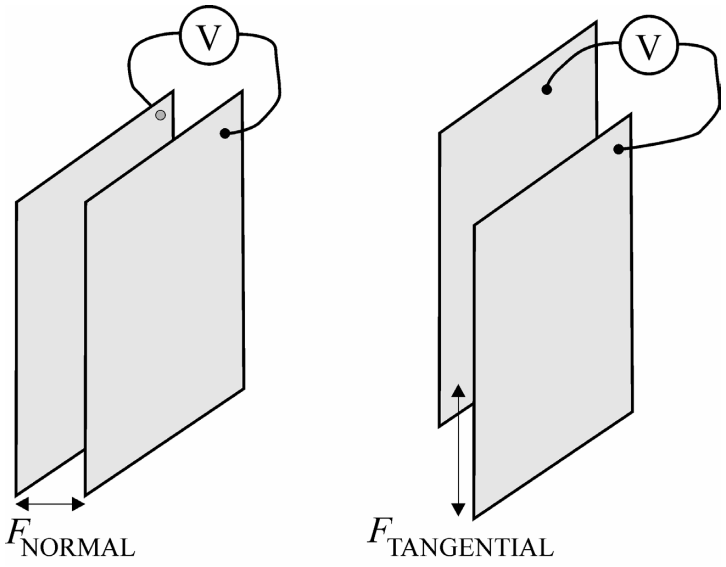


**Figure 1. 3: Parallel-plate actuators: a) *normal* force, b) *tangential* force. The direction of the force and movement of the plates is such that the total capacitance is increased.**

### 1.5.4 Optical Switching: Coupling Mechanisms

For all-optical integrated waveguide MEMS switching, two optical coupling mechanisms were considered in this work: *evanescent*- and *end*-coupling. Both of these approaches are now briefly reviewed. A third application using end-coupled waveguides for environmental sensing is also introduced.

*a) Evanescent–Coupling*

Side (evanescent) coupling is illustrated in Figure 1. 4. Here, coupling occurs between two *parallel* waveguides that have been brought into close proximity over some coupling length, $L_C$. The waveguides and their configuration (separation, coupling length, confinement or evanescent field) can be optimized to yield the desired amount of power transfer from *waveguide 1* to *waveguide 2*. The switch offers great flexibility since coupling can be varied over a large range simply by adjusting the gap between the waveguides. Actuation of the evanescent-coupled switch and movement of the waveguides occurs via electrostatic actuation. This switch is described in detail in Chapter 5.

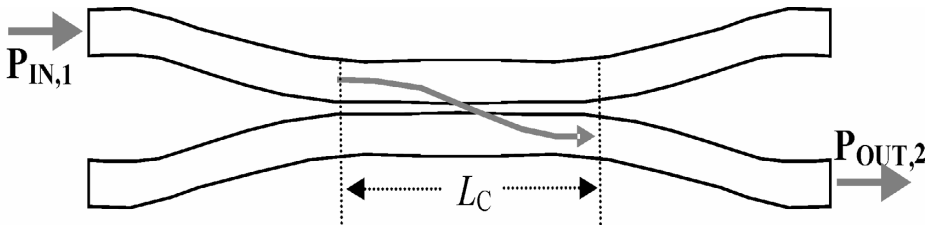


**Figure 1. 4: Lateral (evanescent) coupling (top view schematic).**

*b)* *End–Coupling*

The basic end-coupled switch configuration is illustrated in Figure 1. 5. Light is injected into a movable input waveguide and can be redirected over a small air gap into one of several fixed output waveguides. Movement of the input waveguide occurs via electrostatic actuation, and the coupling mechanism is, in principle, both wavelength and polarization independent. This type of switch configuration is described in detail in Chapter 6.

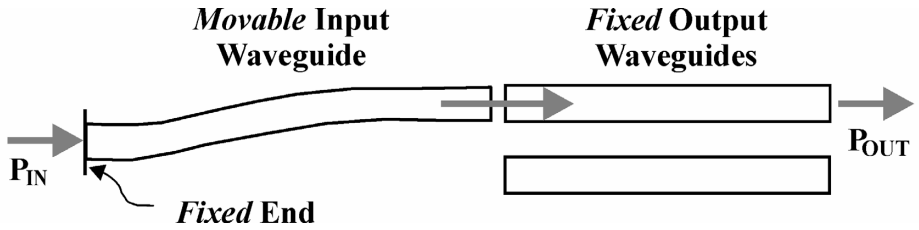


**Figure 1. 5: End–coupling (top view schematic).**

*c)* *End-Coupled Waveguides for Sensing*

The third device presented in this dissertation is a MEMS cantilever waveguide used for environmental sensing. The basic device is similar to the end-coupled switch shown in Figure 1. 5. However, instead of two outputs there is only a single fixed output waveguide (Figure 1. 6). The input cantilever waveguide can be actuated to resonance, and the resonance frequency is obtained by measuring the modulated coupled optical power at the output. The device can act as an environmental sensor by coating it with a polymer. If the polymer adsorbs a specific analyte, the resulting increase in mass will result in a measurable frequency shift. The development of such sensors is described in Chapter 7.

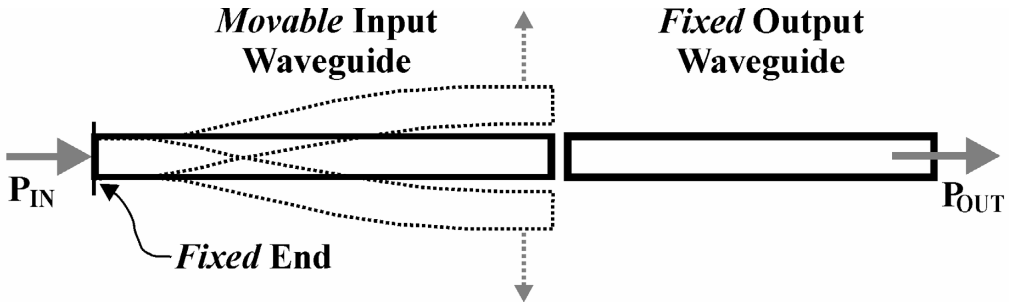


**Figure 1. 6: Resonating cantilever waveguide for environmental sensing.**

## 1.6 Research Objectives and Organization

The purpose of this work is two-fold: technology development and device development. Indium phosphide is not a traditional MEMS material and very little work has been done in this area in the past. Therefore, a significant aspect of this work is the development of a fabrication technology for InP-based MEMS. Included in this technology development is the characterization of InP as a mechanical material for MEMS applications. The second goal of this research is the design, fabrication, and testing of InP-based waveguide optical MEMS switches and devices. To date, few waveguide-based MEMS switches have been reported; most optical MEMS devices utilize the free-space approach that relies on micromirrors. The devices presented here are the first InP-based actuated-waveguide MEMS switches ever reported. Among the devices reported here are also some of the smallest optical waveguide MEMS cantilevers in any material reported to date. Finally, the MEMS evanescent couplers are among the first switches ever reported that vary the spacing between two waveguides to modulate the coupling ratio between two waveguides. The MEMS evanescent coupler switches

reported here also exhibit the lowest switching voltage to date (<10 V) for devices with this coupling mechanism.

The organization of this dissertation is as follows. This chapter has given an introduction to the research performed for this PhD dissertation – InP-based optical waveguide MEMS integrated optical switching and devices – and has also reviewed some of the relevant literature. This places the current accomplishments into context with other work.

Chapter 2 briefly reviews micro-mechanical property measurements of epitaxially-grown InP, preliminary research necessary for the development of more complicated optical MEMS devices. This work was performed for my M.S. thesis [8].

Chapter 3 discusses the 'suspended waveguide' approach used throughout this research. Characterization of typical suspended InP waveguides is reviewed, and Chapter 4, presents the fabrication of InP-based optical waveguide MEMS.

Device development in this dissertation research is presented in Chapters 5–7. Chapter 5 presents the design, fabrication and testing of an evanescent MEMS coupler switch, while Chapter 6 presents an end–coupled InP-based waveguide MEMS switch. The end-coupled switches are modified to enable environmental sensing using resonant cantilever waveguides (Chapter 7).

Chapter 8 summarizes the results and accomplishments of this dissertation research, discusses some other device applications of the MEMS-actuated InP waveguide platform technology, and offers a perspective for future work.

# CHAPTER 2

# InP AS A MICROMECHANICAL MATERIAL

## 2.1 Introduction

This chapter briefly reviews work performed for my M.S. research [8], which involved the micro-mechanical characterization of epitaxially-grown InP for MEMS applications. Only the most relevant results are presented here. Additional results and discussion can be found in the references [7, 78].

## 2.2 Mechanical Characterization of InP

InP is not a traditional MEMS material, and few groups have applied this material to MEMS applications and devices. The few papers reporting InP mechanical property measurements include a demonstration of InP MEMS cantilever beams in 1997 by *Greek et al.* [6] and InGaAs bridges and beams in 1996 by *Seassal et al.* [67]. *Greek et al.* studied the strength of epitaxial InP beams using micro-beam bending, resulting in a measured fracture strength of 3.1 GPa. However, for InP epitaxially deposited on silicon, *Fricke et al.* determined a smaller fracture strength of only 910 MPa using micro-beam bending [79]. The large discrepancy between measured fracture strength and mechanical properties is likely the result of materials growth parameters. For example, the beams of *Greek et al.* were epitaxially grown with lattice-matched beam and sacrificial layers, resulting in pure and low defect density material. In contrast, the beams of *Fricke et al.* were not lattice-matched and resulted in a lower measured fracture strength. Intrinsic

stress resulting from growth or deposition parameters was also observed by *Greek et al.* [6] and can significantly affect material properties.

A significant hurdle for MEMS is control of stress in thin films, especially since the behavior of micro-mechanical devices can be affected significantly by intrinsic stresses. *Chitica et al.* [80] found that InP grown on lattice-matched InGaAs produced films with intrinsic arsenic (As) contamination, resulting in compressive stress and stress gradients. One solution to this problem utilizes trace amounts of gallium (Ga) to introduce slight tensile stress, resulting in a stress-free film [81]. The same conclusion – arsenic as the source of intrinsic stress and gallium as the stress-compensation solution – was independently reached by *Pruessner et al.* in 2002 [7], as will be discussed below.

A few other reports of mechanical characterization of InP can be found in the literature (see, for example [82]), although the data is not nearly as abundant – and, more importantly, consistent – as it is for silicon [83] or polysilicon. Furthermore, the growth method and conditions play a crucial role in determining the material properties of InP, especially the intrinsic stress. Therefore, the micro-mechanical properties of *as grown* InP need to be studied before this material can be used for optical MEMS devices.

### 2.2.1 Stress Measurements: Intrinsic and Gradient Stresses

As previously mentioned, the mechanical properties of thin films, especially intrinsic stress, need to be accurately controlled. This is especially important for MEMS devices since the device behavior of many mechanical structures can be strongly influenced by intrinsic stress. For example, the spring constant of doubly-clamped beams

can be increased (decreased) by incorporating intrinsic tensile (compressive) stress. Therefore, stress is an important device parameter in MEMS.

In this work, instrinsic and gradient stresses were extracted using a passive and non-destructive measurement technique. Cantilever and doubly-clamped beams were fabricated. Due to intrinsic or gradient stresses, the beams curled or buckled out-of-plane (Figure 2. 1). The beam profiles were measured using a laser confocal microscope. From the doubly-clamped beams the instrinsic *compressive* stress was obtained by measuring the buckled beam shapes. Cantilevers enable the extraction of gradient stress (stress variation over the beam thickness) by measuring the beam radius of curvature. The average measured values were $\sigma_o = -5.4$ MPa compressive stress and $\delta\varepsilon_0/\delta t = 4.37 \times 10^{-5}/\mu m$ intrinsic strain gradient ($\delta\sigma_0/\delta t = 4.06$ MPa/μm stress gradient, assuming a Young's modulus $E = 93$ GPa [60]) for 1.7 μm thick beams oriented in the [011] direction on (100) substrates.

The intrinsic stress is the result of inadvertent arsenic (As) contamination of the InP beam layer during molecular beam epitaxy (MBE) growth. The presence of arsenic was confirmed by X-ray diffraction measurements [7, 8]. The lattice constant of $In_{1-X}Ga_XAs_YP_{1-Y}$ depends on the mole fractions $x$ and $y$ of gallium and arsenic, respectively. For pure InP, $x_{Ga} = 0$ and $y_{As} = 0$. Increasing $y_{As}$ (the arsenic mole fraction) increases the lattice constant compared to pure InP and results in compressive strain relative to InP. By incorporating trace amounts of gallium (Ga) in the InP beam layer, the lattice constant will increase compared to pure InP. This results in a slight tensile strain that counters the compressive strain due to arsenic. If devices using doubly-

clamped structures under tensile strain are designed, then we can insure flatness and alignment of the waveguides, as will be discussed in Chapter 3.

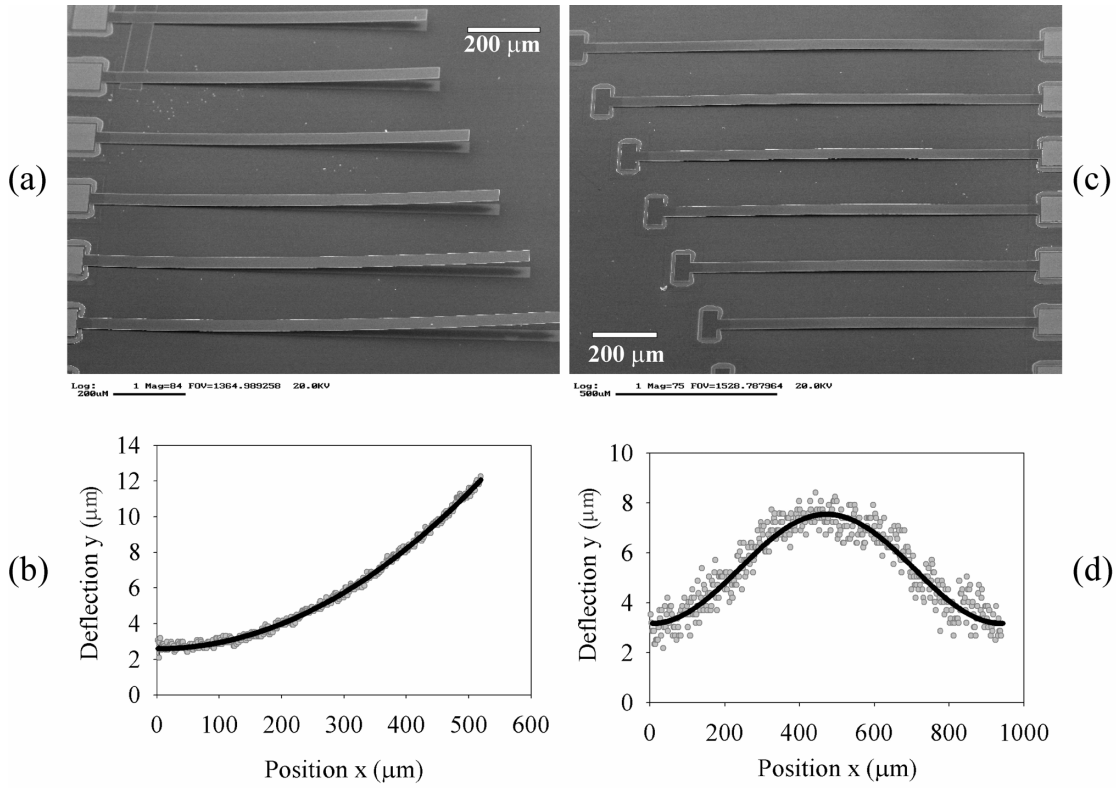


**Figure 2. 1: Intrinsic strain: a) cantilevers, b) measured cantilever curvature, c) doubly-clamped beams, and d) measured doubly-clamped beam buckling.**

### 2.2.2 Nanoindentation

In nanoindentation (Figure 2. 2), a point load is applied to a thin film or bulk substrate using a diamond tip with a radius of a few micrometers, and the resulting tip displacement is measured. A complete measurement cycle consists of loading, hold, and unload cycles. During loading, both elastic and plastic deformation occurs. During hold, the material is allowed to settle, and during unloading only the elastic deformation is

recovered. The elastic deformation (unloading) enables measurement of Young's modulus, while the maximum indent depth and plastic deformation enable measurement of the material hardness.

Nanoindentation experiments were performed on bulk InP substrates and on the various epitaxial layers of the MBE grown wafer. The results are summarized in Table 2. 1. A Young's modulus of 104.8 – 108.9 GPa was measured for the various InP substrate and eitaxial layers, while the hardness varied from 6.08 – 6.98 GPa. This variation in material properties is likely the result of growth conditions (thin-film vs. bulk material) as well as the effects of "lattice hardening" due to the variation in bond strength with doping [82].

The values indicate that InP is significantly more compliant than polysilicon (Young's modulus: $E_{\mathrm{InP}} = 104.8 – 108.9$ GPa vs. $E_{\mathrm{polysilicon}} = 156$ GPa [64]) and also less robust (hardness: $H_{\mathrm{InP}} = 6.2$ GPa vs. $H_{\mathrm{polysilicon}} = 11.0$ GPa [64]). Nonetheless, the nanodindentation experiments on InP show sufficient robustness for small-displacement micro-mechanical devices used in photonics, where movements of more than a micron are often not required.

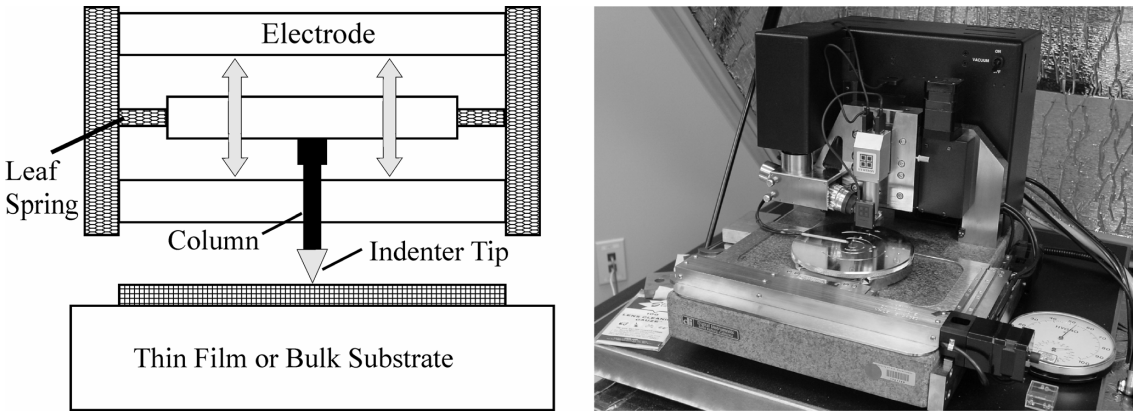


**Figure 2. 2: Nanoindentation setup: a) schematic of nanoindenter with capacitive actuation and sensing (left), b) AFM with nanoindentation setup added on (right).**

**Table 2. 1: Nanoindentation Results**

| Layer | *E* (GPa) | *H* (GPa) |
|---|---|---|
| Bulk InP (n-type) | 104.8 ± 3.1 (± 3.0 %) | 6.53 ± 0.21 (± 3.3 %) |
| 0.4 μm InP buffer (n-type) | 105.8 ± 6.2 (± 5.9 %) | 6.98 ± 0.32 (± 4.6 %) |
| 1.7 μm InP epilayer (p-type) | 108.9 ± 4.0 (± 4.3 %) | 6.08 ± 0.69 (± 11.4 %) |

### 2.2.3 Beam Bending

In beam bending experiments the nanoindenter is used to apply a point load to microbeams (Figure 2. 3) and measure the beam's spring constant, from which Young's modulus (*E*) can be extracted. Bending of doubly-clamped beams also enables the measurement of intrinsic stress ($\sigma_o$). An advantage of beam bending is that it enables the measurement of *E* along the direction of the beam, i.e. measurement along arbitrary crystal orientations. In contrast, nanoindentiation results in contributions of all crystal

orientations since deformation occurs both normal to the indentation surface as well as laterally in the surface plane.

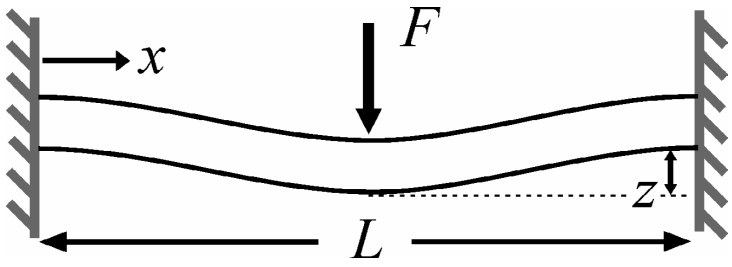


**Figure 2. 3: Beam bending schematic with point load applied to a doubly-clamped beam.**

The spring constant for a doubly-clamped beam consists of three separate terms due to bending (Young's modulus), stress (intrinsic), and stretching components. Beam bending follows the relation [8]:

$$F = k_{bending} \cdot dy + k_{stress} \cdot dy + k_{stretching} \cdot (dy)^3 \tag{2.1}$$

$$= \left(\frac{Ew\pi^4}{6}\right)\left(\frac{t}{L}\right)^3 dy + \left(\frac{w\sigma_o\pi^2}{2}\right)\left(\frac{t}{L}\right)dy + \left(\frac{Ew\pi^4}{8}\right)\left(\frac{t}{L^3}\right)(dy)^3$$

where $E$ is Young's modulus, $\sigma_0$ is the intrinsic stress, $w$ is the beam width, $t$ is the beam thickness, $L$ is the beam length, and $dy$ is the vertical deflection at the beam center during bending. The reader should note the linear dependence of the force $F$ on the displacement $dy$ for the $k_{\text{bending}}$ and $k_{\text{stress}}$ terms and the cubic dependence for the $k_{\text{stretching}}$ component.

The bending and stress components dominate at small loads, while at large loads the stretching term dominates (Figure 2. 4). This can be seen by the linear $F$ vs. $dy$ dependence at small loads ($dy$ < 500 nm) and the nonlinear dependence at large loads ($dy$ > 500 nm). The experiments were therefore carried out in the small-displacement regime ($dy$ < 500 nm) on doubly-clamped beams.

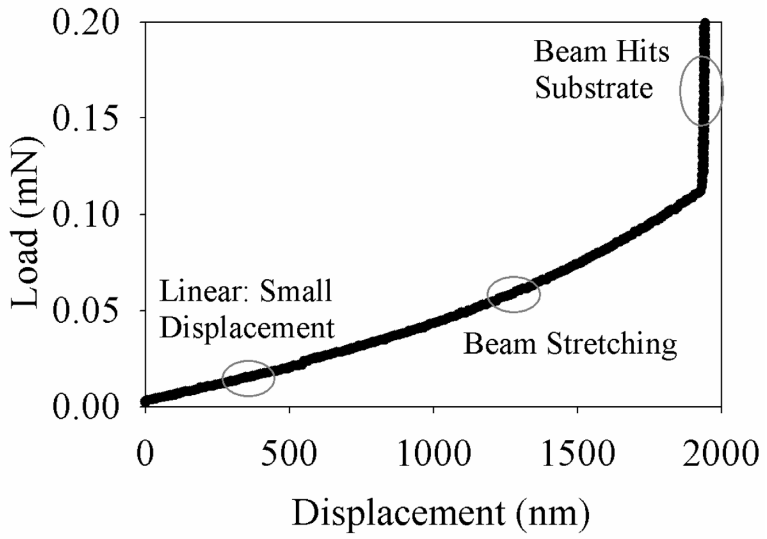


**Figure 2. 4: Beam bending of a doubly clamped beam showing clearly the linear and nonlinear regions of displacement. The experiments were carried out in the linear region (dy < 500 nm).**

The extracted Young's modulus as a function of beam length is plotted in Figure 2. 5. The importance of intrinsic stress measurements is clearly illustrated: the measured Young's modulus appears to decrease with increasing beam length (Figure 2. 5a, left) if the intrinsic compressive stress is neglected. However, Young's modulus is a material property and should be geometry independent. If the intrinsic stress is included in the

Young's modulus extraction, then the results are much more consistent over various beam lengths (Figure 2. 5b, right). The average measured Young's modulus was 80.4 GPa, significantly smaller than that of polysilicon, but similar to that of gallium arsenide ($E_{GaAs}$ = 99.1 GPa [60]). The Young's modulus obtained by beam bending is also smaller than that obtained by nanoindentation (nanoindentiation: $E_{InP}$ = 104.8 – 108.9 GPa). The reason for this discrepancy is that nanoindentation measures an average value of Young's modulus for all crystal orientations since the indentation results in surface normal as well as in-plane deformation. In contrast, beam bending measures Young's modulus only along the beam axis, in this case the [011] crystal direction of InP. Therefore, the two measurements – nanoindentation and beam bending – are not directly comparable.

The beam bending experiments were performed many times on each beam with no significant change in the measured mechanical properties. The beam-substrate gap was 1.7 μm, indicating that displacements of this order of magnitude can achieved in InP-based MEMS with sufficient reliability and without damage to the device. Therefore, thin-film InP mechanical structures achieve sufficient robustness for optical MEMS devices.

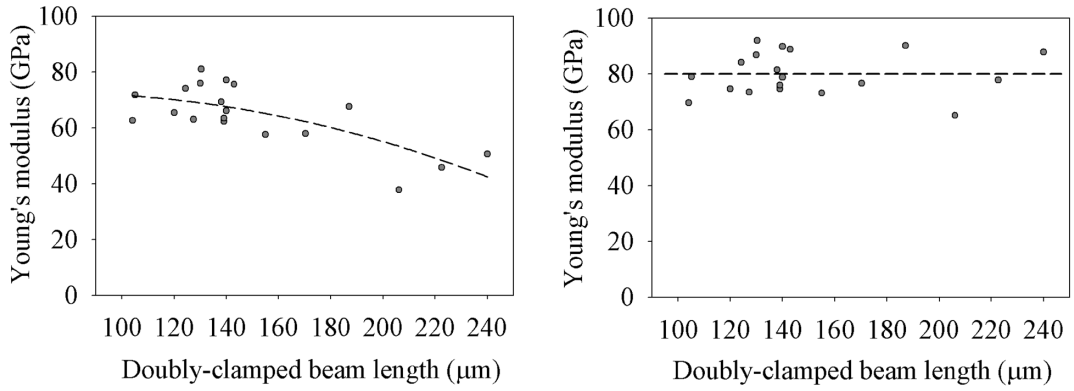


**Figure 2. 5: Young's modulus measurement using beam bending: a) neglecting intrinsic compressive stress (left), and b) including the effects of intrinsic stress (right). In (a) the curve fit is a polynomial, while in (b) the fit is linear.**

### 2.2.4 Electrostatic Testing

In electrostatic testing (Figure 2. 6), an electrostatic pressure load is used to deflect beams in a manner similar to beam bending (Figure 2. 3). Electrostatically actuated beams exhibit an instability that causes them to be "pulled-in" once the applied voltage exceeds a critical threshold called the pull-in voltage, or $V_{PI}$ (see Appendix D). The reason for this instability is the linear increase in mechanical force required for bending as a function of displacement versus the nonlinear increase in electrostatic force with increasing displacement. By measuring $V_{PI}$, Young's modulus and intrinsic stress of thin films can be obtained in a manner similar to beam bending [84]. Either cantilever or doubly clamped beams can be used.

Because an electrostatic force between beam and substrate is used, it is important for the beams to be initially flat. Otherwise, the applied electrostatic pressure load, which depends on the square of the beam-substrate gap, would be difficult to characterize. Any

measured mechanical properties would then be skewed without additional and time consuming analysis of the electrostatic force.

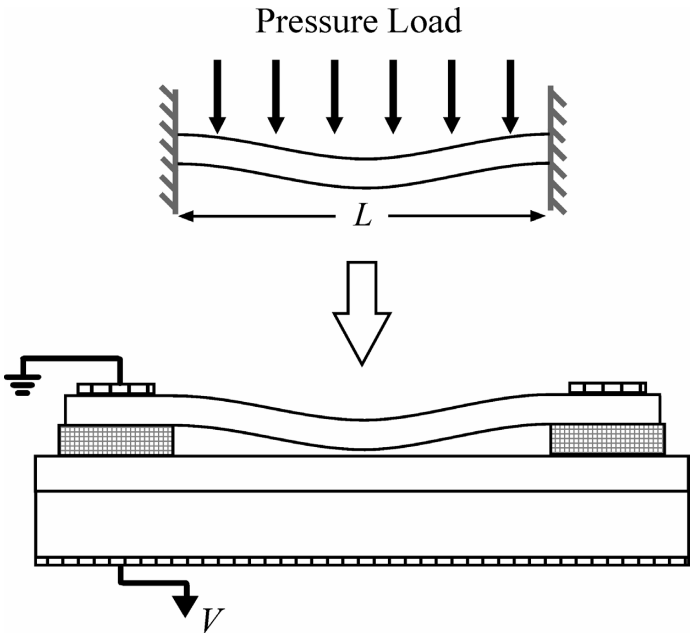


**Figure 2. 6: Electrostatic testing: beam bending with applied electrostatic pressure load.**

A doubly-clamped beam with applied voltage for electrostatic beam bending is shown in Figure 2. 7. Initially, the beam is already curved due to buckling, as indicated by the black and white fringes visible under the differential interference contrast (DIC) filter (Figure 2. 7a, top). The DIC filter images any variation in height as a change in contrast and therefore enables qualitative measurements of surface profiles. As the applied voltage is increased to 8.8V the beam bends down to the substrate and the fringes move to the beam ends (Figure 2. 7, bottom). This initial curvature of the beam prevents accurate mechanical property extraction. Therefore, in this work no mechanical

properties were extracted via electrostatic testing. The electrostatic measurements did demonstrate, however, that electrostatic actuation and pull-in actuators can be realized in thin-film InP. Consequently, this work [8] lays the foundation for InP-based MEMS actuators and opens up the possibility of using InP MEMS for integrated optical devices.

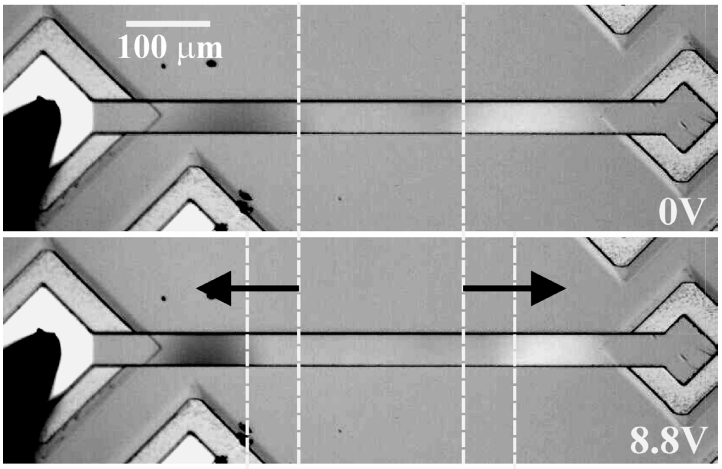


**Figure 2. 7: Electrostatic beam bending: a) 0V (top), b) 8.8V (bottom).**

## 2.3 Stress Engineering

The intrinsic compressive stress and stress gradients discussed previously (section 2.1.1) result in significant out-of-plane bending of beams (Figure 2. 1), even without actuation. This prevents accurate vertical alignment of waveguides, especially when the size of the waveguide core becomes small. Clearly, in order for useful waveguide MEMS devices to be realized, the intrinsic stress must be controlled. This can be accomplished during MBE growth, as mentioned in section 2.2.1, and by effective device design, as will be discussed later in Chapters 5 – 7.

Figure 2. 8 shows flat $In_{0.986}Ga_{0.014}As_{0.013}P_{0.987}$ doubly-clamped beams with engineered tensile stress. Trace amounts of gallium were added to the InP beam layer during the MBE growth. The $x_{Ga} = 0.014$ gallium mole fraction (purposely added) effectively offsets the intrinsic arsenic mole fraction (due to inadvertent contamination), resulting in an overall intrinsic *tensile* strain (due to both gallium and arsenic) of $\varepsilon = +0.057$ %. This tensile strain ensures that doubly-clamped beams remain flat. The reader should note, however, that strain gradients still result in curved cantilevers. Therefore, doubly-clamped structures or very short cantilevers (i.e. $L < 100$ μm) will be used in the InP waveguide MEMS devices. This ensures that the waveguides remain in-plane and enables accurate vertical alignment.

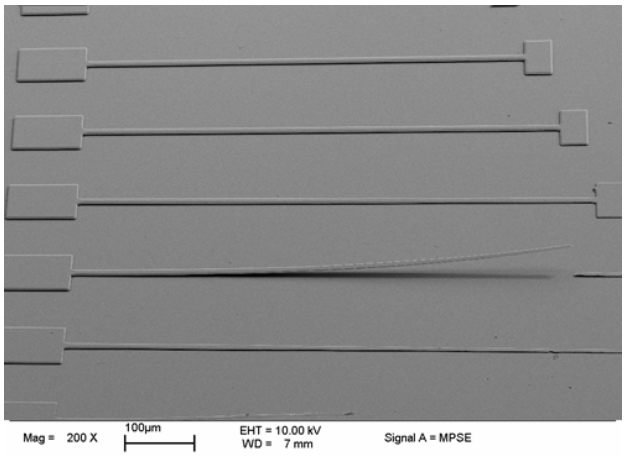


**Figure 2. 8: Tensile stress engineering: trace amounts of gallium (Ga) counter the effects of arsenic (As) contamination during MBE growth. Doubly-clamped beams are flat, while cantilevers are curled due to an intrinsic strain gradient.**

## 2.4 Summary

Mechanical property measurements of InP, as performed for my M.S. research [8], have been reviewed. The results indicate that InP is a suitable material for micro-mechanical devices requiring small displacements on the order of a micron. Stress engineering and compensation during MBE growth has also been presented. This technique enables flat suspended doubly-clamped beams to be realized and will ensure accurate vertical alignment between waveguides.

# CHAPTER 3

# SUSPENDED WAVEGUIDES

## 3.1 Introduction

This chapter describes the 'suspended waveguide technology' developed as a building block for InP-based optical waveguide MEMS. The concept came about from a need to simultaneously control *optical*, *electronic*, *mechanical* and *chemical* properties of the InP MEMS structure while still enabling the epiwafer to be grown using in-house available molecular beam epitaxy (MBE) growth reactors at the Laboratory for Physical Sciences (LPS). This led to a design in which the waveguides are completely removed from the substrate and are suspended by thin tethers.

The majority of this work was carried out by Mr. Daniel P. Kelly for his M.S. thesis research [76]. The importance of the suspended waveguide technology as a building block for the devices presented in this dissertation cannot be emphasized enough, however, and this work is therefore reviewed here. A clear distinction between my contribution and that of Mr. Daniel P. Kelly must be made. My contribution to the suspended waveguide technology is: 1) the basic idea and concept, 2) the design of the layer structure including electrical, optical, mechanical, and chemical properties, and 3) the basic waveguide design. Mr. Daniel P. Kelly's contribution consists of [9, 76]: 1) the tether design, 2) fabrication of the InP waveguides, 3) testing and waveguide loss measurement, and 4) development of a model based on Gaussian beam divergence for characterizing the loss due to tethers.

Mr. Kelly's work was especially important for InP waveguide MEMS device development; without the 'suspended waveguide' technology, none of the InP MEMS optical switches and devices presented in this dissertation would have been possible. Because of the importance of Mr. Kelly's work on suspended waveguides, I am reviewing a large part of his experimental results here in addition to my design contributions.

## 3.2 InP MEMS Epiwafer Design

In order for InP-based optical waveguide MEMS to be realized, several materials requirements need to be met. These requirements include *optical*, *electronic*, *mechanical* and *chemical* properties. In this section, the various materials requirements will be reviewed followed by several possible designs.

The optical requirement is for a low-loss, transparent material (at the wavelengths of interest: $\lambda$=1500 – 1600 nm). This requires that the bandgap energy, $E_g$, of the waveguide is less than the energy of the transmitted light: $E_g < E_0$, where $E_0$ is the photon energy of the guided light. Equivalently, this requires that $\lambda_g > \lambda_0$, where $E = hc/\lambda$ and $n$ is the refractive index, $h = 6.626 \times 10^{-34}$ J·s is Planck's constant and $c$ is the speed of light in vacuum. If this requirement is not met, then the waveguides will exhibit large absorption and will be extremely lossy. Furthermore, in order to ensure the absence of any electro-optic effects, the bandgap edge wavelength $\lambda_g$ is chosen to be greater than 100 nm away from $\lambda_0$ [18, 85]. Finally, as a second optical requirement, the refractive index needs to be controlled in order to obtain a waveguiding structure with core and cladding such that $n_{CORE} > n_{CLADDING}$.

The waveguides are doped in order to electrostatically actuate them. However, high doping levels will also increase loss by introducing free carrier absorption [86]. The waveguide doping is therefore chosen to be n-type and limited to $5 \times 10^{-17}/\text{cm}^3$ so as to limit optical losses to an acceptable level [87] while still enabling electrostatic actuation. N-type doping was chosen instead of p-type because it was found that this induces less free-carrier absorption losses for similar doping concentration [88, 89].

### 3.2.1 InGaAsP Material System and Epilayer Design

The indium-gallium-arsenide-phosphide (InGaAsP) material system [62] enables precise control of the lattice constant as well as the bandgap and other material properties. Furthermore, many of these materials can be grown lattice matched (or near lattice matched) to InP substrates as indicated in Figure 3. 1. By adjusting the relative mole fractions of gallium (Ga) and arsenic (As) in the InGaAsP material, the relevant *optical*, *electronic*, *mechanical* and *chemical* properties for the MEMS waveguide layers are controlled.

The design of the epiwafer structure was accomplished with the help of a MATLAB script written for this research (Appendix A). The material properties of interest are: 1) bandgap, $E_g$, and bandgap wavelength, $\lambda_g$, 2) refractive index, $n$, 3) intrinsic strain, $\varepsilon$, 4) core thickness for single mode operation, $t$, and 5) waveguide width for single mode operation, $w$.

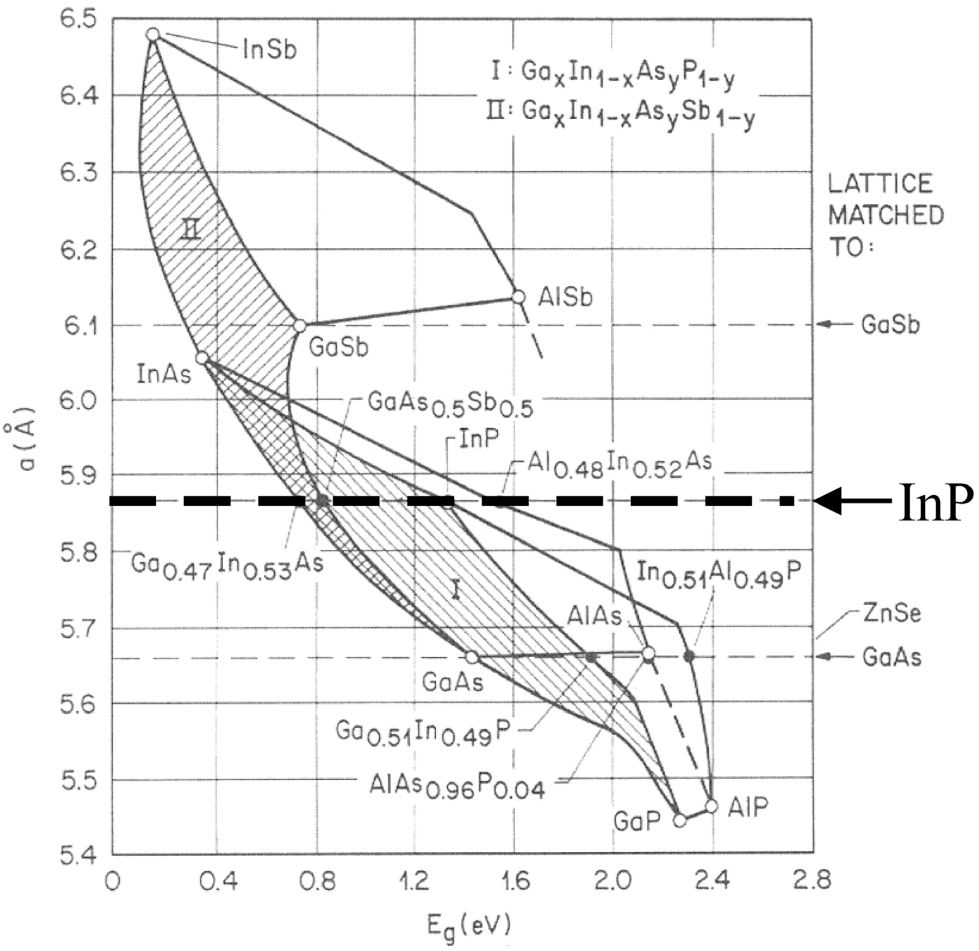


**Figure 3. 1: Various III-V compound semiconductor systems, including the InGaAsP system. The dashed horizontal line indicates materials that can be grown lattice-matched to InP substrates (adapted from reference [62]).**

The equations guiding the design are now briefly reviewed from the relevant references [90-96]. Note that the epitaxial InGaAsP layers are designed to be (nearly) lattice matched to the InP substrate. The lattice constant of $In_{1-X}Ga_XAs_YP_{1-Y}$ can be found using Vegard's Law [90]:

Lattice constant: $$a(x,y) = xya_{GaAs} + x(1-y)a_{GaP} + (1-x)ya_{InAs} + (1-x)(1-y)a_{InP}, \quad (3.1)$$

where $a_{GaAs}$, $a_{GaP}$, $a_{InAs}$, and $a_{InP}$ are the lattice constants of gallium arsenide (GaAs), gallium phosphide (GaP), indium arsenide (InAs), and indium phosphide (InP), respectively. By setting $a(x,y)$ equal to the lattice constant of InP, i.e. $a(x,y) = a_{InP}$ = 5.869 Å, one obtains a relation between $x_{Ga}$ and $y_{As}$ for all materials of the InGaAsP family that are lattice matched to InP. The lattice matched condition is [96]:

Lattice matched condition: $$x_{Ga} = 0.1896\, y_{As} / (0.4176 - 0.0125\, y_{As}), \text{ or} \quad (3.2a)$$

$$x_{Ga} \cong 0.47\, y_{As}, \quad (3.2b)$$

where $x_{Ga}$ and $y_{As}$ are the mole fractions of gallium and arsenic in $Ga_xIn_{1-x}As_yP_{1-y}$ respectively. Excluding the strain calculation, we will now assume that all InGaAsP layers are lattice matched or nearly lattice matched. Using this (nearly) lattice matched condition (Eqn. 3.2b), the bandgap and refractive index can be found using the modified single-oscillator approach in [93]:

Bandgap: $$E_g(eV) = 1.35 - 0.72y_{As} + 0.12y_{As}^2, \quad (3.3)$$

Bandgap wavelength: $\lambda_g(\mu m) = 1.240\ \mu m / E_g(eV)$,

Refractive index: $$n = \left[1 + \frac{E_d}{E_0} + \frac{E_d E^2}{E_0^3} + \frac{\eta E^4}{\pi} \ln\left(\frac{2E_0^2 - E_g^2 - E^2}{E_g^2 - E^2}\right)\right]^{1/2} \quad (3.4)$$

where

$$\eta = \pi E_d \Big/ 2E_0{}^3 \left(E_0{}^2 - E_g{}^2\right), \tag{3.5a}$$

$$E_0 = 0.595 x_{Ga}{}^2 \left(1 - y_{As}\right) + 1.626 x_{Ga} y_{As} - 1.891 y_{As} + 0.524 x_{Ga} + 3.391, \tag{3.5b}$$

$$E_d = \left(12.36 x_{Ga} - 12.71\right) y_{As} + 7.54 x_{Ga} + 28.91 \tag{3.5c}$$

$$E = 1.240 / \lambda \tag{3.5d}$$

From eqns. (3.4) and (3.5d) one can see that there is a slight wavelength dependence of the refractive index, $n$.

The remaining properties of interest are the intrinsic strain, ε, and the single-mode geometry (width, $w$, or thickness, $t$) for the waveguides. The intrinsic strain for any InGaAsP layer grown on an InP substrate can be found by comparing the lattice constant $a_{\mathrm{InGaAsP}}(x,y)$ to that of pure InP:

Intrinsic strain, ε:

$$\varepsilon(x,y) = \frac{a_{InP} - a_{InGaAsP}(x,y)}{a_{InP}}, \tag{3.6}$$

where $a_{\mathrm{InGaAsP}}(x,y)$ is given in eqn. (3.1) and $a_{\mathrm{InP}}$ = 5.869 Å. For MEMS waveguide devices it is useful to have intrinsic tensile strain. This ensures accurate vertical alignment between two butt-coupled or parallel waveguides. The intrinsic strain is limited to less than 0.1 % in order to minimize any dislocations and other defects during the MBE growth; larger strains (i.e. larger lattice mismatch) result in significant defects that increase scattering losses in the waveguides. Furthermore, increased tensile strain also increases the spring constant of any mechanical devices (i.e. movable waveguides) –

a desirable property for increasing resonant frequencies in micro-mechanical resonators, but undesirable if low-voltage actuation is desired.

The final consideration is the waveguide geometry that ensures single-mode behavior. While single-mode devices are needed for long-haul communications applications, multi-mode devices are nonetheless useful, especially for data links over short distances. Modal (or multi-mode) dispersion [56] results from the difference in propagation velocity of different modes in a waveguide. Generally, this dispersion is small so that it is not a problem for short communication links and only becomes significant over long distances. A significant portion of this work therefore focuses on multi-mode waveguides for short data and communication links. Multi-mode waveguides were initially chosen (first generation devices) due to their ease of fabrication and fabrication tolerance compared to single-mode dimensions, which, as calculated below, are prohibitively small for the optical lithography tools available for this work. The single-mode cut-off dimensions [86] can be calculated as:

Single-mode dimension: $$\frac{2d}{\lambda_0}(NA) < 1 \tag{3.7a}$$

$$d < \frac{\lambda_0}{2\sqrt{n_1^2 - n_2^2}} \tag{3.7b}$$

where $d$ is the single-mode cut-off dimension (either width, $w$, or thickness, $t$), $\lambda_0$ is the vacuum wavelength (centered around 1550 nm), and $n_1$ and $n_2$ are the core and cladding refractive indices, respectively.

Two types of waveguides were considered, as shown in Figure 3. 2. The first has air-cladding on the sides and InP-cladding on top and bottom (Figure 3. 2a: "InP-cladding"), while the second has air-cladding all around the core (Figure 3. 2b: "air-cladding"). Therefore, the reader should note that for both designs the single-mode waveguide width, $w$, can be calculated using $n_1 \sim 3.2$ (semiconductor core) and $n_2 = 1$ (air side cladding) resulting in $w \sim 250$ nm (at $\lambda_0 = 1550$ nm). Dimensions of this magnitude are difficult to fabricate using the available lithography tools. Consequently, the first-generation devices were multi-mode with waveguide widths significantly larger than the single-mode cut-off dimension, $w \sim 250$ nm. It has been shown, however, that devices with core dimensions as large as $w = 500$ nm are still quasi single-mode [97], likely due to the increased scattering losses experienced by higher order modes. Such dimensions ($\sim$ 500 nm) can be fabricated using standard projection lithography and fabrication methods; hence, second generation devices in this work were fabricated with dimensions as small as 500 nm and thus approach single-mode behavior.

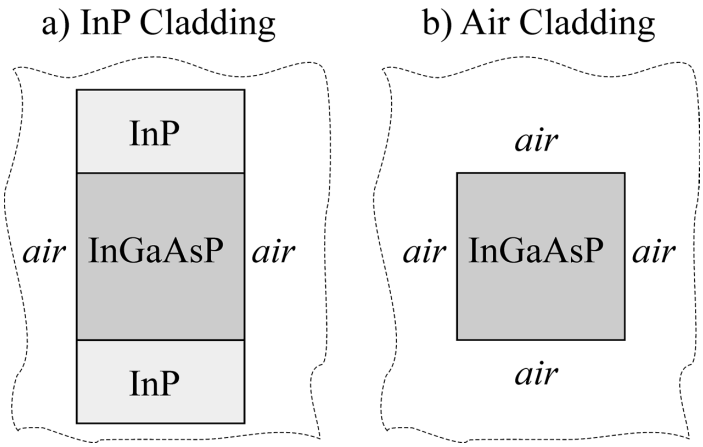


**Figure 3. 2: InP-based waveguide: a) InP top/bottom cladding, b) air cladding.**

A MATLAB script using Eqns. (3.1 – 3.7) was implemented to calculate the refractive index, bandgap wavelength, intrinsic strain, and single-mode waveguide dimensions as a function of InGaAsP composition (see Appendix A). A typical output window is shown in Figure 3. 3. This design utilizes semiconductor claddings (Figure 3. 2a), and is also the design used in the evaluation of the suspended waveguide approach [9] discussed later in this chapter. The input parameters for the script are the mole fractions, $x_{Ga}$ and $y_{As}$, for gallium and arsenic, respectively, as well as the wavelengths of interest (typically, 1500 – 1600 nm). The program calculates the refractive index, bandgap wavelength, intrinsic strain, and the single-mode waveguide width, $w$, and thickness, $t$. The reader should note that here the top and bottom cladding use InP ("InP cladding" design) resulting in a small single-mode waveguide width ($w$ = 255 nm) and a relatively large core thickness ($t$ = 2 μm).

(a)

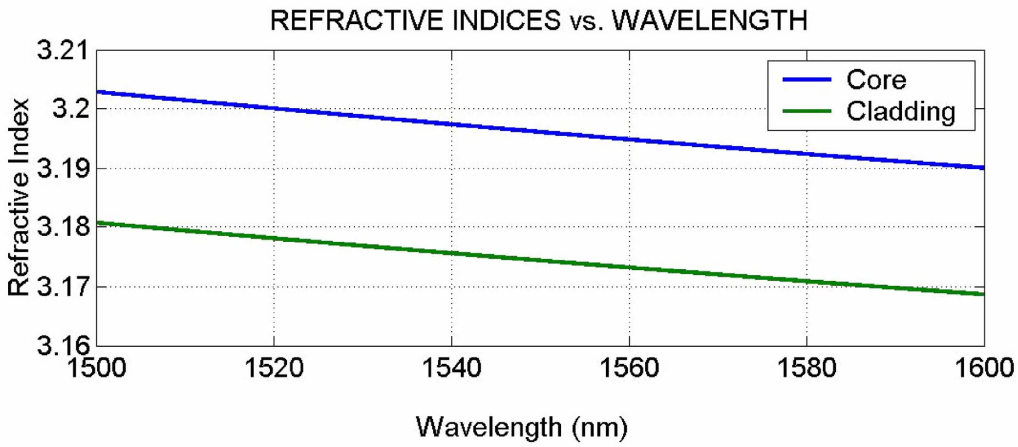


(b)

In(1-X)Ga(X)As(Y)P(1-Y) WAVEGUIDE PROPERTIES

| | X | Y | $n_{mean}$ | $E_g$(um) | e(%) | t(um) | w(um) |
|---|---|---|---|---|---|---|---|
| CLAD | 0.01 | 0.01 | 3.174 | 0.923 | 0.0388 | -- | -- |
| CORE | 0.04 | 0.08 | 3.196 | 0.959 | 0.0253 | 2.083 | 0.255 |

**Figure 3. 3: Typical MATLAB output window for a set of core and cladding layers for an InP-based MEMS waveguide: a) refractive index, *n*, vs. wavelength, b) summary of output parameters. The input parameters are $x_{Ga}$ and $y_{As}$.**

### 3.2.2 Possible Waveguide Designs

In the above discussion, there has been no emphasis on the *chemical* properties of the waveguides. In particular, the etch selectivity between the waveguides and any underlying material, the sacrificial layer, is of critical importance if free-standing and moveable waveguides are to be realized. Two general choices for a waveguide/sacrificial layer in the InGaAsP system are: a) InGaAsP/InGaAs waveguides and InP sacrificial layer, or b) InP waveguide and InGaAsP/InGaAs sacrificial layer. Both designs enable wet etching of the sacrificial layer with complete selectivity over the waveguide layer:

$H_2O_2$-based etchants will attack InGaAsP/InGaAs while HCl-based etchants remove InP [66]. The merits of each design are summarized in Table 3. 1. The benefits and challenges of each design will now be discussed and the reasons for the final design choice will then be given.

**Table 3. 1: Summary of different waveguide designs and their challenges. Waveguide: WG, sacrificial layer: SL.**

| WG Layer | SL Layer | WG Index | SL Index | Challenges |
|---|---|---|---|---|
| InGaAsP/ InGaAs | InP | n ~3.4 | n ~ 3.17 | 1) Thick InGaAsP growth difficult; 2) InGaAs results in absorption: $\lambda < \lambda_g \sim 1600$ nm |
| InP | InGaAs | n ~ 3.17 | n ~ 3.5 | 1) InGaAs *may* cause absorption loss (see below) |

*a) InGaAsP Waveguides*

As presented above in section 3.2.1, the InGaAsP material system enables fine tuning of the bandgap wavelength, $\lambda_g$. Therefore, active optoelectronic devices including lasers and semiconductor optical amplifiers (SOA's) with gain at $\lambda_g = 1.0 - 1.6$ μm can be realized by growing InGaAsP lattice matched onto an InP substrate. Furthermore, one can selectively etch the InP sacrificial layer (substrate) using HCl-based etchants without attacking the InGaAsP waveguides, provided that the $x_{Ga}$ and $y_{As}$ mole fractions are large enough. Finally, a third advantage is the limited number of separate growth steps required: the InP substrate acts as the sacrificial layer so that the growth step of a separate sacrificial layer is eliminated.

With all these benefits of using InGaAsP waveguides there is still a significant hurdle with using this material. The growth of thick ($t \sim 1$ μm) quaternary materials such as InGaAsP is difficult, especially with large mole fractions $x_{Ga}$ and $y_{As}$ required for the present design. The difficulty in growing thick layers of InGaAsP lies in the "spinodal-like decomposition" [98] that occurs during the growth of thick quaternary layers with large mole fractions of Ga and As ($x_{Ga} > 0.15$ and $y_{As} > 0.30$). In the work of reference [98] it was found that the grown material's composition deviated as much as 2.3 % compared to the desired growth as a result of this spinodal-like decomposition. For this reason, it is difficult to grow thick quaternary materials such as InGaAsP.

*b) InP waveguides*

An alternative to the design in (a) using InGaAsP/InGaAs waveguides is the use of pure InP waveguides – or InGaAsP waveguides with small mole fractions of $x_{Ga}$ and $y_{As}$. By keeping the mole fractions small ($x_{Ga} < 0.05$ and $y_{As} < 0.1$) the waveguide material behaves chemically like pure InP. If an InGaAs sacrificial layer is used, then one can selectively release the waveguide from the sacrificial layer using $H_2O_2$:acid (acid: HF, $H_3PO_4$, $H_2SO_4$, etc.) based etchants. Furthermore, InP waveguides are fairly easy to grow with any desired thickness, as is the InGaAs sacrificial layer. The intrinsic strain as well as refractive indices can still be tailored by adjusting the mole fractions $x_{Ga}$ and $y_{As}$.

While InP is transparent at wavelengths $\lambda_g > 950$ nm, the lattice matched InGaAs sacrificial layer poses several problems (from here forward InGaAs lattice matched to InP, i.e. $In_{0.53}Ga_{0.47}As$, is referred to simply as 'InGaAs'). For one, its refractive index is

$n_{InGaAs} \approx 3.5$. Therefore, any portion of the waveguide that is not movable and hence fixed to the substrate via the sacrificial layer will experience large losses. The reason for these losses is that any light in the InP waveguide ($n_{InP} \approx 3.17$) will eventually leak into the higher index InGaAs layer ($n_{InGaAs} \approx 3.5$).

The question then becomes: why not create InGaAs waveguides? Unfortunately, for InGaAs lattice matched to InP the bandgap wavelength is $\lambda_g = 1627$ nm. Therefore, light with wavelength $\lambda < \lambda_g = 1627$ nm will be absorbed by any InGaAs layer, which prevents such waveguides to be realized for operation at $\lambda = 1550$ nm wavelength.

Due to the large absorption inherent in the InP waveguide/InGaAs sacrificial layer design, it becomes necessary to redesign the waveguides themselves. By creating a 'suspended waveguide' design, the InGaAs absorption problem is avoided while enabling freestanding and movable waveguides. This design, discussed in section 3.3, simplifies the MBE growth and enables the use of LPS materials and epitaxial growth facilities.

## 3.3 Suspended Waveguides

### 3.3.1 Approach

The suspended waveguide technology is illustrated in Figure 3. 4, and the cleaved input facet of a fabricated suspended waveguide is shown in Figure 3. 5. The entire InGaAs sacrificial layer is removed from underneath the waveguide including both fixed as well as movable portions. In order to support the waveguide, lateral tethers are used. These are spaced close enough to provide adequate mechanical support, yet they are

separated far enough in order to minimize the total number of tethers and the resulting optical losses.

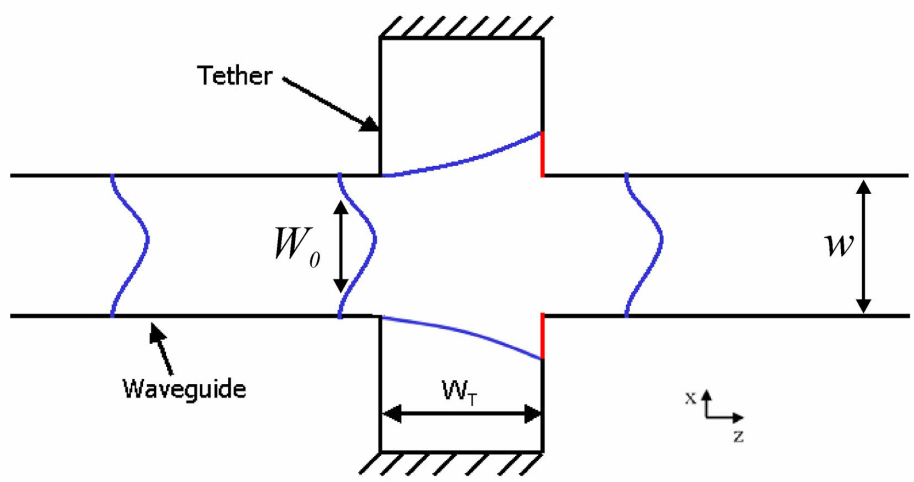


**Figure 3. 4: Top view diagram of suspended waveguide indicating Gaussian expansion of beam waist in the tether region [76].**

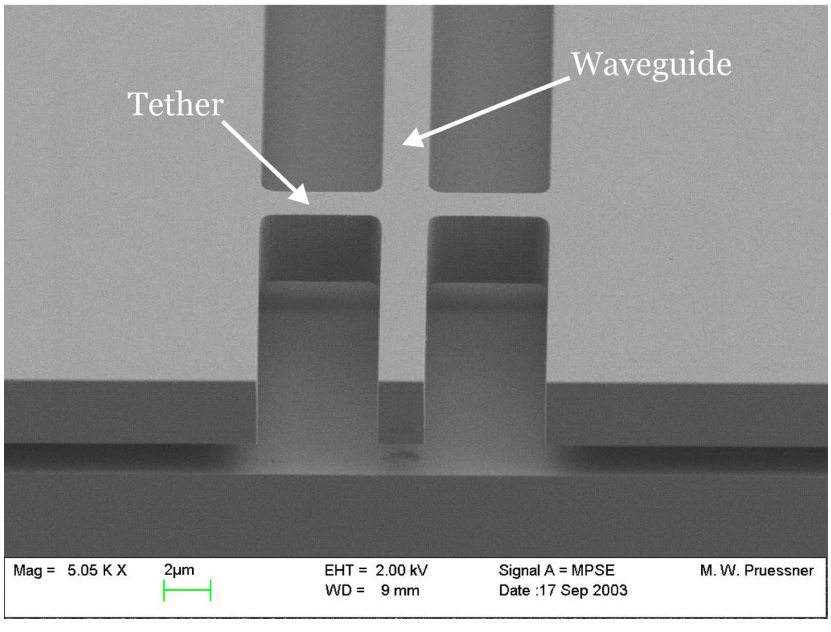


**Figure 3. 5: Released InP waveguide with tethers [9].**

Due to Gaussian expansion of the beam waist in the tether region, each tether will induce some loss. For this reason, the total number of tethers must be minimized. Divergence and expansion is estimated using:

$$\underline{\text{Gaussian beam expansion}}: \quad W(z) = W_0\sqrt{1+\left(\frac{z}{z_0}\right)^2}, \tag{3.8}$$

where $W_0$ is the beam waist in the waveguide and is approximately equal to half the waveguide width so that $W_0 = w/2$, and $z_0$ is called the *Rayleigh range* and is given by:

$$\underline{\text{Rayleigh range}}: \quad z_0 = \frac{\pi W_0^{\,2}}{\lambda}. \tag{3.9}$$

Once the beam divergence in the tether region is known, the tether loss is found by comparing the expanded beam waist, $W(z = W_T)$, to the waveguide width, $w$ [76]:

$$\underline{\text{Tether loss}}: \quad Loss/tether \approx \frac{y_{WG}W(z=W_T) - y_{WG}W_0}{W_0 \cdot W(z=W_T)}, \tag{3.10}$$

where $y_{WG}$ is the height of the waveguide mode.

### 3.3.2 Design

The waveguide design used to study the suspended waveguide approach is as follows [9]. A 1.8 μm thick InGaAs sacrificial layer is grown by MBE on top of an InP substrate. The waveguide layers were then grown on top of the sacrificial layer. Design

(a) in Figure 3. 2 with the InP top and bottom cladding was used. The waveguide core was 2 μm × 2 μm in area with $n_{CORE}$ = 3.195 ($In_{0.96}Ga_{0.04}As_{0.08}P_{0.92}$) and the top and bottom InP cladding was 2 μm wide × 1 μm thick with $n_{CLADDING}$ = 3.173 ($In_{0.99}Ga_{0.01}As_{0.01}P_{0.99}$). The intrinsic tensile strain for the core and cladding layers was $\varepsilon_{CORE}$ = 0.0253 % and $\varepsilon_{CLADDING}$ = 0.0388 %. N-type doped waveguides with $5\times10^{17}/cm^3$ carrier concentration were used in order to take into account any effects of free carrier absorption on the optical losses (the MEMS devices will utilize electrostatic actuation and will therefore require conducting waveguides).

For the devices experimentally studied, the waveguide width was not varied but was fixed at $w$ = 2 μm. The number of tethers was varied to obtain the per tether loss, and the influence of tether width was also measured. The basic loss measurements utilized Fabry-Perot contrast analysis [76] as well as relative power measurements to measure the waveguide and tether losses at 1550 nm wavelength. Because this study is presented in detail elsewhere [9, 76], the detailed experimental procedure is not reviewed here and only the salient results are reported.

## 3.4 Experimental Characterization

The fabrication and experiments discussed in this section were performed by Mr. Daniel Kelly [9, 76] and are presented here for completeness of this dissertation.

The loss per tether in a suspended waveguide after etching of the InGaAs sacrificial is shown in Figure 3. 6 and indicates a linear (dB/cm) increase in loss with increasing number of tethers; the slope is 0.25 dB/tether. Interpolating the data to zero tethers gives a waveguide propagation loss of 2.2 dB/cm. This is the loss incurred in an

identical waveguide with no tether loss. The data indicates that while the tether loss is significant, the total loss is reasonable given that tethers only need to be spaced every 1000 μm or more and that therefore only a few tethers are needed for a particular device, resulting in less than 3 dB of total tether loss.

The same waveguides were also tested without etching the InGaAs sacrificial layer underneath the waveguides in order to measure the effects of InGaAs optical absorption. The results indicate a 17.3 dB gain in power when the sacrificial layer is removed. This demonstrates the necessity of removing the InGaAs underneath the waveguides and validates the suspended waveguide approach.

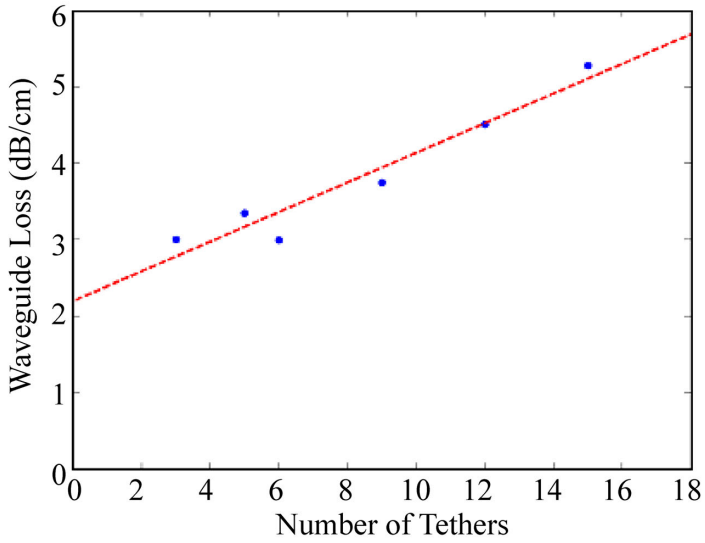


**Figure 3. 6: Waveguide propagation loss as a function of number of tethers [9].**

The influence of the tether width on the waveguide loss is shown in Figure 3. 7. Shown in the inset is the influence of fabrication tolerances on the designed tethers: the effective tether width is approximately 0.5 μm larger than the designed tether width due

to rounding of corners during optical lithography and etching. Consequently, the effective width of the 1.5 μm tethers is $w_{effective} = 2.0$ μm. Tethers ranging from 3 μm width to as small as 0.5 μm width were studied ($w_{effective} = 3.5$ μm – 1.0 μm). The results indicate that tethers as small as 0.5 μm wide provide sufficient mechanical support for static waveguides and result in minimal losses of 0.09 dB/tether for 2 μm wide waveguides. Reducing the waveguide width to single-mode dimensions ($w \leq 500$ nm) will increase losses, but these losses are expected to be reasonably small (< 1 dB/tether) if the tether width is smaller or equal to the waveguide width [76].

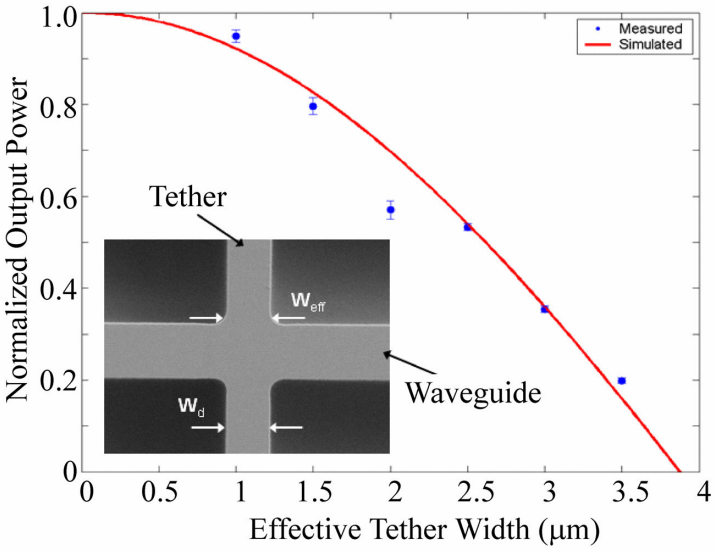


**Figure 3. 7: Waveguide loss as a function of tether width for 15 tethers [9]. The inset shows the effects of lithography and rounding of corners on the effective tether width.**

## 3.5 Active Waveguides

The design presented above results in passive waveguides at $\lambda = 1550$ nm; that is, no optical gain (e.g. lasers, semiconductor optical amplifiers) at 1550 nm is possible. Nonetheless, active devices with gain can be realized by modifying the layer structure appropriately to incorporate InGaAsP layers with bandgap wavelengths $\lambda_g \sim 1550$ nm. For example, an active-passive platform technology was previously developed that enables vertical coupling between various active and passive waveguides [18] on a single chip. Such a technology can be adapted to the present passive MEMS waveguides to provide increased functionality.

## 3.6 Summary

This chapter has reviewed the suspended waveguide approach, which was developed as a platform technology for InP-based optical MEMS. Properties of materials grown from the InGaAsP family of compound semiconductors were reviewed, and specific equations for calculating optical, electronic, mechanical, and chemical properties as a function of mole fraction, $x_{Ga}$ and $y_{As}$, were presented. The difficulty of growing thick quaternary InGaAsP material was highlighted and the suspended waveguide approach as a method for overcoming these MBE growth difficulties was introduced. The experimental results – obtained by Mr. Daniel P. Kelly [9, 76] – indicate that the induced losses resulting from the suspended waveguide approach are small and that this technology is a viable option for developing InP-based optical MEMS with electrostatically actuated waveguides.

Page intentionally left blank.

# CHAPTER 4

# FABRICATION

## 4.1 Introduction

Fabrication of the InP-based MEMS moving waveguide optical devices is straightforward, requiring a two-mask process. Dry etching is utilized to achieve vertical waveguide sidewalls with minimal roughness. Wet etching frees the waveguides from the substrate without compromising the optical quality of the sidewalls and exposed facets. All devices are fabricated using the same process, regardless of device function. Furthermore, the material system and fabrication sequence is applicable not only to waveguide switches (Chapter 5 and Chapter 6), but also to other optical devices including resonating cantilever waveguide sensors (Chapter 7) and tunable filters (Chapter 8). This demonstrates the flexibility of the fabrication approach and the versatility of the InGaAsP material choice, in which many material properties can be tailored by adjusting the layer composition within the InGaAsP system (see Chapter 3).

## 4.2 Epiwafer and Layer Structure

Two epiwafer designs were used in this research. Both use InP substrates with $In_{0.53}Ga_{0.47}As$ sacrificial layer and InP-based waveguides. The InP-based waveguides contain small mole fractions of gallium ($x_{Ga} < 0.05$) and arsenic ($y_{As} < 0.1$) to control material properties such as refractive index, bandgap, and intrinsic strain. The first design consists of waveguide core and cladding layers ("InP cladding") with the

waveguide suspended in air, while the second design utilizes an InP-based core and air as the cladding ("air-cladding"), as presented in Chapter 3. Both layer structures are presented in Figure 4. 1 and Figure 4. 2.

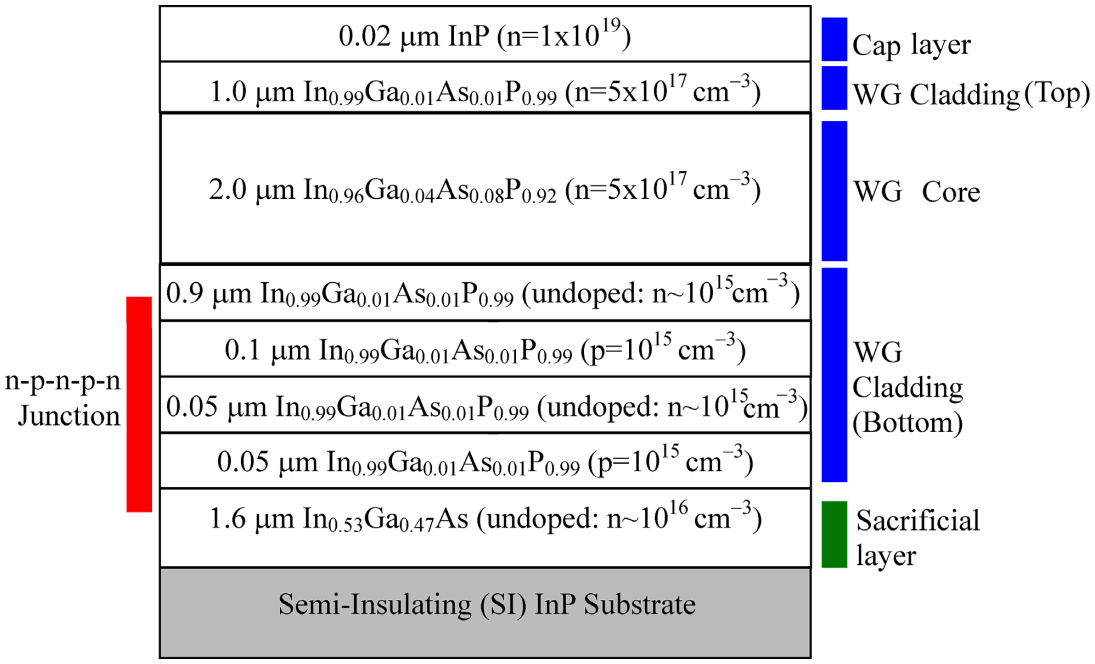


**Figure 4. 1: Layer structure 1 with InP-based 2 μm core and 1 μm top and bottom cladding ("InP cladding" design).**

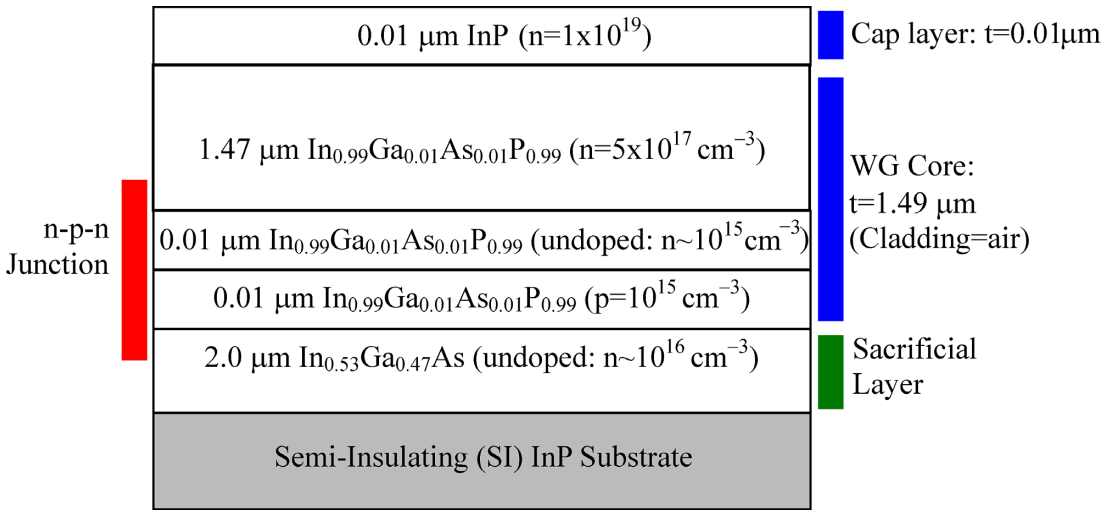


**Figure 4. 2: Layer structure 2 with InP-based 1.5 μm core and air top and bottom cladding ("air cladding" design).**

## 4.3 Processing

Each sample consists of a chip typically measuring 15 mm × 15 mm in area. Device processing consists of depositing and patterning an $SiO_2$ mask on the chip using plasma-enhanced chemical vapor deposition (PECVD) and projection lithography, etching the InP waveguide layers, removing the $SiO_2$ mask, patterning metal electrodes, annealing, thinning and cleaving the devices, and performing a sacrificial wet etch and supercritical dry in $CO_2$. The basic process flow is shown schematically in Figure 4. 3 and details of each process step are described in subsequent sections below.

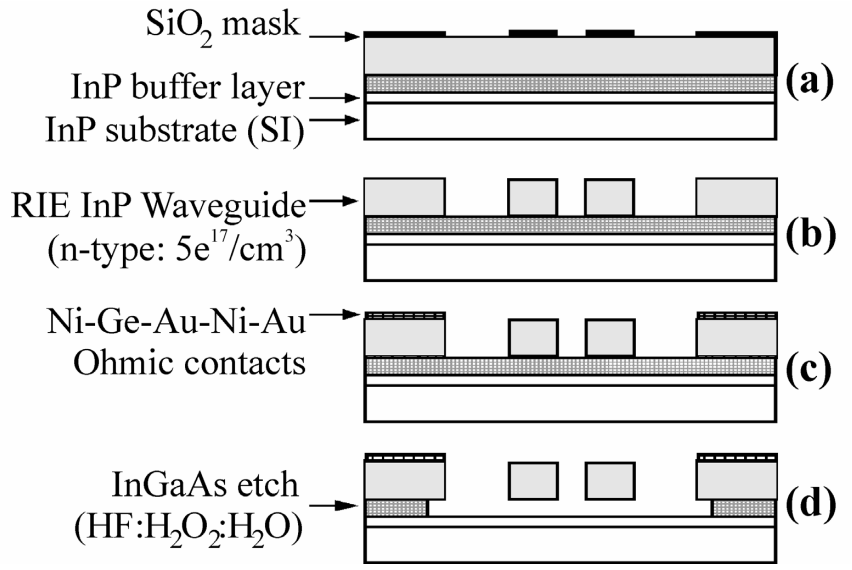


**Figure 4. 3: General process flow for InP-based optical waveguide MEMS devices fabricated on a semi-insulating (SI) substrate.**

### 4.3.1 Standard Clean

A standard clean consists of rinsing the sample in acetone, methanol, and isopropanol alcohol (IPA) successively. The three-step rinse is repeated two or three times followed by drying in forced nitrogen. Any moisture is removed by baking the sample on a hotplate at 120 °C for five minutes (optional). The above process is performed in subsequent processing steps whenever a "standard clean" is mentioned.

### 4.3.2 Lithography: Stepper

Photoresist patterning was performed on two different projection lithography systems (models: GCA DSW 4800 Wafer Stepper and GCA ALS Waferstep 200) as well as on a contact aligner (model: Karl Suss MJB3-HP-IR Contact Aligner). The complete

fabrication process requires only two photoresist patterning steps: 1) definition of the waveguides and mechanical structures using the stepper, and 2) definition of the metal pads using the contact aligner. In this section, only exposures for the stepper are presented; the contact aligner exposures are discussed subsequently in section 4.3.4.

Photolithography for the stepper exposures is as follows. The sample is cleaned using the standard process. Next, the sample is baked on a hotplate for 5 minutes at 120 ºC; subsequently, 5000 – 8500 Å $SiO_2$ is deposited using either a high-density plasma chemical vapor deposition system (Plasmalab System 100 HDPECVD, model 100 ICP) or a plasma-enhanced chemical vapor deposition system (Trion: PECVD Oracle cluster vacuum system). This is followed by a standard clean. After a 5 minute bake at 120 ºC, HMDS adhesion promoter (MicroSi, Inc.) is spun on the wafer at 3000 RPM for 60 seconds followed by Oir906-10 positive photoresist (Arch Chemicals, Inc.) at 3000 RPM for 60 seconds. A 60 second softbake at 90 ºC on a hotplate is performed in order to evaporate any solvents in the photoresist prior to exposure in the stepper.

A focus-exposure matrix (i.e. a matrix of exposures covering a range of focus and exposure values) is performed on a test chip covered with oxide (thickness similar to actual chip to be processed) in order to obtain the best exposure, which enables the minimum linewidth to be patterned in the photoresist. Using the appropriate focus and exposure values, the epilayer chip is then patterned using the stepper. A typical exposure dose for 906-10 photoresist is 100 $mJ/cm^2$ [99] using a UV source operating at i-line (365 nm wavelength). The exposure is followed by a 60 second post-exposure bake at 120 ºC on a hotplate and subsequent development in OPD-4262 developer (Arch Chemicals, Inc.) for 60 seconds with slight agitation. It is important to note that for this first level

mask, which defines the waveguides, it is necessary to align the waveguides along the [011] direction in order to ease cleaving of the chips, as will be discussed later on in section 4.3.5.

### 4.3.3 Dry Etching

Once the desired pattern has been obtained in photoresist, this softmask must be transferred into the underlying $SiO_2$ layer in order to obtain a hardmask suitable for further etching. Pattern transfer of the photoresist mask into $SiO_2$ was accomplished by reactive ion etching (RIE) using $CHF_3$ and $O_2$ plasma in a Plasmatherm 790 (Unaxis, Inc.). The process parameters were P = 40mTorr, flow rates of 18 sccm and 2 sccm for $CHF_3$ and $O_2$, respectively, and an RF power of 175W. The $SiO_2$ etch rate was around 300 Å/min.

Next, the photoresist is removed in a three step process: 1) 60 second strip in $O_2$ plasma (Matrix System One Stripper: Model 102), 2) 20 second flood exposure in the contact aligner followed by 5 minute development in OPD-4262, and 3) standard clean. At this point, the chip is covered only by an $SiO_2$ hardmask and is now ready for InP etching. The Plasmatherm 790 RIE is used with methane-hydrogen plasma to obtain smooth and vertical sidewalls.

InP etching in pure hydrogen ($H_2$) plasma causes preferential loss of P leaving behind In droplets [100, 101]. This leads to surface roughening and prevents optical quality sidewalls. Adding methane ($CH_4$) prevents this preferential loss of P, but the $CH_4/H_2$ ratio is critical: high $CH_4/H_2$ ratios lead to polymer formation [100, 101], which in turn causes micromasking and nanograss. Initially, argon (Ar) was used to limit

micromasking and nanograss [8, 102], but it was subsequently found that this caused excessive wear of the alumina plate in the RIE resulting in increased redeposition of aluminum on to the sample. Therefore, the process was modified to only use methane-hydrogen. This has led to more consistent etching with lower micromasking, but at the expense of sidewall verticality. The verticality is slightly less than the 89º obtained previously [7] (typically, verticality > 85°), but with less mask erosion and micromasking. A typical etch cycle consists of 5 minutes of etching followed by 3 minutes of $O_2$ plasma to remove any polymer buildup on the sample surface and sidewalls. The etch process parameters were P = 30 mTorr, flow rates of 32 sccm, and 8 sccm for hydrogen and methane, respectively, and the DC RF power was 440V. For the $O_2$ cycle the parameters were P = 200 mTorr, 16 sccm flow rate, and DC RF power of 200 V.

Typical etch rates are 250 – 300 nm/cycle of etching (50 – 60 nm/minute). The etch and clean cycles are repeated until the desired etch depth is reached, taking into account that the etch rate slows as the etch proceeds deeper due to microloading effects. Furthermore, once the InGaAs sacrificial layer is reached the etch rate slows to roughly half the value for pure InP. An etched waveguide sidewall is shown in Figure 4. 4 and the cross-section is shown in Figure 4. 5. Typical sidewall roughness is less than 50 nm with verticality of better than 86º. The horizontal lines seen in Figure 4. 4 on the sidewalls are indicative of each etch cycle.

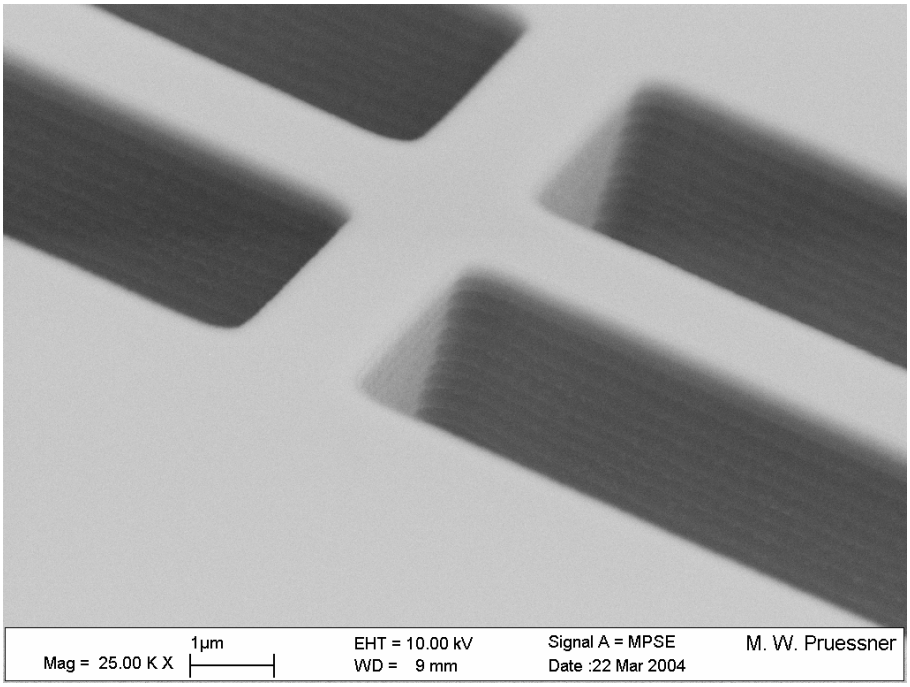


**Figure 4. 4: InP waveguide sidewall after RIE in methane-hydrogen chemistry.**

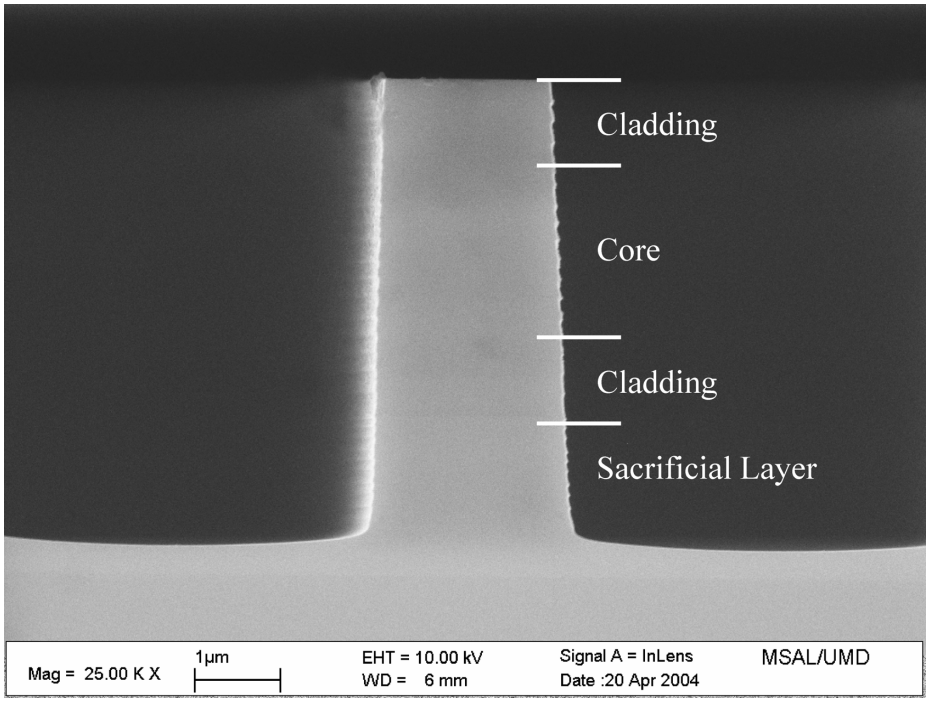


**Figure 4. 5: Cleaved cross-section of InP waveguide (before sacrificial etch).**

### 4.3.4 Metallization

Once the InP has been etched to the desired depth, the $SiO_2$ mask is removed by etching in buffered-oxide etchant (BOE 6:1) for 5 minutes. Metal electrodes are then defined via a three step process. The first is photolithography of negative photoresist (Futurrex, Inc. NR7-3000PY, NR7-1500, or similar). The sample undergoes a standard clean. Next, negative photoresist is spun on the InP chip (typical speed is 3000 RPM). Note that HMDS is not required for good adhesion to InP. The chip is then softbaked at 120 ºC for 60 seconds followed by exposure in the contact aligner. After exposure, the chip undergoes a post-exposure bake at 120 ºC for 60 seconds and the photoresist is developed in RD-6 (Futurrex, Inc.) for 12−15 seconds.

The above process has covered the chip with a protective photoresist coating with open areas for the metal pads. The sample is soaked in $H_2SO_4$:$H_2O$ (1:20) for 15 seconds in order to remove any native oxide from the exposed InP surfaces. A blanket deposition of Ni-Au-Ge-Ni-Au (50 Å – 800 Å – 400 Å – 300 Å – 2000 Å) is then performed using an electron beam evaporation system (CHA Industries, model Mark 40). This metal sequence is necessary for obtaining ohmic, low-resistance contacts to III-V semiconductors [103]. Next, the chip is soaked in acetone for a few hours to remove the photoresist and any metal deposited on top of the photoresist, a process known as "lift-off." Alternatively, lift-off can also be performed by immersing the sample in RR2 resist stripper (Futurrex, Inc.) for 5 – 10 minutes at 110 °C. After a standard clean the chip contains metal electrodes at the desired locations.

The electrodes are then annealed in a rapid thermal annealer or RTA (Metron Technology, model AG Heatpulse 610) for 60 seconds at 400 ºC in an $N_2/H_2$ atmosphere.

This anneal step creates an alloy between gold (Au) and germanium (Ge). Furthermore, the nickel (Ni) consumes any native oxide on the surface of the InP substrate, resulting in enhanced ohmic contact formation [103]. A problem with this type of contact, however, is that the Au and Ge tend to "ball up" when melting and subsequently forming an alloy [103], resulting in localized islands. This can be seen in one of the processed samples in Figure 4. 6 and has on occasion resulted in poor adhesion of the metal contact to the InP substrate.

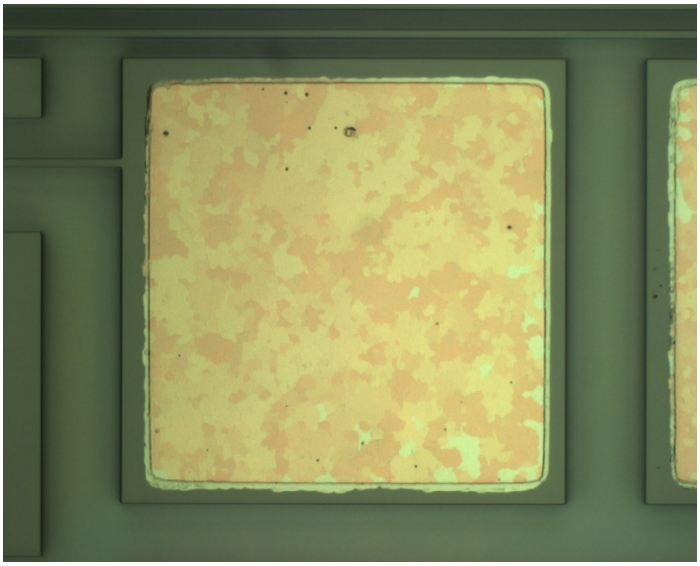

**Figure 4. 6: Island formation due to "balling up" of the AuGe alloy after annealing.**

### 4.3.5 Thinning and Cleaving

In order to efficiently couple light into and out of the chip, smooth, optical quality waveguide facets are necessary. This can be accomplished by cleaving the devices. The chips are first thinned down to a thickness of around 200 μm using a mechanical

polishing machine and 9 μm $AlO_2$ particle grit. In order to protect the devices during thinning, the chip is mounted device side down onto an aluminum holder using wax so that none of the devices are exposed to the mechanical polisher. The device thickness is measured every 50 – 100 μm until the desired thickness is reached. Next, the device is removed from the aluminum holder by heating the holder to melt the wax followed by an acetone soak and a standard clean of the chip. Finally, the chip is cleaved along the $[0\bar{1}1]$ direction in order to expose the <011> facet of the waveguides. A cleaved chip is shown in Figure 4. 7, indicating both the cleaved facets and the tethers, which suspend the waveguide above the substrate (see Chapter 3). Near the cleave, the tethers are spaced 100 μm apart so that the maximum unsupported waveguide length is less than 100 μm at the input and output of the chip.

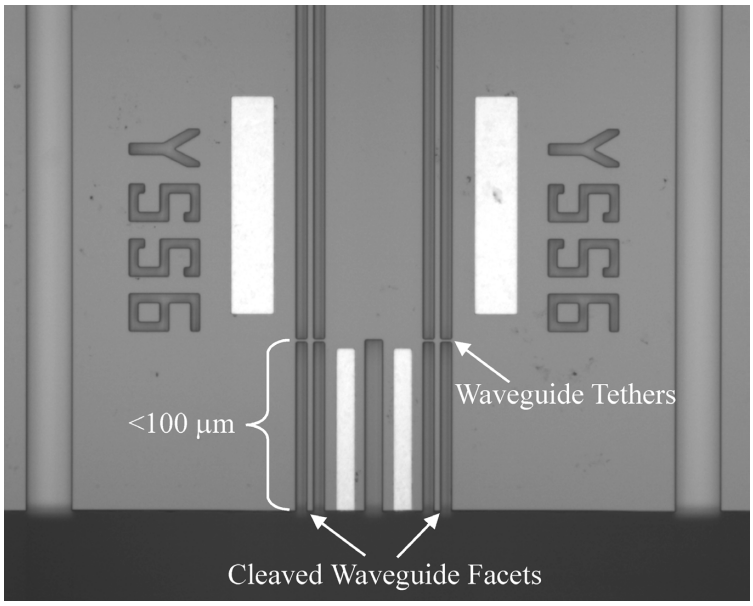


**Figure 4. 7: Cleaved waveguide facets after thinning of the chip.**

### 4.3.6 Sacrificial Wet Etching

After thinning and cleaving, the final processing steps are the sacrificial wet etch to release the waveguides from the substrate and drying the chip using supercritical drying. Care must be taken when handling the chip since it will fracture easily due to the small sample thickness after thinning/cleaving (≈200 μm). Sacrificial etching of the InGaAs layer is performed using $HF:H_2O_2:H_2O$ (1:1:8) giving complete selectivity over the InP waveguides. The reader should note that although the waveguides contain trace amounts of gallium (Ga) and arsenic (As), the waveguides behave like pure InP as far as chemical etching is concerned due to the small mole fractions of Ga and As involved. Typical etch rates for InGaAs are around 1.5 μm/minute with little anisotropy. After etching, no significant degradation of the InP waveguides is observed, indicating complete selectivity of the etchant over InP. While other etchants can be used [66], $HF:H_2O_2:H_2O$ was chosen since it exhibits the least anisotropy in etching InGaAs compared to $H_3PO_4:H_2O_2:H_2O$ and $H_2SO_4:H_2O_2:H_2O$ etchants.

During the sacrificial release, the sample is agitated slightly in order to facilitate etching underneath the suspended structures. The sample is generally etched for 1–2 minutes and then immersed in a small beaker with water and observed under an optical microscope to measure the lateral etch. Sacrificial etch bar test features are included on the chip. These consist of InP bars of varying width (2 – 18 μm in steps of 2 μm). During sacrificial etching, the InGaAs support underneath the InP bars is removed. Over time, some bars will have no InGaAs support left after etching and the bars will be lifted off. This gives an indication of the lateral etch. In Figure 4. 8 the etch bar test structures are shown after the completed sacrificial etch. Bars smaller than 10 μm in width have

been lifted off, indicating that all devices have been properly released since the devices have maximum widths of 4 μm.

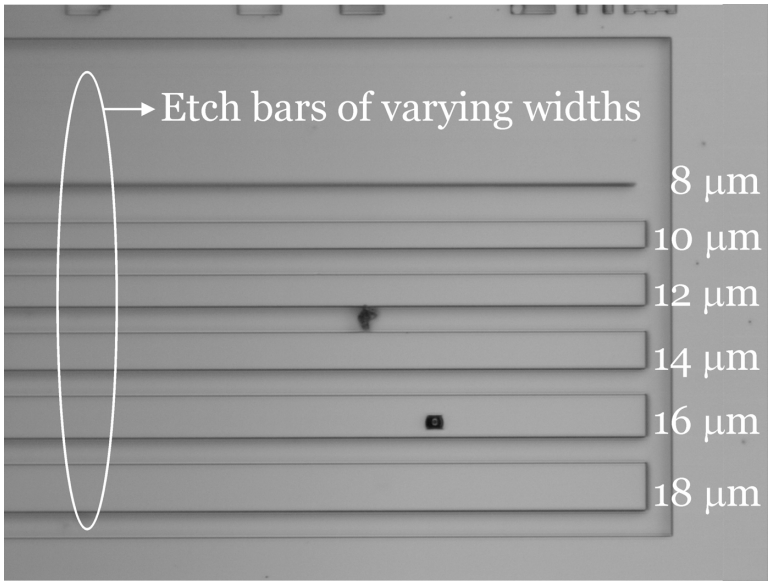


**Figure 4. 8: Sacrificial etch bars with varying widths of 2 – 18 μm. The etch bars of width smaller than 10 μm have been sacrificially etched and lifted off.**

### 4.3.7 Supercritical Drying

The final process step is supercritical drying. This step is necessary to prevent stiction [104], or permanent adhesion of the movable waveguides to the substrate due to surface tension of the rinsing liquid (DI water) after sacrificial etching. The supercritical drying process is discussed elsewhere [8, 105], and only the basic processing steps are reviewed here.

After etching, the sample is immediately immersed in DI water. If the sample dries, then surface tension will cause stiction and permanent damage to the devices.

After immersion in DI water, the sample undergoes a standard clean by immersion in acetone, methanol, and IPA in succession. Next, the sample is immersed in successive beakers of 100 % methanol. This step ensures that any moisture is removed and effectively dehydrates the sample. The chip is then stored in a closed beaker of pure methanol until $CO_2$ drying in the supercritical dryer (Tousimis, model Samdri-795) is performed. Some released and $CO_2$-dried cantilever beams are shown in Figure 4. 9.

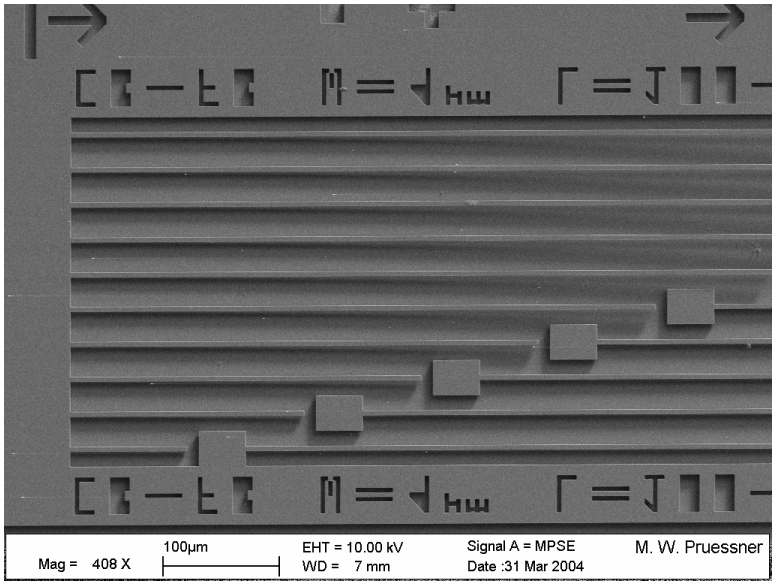


**Figure 4. 9: Released cantilever test structures after supercritical drying.**

## 4.4 Mounting

Once the devices are fabricated, they are mounted onto a 26 mm × 7 mm × 3 mm (L × W × H) aluminum mount with double-sided Scotch$^{TM}$ brand tape. The mount has a 1 mm deep notch (depression) in which the 15 mm × 5 mm × 200 µm chip is placed. This protects the chip during handling. In fact, because none of the facets are directly

exposed (the facets are recessed 1 mm from the mount edge), they are protected should the chip fall on its side.

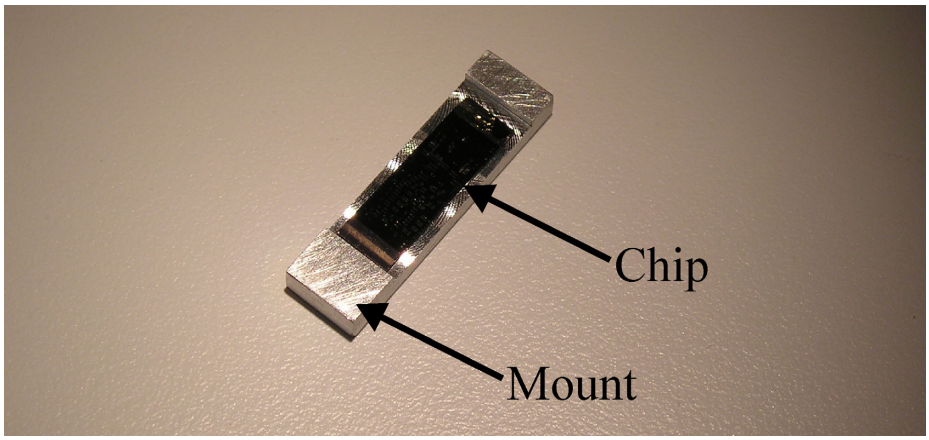


**Figure 4. 10: Aluminum mount (26 mm × 7 mm × 3 mm). The dark region is the chip.**

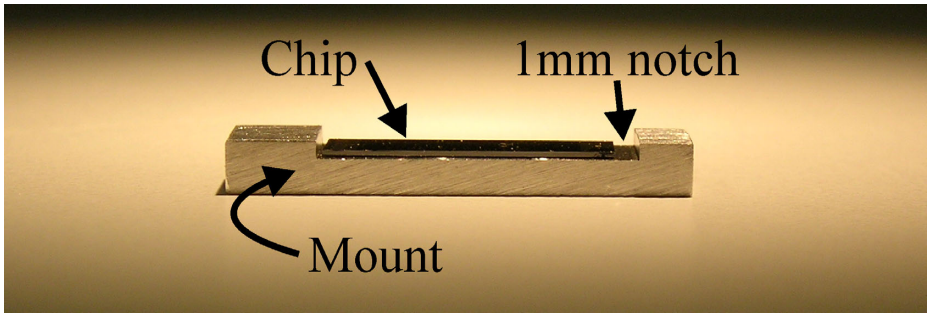


**Figure 4. 11: Side view of aluminum sample holder with mounted chip. This view shows the 1 mm notch (depression) in the holder for mounting the 200 μm thick chip.**

## 4.5 Summary

This chapter has presented a versatile process for fabricating InP-based electrostatically-actuated moving waveguide MEMS devices. The epiwafer layer structure consists of InP-based waveguides with trace amounts of gallium and arsenic to control material properties. The sacrificial layer is InGaAs and offers complete wet etch selectivity over InP. Device processing consists of a dry-etch step using methane-hydrogen RIE to define the waveguides and mechanical structures in InP. This is a non-selective process but enables vertical sidewalls with roughness of less than 50 nm. Metal contact pads are defined by electron-beam evaporation and lift-off. Finally, the waveguides are released from the substrate by selectively etching the InGaAs sacrificial layer.

Device fabrication requires only a two-mask, two-lithography process. Furthermore, the process requires only a single epitaxial growth and no regrowth during processing. Despite its simplicity, the process is versatile and enables a variety of devices to be realized, as will be discussed in subsequent chapters.

# CHAPTER 5

# MEMS EVANESCENT COUPLERS

## 5.1 Introduction

The previous chapters have laid the foundation for developing InP-based optical waveguide MEMS. In this and the following chapters, MEMS-actuated optical waveguide devices are presented. Specifically, in this chapter a MEMS evanescent coupler is presented in which coupling between two parallel waveguides can be modulated by varying the spacing between the waveguides. Theory, device design, and experimental results are presented.

## 5.2 Theory: Evanescent Coupling

The basic theory of thin-film dielectric waveguides is reviewed in Appendix B. Transverse electromagnetic (TEM) modes are guided waves in a waveguide whose amplitude (electric and magnetic field) and polarization do not change with propagation along the waveguide $z$-axis. Both multiple-modes and their evanescent field are plotted in Figure 5. 1. Inside the core region (refractive index $n_1$), the electric field is harmonic (sinusoidal solutions), and in the cladding ($n_2$) it experiences an exponential decay.

A simplified waveguide made with perfect mirrors that supports two distinct modes is shown in Figure 5. 2. Note that the power, $P$, is plotted instead of the electric field, $E$, where $P \sim |E|^2$. Both the $m = 1$ (Figure 5. 2a) and $m = 2$ mode (Figure 5. 2b) satisfy the conditions for a waveguide mode in that they have the same amplitude and

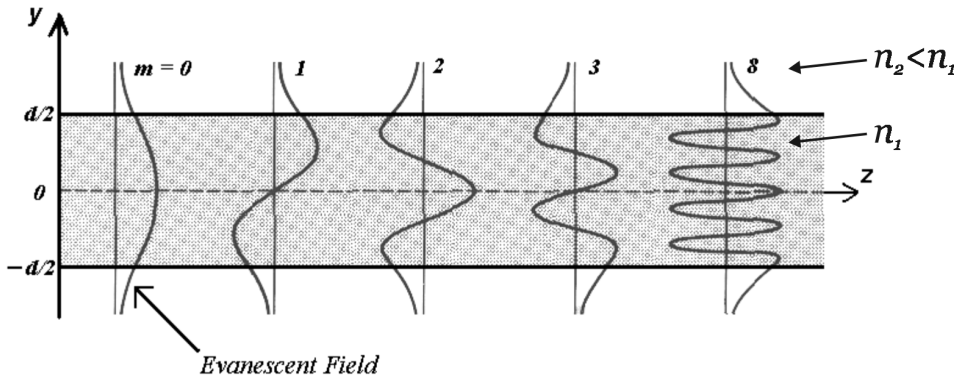


**Figure 5. 1: Guided TE-modes in a two-dimensional slab dielectric waveguide for modes *m*=0, 1, 2, 3, and 8; $n_2 < n_1$. (adapted from [86]).**

polarization along the propagation axis *z*. If any two modes with electric field $E_1$ and $E_2$ and propagation constants $\beta_1$ and $\beta_2$ satisfy Maxwell's wave equation, then the linear superposition of the two fields also is a guided mode. The linear superposition mode is shown in Figure 5. 2c and has the general form [86]:

$$E_{\text{Superposition}} = A_1(y)\exp(-j\beta_1 z) + A_2(y)\exp(-j\beta_2 z), \tag{5.1}$$

where $\beta_1 \neq \beta_2$. Due to the different propagation constants of modes $m = 1$ and $m = 2$, the optical power contained in the superposition mode will not be constant along the z-direction but will vary as the mode propagates (Figure 5. 2c). This mode superposition or interference can be exploited for both coupling and switching between waveguides. Looking at the mode propagation (Figure 5. 1), a small fraction of optical power travels outside of the waveguide core. This 'evanescent field' enables mode coupling between two waveguides, similar to multi-mode coupling in a single waveguide (Figure 5. 2).

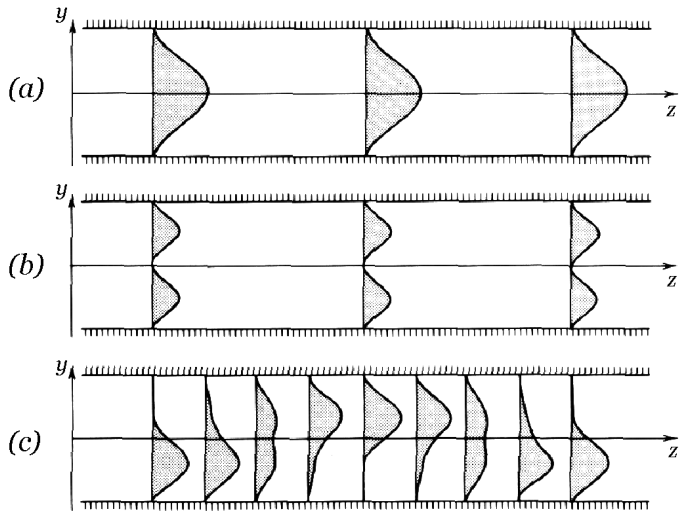


**Figure 5. 2: a) Waveguide with mode 1 and propagation constant $\beta_1$, b) waveguide with mode 2 and $\beta_2$, c) superposition of modes 1 and 2 (adapted from [86]).**

### 5.2.1 Coupling Between Identical Single-Mode Waveguides

Evanescent coupling between two identical single-mode optical waveguides will now be reviewed following the approach of *Saleh and Teich* [86], although similar treatments can be found in many texts [15, 56, 106, 107]. Coupling is not limited to single-mode waveguides, but can also proceed via higher-order modes (see Appendix C). For now, however, only single-mode waveguides are considered.

Two parallel planar waveguides with core refractive indices $n_1$ (*waveguide 1*), $n_2$ (*waveguide 2*), and cladding index $n$ are shown in Figure 5. 3. The mode initially propagates in *waveguide 1* with evanescent field extending into *waveguide 2*. The two waveguides are *weakly-coupled*, which means that the presence of *waveguide 2* has no effect on the propagation constant, $\beta_1$, and the polarization of *waveguide 1* and vice versa.

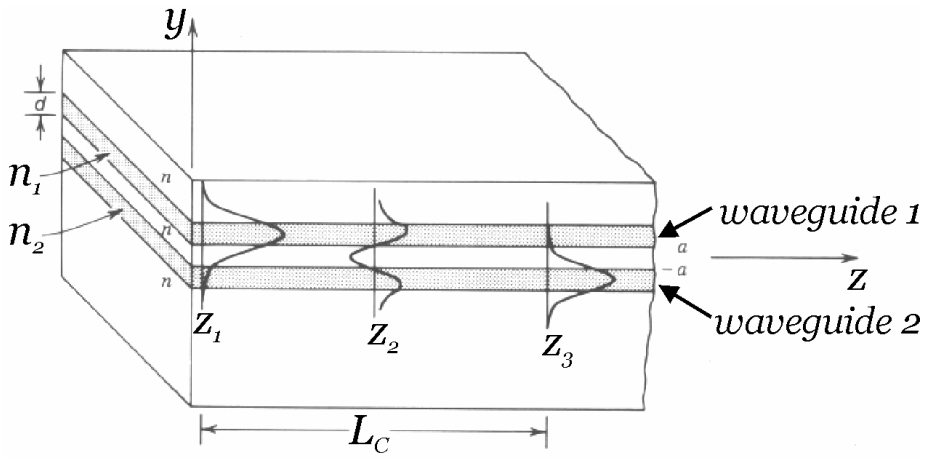


**Figure 5. 3: Coupling between two slab waveguides (core refractive indices $n_1$ and $n_2$ and cladding index $n$). Mode $m = 0$ is initially in waveguide 1 ($z = z_1$), but eventually couples to waveguide 2 ($z = z_2$). It resides completely in waveguide 2 after traveling length $L_C$ ($z = z_3$) (adapted from [86]).**

Coupling between two waveguides can be explained by considering two-mode (multi-mode) propagation. In the multi-mode waveguide of Figure 5. 2, two modes propagate in the waveguide and the superposition of the two modes leads to a periodic modulation of the power along the top and bottom segments of the waveguide. The two parallel single-mode waveguides in Figure 5. 3 form a compound waveguide structure that is no longer single-mode, but which supports two modes, similar to Figure 5. 2. Therefore, two-mode coupling in a multi-mode waveguide via mode-superposition (Figure 5. 2c) can be used to visualize evanescent coupling in two single-mode waveguides (Figure 5. 3).

Coupling between the two identical and weakly-coupled waveguides with refractive indices $n_{\text{CORE}}$ and $n_{\text{CLADDING}}$ can be examined using the *coupled-mode theory* [108] and the *coupled-mode equations* [15]:

$$\frac{dA_1(z)}{dz} = -i\beta A_1(z) - i\kappa A_2(z) \text{ and} \tag{5.2a}$$

$$\frac{dA_2(z)}{dz} = -i\beta A_2(z) - i\kappa A_1(z), \tag{5.2b}$$

where β is the propagation constant for both waveguides and κ is the coupling coefficient that describes the coupling 'strength.' The coupling coefficient is given by the overlap integral between the fundamental modes in the two waveguides [86]:

$$\kappa = \frac{1}{2}\left(n_{core}{}^2 - n_{cladding}{}^2\right)\frac{k_0{}^2}{\beta}\int^{Waveguide} A_1(y)A_2(y)dy, \tag{5.3}$$

where $k_0$=2π/λ. The power in *waveguide 1* and *waveguide 2* as a function of position along the waveguide propagation direction (*z*-axis) is then [15]:

$$P_1(z) = P_1(0)\cos^2(\kappa z) \text{ and} \tag{5.4a}$$

$$P_2(z) = P_2(0)\sin^2(\kappa z). \tag{5.4b}$$

From eqns. (5.4a-b) it is clear that the power in each waveguide increases and decreases periodically with a characteristic length of:

$$L_C = \pi/2\kappa. \tag{5.5}$$

This characteristic coupling length, $L_C$, is required to completely transfer all optical power from *waveguide 1* to *waveguide 2*. Equations (5.1) – (5.5) form the basis of optical coupling in the MEMS coupler.

### 5.2.2 Coupling: General Case

The discussion of coupling between non-identical and multi-mode waveguides is presented in Appendix C, and the main conclusions are briefly reviewed here. The effect of a phase mismatch between two non-identical waveguides results in a shortened characteristic coupling length, $L_C$, as well as a reduction in the coupled power [109]. In multi-mode waveguides, coupling between two modes $m \neq l$ does not occur efficiently without an external perturbation. Therefore, coupling between the $m \neq l$ modes can be neglected. While coupling between higher-order modes $m = l > 1$ can occur, the coupled power is low unless multi-mode interference devices [110] are specifically designed. Therefore, the MEMS coupler presented in this PhD research is based on a single-mode evanescent coupler.

### 5.2.3 Optical Switching via Evanescent Coupling

Optical switches are realized by varying the coupling strength in couplers. This can be achieved by varying the propagation constant, β, in one of the waveguides so that $\Delta\beta \neq 0$. The coupled power from *waveguide 1* to *waveguide 2* is [86]:

$$\frac{P_2(z=L_C)}{P_1(z=0)} = \left(\frac{\pi}{2}\right)^2 \operatorname{sinc}\left\{\frac{1}{2}\left[1+\left(\frac{\Delta\beta L_C}{\pi}\right)^2\right]^{1/2}\right\}, \tag{5.6}$$

where $\Delta\beta = \beta_1 - \beta_2$. The propagation constant β is linearly proportional to the refractive index of the core, $n_{Core}$ (see Appendix B). Therefore, the coupling strength in an

evanescent coupler can be controlled via the refractive index, $n_{core}$. The refractive index can be modulated in a number of ways [19], including via the thermo-optic effect [11], the electro-optic effect [111], and non-linear optical effects [112, 113].

A second method for varying the coupling strength is to vary the waveguide spacing. The evanescent field decays exponentially away from the waveguide core (Figure 5. 1); hence, the coupling coefficient also varies exponentially with waveguide separation according to the overlap integral in eqn. (5.10); that is, $\kappa \sim \exp(-gap)$. Therefore, only a small variation in spacing between the waveguides results in a large modulation of the coupled power. Therefore, low-power MEMS electrostatic actuation is well-suited for such coupler switches and is the approach taken in this research.

## 5.3 Literature Review

Couplers with fixed splitting ratio have been extensively reported in the literature and are widely used in fiber-optic communication networks [56, 86]. They are used as optical power splitters with arbitrary ratio, for example –3 dB or 50%, in order to divide a signal among an arbitrary number of end-users. A second application of fiber couplers is for determining the signal integrity of a network by tapping only a small fraction of power (e.g., one percent). More recently, fixed couplers were demonstrated in integrated optics in various materials, including silica on silicon [114], silicon on insulator (SOI) [115] and InP/InGaAsP [116]. These couplers enable greater integration on a single chip and will lead to increased optical functionality.

A multi-mode interference (MMI) coupler with thermo-optic switching was previously reported. The device exhibited complete switching at 110 mW heating power

with 150 μs switching time [11]. Similarly, the electro-optic effect can be used to create a phase mismatch, $\Delta\beta$, and hence switching. A Y-branch electro-optic polymer coupler was demonstrated with 26 dB extinction ratio at 3.4 V [117]. Non-linear optics for optical switching has also been proposed and simulated [113].

*Chollet* proposed and fabricated a MEMS-actuated evanescent coupler using SiON/$SiO_2$ waveguides [109, 118]. In this device, two wafers containing SiON waveguides were bonded together to form the MEMS coupler with vertical electrostatic actuation. Although optical switching was not possible with this device due to the poor quality of the waveguides, attenuation of 65 dB (TE-polarization, $\lambda = 630$ nm) was demonstrated at 40–85 V with maximum switching speed of 1 ms. A similar MEMS evanescent attenuator was demonstrated by *Veldhuis* [119]. The mechanical design of a $Si_3N_4$ waveguide with a suspended silicon bridge as the absorbing element was optimized. This resulted in a low operating voltage of 2.5 V with 65 dB attenuation. However, this optimized device required a 9.5 mm long suspended absorbing element and exhibited a relatively slow response time of 10 ms. Another MEMS evanescent attenuator was demonstrated by *Hane* [120]. Here, standard optical fibers were fixed to a silicon V-groove and polished to expose the fiber core. A post-processed polysilicon electrostatically-actuated diaphragm enabled variable attenuation. However, the maximum attenuation reported was just 3 dB with no operating voltage reported.

Optical switches using MEMS-actuated evanescent coupling in gallium arsenide waveguides were simulated in [121], and MEMS-actuated displays using cantilevers and evanescent coupling were also experimentally demonstrated recently [122]. Successful controllable coupling using MEMS evanescent coupling was reported by *Lee* [55, 123,

124]. In this device, single-crystal silicon waveguides were suspended above a silicon substrate by an intermediate $SiO_2$ sacrificial layer. The suspended waveguides were electrostatically-actuated in-plane to vary the spacing between the waveguides and an optical micro-disk resonator. The disk resonator serves as an optical filter, and the electrostatically-actuated waveguides enable controlled channel-dropping. An 8 dB increase in optical output power was reported at 120 V actuation, when the suspended waveguide is in close contact with the micro-disk resonator [55]. Recently, *Lee* demonstrated a vertically-coupled MEMS-actuated disk-resonator filter with low-voltage (<35 V) actuation for dispersion compensation [125].

Wavelength-selective switching was also demonstrated using a ring-resonator filter and an electrostatically-actuated membrane [126, 127]. This device behaved as an optical filter ($V = 0$). When a voltage was applied to the membrane (~20 V), it was pulled-in to the ring-resonator. This caused the resonant condition to be shifted so that the device became wavelength-insensitive (all-pass).

## 5.4 MEMS Evanescent Coupler

The top-view schematic for the electrostatically actuated MEMS coupler at $V = 0$ and at $V = V_{PI}$ is shown in Figure 5. 4a-b. Here, $V_{PI}$ is the voltage at which the electrostatic force becomes large enough that the two waveguides abruptly "pull-in." At $V = 0$, there is no coupling and any optical power in the top *BAR* waveguide at the input will remain there at the output. For $V = V_{PI}$, the waveguide gap becomes small enough that coupling occurs and the output will be divided among the *BAR* and *CROSS* waveguides (Figure 5. 4c-d).

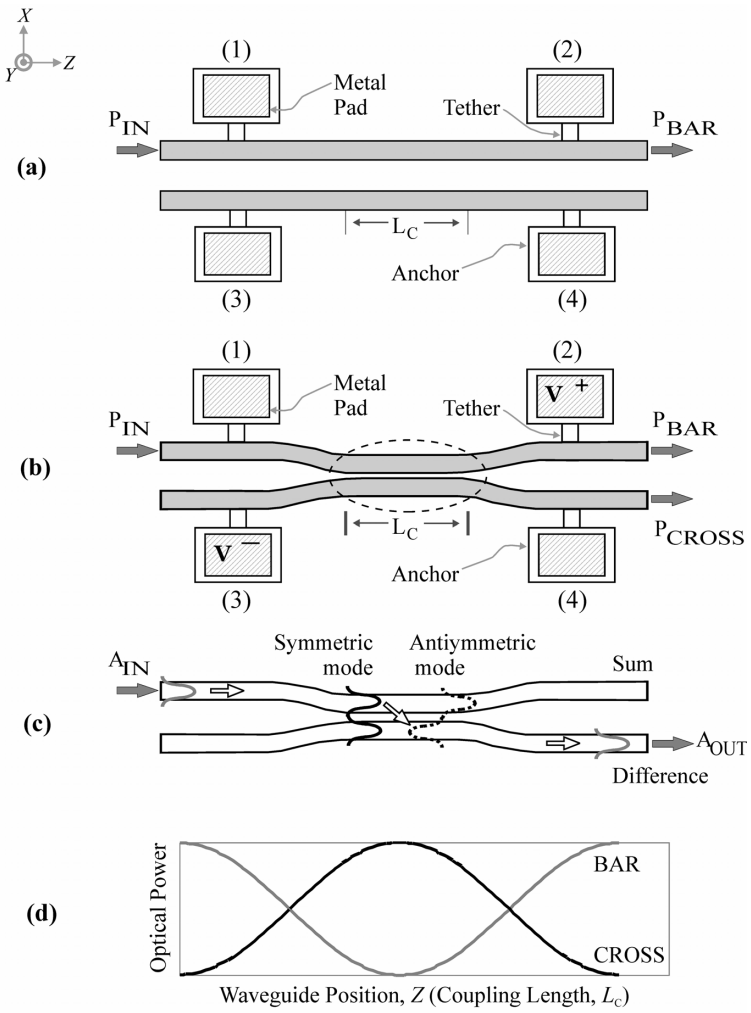


**Figure 5. 4: MEMS evanescent coupler: a) top view schematic at $V$=0, b) schematic of coupled *power* ($P$) with actuated waveguides at $V=V_{PI}$ (pull-in) and coupling length $L_C$, c) optical coupling of *fields* (field amplitude, $A$) via mode interference ($V=V_{PI}$), d) coupled power along z-axis ($V=V_{PI}$).**

Advantages of MEMS actuation in optical applications include low-power switching (electrostatic actuation requires almost no current), relatively high-speed (~ 1 μs), and application to a wide variety of materials (MEMS couplers do not rely on special material properties such as electro-optic effects).

The present device utilizes moderately doped semiconductor waveguides with small gaps (1–2 μm) in order to ensure low-voltage operation. The fabrication process is simple compared to other MEMS-actuated evanescent devices [109, 119], since the waveguides are parallel and actuated in-plane rather than out-of-plane, resulting in a self-aligned process without the need for wafer bonding. This is a significant advantage over devices with vertical coupling [47, 109, 118-120, 125], in which alignment depends on accurate wafer bonding. Device processing is simplified considerably, and only two optical masks are required for fabrication. In-plane actuation also simplifies testing since device actuation can be easily visualized.

Compared to the ring and disk-resonator filters in [47, 55, 123-125], couplers are relatively wavelength insensitive.

Finally, InP enables integration of active devices with optical gain at 1550 nm. To the best of my knowledge, this is the first MEMS-based coupler made of a direct bandgap semiconductor and one of only a handful of MEMS devices made of InP [68-70, 73, 74, 81, 128-130]. Another advantage of using InP-based materials is the growth method using molecular beam epitaxy (MBE). During MBE growth, it is possible to adjust the material composition with high accuracy. This enables precise control of electronic and optical properties as well as intrinsic material strain, which is useful for ensuring accurate vertical alignment of the waveguides and also allows greater control over mechanical properties (i.e. device spring constant and resonant frequency). Finally, it should be pointed out that for passive operation the MEMS-coupler can utilize inexpensive materials – i.e. polymer or $SiO_2/SiN_X$ waveguides on silicon actuators, or silicon/SOI waveguides – without significant design changes.

### 5.4.1 MEMS Actuator Design

The MEMS coupler relies on pull-in actuation, which utilizes the normal force between two oppositely-charged electrodes (Figure 5. 5). If the applied voltage is large enough, then the electrostatic force dominates and exceeds the mechanical restoring force, resulting in pull-in of the electrode to the substrate. The critical voltage at which pull-in occurs is given by:

$$V_{Pull-In} = \sqrt{\frac{8k_{Mechanical}}{27\varepsilon_0 A}}, \tag{5.7}$$

where $k_{\text{Mechanical}}$ is the mechanical spring constant of the electrode, $\varepsilon_0$ is the free-space permittivity, and $A$ is the area of the parallel-plate capacitor formed by the electrode and substrate. While eqn. (5.7) is an approximation it provides a reasonably accurate pull-in voltage expression. For a derivation of the pull-in voltage, see Appendix D.

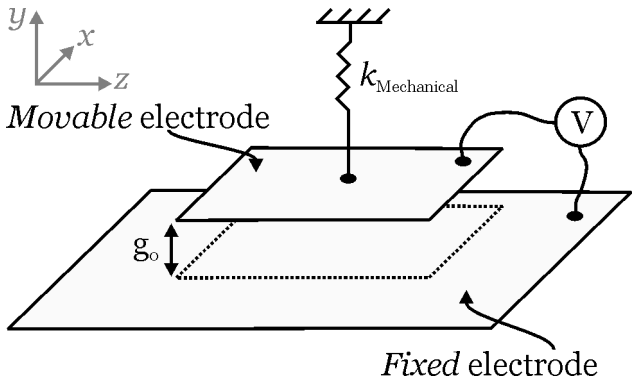


**Figure 5. 5: Pull-in actuator with movable top electrode and fixed bottom electrode separated by initial gap $g_0$.**

In order to analyze the MEMS coupler using the single movable electrode pull-in actuator in Figure 5. 5, a half-structure model is developed (Figure 5. 6). The MEMS coupler consists of two *movable* waveguides with potential difference $V_0$ (Figure 5. 6a). This voltage potential, $V_0$, can be replaced with an equivalent potential $+V_0/2$ and $-V_0/2$ across each waveguide (Figure 5. 6b). This gives the same potential drop (and electrostatic force), but there now is an electrically-neutral axis, indicated by the dashed line in Figure 5. 6b. Since both waveguides are identical and will be bent the same way, this electrically-neutral axis is fixed. The neutral axis can therefore be treated as a ground plane; this enables us to solve for the half-structure pull-in voltage, $V_{PI}/2$ ($V_0/2$).

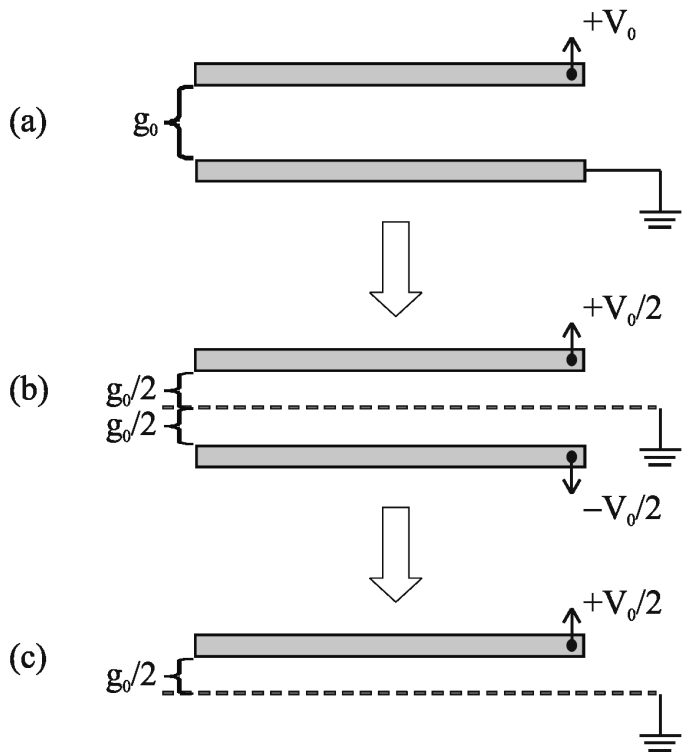


**Figure 5. 6: Half-structure model: a) two movable waveguides with applied actuation voltage, $V_0$, b) equivalent model with electrically-neutral axis (dashed line), c) single movable waveguide at $V_0/2$ and fixed ground plane (dashed line).**

In order to apply eqn. (5.7) the waveguide spring constant is required. Treating each waveguide as an ideal fixed-fixed beam, then for small displacements where the beam exhibits small axial strain, the spring constant is [7, 8]:

$$k_{Mechanical} = k_{Bending} + k_{Stress} = \frac{Et\pi^4}{6}\left(\frac{w}{L}\right)^3 + \frac{t\sigma_0\pi^2}{2}\left(\frac{w}{L}\right), \tag{5.8}$$

where $E$ is Young's modulus, $\sigma_0$ is the intrinsic stress, $t$ is the waveguide height, $w$ is the waveguide width, and $L$ is the length of the suspended segment of the waveguide. The calculated pull-in voltage for various MEMS couplers as a function of suspended waveguide length and initial gap ($g_0$ = 1 μm, 2 μm, 3 μm) is shown in Figure 5. 7. For the simulation, the waveguide width was $w$ = 2 μm, Young's modulus was $E$ = 90 GPa, and the intrinsic stress was $\sigma_0$ = 45 MPa ($\sigma_0 > 0$ during the MBE growth). The results indicate that low-voltage actuation ($V < 20$V) should be readily achievable.

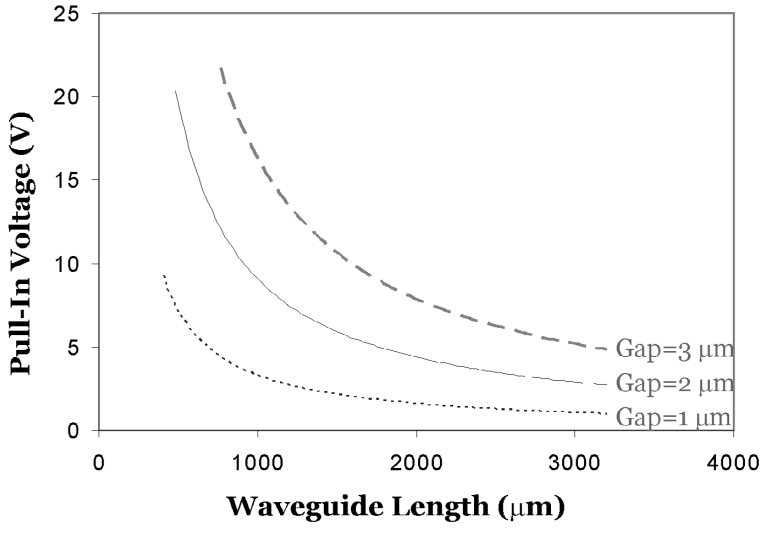


**Figure 5. 7: Calculated pull-in voltage for various MEMS coupler designs.**

### 5.4.2 Optical Design

While coupling can be described by the coupled-mode equations in eqn. (5.2ab), it is much more effective to use software tools to study optical coupling. Simulation software is used to obtain the coupling coefficient, κ, and the propagation constant, β. Once these parameters are known, the optical behavior of the coupler can be derived. To this end, a fullvectorial finite difference mode solver (Apollo OWMS [131]) and a beam propagation method (BPM) solver (RSoft BeamPROP [132]) were used.

Apollo OWMS is an "optical waveguide mode solver." It simulates the electric (or magnetic) field distribution and calculates the effective refractive index, $n_{Effective}$, of a waveguide for specific modes. A typical simulation output is shown in Figure 5. 8 for the $m$ = 0 mode for a waveguide of width $w$=2 μm, 2 μm core thickness ($n_{Core}$=3.195) and 1 μm top and bottom cladding ($n_{Cladding}$=3.173). From $n_{Effective}$, the propagation constant β is:

$$\beta = n_{Effective} / \lambda. \tag{5.9}$$

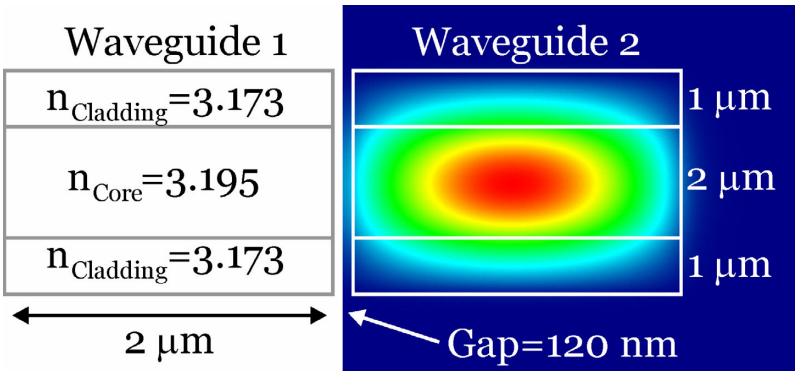


**Figure 5. 8: Typical OWMS simulation of two coupled waveguides (cross-section view). The image on the right shows the simulated optical power in the waveguide.**

The coupling coefficient is obtained by repeating the simulation for two modes: the *symmetric* and the *antisymmetric* modes (as indicated in Figure 5. 4c). Interference of these two modes results in evanescent coupling according to the coupled-mode theory [108], similar to two-mode coupling in Figure 5. 3. The effective index for the two modes $n_{\text{Symmetric}}$ and $n_{\text{Antisymmetric}}$ is simulated and the coupling coefficient, $\kappa$, is subsequently obtained by [106]:

$$\kappa = (\beta_{\text{Symmetric}} - \beta_{\text{Antisymmetric}})/2 = (n_{\text{Symmetric}} - n_{\text{Antisymmetric}})k_o/2, \tag{5.10}$$

where $k_0 = 2\pi/\lambda$. The coupling length, $L_C$, is obtained from $\kappa$ using eqn. (5.5).

The simulated coupling coefficient, $\kappa$, and coupling length, $L_C$, are shown in Figure 5. 9 for various waveguide gaps for both TE- (*E*-field perpendicular to wafer plane, or S-polarization) and TM-polarization (*E*-field parallel to wafer plane, or P-polarization) at $\lambda = 1550$ nm. The simulations predict stronger coupling for TE-polarization than for TM-polarization, as is evident from the smaller $\kappa$ and the larger $L_C$ for this polarization (Figure 5. 9a). The polarization-dependence, defined as $\kappa_{TE}/\kappa_{TM}$, indicates roughly an eight-fold larger coupling for the TE- compared to the TM-fundamental mode. Experiments confirm this polarization dependence (section 5.4.3).

The polarization dependent coupling results from the difference in propagation constants for the two modes for TE- and TM-polarization. The difference between the two propagation constants, $\Delta\beta = \beta_{\text{Symmetric}} - \beta_{\text{Antiymmetric}}$ determines the coupling coefficient according to eqn. (5.10). Detailed simulation analysis of polarization dependence in fixed couplers can be found in the literature showing that geometry plays a

strong role in determining polarization dependence, with tall and narrow waveguides – similar to those used in this PhD research – exhibiting stronger TE coupling [133]. In contrast, TM coupling is more efficient for waveguides with larger width vs. height ratio. Other experimental and simulation studies have also confirmed this strong polarization-dependence in high-index contrast semiconductor waveguide couplers [134].

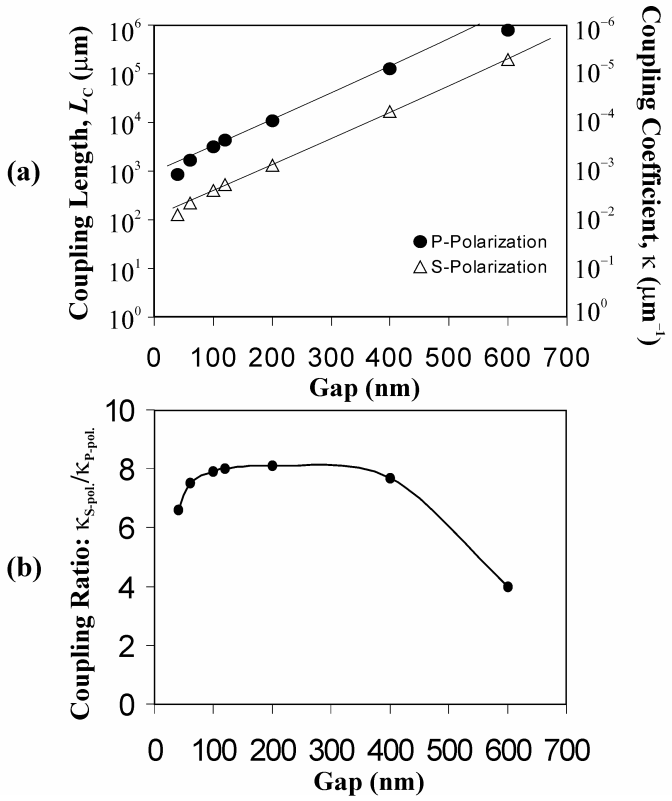


**Figure 5. 9: a) coupling length, $L_C$, and coupling coefficient, κ, vs. waveguide *gap*, b) polarization dependence, $\kappa_{S\text{-polarization}}/\kappa_{P\text{-polarization}}$ (TE vs. TM).**

To study the effect of higher-order modes on optical coupling a beam propagation method (BPM) simulation software called BeamPROP (RSoft BeamPROP [132]) was used. The software calculates the electric field and power in a given optical device

specified by the user. A typical output is shown in Figure 5. 10, where coupling for the $m = 0$ mode was simulated for a coupler with the two waveguides separated by a *gap* = 60 nm.

The simulations in Figure 5. 10 were repeated for the $m = 1$ and 2 modes, and the coupled power is plotted in Figure 5. 11. Two observations regarding higher order modes can be made: 1) majority of the coupled power resides in the fundamental $m = 0$ mode; higher order modes ($m = 1, 2$) contain only one percent or less of the total power; 2) the higher-order modes exhibit stronger coupling (larger κ) and shorter characteristic coupling lengths, $L_C$. These observations are in agreement with section 5.2.2 (and Appendix C).

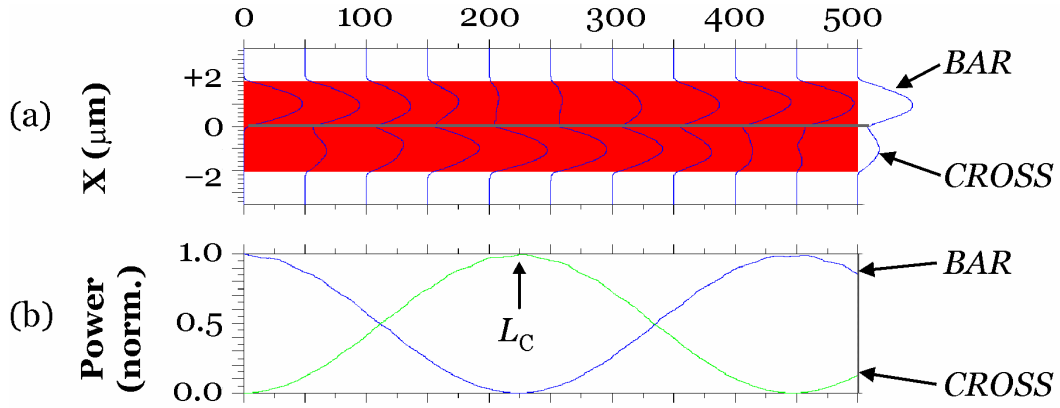


**Figure 5. 10: BeamPROP simulation (mode of *m*=0, λ=1550 nm, TE-polarization) for *gap* = 60 nm: a) top view of power distribution, b) variation in coupled power.**

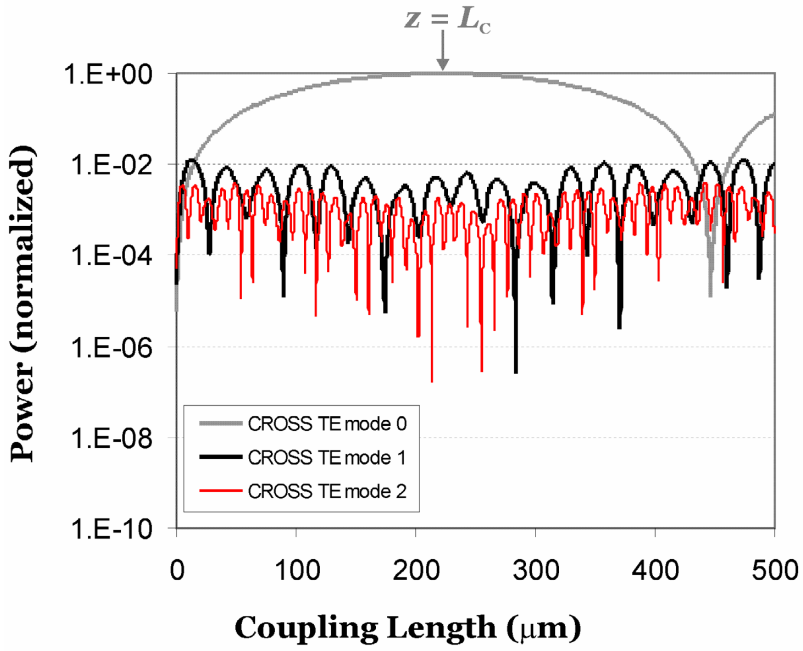


**Figure 5. 11: BeamPROP simulation for modes *m* = 0, 1, 2. The *m* = 0 mode exhibits the longest coupling length, $L_C$ and contains most of the optical coupled power, while the *m* = 1, 2 modes only represent 1 % or less of the power in the *m* = 0 mode. Parameters: waveguide *w* = 2 μm, *gap* = 60 nm, λ = 1550 nm (TE).**

### 5.4.3 Design Summary

All devices use waveguides of width $w = 2$ μm with $t = 2$ μm core thickness ($n_{Core}$=3.195, $In_{0.96}Ga_{0.04}As_{0.08}P_{0.92}$) and $t = 1$ μm top and bottom cladding ($n_{Cladding}$=3.173, $In_{0.99}Ga_{0.01}As_{0.01}P_{0.99}$). The dimensions were chosen in part due to fabrication constraints, which were dictated by the optical lithography system available. According to the discussion in section 5.4.1, pull-in actuation couplers with initial *gap* = 1 μm and 2 μm and lengths spanning 500 – 3000 μm were designed. These device lengths should give actuation voltages in the 4 – 20 V range (Figure 5. 7). From the

optical simulations, characteristic coupling lengths, $L_C$, ranging from 100 – 1000 μm for *pull-in gaps* ranging from 50 – 200 nm are expected (Figure 5. 9a). TM-polarization results in an eight-fold decrease in the coupling coefficient, κ, and increased characteristic coupling length, $L_C$, compared to TE-polarization (Figure 5. 9b).

## 5.5 Experimental Results

Fabrication of all InP-based MEMS optical waveguide devices presented in this work was described in Chapter 4. A completed MEMS coupler is shown in Figure 5. 12 indicating smooth sidewalls with roughness < 50 nm and verticality > 85 degrees. Optical-quality sidewalls (low roughness, high verticality) are necessary for ensuring low scattering losses and efficient coupling in the switch. The first generation devices suffered from substrate leakage currents so that these devices were electro-thermally actuated rather than electrostatically. These devices are described in section 5.5.1. The problem was corrected with new devices fabricated from a redesigned epitaxial wafer. These devices, which were electrostatically-actuated, are described in section 5.5.2.

The basic test setup is shown in Figure 5. 13 and Figure 5. 14. A tunable laser source (Agilent: model 81640B, λ = 1496 – 1639 nm) is coupled to a lensed single-mode fiber. The desired polarization (TE or TM) is set with a polarization control unit. Using electrostrictive actuators, the input fiber is coupled to the input waveguide; similarly, an output lensed fiber connected to an optical detector (Newport: model 818-IS-1 and New Focus, Inc.: model 1811) and optical power meter (Newport: model 2835-C) are used to measure the output optical power of the MEMS coupler. A function generator connected to electrical probes mounted on XYZ-micropositioners is used to actuate the MEMS

coupler. Any actuation and movement of the waveguides is observed using a CCD camera with 20x (or 50x) objective and displayed on a CRT monitor. The actuation and optical signals are fed to an oscilloscope for data recording and subsequent analysis.

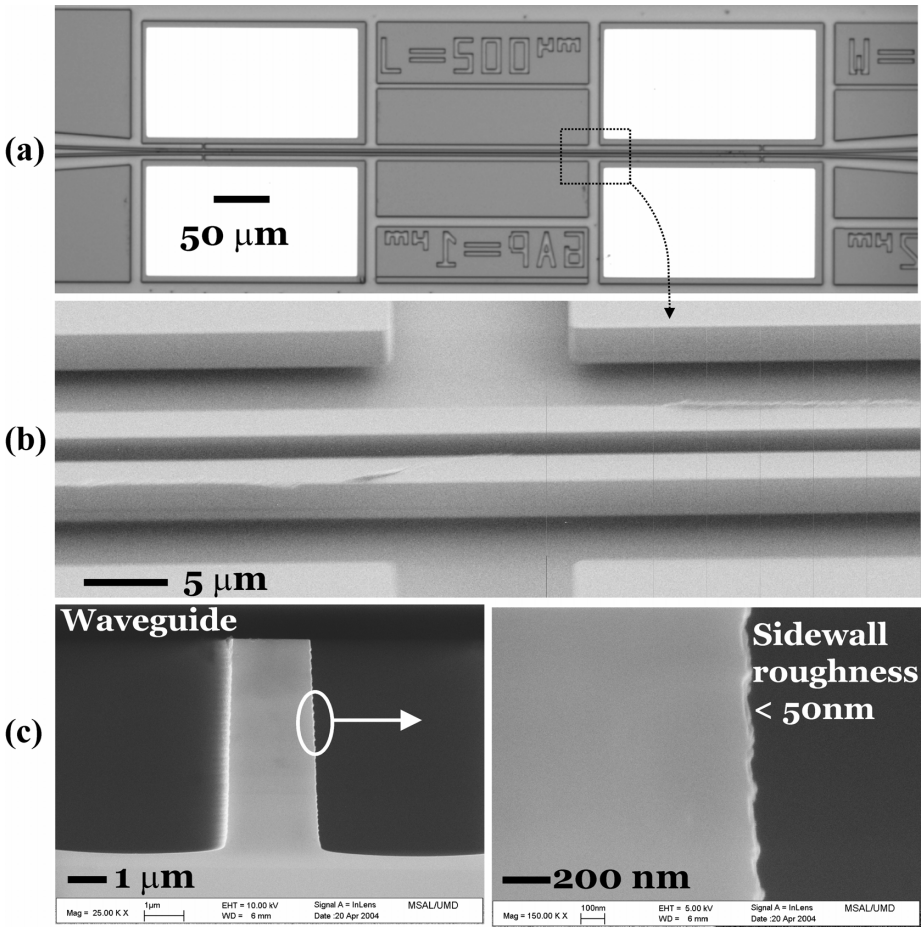


**Figure 5. 12: MEMS coupler: a) top view, b) detail of suspended waveguides in the coupling region (*gap* = 1 μm, before actuation), c) detail of sidewall roughness.**

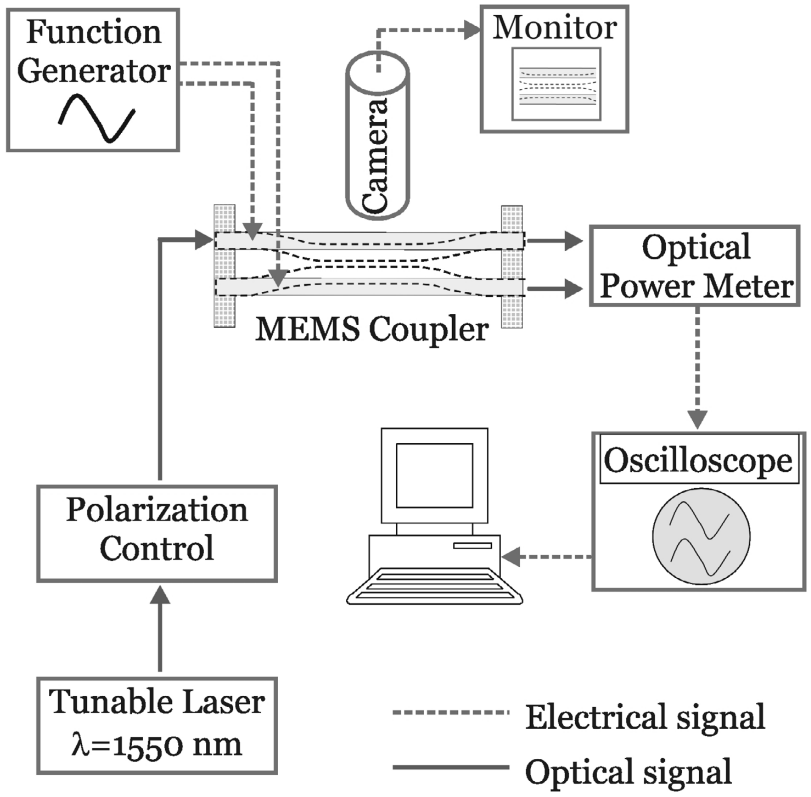


**Figure 5. 13: Optical test setup schematic.**

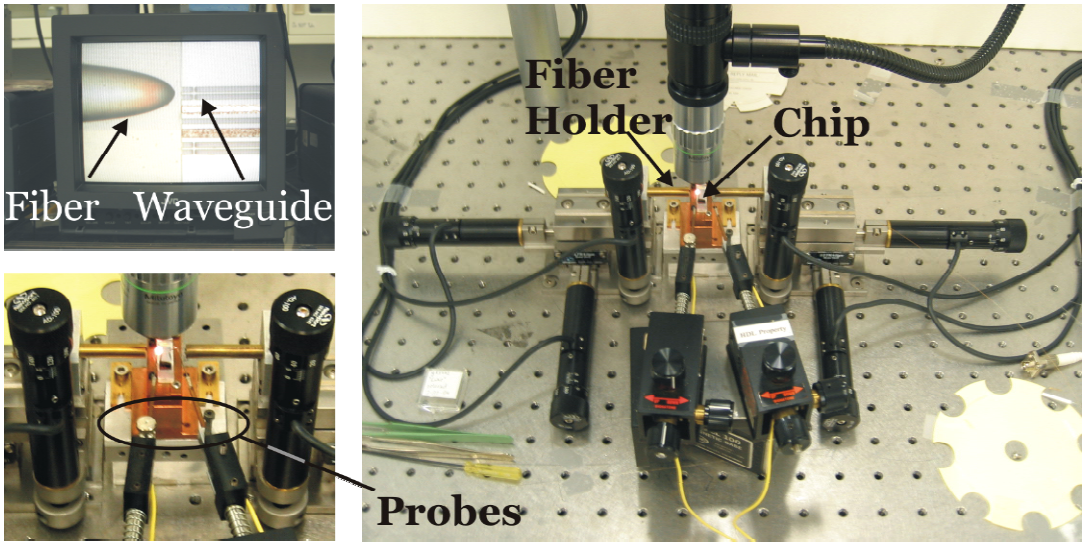


**Figure 5. 14: Optical test setup: a) monitor view of lensed fiber and waveguide (top left), b) complete setup (right), c) detail of chip and probes (bottom left).**

### 5.5.1 Electro-Thermally Actuated MEMS Couplers

The first generation MEMS couplers exhibited large substrate leakage currents (Figure 5. 15). During MBE growth, it is common to first grow an InP "buffer" layer on top of the InP substrate, typically 4500 Å, to obtain uniform surface conditions for additional epitaxial growth. The wafer design used a semi-insulating (SI) substrate. However, the *as-grown* InP buffer layer is intrinsically n-type with a carrier concentration of $n \sim 10^{16}/\text{cm}^3$, which results in a large leakage current between the two waveguides. For electrostatic actuation, a large resistance is required in order to create a voltage potential between the two waveguides. The resistance between the two waveguides was measured to be $R_{23} = 296\ \Omega$ (Figure 5. 16a). The waveguide resistance (measured in identical waveguides on separate samples without InP buffer layer) was $R_{\text{Waveguide}} = 5\ \text{k}\Omega$. Therefore, during actuation several milliwatts of power are dissipated, resulting in significant *Joule* heating (Figure 5. 16b). Waveguide heating causes thermal expansion and deflection, which was used for actuation [135].

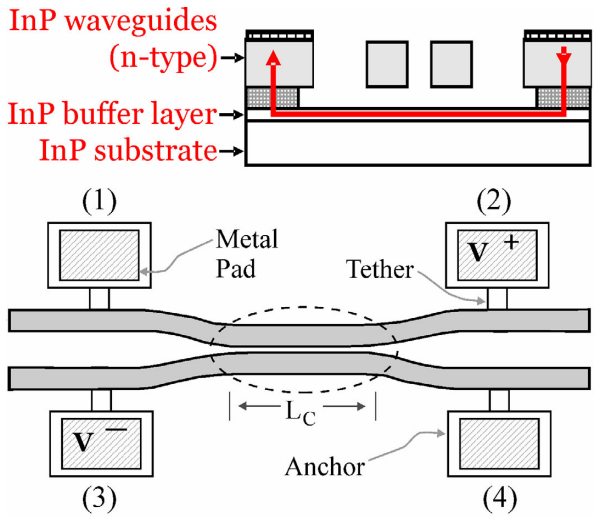


**Figure 5. 15: Substrate leakage current via a 4500 Å thick InP buffer layer.**

Thermal actuation is analyzed as follows. The total actuation strain is [7]:

$$\varepsilon_{THERMAL} = -\left[\frac{\pi^2}{4}\left(\frac{dx}{L}\right)^2 + \frac{\pi^2}{3}\left(\frac{w}{L}\right)^2 + \varepsilon_o\right], \tag{5.11}$$

where $dx$ = 0.5 μm is the actuation distance of each waveguide ($gap$ = 1 μm), $L$ = 500 μm is the waveguide length, and $w$ = 2 μm is the waveguide width. The first term represents the induced axial strain, the second is the *Euler* buckling strain, and $\varepsilon_o$ is the intrinsic tensile strain of the waveguides. Assuming $\varepsilon_o = 0.04$ %, the thermal strain is $\varepsilon_{THERMAL} = 0.0455$ %. The coefficient of thermal expansion is $\varepsilon = 4.56\times10^{-6}$/K [95], which implies a temperature increase of $\Delta T = \varepsilon_{THERMAL}/\alpha = 100$ K for thermal actuation. This is a modest temperature increase and is reasonable considering that 2.5 mW of power (Joule heating) is dissipated in the waveguides at 5.4 V (Figure 5. 16). Therefore, actuation is a combination of electrostatic and thermal effects.

Although thermal actuation consumes more power than electrostatic actuation, switching of the MEMS evanescent coupler can still be demonstrated. Optical coupling is shown in Figure 5. 17. Laser light (λ = 1550 nm, TE-polarization) was coupled into the *BAR* waveguide, and the optical output was measured in the *BAR* and *CROSS* output waveguides during separate experiments. Care was taken to maximize the measured power by adjusting the output fiber for each *BAR* and *CROSS* waveguide measurement. Actuation was achieved using an external function generator and electrical probes using the measurement setup described previously. From Figure 5. 17 it is apparent that the *CROSS* output is in-phase with the actuation signal, whereas the *BAR* output is the complement. This demonstrates that MEMS-based evanescent coupling is feasible.

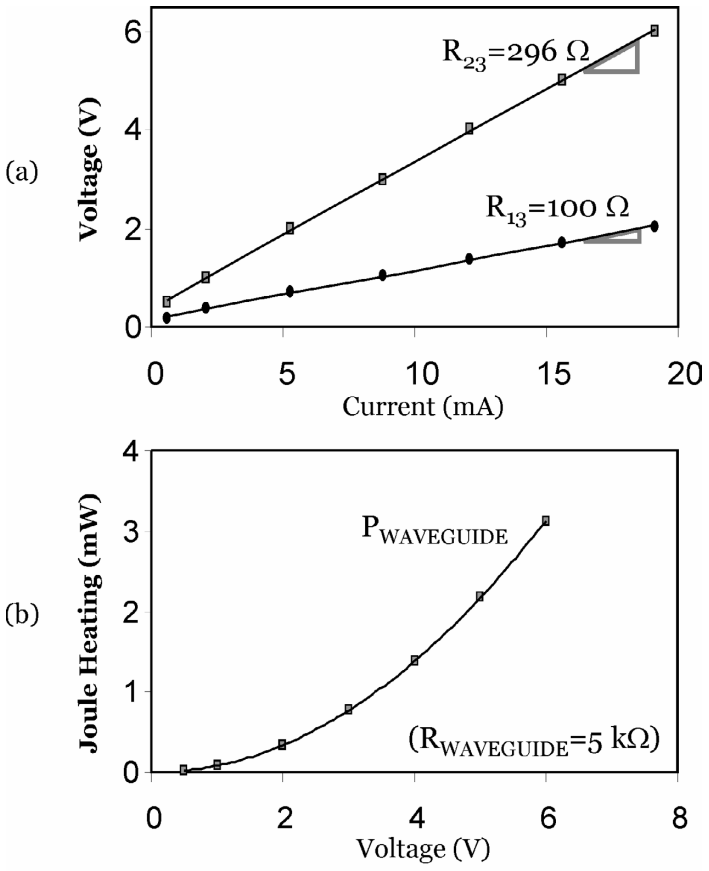


**Figure 5. 16: a) I-V measurements for $R_{13}$ and $R_{23}$, b) calculated Joule heating.**

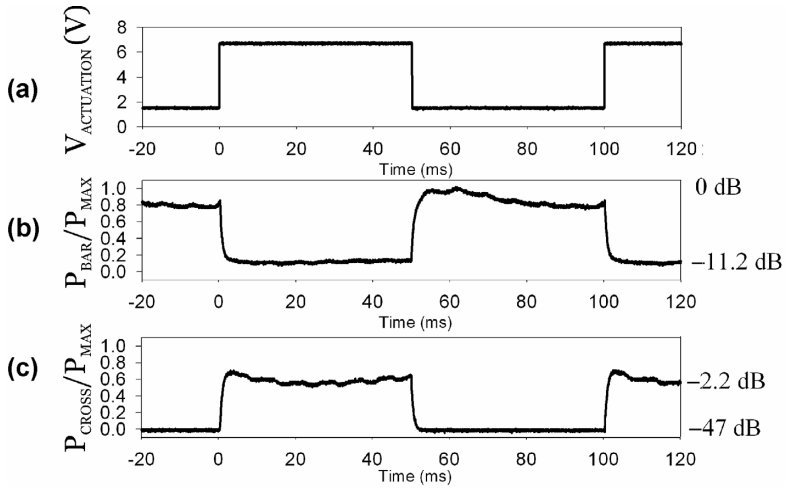


**Figure 5. 17: Electro-thermally actuated coupler: a) actuation, b) *BAR* output, c) *CROSS* waveguide optical output.**

### 5.5.2 Electrostatically Actuated MEMS Couplers

For the electrostatically actuated MEMS couplers, the following nomenclature and device designations are used ($W$ = waveguide width, *gap* = waveguide separation):

$L$: device length; length of movable waveguide segment;

$L_{PI}$: measured waveguide pull-in length and physical coupling length;

$L_C$: theoretical characteristic coupling length (results in 100 % coupling);

*Coupler 1a*: $L$ = 500 μm, $W$ = 2 μm, *gap* = 1 μm (pull-in actuation);

*Coupler 2a*: $L$ = 1000 μm, $W$ = 2 μm, *gap* = 2 μm (pull-in actuation);

*Coupler 2b*: $L$ = 1000 μm, $W$ = 2 μm, *gap* ≤ 2 μm (pull-in actuation; stiction);

*Coupler 3b*: $L$ = 3000 μm, $W$ = 2 μm, *gap* ≤ 2 μm (pull-in actuation; stiction);

*Coupler C-D*: $L$ = 4000 μm, $W$ = 2 μm (comb-drive actuation).

*a) Pull-In Actuation Voltage*

MEMS couplers identical to those in section 5.5.1 were fabricated on a new epitaxial wafer without the InP buffer layer in Figure 4.1. Pull-in test structures were actuated under a probe station to measure the pull-in voltage and to ascertain that no substrate leakage current was present. The devices exhibited large isolation (> 1 MΩ), indicating that substrate leakage was no longer a problem. The measured pull-in voltage in Figure 5. 18 shows excellent agreement with the simulated values from Figure 5. 7. This indicates that the half-structure model in section 5.4.1 gives a good approximation of actual device behavior. It should be noted, however, that the test structures have ideal supports whereas the MEMS coupler waveguides will exhibit tether compliance that influences the pull-in voltage slightly.

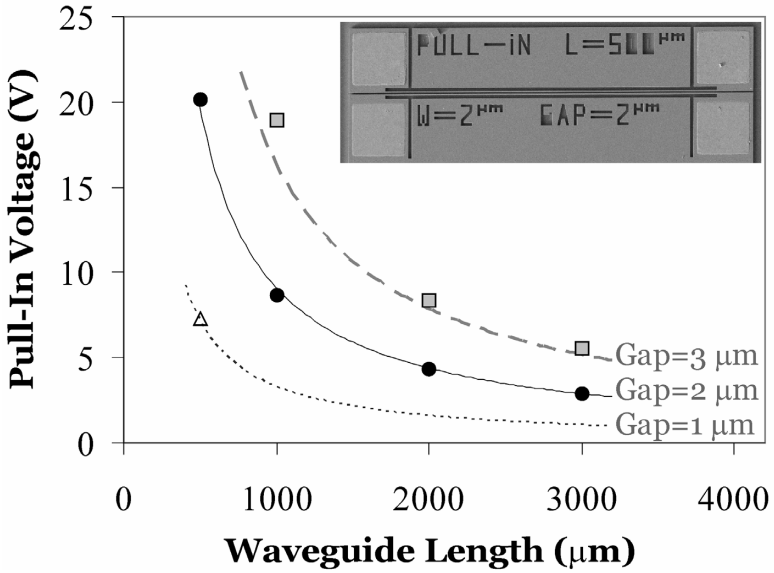


**Figure 5. 18: Measured pull-in voltage for various coupler test structures along with the calculated pull-in voltage from Figure 5. 7. Inset: pull-in test structure.**

Short devices ($L$ = 500 μm, *coupler 1a*) operated very reliably for actuation at the pull-in voltage. *Coupler 1a* proved reliable even at low-frequency ($f$ < 0.1 Hz) operation as long as the actuation voltage did not exceed the initial pull-in voltage significantly. Longer and more compliant devices, however, ($L \geq$ 1000 μm, *coupler 2b* and *coupler 3b*) suffer from stiction [104] after initial or repeated pull-in when low-frequency actuation ($f \leq$ 100 Hz) is used. For high frequency operation ($f \geq$ 1 kHz), reliable operation was obtained for $L$=1000 μm devices (*coupler 2a*) with no observable stiction effects. In excess of 10 million switching cycles have been performed with *coupler 2a* at $f$ = 10 kHz with no change in device performance. Therefore, although stiction may affect long-term device reliability, the experiments indicate that short devices with large spring constant can exhibit very reliable operation, provided that proper operating conditions (actuation voltage, frequency) are met.

Pull-in current flow is also a concern. Landing electrodes or mechanical stops are a possible solution for preventing stiction and current flow. However, for efficient optical coupling very small waveguide gaps (~100 nm) are required, so that fabrication of precise landing structures becomes a challenge. Concerning pull-in current, the waveguides are doped $n = 5\times10^{17}/cm^3$ with typical resistance of 10 Ω/μm unit length. Pull-in currents of 1.5 μA were measured for *coupler 2a*, which is sufficiently small to prevent heating. While the current is increased slightly for *coupler 2b* (stiction), it is limited to less than 25 μA for actuation up to 7 V, so heating is minimal. Future devices can utilize waveguides with lower doping to reduce pull-in current flow. Alternatively, $SiO_2$ or $SiN_X$ can be deposited on the waveguide sidewalls to prevent current flow and stiction effects.

*b) Optical Switching*

Various couplers were tested. *Coupler 1a* exhibited better than –47 dB crosstalk in the 'OFF' state [135]. *Coupler 1a* was actuated at 8 Vp-p square wave ($f$ = 10 Hz) and the *CROSS* coupled power was measured during pull-in, which was $P_{CROSS}$ = 10 %. The small coupling is the result of the short coupling length obtained as well as the waveguide separation at pull-in. The coupling length was measured to be $L_{PI}$ = 225 μm (Figure 5. 19). Using eqn. (5.4), i.e. $\kappa_{S\text{-}pol}\cdot L_{PI} = 0.322$, enables the coupling coefficient to be extracted: $\kappa_{S\text{-}pol} = 1.43\times10^{-3}/\mu m$. From the simulation (Figure 5. 9) the measured $\kappa_{S\text{-}pol}$ corresponds to a waveguide gap of 200 nm, a reasonable value considering sidewall roughness and sidewall angle. Longer devices will have similar $\kappa_{S\text{-}pol}$, but the increased coupling length, $L_{PI}$, should result in larger coupled power, $P_{CROSS}$.

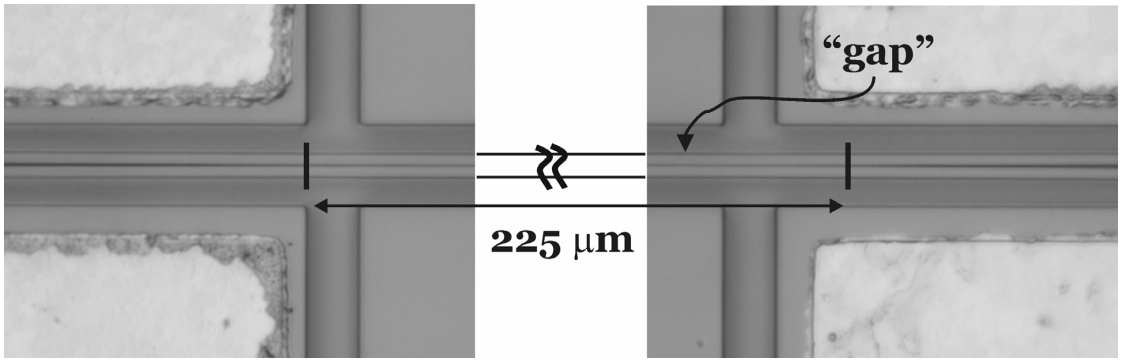


**Figure 5. 19: Coupling length during pull-in for an $L$ = 500 μm device (*coupler 1a*).**

A longer device (*coupler 2b*) is shown in Figure 5. 20. Although stiction is present in this device after initial pull-in, the stiction region is small (solid circle) and for most of the device the waveguides are sufficiently far apart to prevent significant optical coupling. Furthermore, because the waveguides are not completely vertical, the actual contact area is very small – close to the bottom the waveguides are in contact and closer to the top the measured gap is 750 nm in the 'OFF' state. This results in a large contact resistance between the waveguides with measured $R_{stiction}$ greater than 1 MΩ. This is significantly larger than the waveguide resistance, which is 10 Ω/μm (i.e. a 1000 μm waveguide has $R$ = 10 kΩ). Therefore, the coupler can still be electrostatically actuated and tested in the stiction state.

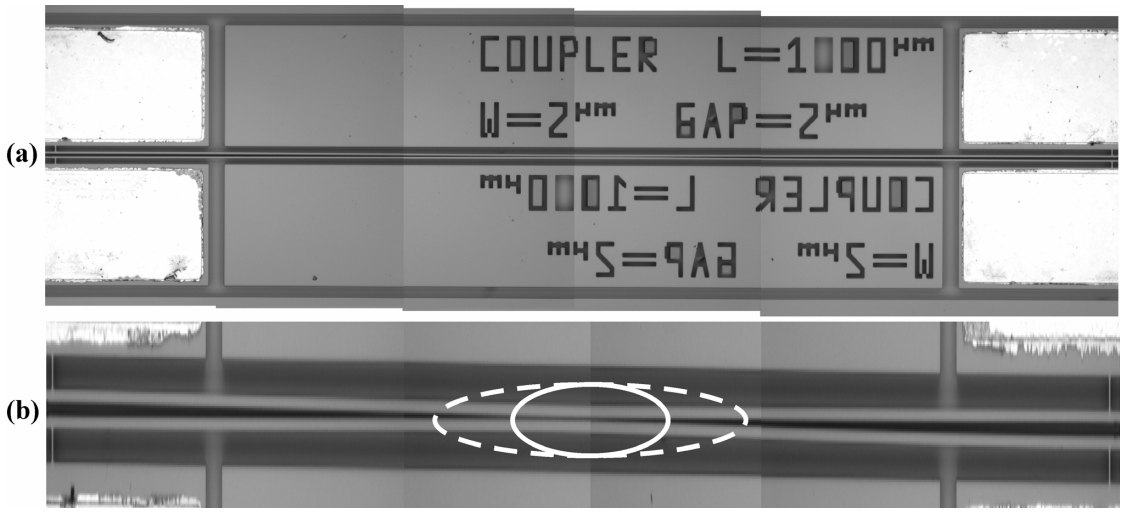


**Figure 5. 20: Stiction in an $L = 1000$ μm coupler (*coupler 2b*) at $V = 0$ after initial pull-in: a) top view of complete coupler, b) magnified view of stiction region.**

The optical response of *coupler 2b* is shown in Figure 5. 21. In the 'OFF' state, 1.2 % *CROSS* coupled power is measured ($V$ = 0). This results in −19.2 dB channel isolation. At $V$ = 8 Vp-p, 66 % *CROSS* coupled power and a minimum uncoupled *BAR* power during actuation of 25 % is obtained. The switching loss, which is defined here as $loss = 1 - (P_{BAR}+P_{CROSS})$, is less than 10 % (0.45 dB). For actuation at 8 Vp-p the measured coupling length is $L_{PI} = 550$ μm, from which the coupling coefficient is obtained: $\kappa_{S\text{-}pol} = 1.72\times10^{-3}/\mu m$. Comparing the two couplers, the coupling coefficient for *coupler 2b* is similar to *coupler 1a* ($\kappa_{S\text{-}pol} = 1.43\times10^{-3}/\mu m$). Looking at the simulations, the expected coupling gap for *coupler 2b* is 190 nm, similar to the 200 nm gap obtained for *coupler 1a*.

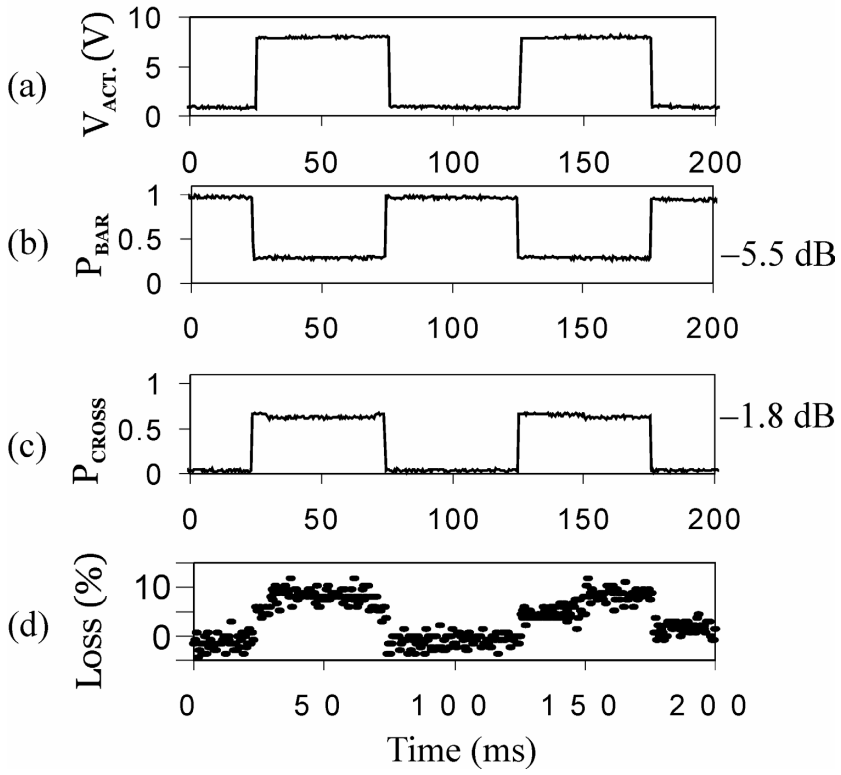


**Figure 5. 21: Switching in *coupler 2b*: a) actuation, b) $P_{BAR}$, c) $P_{CROSS}$, d) loss.**

*c) Switching Speed*

The measured switching speed of three electrostatically actuated couplers (*coupler 1a*, *coupler 2a*, and *coupler 2b*) is shown in Figure 5. 22. The risetime (Figure 5. 22a, c, and e) exhibits a delay before optical coupling occurs due to the waveguide travel time, the time required for the waveguides to come into sufficiently close contact in order for optical coupling to occur. It is interesting to note that *coupler 1a* and *coupler 2a* exhibit a clear delay (10 μs, 18 μs) due to the 1–2 μm gap (Figure 5. 22a, c). *Coupler 2b* has a fairly small delay (< 1 μs) resulting from the close proximity of the waveguides due to stiction (Figure 5. 22e). This is in good agreement with theory: due to the exponential dependence of the coupling coefficient on the waveguide separation,

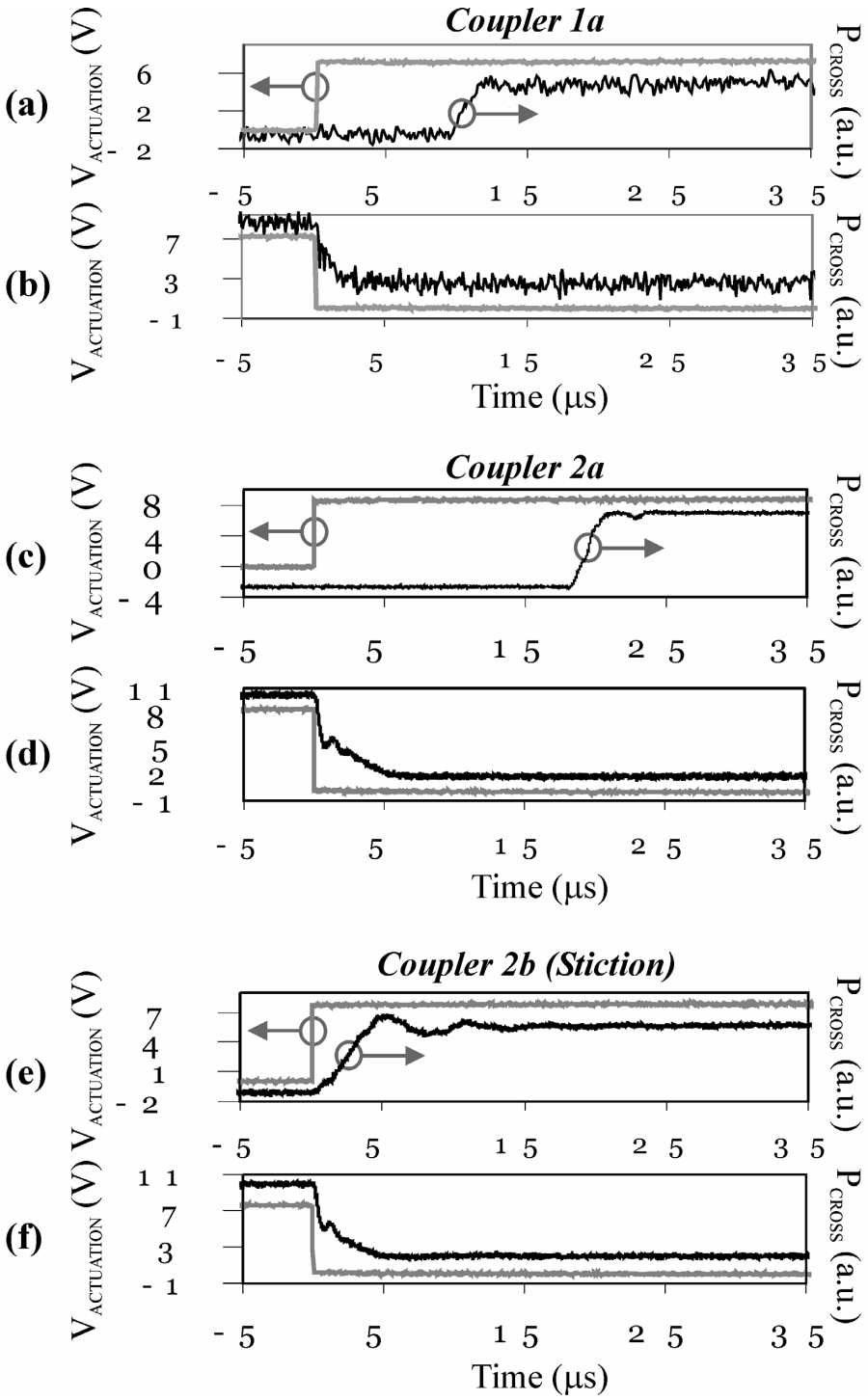


**Figure 5. 22: Switching speed: a) risetime for coupler 1a, b) falltime for coupler 1a, c) risetime for coupler 2a, d) falltime for coupler 2a, e) risetime for coupler 2b (gap << 2 μm), e) falltime for coupler 2b (gap << 2 μm).**

only small gaps (~100 nm) result in measurable optical coupling. For this same reason, the falltime (Figure 5. 22b, d, and f) does not show a delay since the beams separate immediately upon removal of the actuation signal and optical coupling decreases.

There is a slight ripple during the initial risetime cycle (Figure 5. 22c and e), which results from the beam dynamics and vibration after initial pull-in. Similarly, the non-linear beam dynamics during waveguide separation coupled with the $\sin^2(\kappa \cdot L)$ dependence of the CROSS coupled power accounts for the ripple seen during the falltime measurement (Figure 5. 22d and f). The fastest switching speed obtained was 4 μs (*coupler 2b*). Concerning frequency and lifetime, *coupler 1a* was actuated at up to 25 kHz and *coupler 2a* was actuated over 10 million cycles (at $f$ = 10 kHz) with no change in device performance.

*d) Variable Optical Coupling*

The devices discussed above are switches and are digital in nature: they are either 'ON' or 'OFF.' However, the amount of optical coupling can be controlled by varying either the waveguide gap or the coupling length. Due to the pull-in nature of the MEMS couplers, it is not possible to continuously vary the waveguide gap to tune the amount of coupling. Experiments that involve varying the coupling length, $L_{PI}$, in order to achieve variable optical coupling are now presented.

*Coupler 2b* was shown in Figure 5. 20. The solid circle represents the coupling region in the rest state ($V$ = 0). As the actuation voltage is increased, the coupling length increases as the two waveguides come into contact over a larger length (dashed circle), resulting in increased optical coupling. The measured optical coupling as a function of

actuation voltage is shown in Figure 5. 23. As the actuation voltage increases, coupling increases from −19.2 dB ($V$ = 0) until the device acts as a −3 dB splitter (7 Vp-p). Further increase in actuation voltage to 8 Vp-p results in 66 % coupling (−1.8 dB). This represents a 17.4 dB dynamic variable coupling range with less than 10 % loss. Such low-loss variable optical coupling is not possible with end-coupled switches [43, 50, 51, 136, 137] in which any uncoupled power is lost. Therefore, the MEMS coupler has a unique advantage over other MEMS-based switching approaches.

The coupling lengths for this device (*coupler 2b*) were measured at 6 Vp-p and 8 Vp-p actuation, resulting in $L_{PI}$ = 390 μm and 550 μm, respectively. As before, the coupling coefficients are extracted, resulting in $\kappa_{S\text{-}pol} = 1.51\times10^{-3}$/μm (at 6 Vp-p) and $\kappa_{S\text{-}pol}=1.72\times10^{-3}$/μm (at 8 Vp-p). The results are summarized in Table 5. 1 and are in general agreement with the coupling coefficient obtained for *coupler 1a*, which exhibited a $\kappa_{S\text{-}pol} = 1.43\times10^{-3}$/μm. In the present experiments, the measured coupling coefficient increases slightly with both increasing device length as well as increasing actuation voltage. This is likely due to the slight decrease in waveguide gap with increased actuation voltage. In addition, longer devices are more compliant and will also result in a slightly decreased actuation gap and increased coupling.

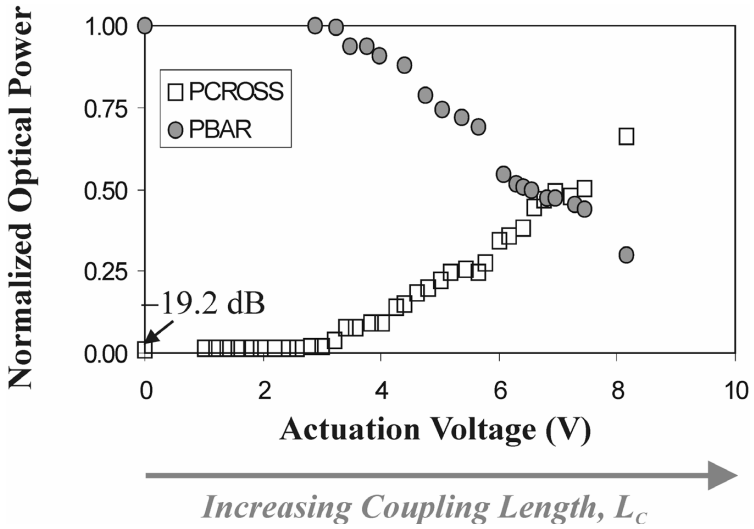


**Figure 5. 23: Variable optical coupling in *coupler 2b*.**

**Table 5. 1: Summary of variable optical coupling (λ = 1550 nm, TE-polarization).**

| **Device: Length (gap)** | **Measured $P_{CROSS}$ (norm.)** | **Actuation Voltage (Vp-p)** | **Coupling Length, $L_{PI}$ (μm)** | **Coupling Coefficient, κ ($\mu m^{-1}$)** |
|---|---|---|---|---|
| *Coupler 1:* $L$ = 500 μm (*gap* = 1 μm) | 0.10 | 7.5 | 225 | $1.43\times10^{-3}$ |
| *Coupler 2:* $L$ = 1000 μm (stiction) | 0.30 | 6.0 | 390 | $1.51\times10^{-3}$ |
| *Coupler 2:* $L$ = 1000 μm (stiction) | 0.66 | 8.0 | 550 | $1.72\times10^{-3}$ |

A second device (*coupler 3b*) initially behaves as a −3 dB power splitter due to stiction at $V$ = 0 (Figure 5. 24). The reason is that the stiction length, and hence the coupling length ($L_{PI}$), is longer than for *coupler 2b*. As the actuation voltage is increased, $L_{PI}$ is also increased resulting in an initial decrease in the *CROSS* power and an increase

in the *BAR* power (Figure 5. 24). At $V$=5 V *coupler 3b* is turned completely 'OFF' so that all the optical power is in the *BAR* waveguide. By increasing the actuation voltage to 10 V the *CROSS* power is increased and the *BAR* power is decreased so that *coupler 3b* again acts as a −3 dB coupler. This clearly demonstrates the mode interference picture predicted by eqns. (5.2−5.5) and Figure 5. 3.

While the above experiments utilized couplers and stiction, similar experiments can be made with couplers that do not rely on pull-in actuation. From Table 5. 1 it is apparant that increased coupling length, $L_{PI}$, results in larger coupled power. Alternatively, eqn. (5.4) indicates that an increased coupling coefficient, κ, results in an increased coupled power, since $P_{CROSS} = \sin^2(\kappa L_{PI})$. Smaller waveguide gaps result in larger coupling coefficient, κ. Therefore, variable optical coupling can also be achieved using actuators that enable continuous variation of the waveguide gap, such as comb-drives, as will be presented later on.

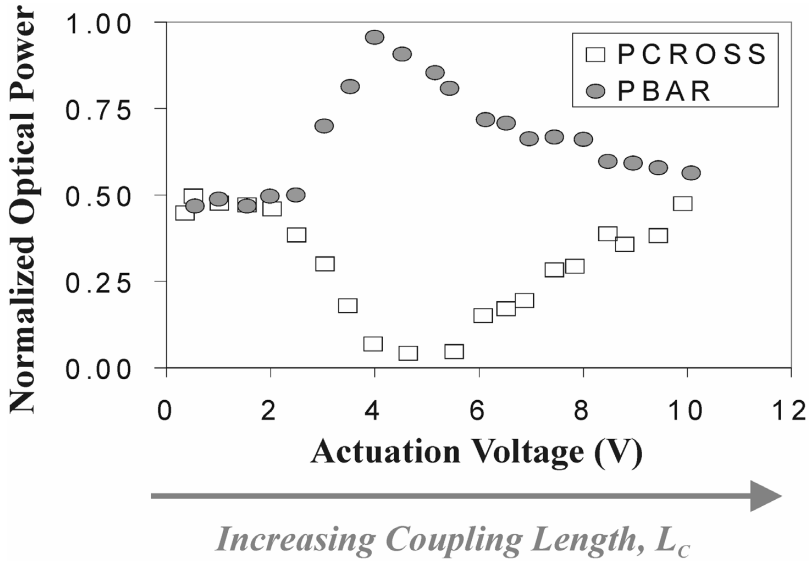


**Figure 5. 24: Variable optical coupling in *coupler 3b*.**

*e) Polarization and Wavelength Dependence*

Polarization-dependent coupling was measured using *coupler 2b* (Figure 5. 20) during actuation. The measured *CROSS* coupled power for both S- (TE) and P- (TM) polarizations during actuation is shown in Figure 5. 25. S-polarization results in 66 % coupling and P-polarization exhibits 2.8 % coupling. From the measurements, one obtains $\kappa_{S\text{-}pol} \cdot L_{PI} = 0.89$ and $\kappa_{P\text{-}pol} \cdot L_{PI} = 0.17$. The polarization-dependent *coupling ratio* is then $\kappa_{S\text{-}pol}/\kappa_{P\text{-}pol} = 5.6$, in general agreement with the simulated value $\kappa_{S\text{-}pol}/\kappa_{P\text{-}pol} = 8$ (Figure 5. 9b).

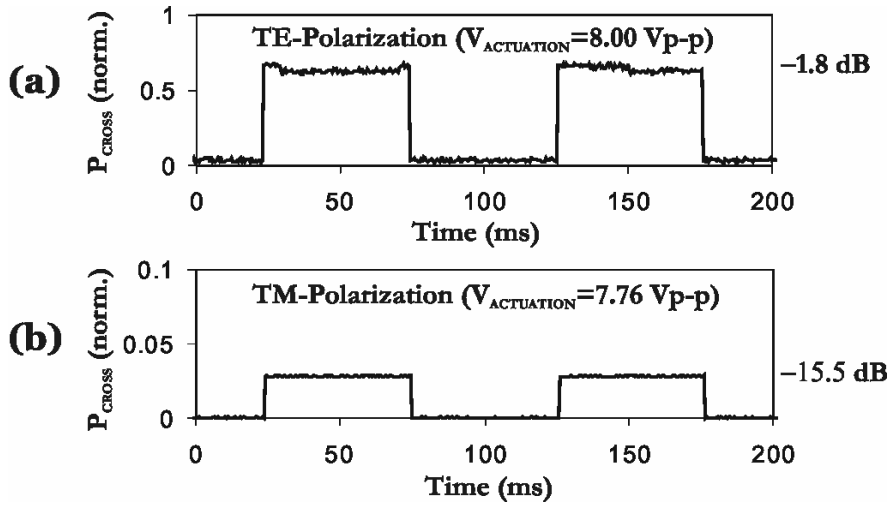


**Figure 5. 25: Polarization dependence: a) TE-, b) TM-polarization (λ = 1550 nm).**

Some of the discrepancy between simulation and experiment is due to measurement error, taking into account scattered light in the measurement setup. The coupled power for P-polarization is small (2.8 %, or sub-μW levels) so that measurement errors are increased compared to S-polarization. Furthermore, some polarization conversion is to be expected in the waveguides due to sidewall roughness [138] and the

trapezoidal waveguide cross-section. Therefore, if completely (100 %) P-polarized light is injected into the *BAR* input, then some portion will be converted to S-polarized light resulting in increased coupling compared to completely P-polarized light. A third factor is that the waveguides are not strictly single-mode so that higher order modes may also contribute to the coupling. The simulations, in contrast, assume single-mode waveguides and therefore predict slightly lower coupling than obtained experimentally. Nonetheless, the general agreement in predicting stronger coupling for S- compared to P-polarized light indicates that the simulations give a reasonable approximation for future device design.

Optical couplers also exhibit a slight wavelength-dependence. Eqn. (5.10) indicates that the coupling coefficient, $\kappa$, is proportional to the wavevector $k_0 = 2\pi/\lambda$. Although $n_{\text{Symmetric}}$ and $n_{\text{Antisymmetric}}$ in eqn. (5.10) are also wavelength-dependent, to first order the coupling coefficient has a simple relation to wavelength: $\kappa \sim k_0 \sim 1/\lambda$. Therefore, for small wavelength ranges centered about $\lambda_0 = 1550$ nm (typical WDM communications sub-bands span 20–30 nm range), the coupling coefficient is relatively wavelength insensitive.

While evanescent coupling results in polarization and some wavelength sensitivity, there are methods to overcome such dependence. For example, it has been shown that polarization-independent and wavelength-insensitive fixed couplers can be demonstrated by connecting two passive couplers in series with an optical phase shift [139, 140]. Such devices can be readily adapted to the present device by cascading two MEMS couplers in series and actuating both simultaneously during switching. A second approach requires redesign of the waveguides. Polarization-insensitive MEMS couplers

have been simulated by *Povinelli et al.* [121]. However, these devices required waveguides of $a$ = 280 nm width and precise waveguide gaps of similar dimension $a$, which requires electron-beam lithography and is beyond the scope of this work.

## 5.6 Discussion

Coupled-mode theory [15, 141] is accurate for waveguides that are weakly-coupled. The waveguide dimensions (2 μm × 2 μm core cross-section) were chosen for mechanical robustness based on prior work on similar dimensioned structures (Chapter 2 and [7]). However, this results in a waveguide that supports more than one optical mode. Furthermore, one might argue that during pull-in the waveguides are in contact and therefore strongly-coupled so that the coupled-mode theory no longer applies.

The experimental results indicate that MEMS couplers in this work can be modeled by single-mode waveguides. Looking at the single-mode optical coupling simulations (Figure 5. 9), waveguide gaps of 100 – 200 nm result in characteristic coupling lengths $L_C$ = 200 – 1000 μm. This length scale agrees well with the measured pull-in coupling lengths, $L_{PI}$, for *coupler 1a* and *coupler 2b* (Table 5. 1). For *coupler 3b* increased actuation voltage initially results in lower coupling due to destructive interference, in agreement with the coupled-mode theory assuming single-mode waveguides.

If higher-order modes contribute significantly to coupling, the devices should exhibit much stronger coupling than what is predicted by simulation (Figure 5. 9). This stronger coupling should result in significantly shorter characteristic coupling lengths, $L_C$. However, the experimental results are in good agreement with simulation based on the

fundamental mode, both in the coupling lengths required as well as the polarization-dependence. Furthermore, due to the suspended waveguide design in which tethers are utilized for support [9], higher order modes will experience increased losses compared to the first-order mode. The reason for this increased loss is the tighter confinement of the fundamental mode to the core of the waveguide, while higher order modes are less confined. Therefore, the fundamental mode dominates optical coupling from the BAR to the CROSS waveguide.

In order to obtain more efficient coupling with greater than 66 % coupled power to the CROSS waveguide, either 1) the coupling coefficient, $\kappa$, or 2) the physical coupling length, $L_{PI}$, need to be increased. Table 5. 1 indicates that the coupling coefficient, $\kappa$, is relatively constant for different devices and actuation voltages. From $\kappa$ and eqn. (5.5) the characteristic coupling length, $L_C$, is obtained, which determines the 100 % coupling length. Looking at Table 5. 1, the physical coupling length is well below the characteristic coupling length, so that $L_{PI} < L_C$ for *coupler 1a* and *coupler 2b*. In order to increase coupling in the present devices to 100 % the pull-in length needs to be increased to $L_{PI} = L_C$. Alternatively, by designing narrower single-mode waveguides (width < 2 $\mu$m) the evanescent field is increased, resulting in a larger coupling coefficient, $\kappa$, and increased coupled power.

A secondary consideration for the incomplete coupling is higher-order modes. The coupling length of any higher-order modes will differ from that of the fundamental mode. Therefore, any power propagating in higher-order modes may not be completely coupled to the CROSS waveguide. In general, however, optical power is concentrated in the fundamental mode. This is supported by the good agreement between the single-

mode simulations (Figure 5. 9) and the experimental results (Table 5. 1).

Despite these considerations and the incomplete (<100 %) coupling in the present devices, it should be noted that the MEMS couplers exhibit strong switching contrast. *Coupler 1a* shows –47 dB channel isolation at V = 0, with 10 % (–10 dB) coupled power at pull-in. This represents a 37 dB ON/OFF contrast for the CROSS waveguide, sufficient for many switching applications.

## 5.7 Improved Designs

### 5.7.1 Comb-Drive Couplers, Third Electrode Couplers, and Surface Coatings

One modification of the present devices concerns the actuation mechanism. Using pull-in, the coupling gap cannot be continuously varied. While variable optical coupling was demonstrated by taking advantage of stiction to vary the coupling length, this impacts the long-term device operation and reliability. An alternate approach prevents pull-in by using comb-drive actuators to enable continuous tuning of the waveguide separation in variable optical couplers (Figure 5. 26a).

A second approach utilizes a third electrode to actuate the *BAR* waveguide while keeping the *CROSS* waveguide fixed (Figure 5. 26b). If the spacing between the *BAR* waveguide and the actuation electrode is greater than three times the *BAR* to *CROSS* waveguide separation, then pull-in is avoided since pull-in occurs after a travel range of *gap*/3 [61]. This enables continuous variation of the gap and variable optical coupling.

A third approach for increasing reliability makes use of surface coatings. Self-assembled monolayers [142] increase the water contact angle of InP surfaces, thereby making InP hydrophobic. This will prevent stiction in pull-in type MEMS couplers.

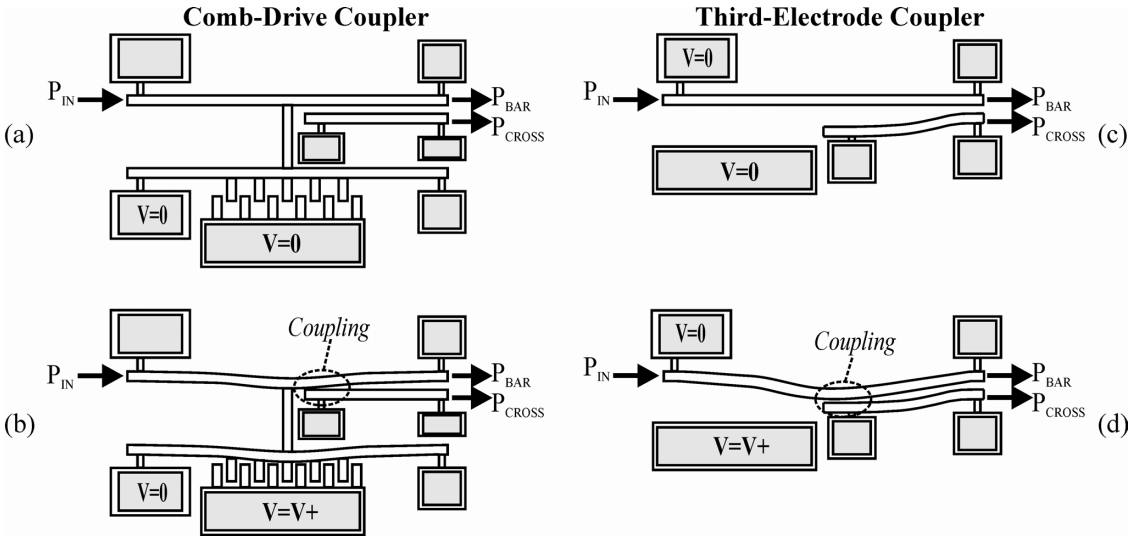


**Figure 5. 26: a) Comb-drive coupler (OFF), b) comb-drive coupler (ON, V > 0), c) third-electrode coupler (OFF), d) third-electrode coupler (ON, V > 0).**

### 5.7.2 Experimental: Comb-Drive and Third Electrode Couplers

Experiments using 1×2 comb-drive couplers (*coupler C-D*) have shown that this approach prevents stiction in long and compliant waveguides ($L$ = 4000 μm). The results (Figure 5. 27) successfully demonstrate variable optical coupling. The measurements, however, show significantly smaller coupling (tens of nW power) compared to the pull-in actuated couplers (μW power). The weak coupling likely is the result of the increased waveguide gap and short coupling length during actuation in the comb-drive couplers compared to the pull-in devices, in which the waveguides come into intimate contact (~100 nm pull-in gap) over a large coupler segment during actuation. Nonetheless, the results in Figure 5. 27 demonstrate the feasibility of optical switching and variable coupling without pull-in, which results in increased reliability.

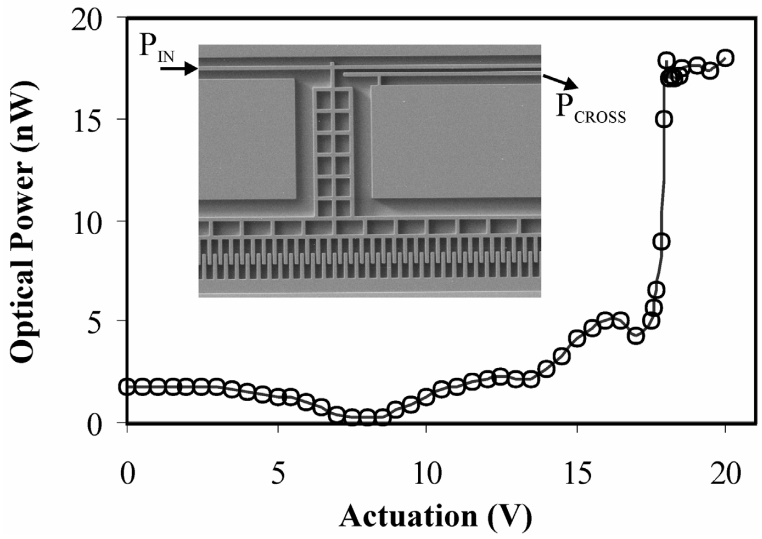


**Figure 5. 27: Measured optical power in the comb-drive coupler.**

Third electrode couplers were also fabricated and tested. In this coupler, the waveguide consisted of a 1.5 μm thick core ($In_{0.99}Ga_{0.01}As_{0.01}P_{0.99}$, $n$ = 3.173) with air cladding. Figure 5. 28 shows results for an $L$ = 1000 μm long device with $w$ = 0.8 μm wide waveguides. In this device, the initial waveguide separation ($V$ = 0) varies from *gap* = 0.8 μm to 1.0 μm due to the angled CROSS waveguide (Figure 5. 26c).

The third electrode coupler was actuated with a sinusoidal signal less than the pull-in voltage (i.e. $V < V_{PI}$ = 9.3 V, Figure 5. 28a). At $V$ = 0, there is some evanescent coupling with $P_{BAR}$ = 13 μW and $P_{CROSS}$ = 12 nW. At $V$ = 5.029 V, the BAR waveguide is actuated, which results in a decreased gap and increased coupled power $P_{CROSS}$. The CROSS coupled power varies sinusoidally with the actuation signal (Figure 5. 28b). Increasing the actuation voltage to 6.226 V does not further increase $P_{CROSS}$. Rather, the CROSS coupled power exhibits a relative minimum (Figure 5. 28c). Increasing the voltage further to 6.601 V results in an even more pronounced dip (Figure 5. 28d).

Finally, increasing the voltage even further to 6.820 V produces another local maximum (Figure 5. 28e).

The results in Figure 5. 28 can be explained by looking at eqn. (5.4): $P_{CROSS} = P_0 \sin^2(\kappa L)$. For simplicity, the coupling length, $L$, is assumed to remain constant. However, the coupling coefficient, $\kappa$, varies exponentially with waveguide separation so that small increases in voltage affect $\kappa$ significantly. The local maxima and minima result from the $\sin^2(\kappa L)$ dependence, which requires that local maxima occur for $(\kappa L)=(2n+1)\pi/2$ and local minima occur at $(\kappa L)=(2n+1)\pi/2$, $n$ = integer. The extrema in Figure 5. 28 verify that optical mode coupling occurs via the evanescent field, without pull-in actuation.

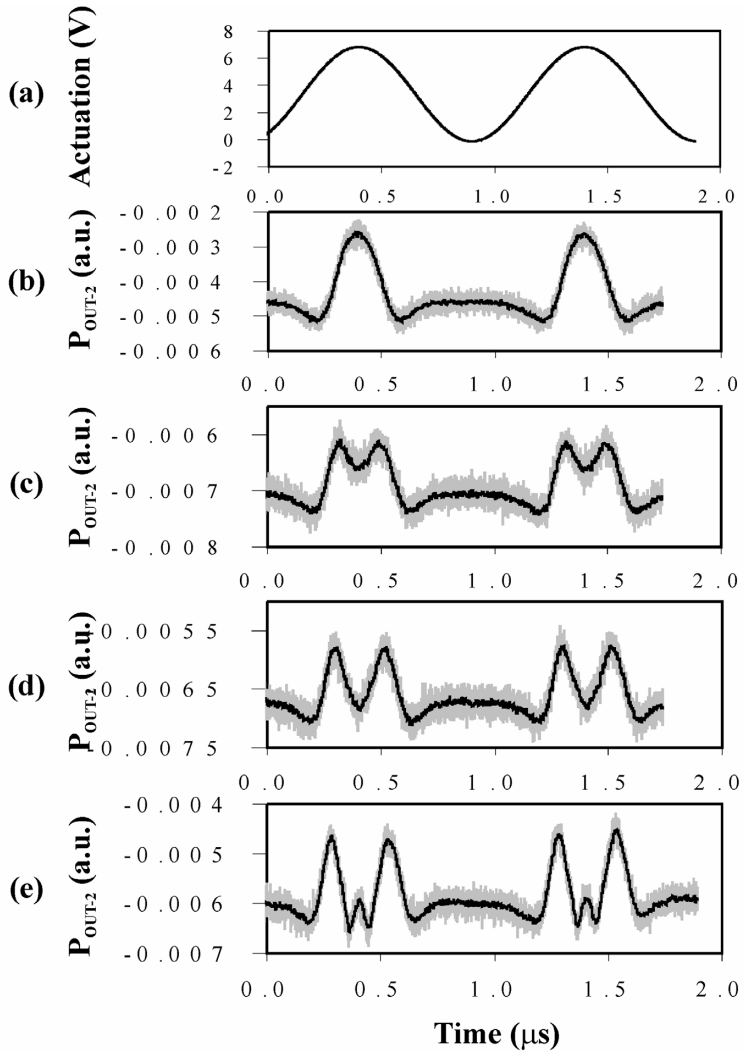


**Figure 5. 28: Third-electrode coupler: a) actuation; b)-f): $P_{CROSS}$; b) $V_{Sine}$=5.029 V, c) 6.226 V, d) 6.601 V, e) 6.820 V. Grey line: data; black line: 20 point average.**

### 5.7.3 Single-Mode Devices

For long-haul optical communications, single-mode fibers and optical switches are needed. Single-mode waveguides are obtained by simply reducing the cross-sectional area down to 0.5 μm × 0.5 μm or smaller [97]. While such small cross-section may impact the mechanical robustness of the device, other materials (i.e. silicon-on-insulator)

can be substituted in place of InP for passive device operation. By reducing the waveguide cross-section, the evanescent field increases so that more optical power travels just outside of the waveguide. Simulations have shown that devices with waveguide widths of 0.5 – 1.0 μm (1.0 μm height, $n_{CORE}$ = 3.173) enable characteristic coupling lengths of $L_C$ < 100 μm for complete coupling for both S- and P-polarizations (Figure 5. 29). Therefore, very compact devices can be realized with the present approach scaled down to single-mode waveguides. By reducing the size of the moving waveguides, lower actuation voltage, and reduced switching time can also be expected.

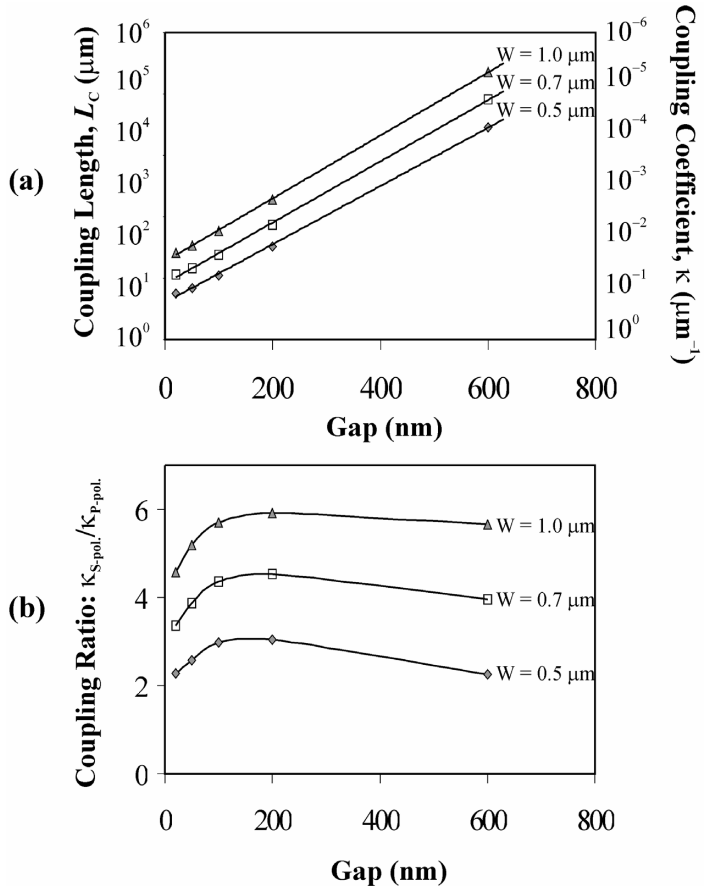


**Figure 5. 29: Air cladding couplers with 1.0 μm thick core (n=3.173): a) characteristic coupling length, $L_C$, for S-polarization, b) $\kappa_{S\text{-}pol}/\kappa_{P\text{-}pol}$.**

## 5.8 Summary

In this chapter, the theory of evanescent coupling has been reviewed and various approaches to optical switching with couplers were discussed. A MEMS-based coupler, in which the coupling strength can be modulated by varying the separation between two parallel waveguides, has been introduced. The experiments demonstrate the first successful optical switches based on a simple evanescent coupler waveguide geometry. Compared to previously demonstrated MEMS-actuated micro-disk [55, 123, 124] and micro-ring resonator filters [126, 127], the MEMS couplers developed in this work are relatively wavelength-insensitive over small wavelength ranges commonly used in WDM communications sub-bands ($\Delta\lambda \sim 30$ nm). The performance of these MEMS couplers has been thoroughly investigated, both experimentally and via simulation.

The MEMS coupler experiments show excellent performance compared with other competing designs, such as electro-thermal and electro-optic coupler switches. Low-voltage and low-power electrostatic actuation was demonstrated. Electro-thermal couplers typically consume mW power [23], so even the μA of pull-in current in the MEMS couplers results in significantly lower power consumption. Fabrication of the devices is simple since the waveguides and actuation elements are fabricated using standard optical lithography. Although InP was used, the MEMS coupler can be implemented in low-cost silicon-based materials and does not rely on special material properties (such as electro-optic effects [24]). The 4 – 20 μs switching speed is significantly faster than that of electro-thermal couplers [23] as well as other MEMS optical switches [16-19], although it does not compare with the ns (or even sub-ns) speed obtainable with electro-optic switching. The channel isolation (at V = 0) of the MEMS

coupler is excellent (47 dB) due to the exponential dependence of the coupling coefficient on waveguide gap. This is a significant advantage of the MEMS approach, since small actuation distances result in large changes in coupling. Finally, while the coupling efficiency in the present devices can be improved compared to other more mature coupler approaches, single-mode waveguides with matched coupling lengths (i.e. $L_{PI} = L_C$) should result in complete optical power transfer in the MEMS coupler.

# CHAPTER 6

# END-COUPLED OPTICAL WAVEGUIDE SWITCHES

## 6.1 Introduction

In this chapter, the design, modeling, and experimental characterization of end-coupled optical waveguide MEMS switches is presented. First, previous work on similar switches is reviewed and the distinguishing features of the present devices are highlighted. Next, the basic approach and design considerations, including MEMS actuator and optical design, are presented. Finite-element simulations and calculations are discussed for various mechanical and optical designs. Device fabrication was discussed in Chapter 4 and is not reviewed here. Experiments to characterize 1×2 end-coupled switches are presented and the performance of these devices is evaluated.

## 6.2 Theory: End-Coupling between Optical Waveguides

The coupling mechanism in the end-coupled switches presented in this chapter differs from the evanescent couplers presented in Chapter 5. Rather than coupling occurring between two parallel waveguides, coupling occurs via aligning two end-coupled waveguides (Figure 6. 1). The coupling or transmission efficiency, *T*, is given by so-called overlap integral [143]:

$$T = \left| \int \phi_1(x, y, z_0) \phi_2(x, y, z_0) dx dy \right|^2, \tag{6.1}$$

where $\phi_1(x, y, z_0)$ and $\phi_2(x, y, z_0)$ are the mode shape functions for *waveguide 1* and *waveguide 2* at position $z = z_0$, respectively. The mode shape functions describe the profile of the electric (or magnetic) field for a given mode as a function of position. For a slab waveguide confined only in the $x$-direction, the mode shape function can be approximated by a Gaussian and is given by [143]:

$$\phi(x,y,z) = \left[\frac{2}{\pi}\right]^{\frac{1}{4}} \frac{1}{\sqrt{w}} \exp\left[-\left(\frac{x}{2}\right)^2\right] \exp\left(-i\beta z\right), \tag{6.2}$$

where $w$ is the Gaussian beam width and $\beta$ is the waveguide propagation constant along the $z$-direction. The mode shape function is normalized over all space so that:

$$\int_{-\infty}^{+\infty}\int_{-\infty}^{+\infty}\int_{-\infty}^{+\infty} |\phi(x,y,z)|^2 dxdydz = 1. \tag{6.2a}$$

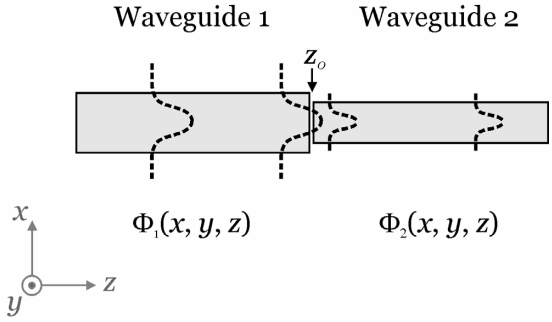


**Figure 6. 1: End-coupling between waveguides with $\phi_1(x,y,z)$ and $\phi_2(x,y,z)$.**

From eqn. (6.1) and Figure 6. 1 it is clear that identical waveguides will have identical mode shape functions and therefore maximum coupling or transmission, *T*. Dissimilar waveguides will have mode shape functions that differ greatly so that the transmission, *T*, may be significantly reduced. Other means by which coupling losses occur include: a) axial- or end-separation, in which there is a gap along the *z*-axis between the two waveguides, b) axial offset, in which the two waveguides are displaced by an amount $x_0$ along the x-axis from each other, and c) angular misalignment, in which the "*z*-axis" of each waveguide is at an angle relative to the other waveguide. These cases are discussed in section 6.5.2, in which the optical design of the switches is presented.

## 6.3 Literature Review

### 6.3.1 Prior MEMS End-Coupled Optical Waveguide Switches

There have been several reports in the literature of MEMS optical waveguide switches with end-coupling. The first demonstration was by *Ollier* [50] in 1995, who fabricated suspended silica ($SiO_2$) waveguides by etching the silicon substrate underneath the waveguides. The input $SiO_2$ waveguide consisted of a long cantilever beam with two support beams at the free end, making the waveguide essentially a doubly-clamped structure. These support beams were necessary due to the large intrinsic stress (and stress gradient) in the silica waveguide layers. Metal electrodes were evaporated on the 25 μm tall waveguide sidewalls as well as on parallel electrodes so that the input waveguide could be electrostatically actuated laterally to select one of two fixed output waveguides. The initial demonstration required 270–346 V for optical switching, exhibited insertion

loss of 4.5–6.3 dB and channel isolation of –24.2 dB to –26.4 dB (both at λ=1550 nm wavelength), and had a switching time of 0.6 ms. Improved versions of that initial switch demonstration resulted in 70 V actuation voltage, 1.5 dB insertion loss, –42 dB crosstalk, and less than 1 ms switching speed [43]. The increase in switching time is likely the result of index-matching gel used in the switches; index-matching gel was placed in the air gap between the input and output waveguides in order to decrease the index contrast and thereby reduce coupling losses. This technique resulted in low wavelength- and polarization-dependent losses, which were measured to be 0.2 dB and 0.3 dB, respectively. However, the index-matching gel also increases damping and reduces the switching speed. Furthermore, while the device of *Ollier* exhibits low loss, the switching voltage is quite high and the material system ($Si/SiO_2$) limits the device to passive optical functionality with no possibility of optical gain.

A similar device was demonstrated by *Shubin et al.* [137] in 2001. This device utilized silicon oxy-nitride (SiON) waveguides on a silicon substrate with $SiO_2$ sacrificial layer. The input waveguide consisted of a cantilever with a thin chromium layer and could be actuated vertically by application of a voltage between the metal layer and substrate. Here, the waveguide was actuated until pull-in so that the waveguide touched the substrate during actuation. Switching voltages of 25–85 V, losses of 4–10 dB, 11–24 dB channel isolation (with index-matching fluid), and a switching speed of 25–50 μs were achieved with this device. Due to the cantilever design as well as the large intrinsic stress of the SiON waveguides, there was significant vertical deflection of the input waveguide at zero applied voltage. This effect was compensated somewhat by a thin (70–90 nm) chromium layer on top of the waveguides to induce an opposite strain to

counter the intrinsic material stress and to ensure flatness of the input cantilever waveguide. The reported device was operated over 100 million cycles without failure (stiction effects [104]), likely with help from the intrinsic stress gradient of the cantilever waveguide. While the switching speed of this device is quite fast, it does not lend itself to active optical gain due to the Si/SiON material system used. Furthermore, the switching voltage is quite large.

Polymer optical waveguide switches on silicon-on-insulator (SOI) have also recently been developed by *Bakke et al.* [136]. These switches consist of silicon electrostatic actuators (SOI substrates) with post-processed polymer optical waveguides. The basic design was a suspended waveguide, similar to the one used by *Ollier* [43, 50], actuated laterally using comb-drive actuators. Switching voltages of 20–50V, losses of 3.4 dB, –35 dB channel isolation, and a speed of 30 μs were measured. The relatively fast switching speed was obtained by using a two-step actuation sequence to prevent oscillation of the input waveguide during switching. Again, these switches are inherently passive without possibility for active optical functionality due to the indirect bandgap of Si; the switching voltage can also be reduced.

End-coupled optical waveguide MEMS switches have also been developed in gallium arsenide (GaAs) based materials [51]. In the 2002 work, *Bakke et al.* utilized GaAs/AlGaAs cantilever input waveguides with comb-drive actuators. The input waveguides had mechanical stoppers that ensured accurate alignment of the input- with the output waveguides during switching. However, the authors concede that this approach results in reliability issues since the input cantilever tends to permanently adhere to the mechanical stopper after initial actuation (stiction). Therefore, they

recommend that this approach not be used for reliable device operation. Testing of the GaAs-based switches resulted in actuation voltages of 3.3–12.3 V, fiber-to-switch insertion loss of 7 dB, switching loss of 1.3–4.5 dB, –31 dB channel isolation, and 32–194 μs switching speed; the shorter switching times were obtained using multiple-valued actuation pulses for acceleration and braking of the cantilever waveguide. Of the MEMS-actuated optical waveguide switches reported in the literature, the device by *Bakke et al.* is the only one which potentially enables active optical gain on-chip due to the direct bandgap of GaAs. However, GaAs and GaAs-based materials are limited to emission wavelengths of $\lambda_g < 900$ nm and can therefore not be used to provide optical gain at the $\lambda = 1550$ nm communications wavelength band.

### 6.3.2 Novelty

The above literature review indicates that end-coupled MEMS electrostatically-actuated waveguide optical switches have been developed in a number of material systems. These include $SiO_2$–Si, SiON–Si, polymer–Si, and GaAs. Nonetheless, the approach developed here has some unique features compared to previous work.

Previous demonstrations of MEMS optical waveguide switches were inherently passive due to the material choice [43, 50, 136, 137]. Only the GaAs device developed by *Bakke et al.* [51] potentially enables optical gain. However, while GaAs has a direct bandgap, the emission/gain is limited to the near-infrared ($\lambda = 870$ nm) and hence does not enable on-chip compensation of optical losses at the preferred 1550 nm wavelength.

In this work InP and InP-based materials of the indium-gallium-arsenide-phosphide family ($In_{1-X}Ga_XAs_YP_{1-Y}$) are utilized for the waveguide and MEMS-actuator. These materials have only recently been studied for MEMS applications and have never – to the best of my knowledge – been applied to the type of switches presented above. Due to the direct bandgap of InP and the ability to grow $In_{1-X}Ga_XAs_YP_{1-Y}$ lattice-matched to InP substrates, the device presented in this work can be extended to incorporate optical gain in the 1550 nm wavelength region. At this wavelength, standard optical fibers exhibit minimum attenuation [56] and hence it is desirable to operate at this wavelength. The switches presented in this work thus have a unique advantage over previous MEMS-waveguide switch demonstrations.

Second, a doubly-clamped serpentine design is used in order to overcome intrinsic stresses within the waveguide layers resulting from molecular beam epitaxy (MBE) growth while minimizing the actuation voltage. Although a similar approach has been utilized by both *Ollier et al.* [43, 50] and *Bakke et al.* [136], their designs increased the spring constant significantly and resulted in large operating voltage in the 20–70V range. In contrast, the simple doubly-clamped beam designs of *Ollier* and *Bakke* are modified in some of the present devices by incorporating a serpentine-like structure to lower the operating voltage to well below 10 V. This enables compensation of intrinsic material stress without sacrificing low-voltage operation.

Finally, the present design utilizes the 'suspended waveguide' platform discussed in Chapter 3. Benefits of this approach include tight confinement of the optical beam (which enables reduced device size and tight waveguide bends with low loss), negligible losses from substrate radiation modes [15], and a simple one-mask fabrication sequence

for both static and movable waveguide portions on the same chip. In contrast, all of the devices reviewed in section 6.3.1 utilize complex fabrication schemes and require careful design in order to minimize substrate radiation losses. As will be shown later on, the losses in the present devices are very competitive with previous MEMS-actuated optical waveguide switches [43, 50, 51, 136, 137], but with the advantage of low-voltage operation and the potential for providing active optical gain at the $\lambda$=1550 nm wavelength.

## 6.4 Approach

The basic 1×2 end-coupled optical waveguide switch is shown in Figure 6. 2. It consists of a movable input waveguide, fixed output waveguides, mechanical suspensions (springs), and capacitive (electrostatic) actuators. In the 'OFF' state, the input waveguide is not aligned with either output. However, as the actuation voltage is increased, the capacitive actuator force increases and the input waveguide aligns axially with one of the output waveguides. Once the waveguides start to align, optical power end-couples from the input to the output via the air gap. The coupled optical power is maximized when the overlap integral in eqn. (6.1) reaches its maximum value; this occurs when input and output waveguides are fully aligned.

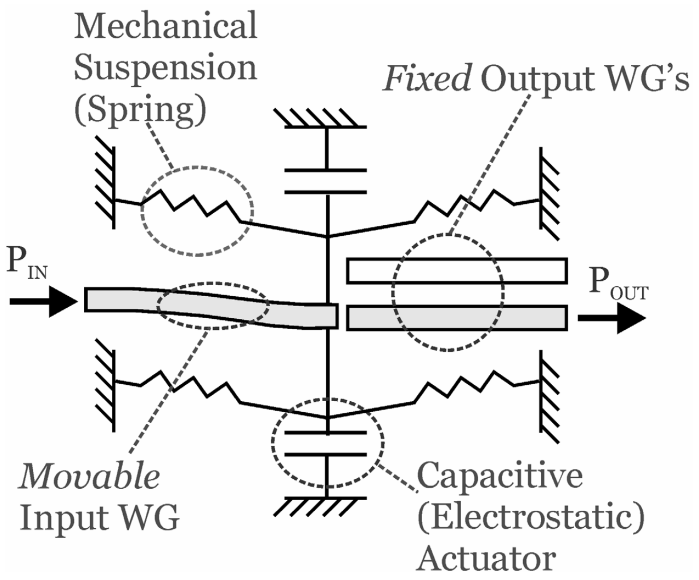


**Figure 6. 2: Schematic of 1×2 end-coupled waveguide switch.**

## 6.5 Design Considerations

The output waveguides have a pitch of 4 μm and a waveguide width of 2 μm. Therefore, in the 'OFF' state ($V = 0$), the input waveguide is located in the center between the two output waveguides. For a displacement of +/– 2 μm, the input waveguide is fully alligned with one of the two output waveguides. Simulations using finite-element software as well as analytical equations are used to predict the device performance, given the waveguide pitch and required displacements. Specific design criteria include actuation/switching voltage (<20 V) and optical coupling loss (< 3dB).

### 6.5.1 Actuator Design

The electrostatic force required for aligning the input and output waveguides is provided by comb-drive or pull-in actuators. Pull-in actuators utilize the normal force

between two charged electrodes (Appendix D); comb-drive actuators (Figure 6. 3) use the tangential force (Appendix E). Both forces are illustrated in Figure 6. 4.

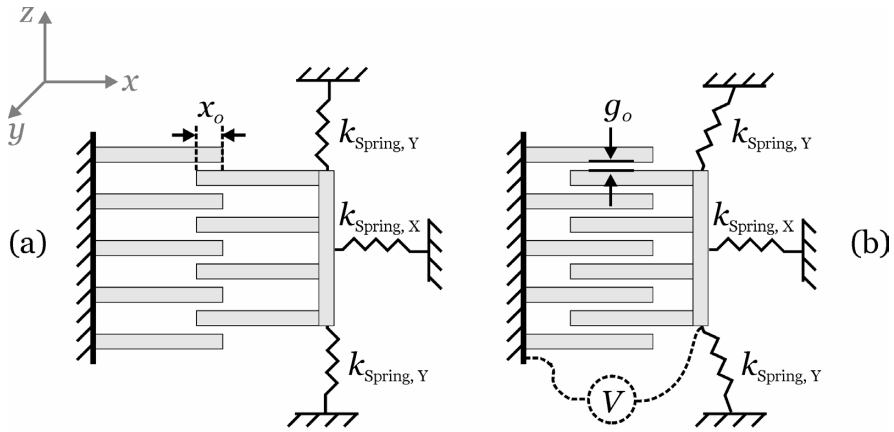


**Figure 6. 3: Comb-drive actuator: a) rest state ($V = 0$), b) actuated state ($V > 0$).**

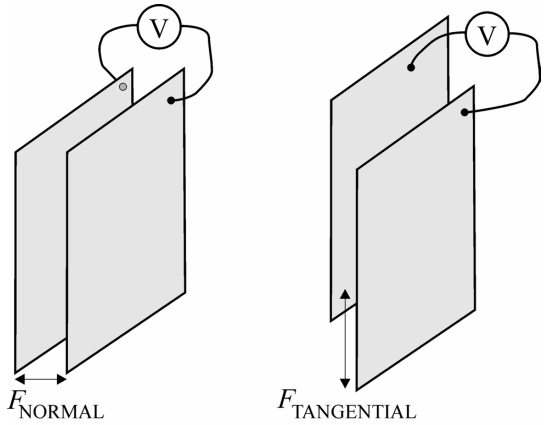


**Figure 6. 4: Capacitive actuation via the normal and tangential electrostatic forces between two electrodes.**

The comb-drive actuator for the 1×2 end-coupled waveguide switch was designed with $N = 80$ comb-finger pairs with *gap* = 1–4 μm. The electrostatic force was calculated from analytical equations (see Appendix E) and is given by:

$$F_{Comb-Drive} = 2N \times F_{Tangential} = N \frac{\varepsilon_0 h}{g_0} V^2, \tag{6.3}$$

where $\varepsilon_0$ is the free-space permittivity, $h$ is the comb-finger height, $g_0$ is the initial finger separation (Figure 6. 3), and $V$ is the voltage applied across the two sets of comb-fingers. The calculated electrostatic force is shown in Figure 6. 5, assuming $h = 4$ μm. As expected, a smaller *gap* results in a larger force. The target switching voltage is <20 V, which results in a comb-drive actuator force in the μN-range (for *gap* = 1 μm). Consequently, the mechanical suspension should require less than ~1 μN force for actuation of the input waveguide.

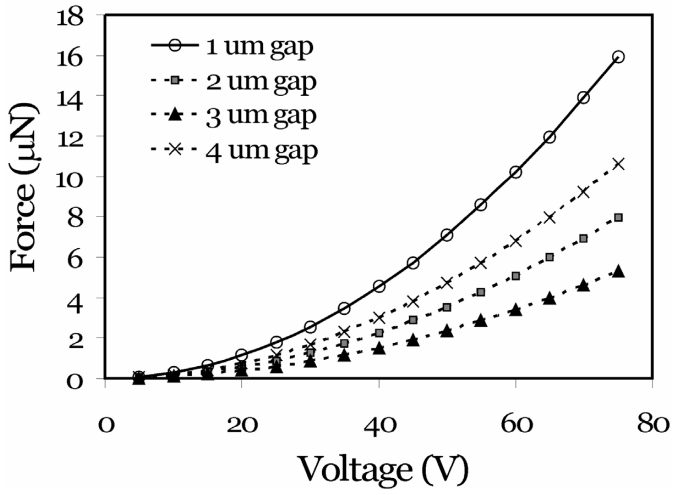


**Figure 6. 5: Calculated comb-drive force for $N = 80$ comb-pairs ($h = 4$ μm).**

Various mechanical suspensions were evaluated via finite-element method (FEM) simulation (CoventorWare, MemCAD [144]). Due to intrinsic strain gradients in the grown InP epiwafer (see [7, 8] and Chapter 2), long and compliant cantilever waveguides can not be used since these curl out-of-plane. Instead, the InP waveguides are grown with a small intrinsic *tensile* strain ($\varepsilon < 0.05$ %). When doubly-clamped structures are used, the input and output waveguides will remain aligned vertically. While the doubly-clamped suspension approach has previously been used [43, 50], it results in an increased spring constant and consequently a larger actuation voltage.

In order to lower the required actuation voltage, several alternative doubly-clamped suspensions were simulated by applying a uniform pressure load across the 400 μm wide comb-drive section. In addition to the fixed-fixed beam suspension (FB), alternative suspensions were studied, including: Y-suspension (Y-S), double-serpentine suspension (2-SS), and Y-serpentine suspension (Y-SS), as in Figure 6. 6. For the simulations, Young's modulus is $E = 93$ GPa [60] with intrinsic stress $\sigma = 50$ MPa. The waveguides and suspensions are 2 μm wide and 4 μm tall.

In Figure 6. 7 the required actuation force is plotted for various suspensions and device lengths. For all FEM simulations (CoventorWare, MEMCAD), a displacement of 2 μm was assumed to fully align the input with one of the output waveguides. For the simulations, the force was distributed over a 400 μm wide area (representing the comb-drive area and available electrostatic force); the material properties used for the simulations were $E = 93$ GPa and $\sigma = 50$ MPa. As expected, serpentine suspensions result in much smaller required force than the Y-suspension due to the larger compliance of these types of structures.

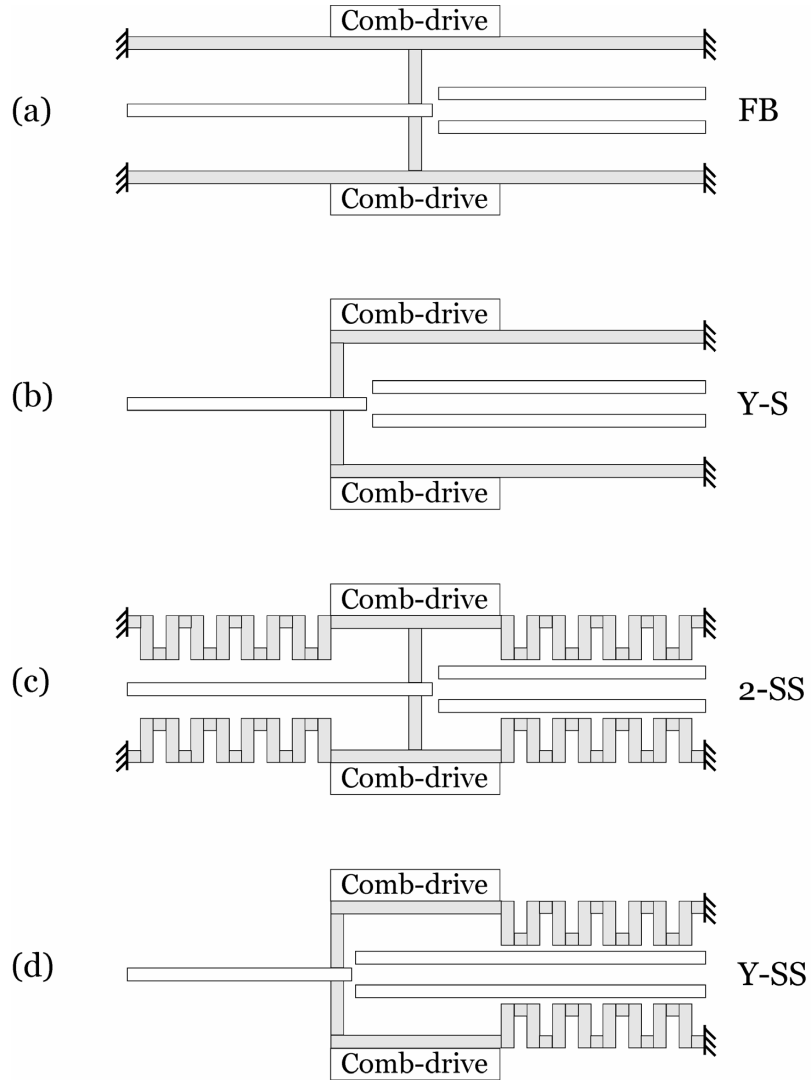


**Figure 6. 6: a) fixed-fixed beam (FB) suspension, b) Y-suspension (Y-S), c) double-serpentine suspension (2-SS), d) Y-serpentine suspension (Y-SS).**

From the suspension displacement-force simulations in Figure 6. 7 and the comb-drive force simulations in Figure 6. 5, the actuation voltage for various devices can be found. In Figure 6. 8, the calculated switching voltage for a switch with double-serpentine suspension (2-SS) is plotted for three device lengths: 800 μm, 1200 μm, and 1600 μm. The results (for 2 μm input waveguide displacement) indicate that low-voltage

operation (<20 V actuation) is possible with reasonable device size. However, the low-voltage design also can result in limited travel range of the actuators due to the mechanical compliance of the suspension designs, as will be discussed in section 6.6.1.

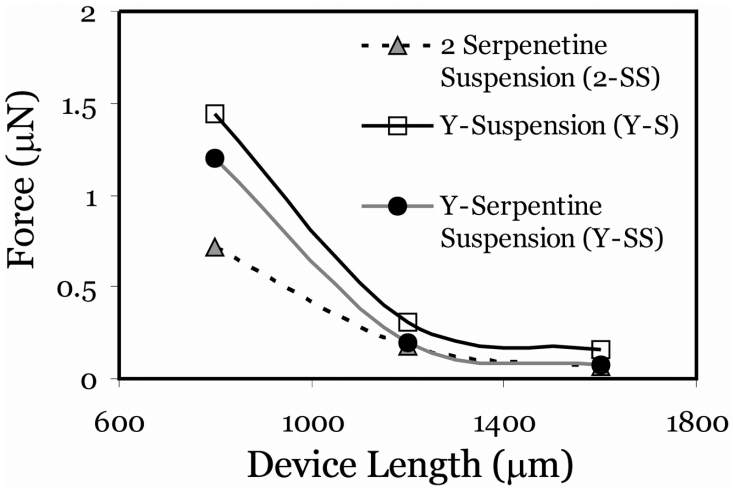


**Figure 6. 7: Simulated switching force for various suspensions, assuming 2 μm displacement. Parameters: 400 μm wide comb-drive (*N* = 80 comb-pairs).**

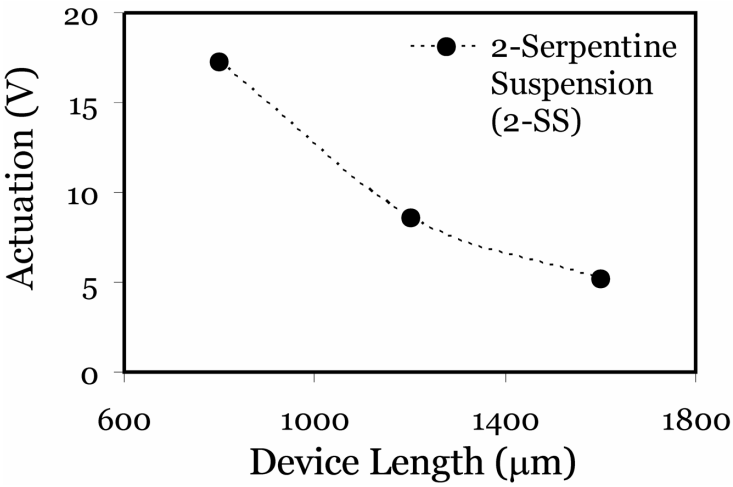


**Figure 6. 8: Calculated switching voltage: double-serpentine suspension (2-SS).**

### 6.5.2 Optical Design

For the optical switch design, various losses and effects need to be considered for the cases shown in Figure 6. 9. These include: a) loss due to divergence as the optical beam crosses the air gap between the waveguides, b) Fresnel reflection and loss due to Fabry-Perot interference in the optical cavity formed by the semiconductor/air facets and the air gap, c) optical crosstalk as the input waveguide is offset axially from the output waveguides, d) angular misalignment between input and output waveguides, and e) scattering losses due to waveguide facet roughness.

In order to analyze the various end-coupling losses, the overlap integral in eqn. (6.1) is used. For simplicity, only the fundamental mode is considered and is approximated by a Gaussian function [143, 145]. This is a reasonable approximation: although the waveguides used in the present devices support more than one mode (core cross-section: 2 μm × 2 μm), the device length is short (4 – 5 mm). Therefore, if we inject light in the fundamental mode into the waveguides, little (if any) power is lost to higher-order modes during propagation through the device waveguides.

By assuming a Gaussian mode, simple analytical relations can be applied to evaluate the end-coupling loss for various waveguide misalignments (Figure 6. 9). Since the waveguides in this work are confined in two-dimensions, as opposed to slab waveguides which exhibit confinement in only a single dimension, the losses are computed for the *x*- and *y*-directions separately ($T_X$ and $T_Y$). The total transmitted power is then:

$$T_{Total} = T_X \cdot T_Y , \tag{6.4}$$

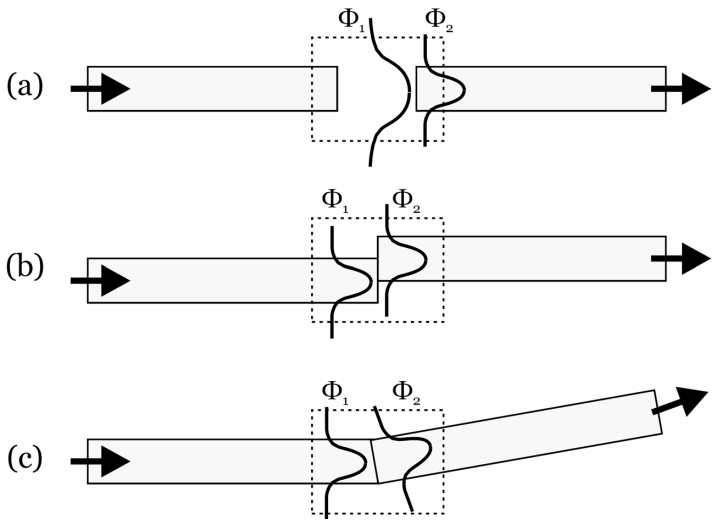


**Figure 6. 9: a) End-separation, b) axial offset, and c) angular misalignment.**

*a) Gaussian Beam Width*

The mode-shape function defined by eqn. (6.2) requires knowledge of the Gaussian beam width, $w$. Finite-element simulations (FemLab, Version 3.0) are used to simulate the fundamental mode for the waveguides, assuming a 2 μm × 2 μm core ($n_{CORE}$ = 3.195) and 2 μm × 1 μm top and bottom cladding ($n_{CLADDING}$ = 3.173). The $x$- and $y$-direction beam waists are found from the point at which the electric field amplitude has fallen to 1/e (Figure 6. 10). The results are summarized in Table 6. 1 for TE- and TM-modes (λ=1550 nm). Although the Gaussian waist is slightly different for TE- and TM-polarization, the beam size variation is only a few percent. Therefore, the loss calculations will only consider TE-polarization: $w_X$ = 0.766 μm and $w_Y$ = 1.278 μm.

**Table 6. 1: Summary of Gaussian waist for TE- and TM-modes (λ=1550 nm).**

| | TE (λ=1550 nm) | TM (λ=1550 nm) |
|---|---|---|
| $w_X$ (μm) | 0.7663 | 0.8221 |
| $w_Y$ (μm) | 1.2782 | 1.2910 |

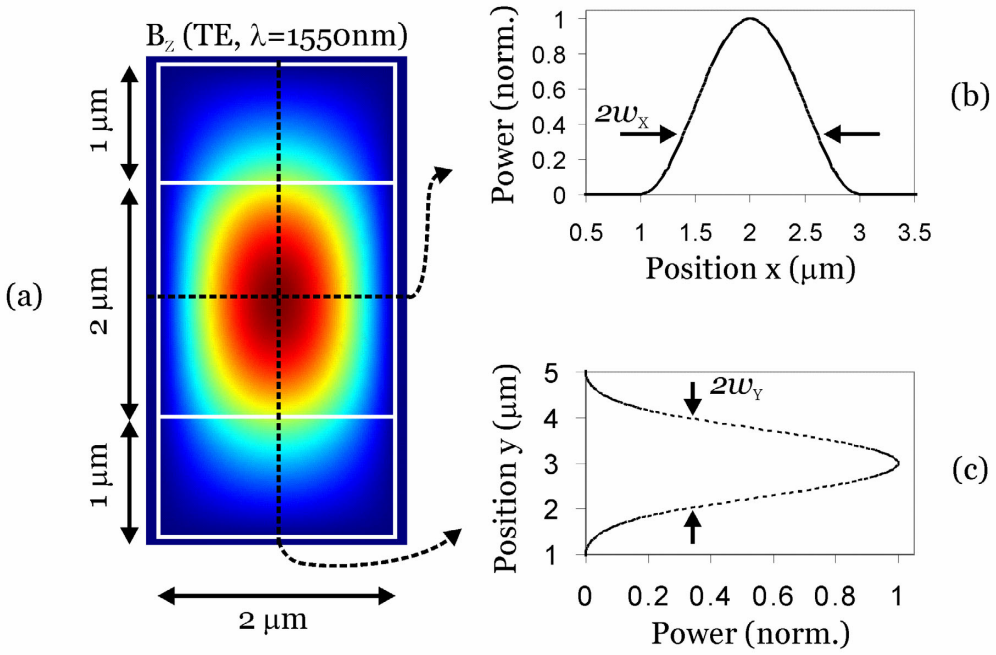


**Figure 6. 10: a) Simulated Gaussian mode, b) 1/e beam waist, $w_X$, c) 1/e waist, $w_Y$.**

*b) End-Separation Coupling Losses*

End-separation losses (Figure 6. 9a) result from beam divergence as the optical beam traverses the air gap. Within the waveguide the optical beam is confined and guided; however, in the air gap region it is no longer confined and will expand due to divergence. Therefore, the two mode-shape functions, $\phi_1(z)$ and $\phi_2(z)$ are no longer identical. The transmitted power, $T$, for two waveguides with end-separation $d$ is [143]:

$$T_{End-Separation} = 1/\sqrt{1+\left(\frac{d}{n_{CLADDING}\cdot k\cdot w^2}\right)^2}\ , \tag{6.5}$$

where $k = 2\pi/\lambda$ is the wavevector, $\lambda$ is the wavelength, and $w$ is the Gaussian beam width ($w_X$ and $w_Y$) of the confined beam (guided beam) in the waveguide. In Figure 6. 11 the loss due to end-separation and beam divergence is plotted, including the loss due to divergence along the $x$-axis (waveguide width), the $y$-axis (waveguide height) and the total loss due to beam divergence (using eqn. (6.4)). The results indicate a total divergence loss of 15–20 % (0.70–0.97 dB, for 1.55 μm air gap).

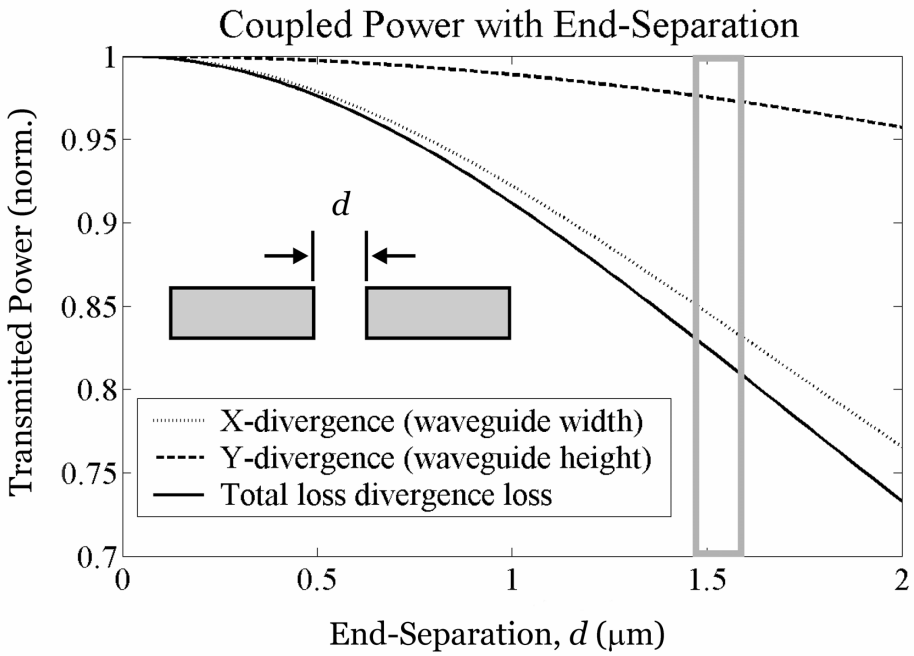


**Figure 6. 11: Calculated end-separation coupling loss due to beam divergence (gray box: 1.55 μm air gap).**

*c) Fresnel Reflection and Fabry-Perot Losses*

Due to the large refractive index of InP ($n_{CORE} \sim 3.195$), there will be significant reflection at each waveguide facet or InP/air interface. The *Fresnel* reflectivity, $r$, for the InP/air interface is given by:

$$r = \frac{n-1}{n+1}, \tag{6.6}$$

where $n$ is the index of refraction of InP. For powers, the reflectance, $R = |r|^2$, is used. Assuming negligible surface roughness and losses, the facet reflectivity is $r \sim 0.52$ ($R = 0.27$). When the *Fresnel* reflectivity is combined with the air gap separating the input and output waveguides, an optical cavity is formed. This optical cavity forms a Fabry-Perot resonator, in which constructive and destructive interference occurs.

The intensity variation in a Fabry-Perot etalon or resonator is given by [86]:

$$I = \frac{I_{Max.}}{1+\left(\frac{2F}{\pi}\right)^2 \sin^2\left(\frac{\varphi}{2}\right)}, \tag{6.7}$$

where $I_{MAX}$ is the maximum transmitted intensity, $F$ is the finesse of the resonator, and φ is the phase difference in one trip, assuming a cavity mode frequency, ν [86]:

$$\varphi = 2kd = \frac{4\pi\nu d}{\lambda}, \tag{6.8}$$

$$F = \frac{\pi\sqrt{r}}{1-r}. \tag{6.9}$$

The calculated Fabry-Perot transmission as a function of air gap, $d$, is plotted in Figure 6. 12. The calculations are repeated for different facet reflectance, $R$, since the calculated $R$ may be lowered in practice due to waveguide facet roughness. As expected, Fabry-Perot interference results in relative maxima or constructive interference for air gaps, $d = \{0, \lambda/2, \lambda, 3\lambda/2, \ldots, N\lambda/2\}$ and relative minima or destructive interference for air gaps, $d = \{\lambda/4, 3\lambda/4, 5\lambda/4, \ldots, (2N+1)\lambda/4\}$. While this may appear to be a significant source of loss, it turns out that the *Fabry-Perot* interference effects are not quite as severe during practical operation of the switch.

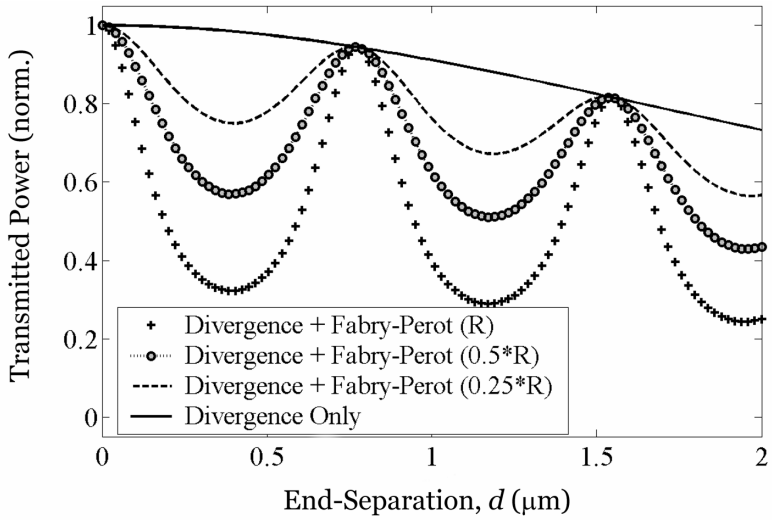


**Figure 6. 12: Calculated coupling loss due to end-separation.**

If the air gap is fixed so that $d = \lambda = 1.55$ μm, then the wavelength-dependent losses in the switch are minimal. Figure 6. 13 indicates that over a $\Delta\lambda = 100$ nm range centered at $\lambda_0 = 1550$ nm, Fabry-Perot interference results in a variation in transmitted power of less than 10 % (–0.45 dB). Furthermore, the calculation in Figure 6. 13

assumes perfect facets with reflectivity, $r$, calculated from eqn. (6.6). However, due to facet roughness, the reflectivity, $r$, and reflectance, $R$, will likely be much smaller than the ideal value give by eqn. (6.6). Consequently, Fabry-Perot interference is minimal in the end-coupled switches, as indicated by the decrease in wavelength-dependence for reflectance of R={$R$, 0.5$R$, and 0.25$R$} in Figure 6. 12 and Figure 6. 13.

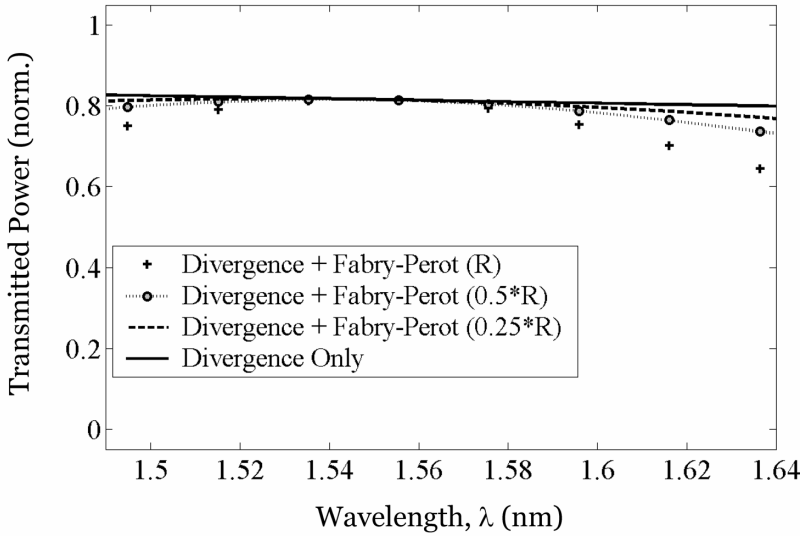


**Figure 6. 13: Calculated Fabry-Perot loss vs. wavelength for fixed gap=1.55 μm.**

*d) Crosstalk: Axial Offset*

The loss due to axial offset (Figure 6. 9b) can be calculated in a similar manner as the loss due to end-separation, namely by computing the overlap integral. For two identical waveguides with an axial offset, $t$, the transmitted power is [143]:

$$T_{Axial-Offset} = \exp\left[-\left(\frac{t}{w}\right)^2\right], \tag{6.10}$$

where $w$ is the Gaussian beam width.

The calculated loss due to axial offset is plotted in Figure 6. 14. The simulations are interpreted as follows: 1) for an offset of −2 μm, the input and output waveguides are fully aligned ($V = V_{SWITCH}$, Figure 6. 14a), 2) for an offset of 0 μm, the input waveguide is in the rest position ($V = 0$, Figure 6. 14a), and 3) for offsets ranging from −2 μm to −1.5 μm the input and output waveguides are partially aligned (Figure 6. 14b). Figure 6. 14 also includes end-separation losses due to beam divergence, assuming a 1.55 μm air gap separating the input and output waveguides.

It should be noted that the calculations in Figure 6. 14 are performed only for in-plane displacement of the input waveguide. The input and output waveguides are assumed to remain aligned vertically at all times so that axial misalignment in the vertical axis need not be considered. The calculations indicate that crosstalk of better than −30 dB is possible with the present optical design. Even smaller crosstalk is possible if the output waveguide pitch is increased to greater than the current 4 μm separation.

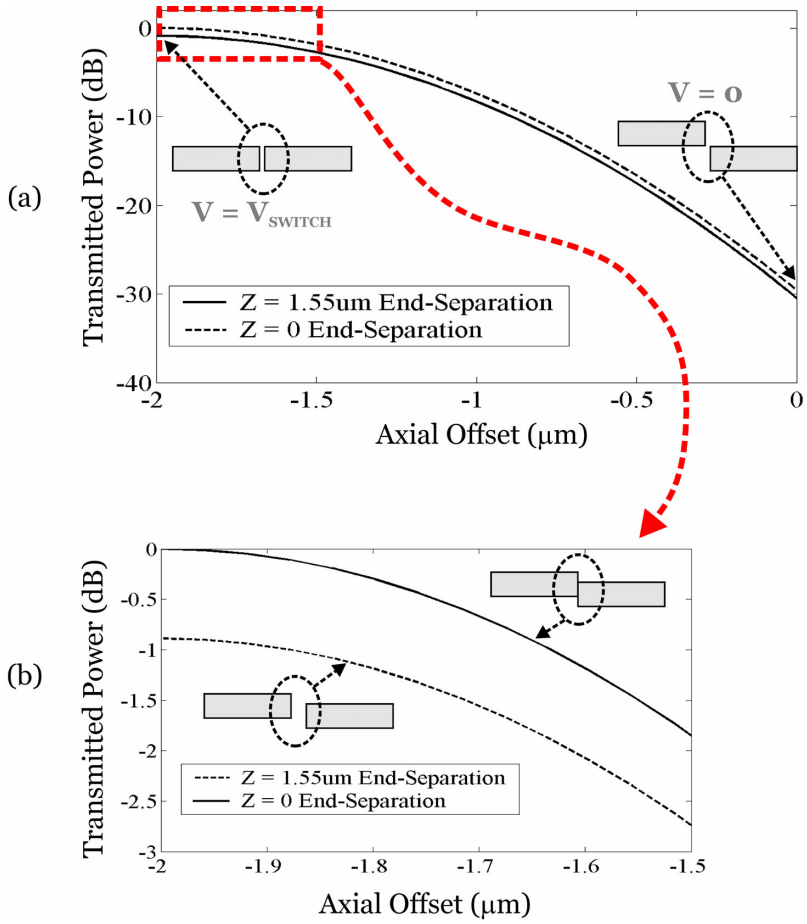


**Figure 6. 14: Crosstalk: a) 2.0 μm maximum offset, b) detail, showing only 0.5 μm maximum offset. Offset = 0 μm is the $V = 0$ rest position of the input waveguide. At offset = –2 μm the input and output waveguides are fully aligned.**

*e) Angular Misalignment*

Angular misalignment losses occur when the input and output waveguides have a slight angle with respect to their axes [143]:

$$T_{Angular-Misalignment} = \exp\left[-\left(\frac{1}{2} w \cdot n_{CLADDING} \cdot k \cdot \alpha\right)^2\right], \tag{6.11}$$

where α is the angle between the input and output waveguide axes (in radians), *w* is the Gaussian beam width, and *k* is the wavevector.

The calculated angular misalignment loss is shown in Figure 6. 15 for angular misalignment along the *x*- (in-plane) and *y*-direction (out-of-plane). Several observations are made. First, only in-plane angular misalignment (*x*-direction) needs to be considered since the input and output waveguides are aligned vertically due to the suspension design. Second, the *y*-direction exhibits larger losses compared to the *x*-direction. This results from the different beam widths, $w_X = 0.766$ μm and $w_Y = 1.278$ μm. Thus, narrower waveguides are less sensitive to angular misalignments. Finally, in the developed devices the angular misalignment losses are negligible since the suspension design ensures good vertical alignment and the expected angles of <5° result in small loss.

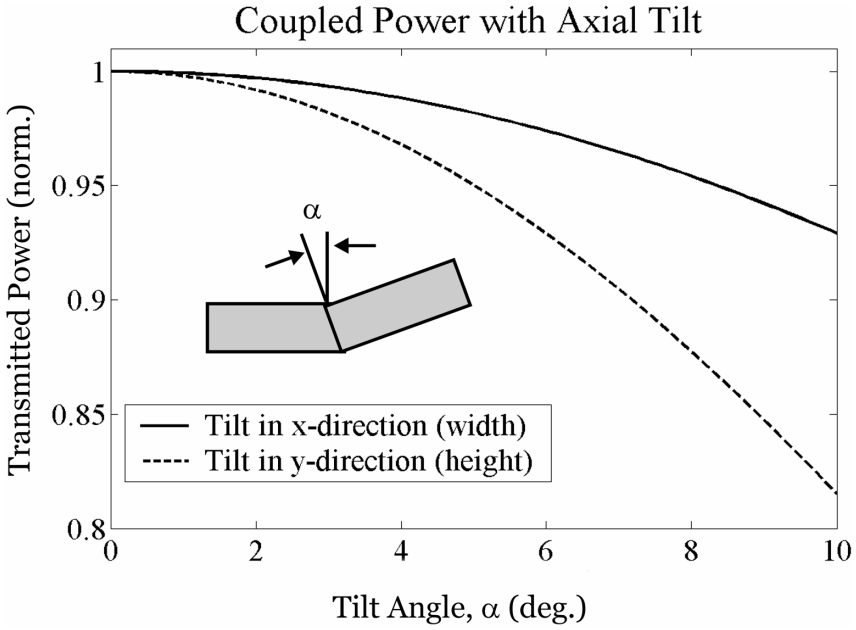


**Figure 6. 15: Coupling loss due to angular misalignment in *x*- and *y*-direction.**

*f) Scattering Loss due to Facet Roughness*

The final source of loss considered is scattering loss at the waveguide facets. Previously, losses due to *Fresnel* reflection and Fabry-Perot interference were considered. However, the *Fresnel* reflection assumed perfect waveguide facets with no roughness. Any roughness will decrease the facet reflectivity (and will reduce Fabry-Perot effects) but will also increase scattering losses.

Assuming initially perfect mirrors, the reflectivity is reduced due to surface roughness at the waveguide facets. This modified reflectivity is calculated as [146]:

$$\rho = \exp\left[-\frac{1}{2}\left(\frac{4\pi\sigma\cos\theta}{\lambda}\right)^2\right], \tag{6.12}$$

where $\sigma$ is the RMS roughness (i.e. the "height" of the random surface roughness), $\theta$ is the incidence angle (where $\theta \approx 0°$), and $\lambda$ is the wavelength ($\lambda = 1550$ nm). The transmitted power is then calculated from the reflectance, $R = |\rho|^2$.

The calculated reflectance (and hence scattering loss) as a function of surface roughness, $\sigma$, is shown in Figure 6. 16. The calculations show that for realistic values of $\sigma \leq 50$ nm, scattering losses can be significant. For $\sigma = 40$ nm, the facet reflectance is reduced by 10 %. This reduction in reflectance is due to scattering of light. Therefore, the transmitted power will also be reduced by 10 % at each waveguide facet. Consequently, scattering due to facet roughness is a significant source of loss, as it accounts for up to 20 % additional coupling loss (10 % per facet).

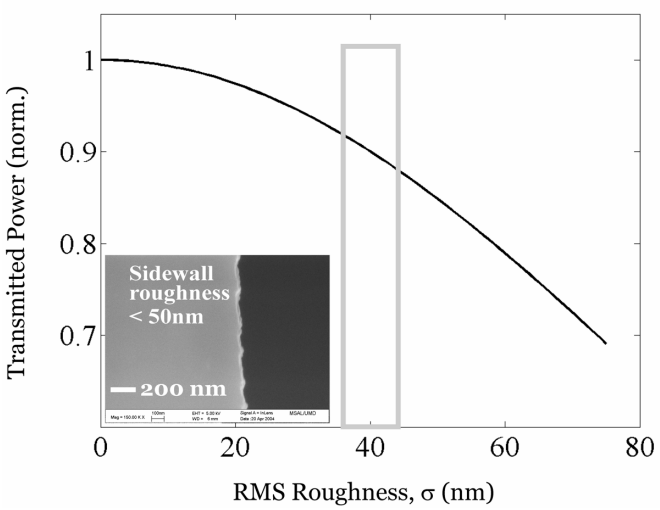


**Figure 6. 16: Scattering loss per facet as a function of RMS surface roughness.**

Estimated values for all sources of optical end-coupling losses described in this section are summarized in Table 6. 2. Up to 50 % (–3 dB) total loss is expected.

**Table 6. 2: Summary of expected optical losses in end-coupled switch.**

| **Source of Loss** | **Magnitude** | **Comments** |
|---|---|---|
| End-Separation | 15–20 % (0.70–0.97 dB) | 1.55 μm air gap; smaller for reduced size air gap |
| Fabry-Perot | Minimal | Design for {λ/2, λ,…, Nλ/2} air gap |
| Axial offset | <10 % (0.5 dB) | Actuator: good axial alignment |
| Angular Misalignment | < 5 % (0.25 dB) | Suspension: good angular alignment |
| Surface Roughness | 20 % (0.97 dB) | 10 % per facet for σ ~ 40 nm roughness |

## 6.6 Experimental Results

Experimental characterization of the 1×2 end-coupled switches was performed in a similar manner as for the MEMS couplers in Chapter 5. Lensed fibers were used to couple laser light in and out of the chip, and electrical probes supplied the actuation signals for the comb-drive actuators.

### 6.6.1 Sacrificial Release and Strain Relaxation

The various suspensions in Figure 6. 6 ensure low-voltage actuation, and the doubly-clamped design combined with intrinsic tensile stress ($\varepsilon \sim 0.05$ %) ensures vertical alignment between the input and output waveguides. However, low-voltage operation implies very compliant suspensions, which limit the performance of the end-coupled switches. Figure 6. 17 shows various devices after etching of the sacrificial $In_{0.53}Ga_{0.47}As$ layer and release of the comb-drive actuators. Due to the compliance of the suspensions combined with the intrinsic tensile strain in the InP layers and the asymmetry of the suspension design, the set of movable comb-drive fingers is displaced relative to the fixed set of comb-fingers. The strain relaxation and accompanying displacement is especially severe for longer suspensions, whose spring constant is smaller than that of shorter suspensions. For this reason, all the long devices ($L$ = 1600 μm) could not be tested optically.

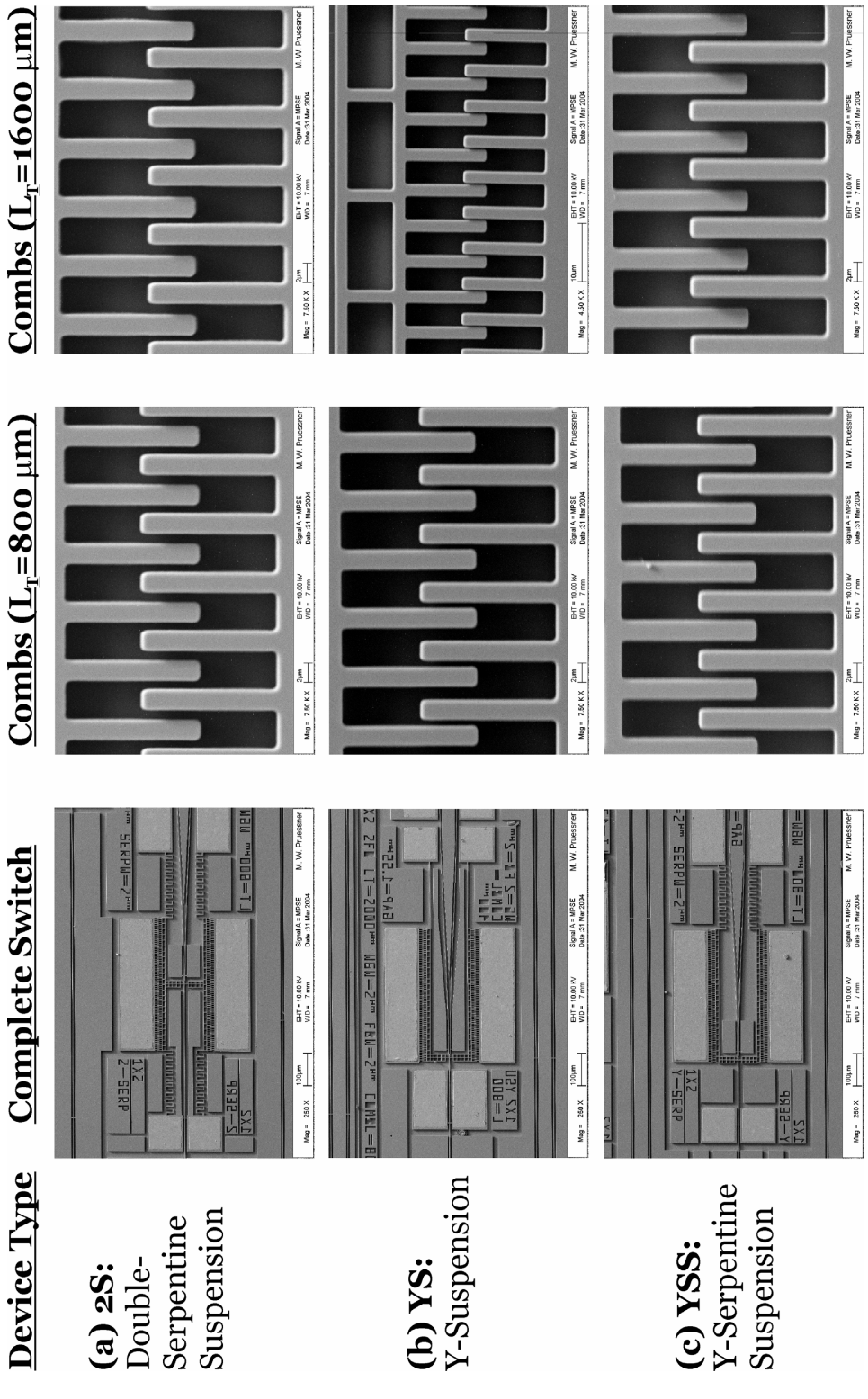


**Figure 6. 17: Strain relaxation in various 1×2 end-coupled switches after release. The L = 1600 μm exhibit strain relaxation and displacement of the comb-fingers.**

It should be noted that even a slight displacement of the comb-fingers results in a non-zero force between the comb-fingers and side pull-in between neighboring fingers (i.e. $F_{NORMAL} \neq 0$). Side pull-in between neighboring comb-fingers is the result of the small spring constant of the suspension designs, especially in the normal direction along the waveguide axis. For this reason, only the $L$ = 1200 μm double-serpentine suspension (2-SS) switch was successfully tested optically (similar to the device in Figure 6. 18). All short devices ($L$ = 800 μm) exhibited comb-finger side pull-in before significant input waveguide displacement was achieved for measurable optical coupling between input and output waveguides.

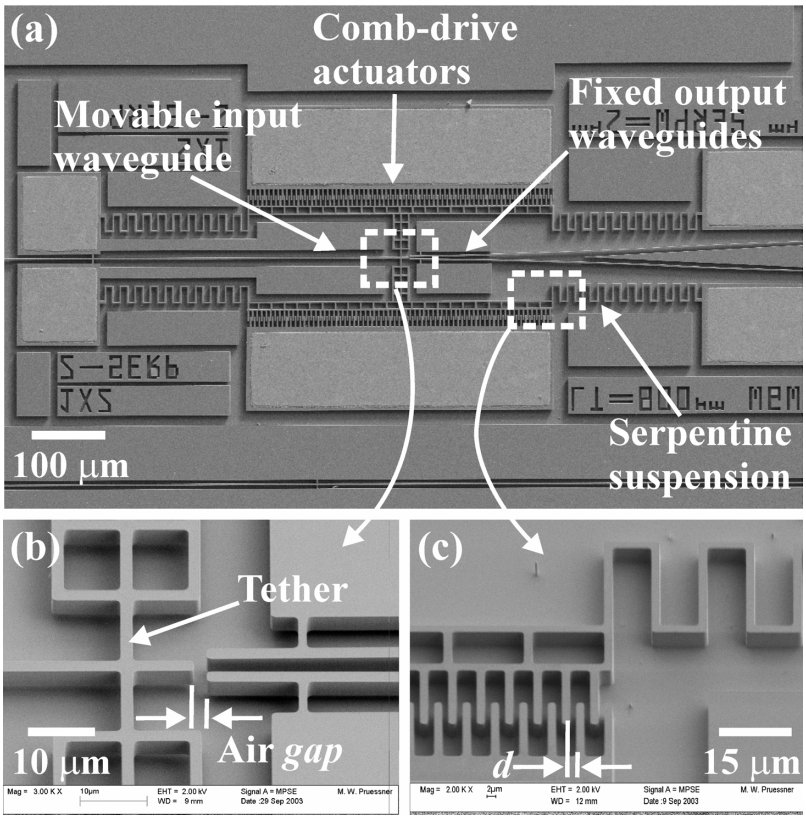


**Figure 6. 18: a) Complete 2-SS type end-coupled switch, b) detail of movable input and fixed output waveguides, c) detail of comb-drive actuator.**

### 6.6.2 Optical Coupling Efficiency and Crosstalk

The optical coupled power as a function of applied DC actuation voltage for device 2-SS (double-serpentine suspension, $L$ = 1200 μm) is plotted in Figure 6. 19. At zero applied voltage, the input waveguide is in the rest position and little power is coupled to the output. As the applied voltage is increased, the input waveguide is displaced and is increasingly aligned to one of the output waveguides resulting in an increase in coupled power. The maximum coupled power was obtained at $V$ = 6.9 V. At voltages greater than 7 V the comb-drive exhibited a side instability [147] and the set of movable comb-drive fingers pulled-in to the fixed set of comb-drive fingers. The side instability is likely the result of the low spring constant of the serpentine suspensions in the direction perpendicular to the comb-fingers. Nonetheless, the input and output waveguides were aligned to within a few hundred nanometers so that significant optical power was coupled before comb-drive pull-in occurred.

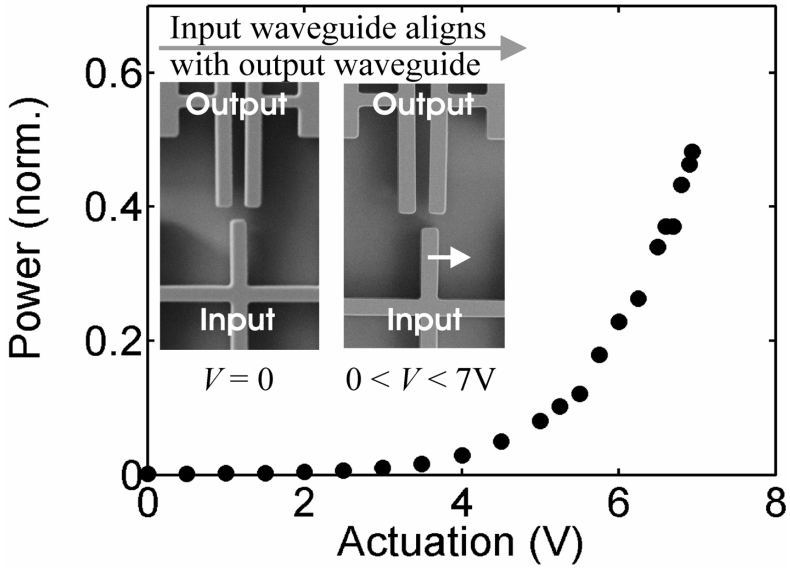


**Figure 6. 19: Optical end-coupled power vs. DC actuation voltage.**

The coupled power in Figure 6. 19 is normalized to the power in a straight waveguide located on the same chip. This enables the coupling loss due to beam divergence, angular misalignment, and scattering to be extracted. Using this technique, the coupling loss was found to be –3.16 dB. Smaller losses can be expected if the air gap separating input and output waveguides is reduced from λ (1.55 μm) to λ/2 (775 nm). Optical crosstalk was measured to be –26 dB (at $V = 0$).

Good agreement between the experimental results and the optical modeling in section 6.5.2 was obtained. For the model in Figure 6. 20, the measured coupled power as a function of displacement was plotted. The model incorporates end-separation losses, assuming an air gap of λ=1.55 μm (1 dB or 20%, see Figure 6. 11). Other losses were also addressed in the model, including: a) 10 % scattering losses at each waveguide facet (20 % for both facets, according to Figure 6. 16), b) angular misalignment losses (<5 %, according to Figure 6. 15), and c) axial offset in both the vertical (*y*-) direction and horizontal (*x*-) direction (10 %, according to Figure 6. 14). The experimental data is plotted as a function of the square of the applied voltage, from which the electrostatic force and hence the input waveguide displacement is extracted (the spring constant results in a linear relationship between displacement and electrostatic force, which goes as the square of the applied voltage).

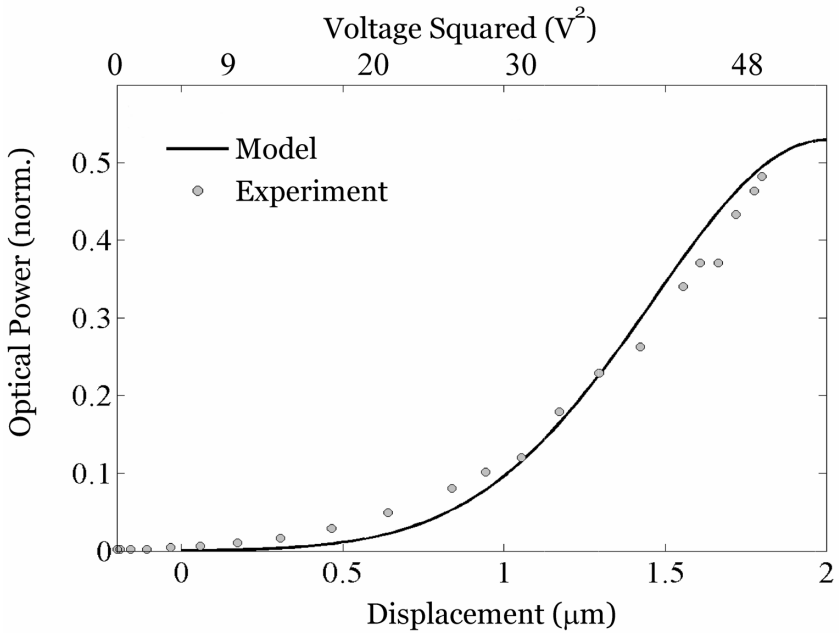


**Figure 6. 20: Comparison of the experiment (Figure 6. 19) with the optical model.**

While there is good agreement between the optical model and experiment, there are many variables that affect the end-coupling loss so that exact forecasting of the coupled optical power is difficult. The model presented in section 6.5.2 gives the designer a reasonable guide for device design and predicts the general behavior of the end-coupled switches in terms of loss and crosstalk. The scattering loss due to facet roughness is an estimate, since precise roughness is difficult to measure ($\sigma \leq 50$ nm). Similarly, the angular misalignment is small (< 5 degrees) but is difficult to measure accurately. Finally, the experimentally measured crosstalk (–26 dB at $V = 0$) is significantly larger than that predicted by the model (–30.5 dB at $V = 0$). However, due to beam divergence and reflections, scattered light can couple to the output waveguide resulting in an increase in crosstalk.

### 6.6.3 Temporal and Frequency Response

The temporal and frequency response of device 2-SS (double-serpentine suspension, $L$ = 1200 μm) is shown in Figure 6. 21. The device was tested by applying a square-wave actuation signal to the comb-drive actuator and measuring the optical response. From Figure 6. 21 the initial switching time is 140 μs, but there is significant 'ringing' for 2 ms until the switch reaches the steady state. The ringing is the result of the underdamped electrostatic actuator, whose serpentine-suspensions were designed with low-voltage operation in mind. Nonetheless, for network restoration applications the 2 ms settling time is more than sufficient [5].

From the ringing period in Figure 6. 21 the approximate resonance frequency can be found by $f_0 = 1/T$. Using this approach the (damped) resonance frequency is $f_0 = 3.13$ kHz. A second method for determining the resonance frequency is by measuring the mechanical displacement directly from the coupled optical power. If a sinusoidal voltage signal is used to actuate the comb-drives, then the displacement of the input waveguide will depend on the frequency of actuation. Far from resonance, the displacement will be small and close to resonance there will be a sharp peak and maximum displacement. The large displacement results in increased alignment between input and output waveguides and hence larger coupling. This approach is shown in Figure 6. 22, resulting in a resonant frequency of $f_0 = 3.2$ kHz, in good agreement with the ringing approach in Figure 6. 21.

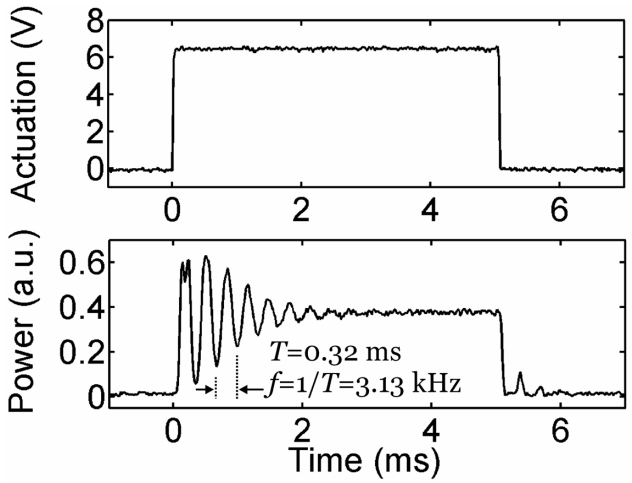


**Figure 6. 21: Temporal response of optical switch (square actuation voltage).**

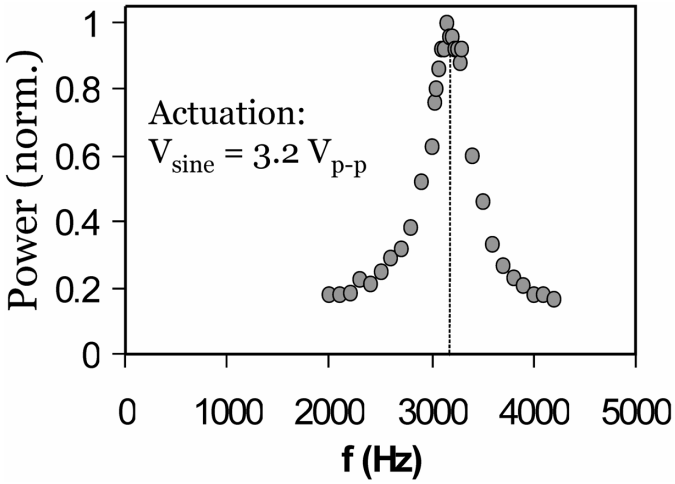


**Figure 6. 22: Resonance behavior of the optical switch (sinusoidal actuation).**

## 6.7 Discussion

The devices tested can be improved in a number of ways. First, the air gap, as shown in Figure 6. 18b can be reduced from λ (1.55 μm) to λ/2 (0.775 μm). By reducing the air gap, the beam divergence predicted by eqn. (6.5) will be smaller and the coupled

power will be larger. Therefore, reduced air gap results in reduced losses. However, the reduced air gap also places tighter fabrication tolerances on the device, which may require electron-beam or other non-traditional lithography.

Second, by reducing the air gap the crosstalk will also be reduced since the reduction in beam divergence results in less coupling of stray (diverged) light into the opposite output waveguide. A second method for reducing crosstalk is to increase the output waveguide pitch. However, this will also increase the required displacement of the input waveguide during switching and may require increased actuation voltage.

The third issue is strain relaxation, as shown in Figure 6. 17. The various suspensions relax and cause a deformation of the comb-drive actuators after the sacrificial release etch. The reason for this deformation is the combination of intrinsic tensile stress in the waveguides combined with the non-symmetric device structure: that is, the input waveguide induces a net force that results in a slight pull-back of the input side of the comb-drive actuator (Figure 6. 23). The net force is caused by the intrinsic tensile strain and the smaller cross-sectional area on the input side compared to the output side. Figure 6. 23 illustrates this pull-back effect for a Y-suspension device with cross-sectional area $A$ on the input and area $2A$ on the output. Pull-back results in a very low yield of usable devices.

One solution to the strain relaxation problem is to reduce the intrinsic tensile stress in the waveguides – at the risk of encountering *compressive* stress and buckling of the waveguides due to arsenic contamination during MBE growth (see discussion of InP mechanical characterization in Chapter 2). A second approach is to simply design devices with identical cross-sectional area and spring constant at the input and output.

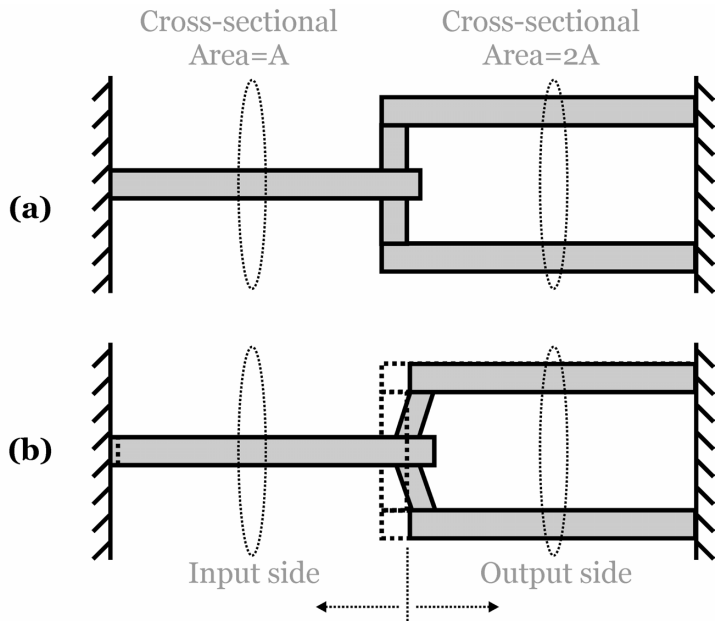


**Figure 6. 23: Asymmetric structure with regard to input and output cross-sectional area for a Y-suspension (Y-S) type device: a) before sacrificial release etch, b) after release etch and strain relaxation.**

The ringing exhibited by the electrostatic actuator design (Figure 6. 21) can be reduced in order to increase the total switching time to less than 2 ms. Currently, the low-voltage design results in an underdamped system. Mechanical stoppers can be used to prevent overshooting of the input waveguide during actuation, although this has resulted in stiction, or permanent adhesion of the input waveguide to the mechanical stops [51]. Therefore, such a design was not initially pursued since it affects device reliability. A complex actuation voltage, in which an initial actuation pulse followed by a braking pulse are used, may decrease the actuator ringing and has been demonstrated by *Bakke et al.* [51]. However, this complicates the switch circuitry and is not really

necessary if the ultimate application is in network restoration, where millisecond switching speeds are adequate [5].

## 6.8 Alternative Designs

In light of the problems with strain relaxation (Figure 6. 17), several symmetric end-coupled switches were designed, fabricated, and tested. Instead of comb-drive actuators, pull-in type actuators were used. Both doubly-clamped structures and simple cantilever-type end-coupled switches were studied.

### 6.8.1 Doubly-Clamped Pull-In Actuator Switches

The basic design for a doubly-clamped pull-in type actuator end-coupled switch is shown in Figure 6. 24. The pull-in actuator (see Appendix D) is formed by the doubly-clamped beam and the fixed electrode, as indicated by the voltage source. An advantage of pull-in actuators is their compact size and their ability to generate large forces if the actuation gaps are small. Another feature of the design is the equal input and output cross-sectional area to prevent strain relaxation. The input side consists of the input waveguide (width $W$) and two suspended beams (each has width $W/2$). Conversely, the output side has two suspended beams of width $W$. The equal cross-sectional areas result in minimal pull-back after sacrificial release, in contrast to the asymmetric design (Figure 6. 23). The actuators were designed to pull-in at voltages ranging from $V_{PI}$ = 8 – 20 V. The waveguides consisted of a 1.5 μm thick core ($In_{0.99}Ga_{0.01}As_{0.01}P_{0.99}$, $n$ = 3.173, ε = 0.0388 %) with air cladding, as described in Chapter 3 and Chapter 4. A fabricated switch is shown in Figure 6. 25.

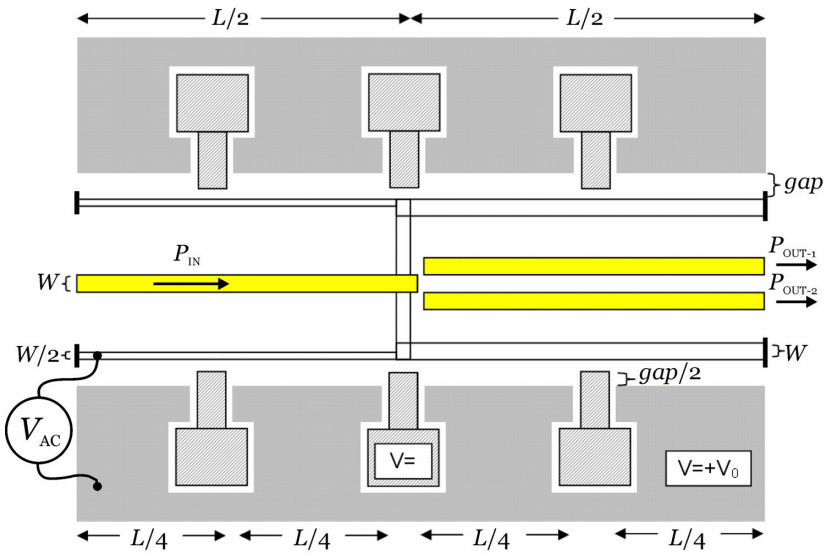


**Figure 6. 24: Pull-in type switch. As shown, the input will align with output 2.**

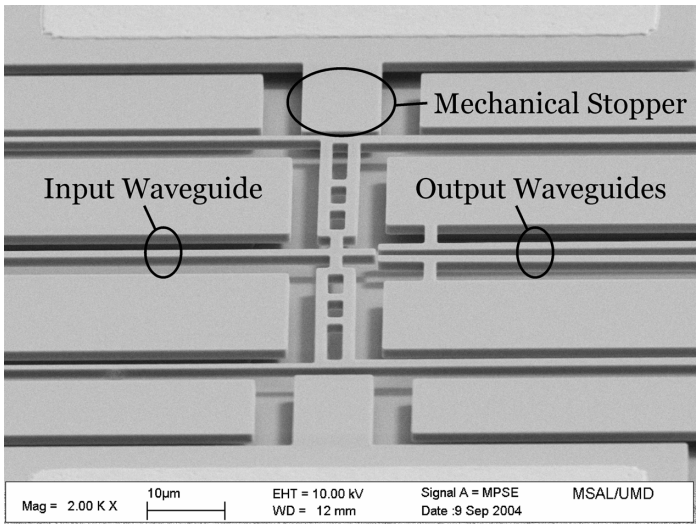


**Figure 6. 25: SEM of pull-in type end-coupled switch.**

Although the doubly-clamped structure coupled with intrinsic tensile strain ($\varepsilon = 0.0388$ %) prevent significant buckling, the intrinsic strain gradient ($d\varepsilon/dt$) still results in some out-of-plane curvature of the input waveguide. For most devices, the out-

of-plane curvature was limited to less than 500 nm (Figure 6. 26). However, due to the relatively thin waveguides ($t$ = 1.5 μm) a vertical deflection of only a few hundred nanometers is significant and results in considerable optical coupling losses. Furthermore, the vertical misalignment of the pull-in type actuator results in an a vertical aligning force in addition to the in-plane actuation force (see Appendix D). This vertical force prevents testing of the longer devices.

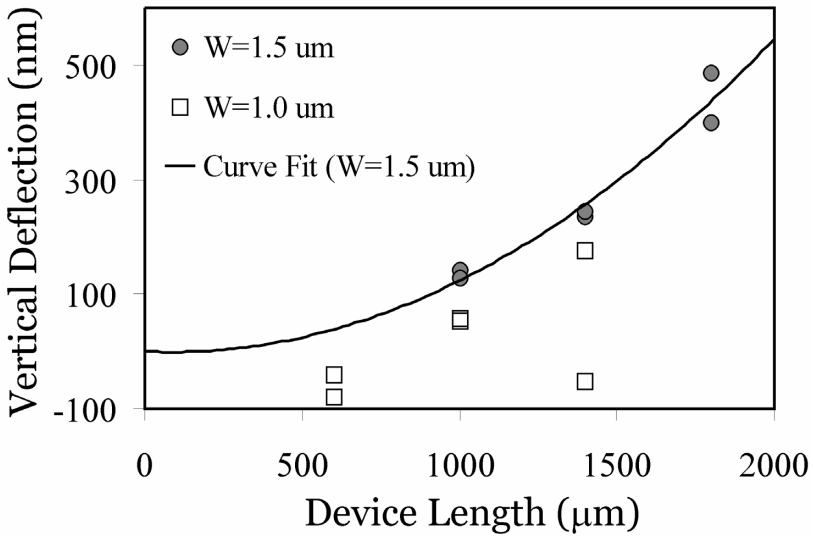


**Figure 6. 26: Out-of-plane deflection of cantilever tip after sacrificial release for $W$ = 1.0 and 1.5 μm wide waveguides. Note: $W$ = 1.0 μm has a uniform measurement error.**

An optical switching measurement for an $L$ = 600 μm, $W$ = 1.0 μm doubly-clamped pull-in device (FB-8 with waveguide end-separation: *gap* = 775 nm, actuation gap: 2.0 μm) is shown in Figure 6. 27. The switch was actuated at 12.9 Vp-p with an $f$ = 1kHz square wave. The optical signal was S-polarized (TE) at λ = 1550.14 nm

wavelength. As with previous devices, there is significant ringing, although the decay constant is much shorter so that device reaches steady state in about 200 μs. The initial switching speed is 20 μs. From the ringing period the resonance frequency is $f_0 \approx 37$ kHz. The results are a significant improvement compared to the previous devices in section 6.6. The total coupled power was relatively low (1 – 2 μW), however, due to the switching measurement, in which the input waveguide was only partially actuated and not to pull-in. Ideally, the mechanical stoppers (Figure 6. 25) should prevent any oscillation and ringing during actuation. In practice, the mechanical stoppers resulted in reliability problems so that the temporal measurements were performed for actuation voltages $V < V_{PI}$.

Stiction during pull-in is a problem in the present, however. The switches were designed with mechanical stoppers that are electrically neutral (Figure 6. 25). While the stoppers ensure accurate alignment of input and output waveguides during switching, the optically smooth and vertical surfaces ($\sigma < 50$ nm) combined with the uncontrolled testing environment (roughly 30–40 % humidity) results in stiction for most devices upon pull-in. Future devices should omit the mechanical stoppers or may utilize stoppers with surface coatings (SAM's [142]). Alternatively, the contact area can be reduced (i.e. roughened contact surfaces) to prevent stiction.

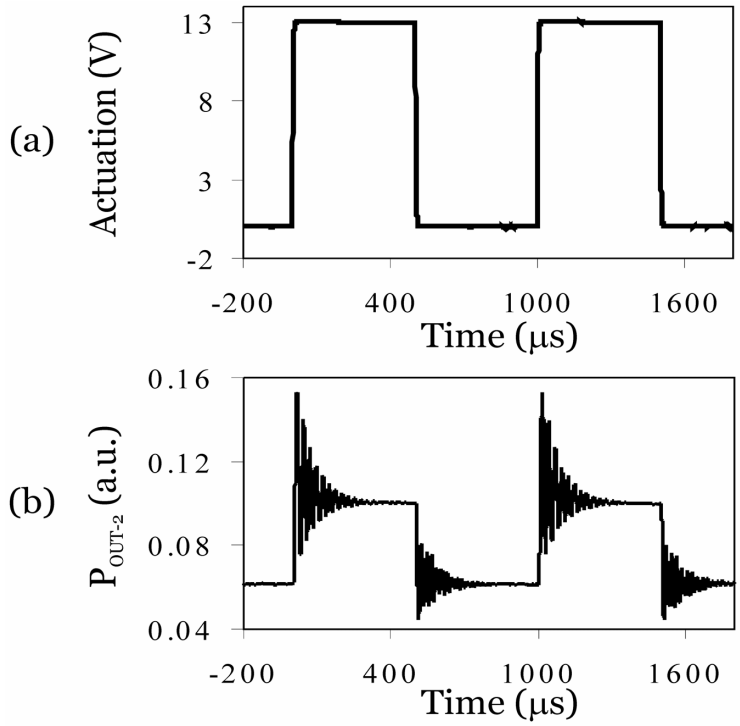


**Figure 6. 27: Temporal response: a) actuation signal, b) optical coupled output.**

### 6.8.2 Cantilever Pull-In Actuator Switches

Cantilever type pull-in actuated switches were also designed, fabricated, and tested. The device schematic is shown in Figure 6. 28 and a fabricated device is shown in Figure 6. 29. In most respects, the operation is similar to the doubly-clamped devices in Figure 6. 24; however, a cantilever input waveguide is used. Due to the intrinsic strain gradient, which causes cantilevers to curl out-of-plane, the length of the devices is limited to less than 100 μm. Measurements have shown the deflection to be less than 300 nm for $L$ = 100 μm long cantilevers. The waveguide widths were chosen to be $W$ = 0.6 and 0.8 μm. This ensures low-voltage operation (calculated pull-in voltage: $V_{PI}$ = 5 – 20 V), even for the short $L$ = 50 μm cantilevers.

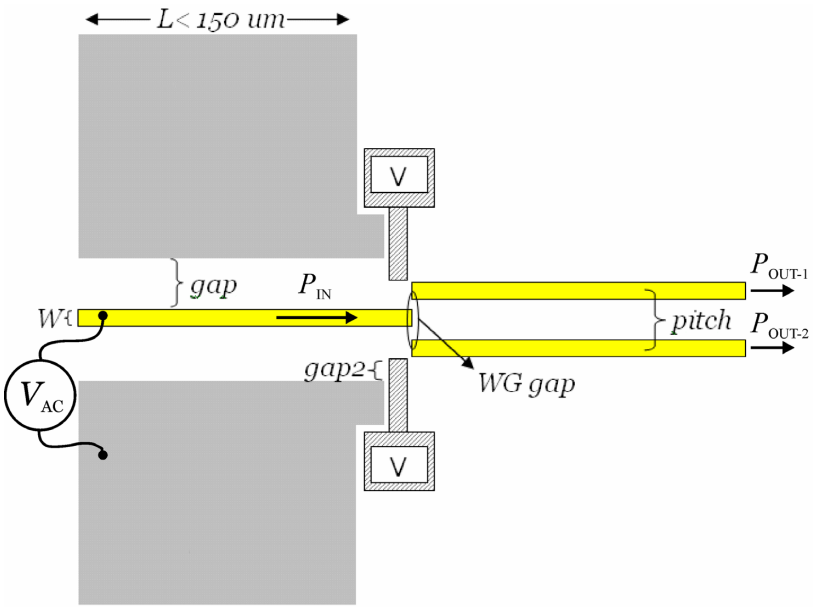


**Figure 6. 28: Schematic of pull-in type cantilever switch.**

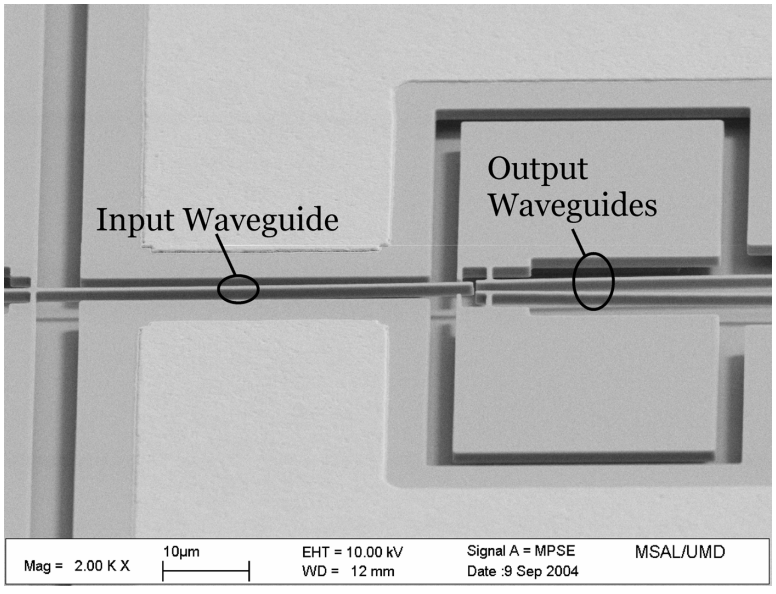


**Figure 6. 29: SEM of cantilever waveguide switch.**

Low-voltage pull-in actuation was demonstrated with the devices. However, significant optical coupling could not be measured. This is likely the result of fabrication

limitations, which result in curved waveguide facets and mechanical stoppers that cause a misalignment between input and output waveguides during switching. Better lithography tools (electron-beam lithograph) will be needed if these sub-micron features are to be realized in future devices. In addition, more uniform materials growth with smaller strain gradients will be required to ensure in-plane alignment between input and output waveguides for increased efficiency optical coupling.

## 6.9 Summary

In this chapter, end-coupled optical waveguide MEMS switches were demonstrated. The devices represent the first demonstration of end-coupled MEMS switches fabricated entirely from InP and InP-based materials. The performance of the switches is comparable to or better than other previously demonstrated end-coupled MEMS switches in terms of switching voltage (<7 V), switching speed (140 μs, 2 ms settling time), and loss (3.16 dB). Other devices demonstrated even faster switching speed (20 μs, 200 μs settling time) with low voltage actuation (<13 V), although their coupling efficiency was lower. Compared to other demonstrations, the present devices enable monolithic integration of InGaAsP lasers, semiconductor optical amplifiers (SOA's), and p-i-n photodetectors on-chip for operation at $\lambda$ = 1550 nm, thereby paving the way for increased optical functionality.

Page intentionally left blank.

# CHAPTER 7

# MICROMECHANICAL RESONATOR SENSORS

## 7.1 Introduction

In this chapter, another application for InP-based optical waveguide MEMS is presented. The end-coupled switches in Chapter 6 are adapted for environmental sensing using resonating cantilevers. First, the operating principle of MEMS resonant sensors is reviewed and the difficulty of developing single-chip sensors using present devices is highlighted. Next, the basic approach and design of resonant cantilever waveguide sensors is reviewed. Finally, experimental results characterizing the sensors are presented along with plans for future work.

## 7.2 Resonant Sensors

### 7.2.1 Background: MEMS Resonant Sensors

Many different environmental sensors have been proposed and demonstrated [36, 148-153]. The basic sensor consists of a transducer coated with a polymer (Figure 7. 1). The polymer is agent-specific so that it adsorbs only specific analytes. Exposure to specific chemical or biological agents causes the agent of interest to be adsorbed by the polymer. This adsorption results in a change in the transducer behavior. By measuring the change in transducer response, information about the environment can be deduced, including the presence of specific chemical or biological agents.

The two primary approaches are summarized in Figure 7. 2: a) resonant or dynamic mode, and b) static mode. In the resonant mode, the adsorption of mass by the polymer receptor coating results in a measurable shift in resonance frequency. According to Figure 7. 2, the change in resonance frequency results from changes in transducer elasticity, changes in mass, or changes in damping. From the shift in resonance frequency, as well as the preferential adsorption properties of the receptor coating, information about the environment can be obtained.

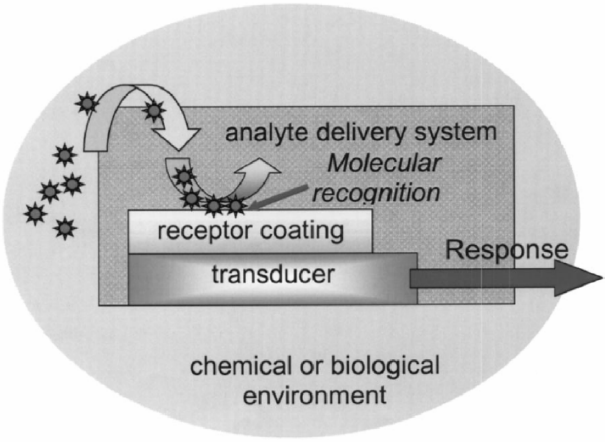


**Figure 7. 1: Basic measurement approach of environmental (chemical/biological) sensors using MEMS transducers [36].**

A second technique comprises measurement of the static behavior of the transducer. Generally, the static behavior refers to steady-state deformation of the transducer that results from thermal effects, modulation of mechanical stresses, or modulation of the electric or magnetic field. For example, if the transducer is a cantilever, then mass adsorption on the cantilever surface will result in a stress gradient that will cause the cantilever to deflect.

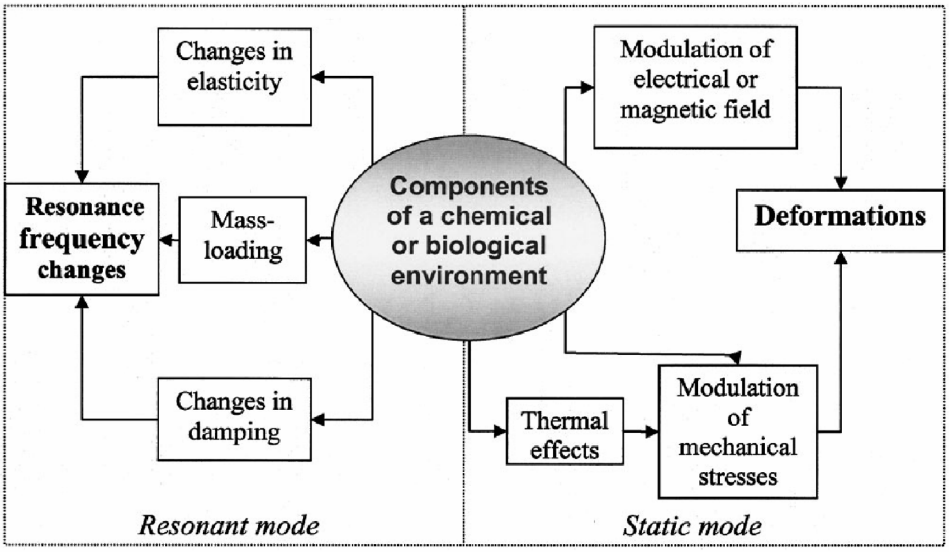


**Figure 7. 2: Environmental sensors: resonant (left) and static (right) [36].**

In this work, only resonant transducers are considered for sensors based on mass adsorption. The reason is that static deformations generally are the result of the presence of an agent of interest (which needs to be measured) as well as other environmental factors such as gravitational/magnetic/electrostatic forces or thermal effects (which represent noise). Therefore, the environment induces significant error in the measurement. Secondly, resonant transducers can have high Q-factors (even in gaseous media), which results in very high sensitivity devices, whose resonance can be measured accurately in the presence of "environmental noise." Finally, by scaling the transducers down in size, the vibrational energy approaches those of single molecules (Figure 7. 3). This enhances the sensitivity of MEMS resonators for detection of cells/molecules and makes them well-suited for bio-chemical sensing.

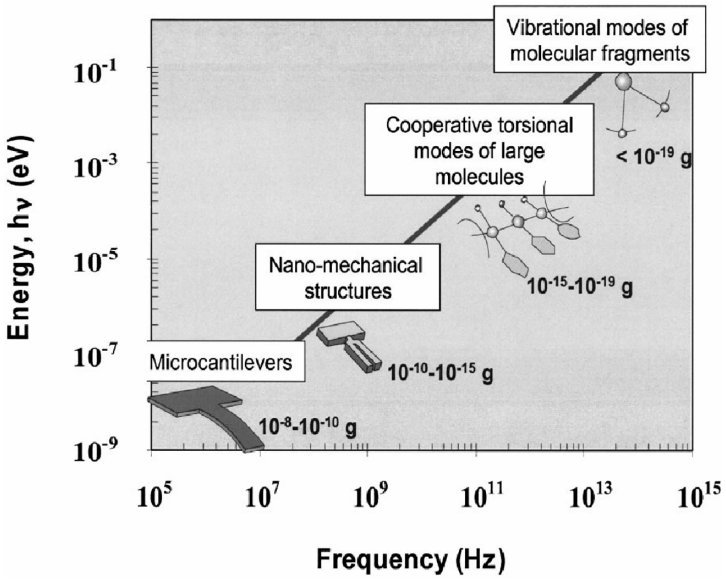


**Figure 7. 3: Micro- and nanoscale structures have energies and resonant frequencies approaching the vibrational modes of single molecules [36].**

### 7.2.2 Literature Review

Many MEMS-based sensors have been demonstrated in the past [150-155]. In 1986, *R. T. Howe* studied resonant poly-silicon micro-bridges coated with negative photoresist for xylene vapor sensing [156]; the resonators included an on-chip NMOS readout circuit. More recently, *Thundat et al*. utilized gold coated cantilevers to detect mercury vapor (1995) [153]. The silicon nitride cantilevers had one side completely or partially covered with a 20–50 nm thick layer of gold. Dynamic (resonant) as well as static (cantilever bending) measurements were performed in air inside an atomic force microscope (AFM) chamber using a laser position imaging system. Upon exposure to mercury vapor (concentration: 30 $\mu g/m^3$), mercury is permanently adsorbed by the gold coating and the response of the cantilever changes. The resonant frequency *increased* for

cantilevers whose whole top surface was coated with gold, likely the result of an increase in cantilever spring constant with adsorption of mercury. For cantilevers with only a small region covered with gold, the resonance frequency *decreased* linearly with mercury vapor exposure time. This decrease is expected due to the increased mass loading. Typical resonance frequency shifts of 200 – 300 Hz were measured, yielding a sensitivity of 0.7 pg/Hz. In addition to dynamic resonance measurements, *static* deflection of the cantilever upon mercury vapor exposure was also observed, the result of induced strain upon mercury adsorption.

*Baller et al.* developed an artificial nose using an array of eight cantilevers [154]. The bending response (i.e. static response in Figure 7. 2) of the cantilevers was measured using an array of eight lasers and corresponding sets of position-sensitive photodetectors. The cantilevers were coated with various polymers, including polyvinylpyridine (PVP), polyurethane (PU), polystyrene (PS), and polymethylmethacrylate (PMMA). Exposure to various alcohols (methanol, ethanol, propanol, etc.), solvents (acetone, dichloro-methane, toluene, etc.) and natural flavors (vanilla, lemon, orange, etc.) resulted in bending of the cantilevers. The array of cantilevers has the advantage of allowing compound vapors consisting of subsets of unique chemicals to be measured, since each cantilever can be coated with a unique receptor. A significant shortcoming of the device is the measurement setup complexity, since eight laser beams need to be focused on eight cantilevers, and a corresponding number of position-sensitive photodetectors are required for cantilever beam bending measurements.

Single-cell detection was demonstrated by *Ilic et al.*[150]. Low-stress silicon nitride (320 nm thick) cantilevers were coated with *E. coli* antibodies (O157:H7). Upon

exposure to a solution containing *E. coli* cells, the bacteria adhered to the cantilever. By measuring the *dynamic* resonance frequency shift of the cantilevers using a laser-based optical detection system in an AFM, the mass of an individual *E. coli* cell as well as the number of cells could be determined. Single cells were measured and the extracted mass for an *E. coli* cell was found to be 665 fg. Based on these measurements, the maximum sensitivity of the cantilever sensors was calculated to be 7.1 Hz/fg (equivalently, 0.14 fg/Hz).

More recently, true femtogram mass detection was experimentally demonstrated by *Lavrik et al.* [151]. Using a focused ion beam (FIB) system, silicon cantilevers were micromachined to 50–100 nm thickness and 2–6 μm length (the width was 2 μm), resulting in resonance frequencies of 1–6 MHz. These nano-mechanical resonators were then coated with a 35 nm thick gold layer. Exposure to 11-mercaptoundecanoic acid vapors resulted in mass adsorption, which resulted in a measurable resonant frequency shift. Again, an external laser-based optical detection setup was utilized for cantilever displacement sensing. The experiments resulted in a resonant frequency shift of $\Delta f = 2$ kHz ($f_0 = 2.25$ MHz), from which the added mass was calculated to be $\Delta m = 5.5$ fg. This work demonstrates the high sensitivity that is gained by scaling the sensor size down to the nanoscale regime.

While the above examples have used external optical detection means (e.g. AFM based laser system), other position measurement approaches are possible. For example, piezoresistive, piezoelectric, capacitive, and electron tunneling readout schemes have all been previously demonstrated [36]. However, optical detection appears to offer the highest sensitivity with the greatest noise immunity and simplicity.

### 7.2.3 Limitations of Current MEMS Resonant Sensors

The literature shows that high sensitivity and versatility in measuring different chemical and biological agents is possible with resonant cantilever sensors [150-155]. While piezoresistive, piezoelectric, capacitive, and electron tunneling readout schemes enable on-chip cantilever displacement measurement, optical detection methods appear to be the most sensitive, are relatively simple to implement, and exhibit large noise immunity. However, optical detection schemes reported to date also present significant problems if single-chip sensors are to be realized, as shown in Figure 7. 4.

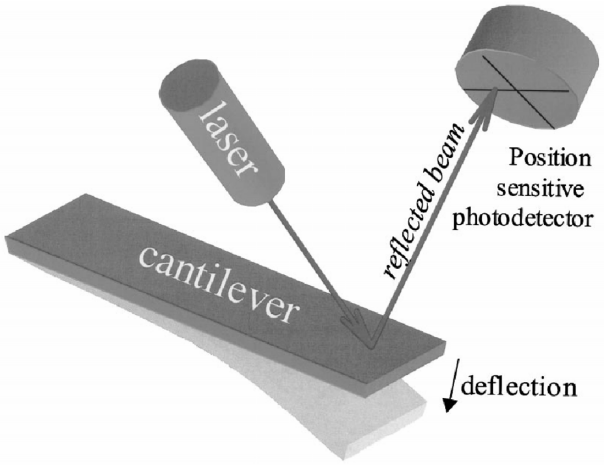


**Figure 7. 4: Cantilever position measurement using an optical detection technique commonly used in atomic force microscopes (AFM's) [36].**

In most position sensing optical detection schemes, an external laser is directed at the tip of the cantilever and the reflected beam is measured using a position-sensitive photodetector typically consisting of four photodetectors placed in four quadrants (Figure 7. 4). While this results in extremely high displacement measurement sensitivity (as

small as $10^{-14}$ m [36]), it also places tight tolerances on the cantilever and measurement setup. For one, alignment of the laser beam to the cantilever tip can be a time consuming task in the laboratory and may prohibit portable sensors. Second, the external laser system implies that the cantilever beam size (area) be large enough for ease of focus and alignment, typically several μm in width and length. However, increasing the cantilever dimensions reduces sensitivity. For example, by shortening the cantilever to length $L' = L_0/2$, the sensitivity goes up by a factor of four. Thus, smaller devices have clear advantages concerning sensitivity. Finally, the external optical measurement setup implies a component-based or multi-chip sensor rather than a monolithically integrated single-chip sensor.

### 7.2.4 MEMS Cantilever Waveguide Resonant Sensors

A cantilever resonant sensor, which integrates an optical detection scheme on chip, can be realized using the end-coupled optical switches presented in Chapter 6. The basic device consists of a 1×1 end-coupled switch with an electrostatically-actuated cantilever input waveguide and a single fixed output waveguide (Figure 7. 5). Light is injected into the input cantilever waveguide on the left and is coupled via the air gap to the output waveguide on the right. The cantilever is free to oscillate. If an actuation voltage is applied between the cantilever and the fixed electrode, then the cantilever tip will be deflected and the optical power coupled to the output waveguide will decrease. Therefore, cantilever position and oscillation frequency information can be measured simply by measuring the modulated coupled output power.

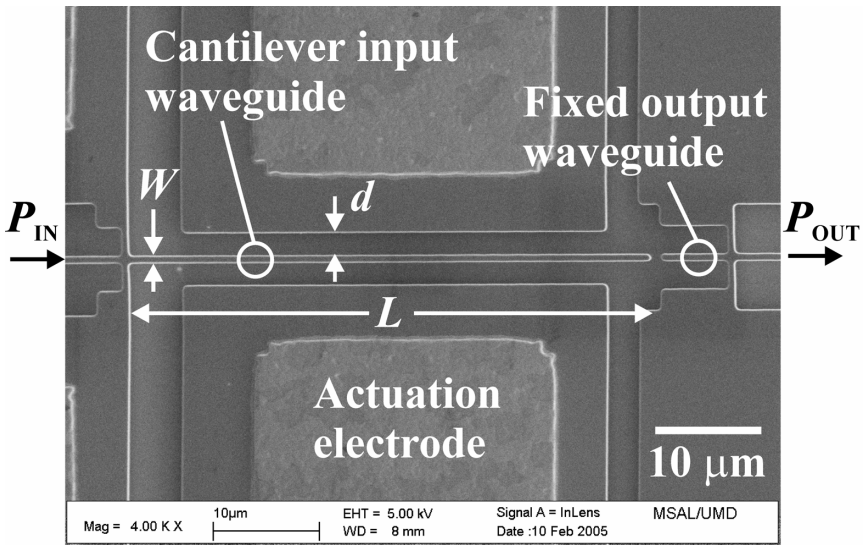


**Figure 7. 5: Electrostatically-actuated cantilever waveguide sensor.**

The advantages of this approach over previous resonating cantilever sensor demonstrations are numerous:

- The device has all the benefits of optical detection, including high sensitivity and low noise. However, in contrast to the external measurement approach in Figure 7. 4, the position measurement for the proposed sensor is located on-chip via integrated waveguides, thereby enabling increased device and system integration;
- The approach results in a self-aligned process. In contrast to the external laser approach, which requires extensive alignment from the user, the input/output waveguides in the sensor shown in Figure 7. 5 are self-aligned during fabrication. This eliminates the need for time consuming alignment prior to measurements;
- The integrated waveguides result in an extremely compact sensor. Therefore, large arrays of devices, such as an artificial 'nose' with the ability to discern many chemical and biological agents simultaneously can be realized. If direct bandgap

materials are used, the device enables monolithic integration of optical detectors and optical sources as well as signal processing circuitry on-chip. This enables true single-chip sensors with low power consumption. In contrast, external optical detection results in increased sensor volume if external components (laser, position-sensitive photodetector, etc.) are included;

- The on-chip electrostatic actuation enables relatively large cantilever displacements (from 10 nm to 1 μm range) to be realized, which results in large optical output signals. This increases the signal-to-noise ratio since thermo-mechanical fluctuations [157] are no longer a significant source of noise in the displacement measurement. In contrast, most previous cantilever sensors utilized external actuation mechanisms, including photothermal actuation [151] or piezoelectric actuation [153] that result in relatively small displacement amplitude.

It should be noted that MEMS integrated waveguide devices have previously been reported in the literature, although not for application to bio-chemical sensing. For example, various electrostatically actuated end-coupled optical waveguide switches have been previously demonstrated [43, 50, 51, 136, 137], as discussed in Chapter 6. Suspended end-coupled optical waveguides have also been used by *Ollier et al.* for vibration sensing [158]. In *Ollier's* work, a silica cantilever input waveguide was fabricated with a proof mass at the end. The cantilever was end-coupled with a fixed output waveguide connected to a multi-mode interference (MMI) coupler. This enabled high sensitivity to vibration and acceleration. Recently, a silicon-on-insulator (SOI) cantilever waveguide was fabricated for sensing (*Wang et al.*, 2005 [159]). *Wang*

demonstrated the fabrication of end-coupled waveguides with gaps as small as 50 nm, but the resonant frequency measurements were performed on optical fiber test structures with features one hundred times larger than their fabricated nano-scale waveguides. I demonstrated and presented true micromechanical resonators with integrated optical waveguides well before the work of *Wang et al.* [160, 161].

The present cantilever sensors also differ significantly from previous work in that the devices are specifically operated in resonant mode with on-chip actuation to enable environmental sensing via mass adsorption, not just external vibration, as is the case in *Ollier's* sensors [158]. Furthermore, compound semiconductors (InP, InGaAs) are used instead of silica [158] or silicon [159]. This enables on-chip integration of optical sources and detectors towards single-chip sensors, a significant advantage over other approaches.

## 7.3 Device Design

The devices studied are as shown in Figure 7. 5. In contrast to the waveguide design of the MEMS evanescent couplers (Chapter 5) and the end-coupled switches (Chapter 6), the present sensors utilize waveguides with a semiconductor core and an air cladding. The waveguide core was 1.5 μm thick with refractive index $n = 3.173$ and a designed intrinsic tensile strain $\varepsilon = 0.039$ % ($In_{0.99}Ga_{0.01}As_{0.01}P_{0.99}$). At the input and output of the chip, the waveguide width was 2.5 μm, which was tapered down to 0.6 – 0.8 μm width at the sensor region.

### 7.3.1 Mechanical Design

The resonant frequency for a cantilever beam oscillating *in-plane* is [36, 162]:

$$f_0 = \frac{1}{2\pi}\sqrt{\frac{3EI}{L^3 c_0 m_0}}, \tag{7.1}$$

where $E = 80$ GPa for InP [7], $L$ is the cantilever beam length, $m_0$ is the cantilever mass, $c_0 = 0.24$ is a constant that describes the effective mass of the cantilever, and $I$ is the area moment of inertia for a rectangular cantilever of width, $w$, and thickness, $t$:

$$I = \frac{tw^3}{12}. \tag{7.2}$$

Calculated resonance frequencies for beam widths $w = 0.6$ μm and $w = 0.8$ μm are shown in Figure 7. 6, assuming oscillation in the direction of the beam width.

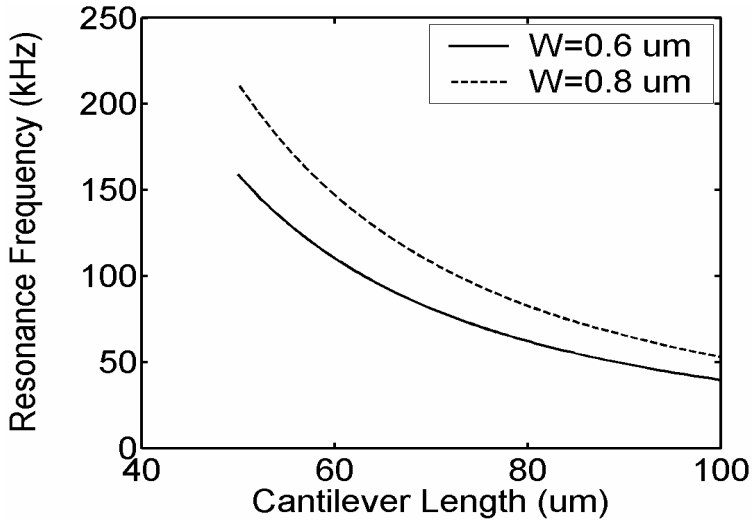


**Figure 7. 6: Calculated resonance frequencies for cantilever sensors.**

Next, the sensitivity of the cantilever sensors is calculated in terms of minimum detectable mass loading (the sensors rely on mass adsorption of bio-chemical agents). Here, it is important to distinguish between added (adsorbed) mass which is distributed uniformly over the cantilever surface versus mass which is confined to the cantilever free end. Assuming a mass, $m_A$, is added to the cantilever, then the shifted resonance frequency is [36, 162]:

$$f_{Shifted} = \frac{1}{2\pi}\sqrt{\frac{3EI}{L^3\left(c_A m_A + c_0 m_0\right)}}, \tag{7.3}$$

where the constant $c_A = c_0 = 0.24$ for an added mass that is uniformly distributed over the cantilever surface and $c_A \to 1$ as the added mass becomes concentrated on the free end of the cantilever. Using Eqns. (7.1) and (7.3), the mass sensitivity is found:

$$\Delta f = f_{Shifted} - f_0 = \frac{1}{2\pi}\sqrt{\frac{3EI}{L^3\left(c_A m_A + c_0 m_0\right)}} - \frac{1}{2\pi}\sqrt{\frac{3EI}{L^3 c_0 m_0}}. \tag{7.4}$$

By using the relation $\frac{1}{\sqrt{1+\Delta}} - 1 \cong -\frac{\Delta}{2}$ (as $\Delta \to 0$), Eqn. (7.4) can be approximated as:

$$\Delta f \approx -\frac{1}{2} f_0 \left(\frac{c_A}{c_0}\right)\left(\frac{m_A}{m_0}\right), \text{ or equivalently} \tag{7.5a}$$

$$\left|\frac{m_A}{\Delta f}\right| \approx 2\left(\frac{m_0}{f_0}\right)\left(\frac{c_0}{c_A}\right) \text{ (sensitivity in g/Hz).} \tag{7.5b}$$

From Eqn. (7.5a) we can make the following observations. First, smaller cantilever mass, $m_0$, results in higher mass sensitivity or larger $\Delta f$. This supports the drive to go towards nanoscale resonant sensors, where the fractional added mass is large. Second, large initial resonant frequency, $f_0$, results in greater sensitivity, provided that the resonator exhibits sufficiently large Q-factor. Large Q-factors enable the precise measurement of the resonant frequency and reduce the measurement uncertainty. As an example of the increased sensitivity obtained by scaling the cantilever in size, consider two cantilevers: one with length $L_0$, the other with length $L_2 = L_0/2$. As illustrated in Table 7. 1, even with the reduction in available sensing area by 50 % (therefore, the added mass is halved), the sensitivity is doubled.

**Table 7. 1: Length scaling of cantilever sensors.**

| **Property** | **Cantilever 1: $L_0$** | **Cantilever 2: $L_2 = L_0/2$** |
|---|---|---|
| Spring constant, $k$ | $k_0$ | $8k_0$ |
| Mass, $m$ | $m_0$ | $m_0/2$ |
| Resonant frequency, $f_{res.}$ | $f_0$ | $4f_0$ |
| Added mass, $\Delta m$ | $m_A$ | $m_A/2$ |
| Sensitivity, $\Delta f \sim f_0 m_A/m_0$ | $f_0 m_A/m_0$ | $2 f_0 m_A/m_0$ |

Finally, in eqn. (7.5b) the ratio $c_A/c_0$ implies that as $c_A \rightarrow 1$, maximum sensitivity is obtained. In other words, if the adsorbed mass is confined to the cantilever free end, then a larger frequency shift is expected compared to an identical adsorbed mass uniformly distributed over the cantilever surface. This last point must be considered carefully, however, since confining the receptor coating to the cantilever tip results in

reduced sensing area and hence reduced total adsorbed mass. Nonetheless, confining the mass loading to an area near the cantilever tip can increase the sensitivity significantly.

The calculated sensitivity for three different cantilever waveguide sensors is listed in Table 7. 2, which indicates that femtogram-level ($10^{-15}$ g) mass detection is possible, provided the resonance frequency can be measured to an accuracy of 1 Hz. Measurement accuracies as low as 100 Hz still result in better than pg sensitivity. The sensitivity for both a uniformly distributed mass ($c_A = 0.24$) and for a hypothetical point mass located on the cantilever free end ($c_A \rightarrow 1$) is calculated using eqn. (7.5b) and a mass density of $\rho = 4.810$ g/m$^3$ for InP [60].

**Table 7. 2: Calculated sensitivity ($\Delta m/\Delta f$) for three cantilever waveguide sensors.**

| $W$ / $L$ (μm/μm) | $f_0$ (kHz) | $m_0$ (g) | Uniform: $\Delta m/\Delta f$ (g/Hz) | Free End: $\Delta m/\Delta f$ (g/Hz) |
|---|---|---|---|---|
| 0.6 / 50 | 159.0 | $2.16\times10^{-10}$ | $2.72\times10^{-15}$ | $0.65\times10^{-15}$ |
| 0.6 / 100 | 39.7 | $4.32\times10^{-10}$ | $21.8\times10^{-15}$ | $5.22\times10^{-15}$ |
| 0.8 / 100 | 54.3 | $5.76\times10^{-10}$ | $21.2\times10^{-15}$ | $5.09\times10^{-15}$ |

### 7.3.2 Optical Design

The final design consideration is the change in optical output power as the input cantilever waveguide is displaced during actuation. As for the switches in Chapter 6, the change in coupled power is obtained via the overlap integral for identical end-coupled waveguides with axial offset [143]:

$$T_{Axial-Offset} = \exp\left[-\left(\frac{t}{w}\right)^2\right], \tag{7.6}$$

where $t$ is the axial offset and $w$ is the Gaussian beam waist. As in Chapter 6, first the Gaussian beam waist (fundamental mode, $m$ = 0) is simulated using Femlab software [163]. The beam waists are summarized in Table 7. 3 ($n_{CORE}$=3.173, $n_{CLAD}$=air).

**Table 7. 3: Summary of Femlab mode simulation ($m$ = 0): a) 0.6 μm wide (top), b) 0.8 μm wide (bottom). For both waveguides: height=1.5 μm, $n_{Core}$ = 3.173.**

| Mode | $w$ (μm) | $2w_X$ (μm) | $2w_Y$ (μm) |
|---|---|---|---|
| TE | 0.6 | 0.473 | 1.154 |
| TM | 0.6 | 0.558 | 1.267 |

| Mode | $w$ (μm) | $2w_X$ (μm) | $2w_Y$ (μm) |
|---|---|---|---|
| TE | 0.8 | 0.621 | 1.143 |
| TM | 0.8 | 0.738 | 1.260 |

Because the cantilever input waveguides are only actuated in the $x$-direction (i.e. along the waveguide width), only the beam waist, $w_X$, must be considered, as is highlighted in Table 7. 3. Using this beam waist, the change in coupled output power vs. cantilever input waveguide displacement is calculated using eqn. (7.6). Figure 7. 7 indicates that displacements of a few tens of nanometers result in changes in coupled output power of a few percent. Depending on the total coupled power, displacements of the order of tens of nanometers can therefore be detected with the end-coupled

waveguide sensors. Furthermore, the results also indicate that narrower waveguides (width $w = 0.6$ μm) are more sensitive to displacement than wider waveguides ($w = 0.8$ μm), as expected. Therefore, even higher displacement sensitivity is expected for true nanoscale cantilever waveguides. It is important to note that the calculation assumes that the air gap between the end-coupled waveguide facets is zero (Figure 7. 7) so that the calculation neglects beam divergence. Beam divergence (Chapter 6) causes the beam waist to expand with increasing air gap and results in decreased displacement sensitivity compared to the results in Figure 7. 7. Therefore, the air gap between the end-coupled waveguides should be made as small as possible.

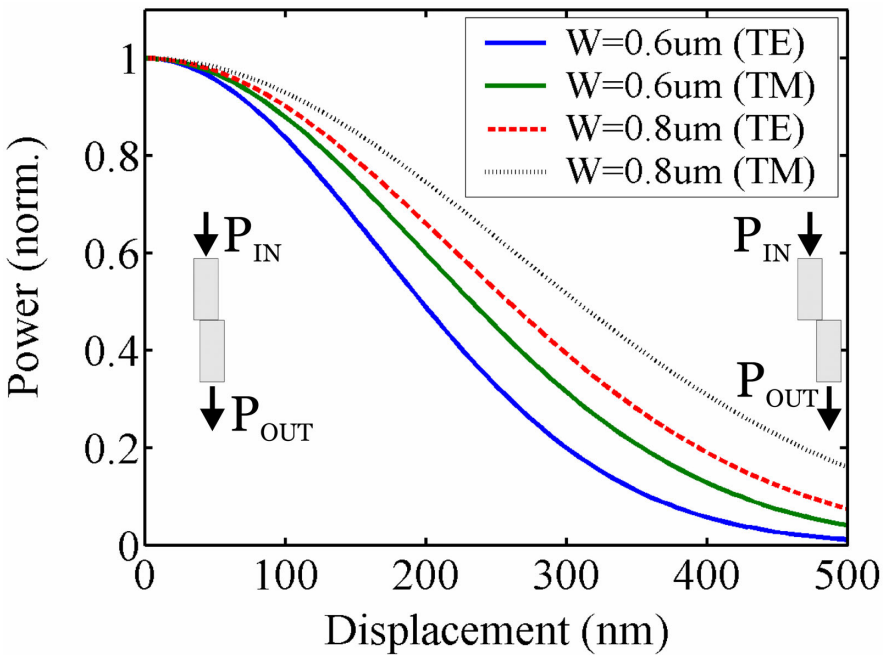


**Figure 7. 7: Calculated optical power vs. cantilever waveguide displacement, assuming zero gap between waveguide facets.**

## 7.4 Experimental Results

Characterization of the resonant cantilever sensors was performed using the same experimental setup as was used for the MEMS couplers (Chapter 5) and the end-coupled switches (Chapter 6). For these experiments, however, a larger objective (50x) was used to image the sample during actuation due to the small cantilever dimensions. For all experiments, TE-polarized light was used with $\lambda \sim 1550$ nm.

Several techniques can be used to obtain the cantilever resonance frequency by measuring the modulated coupled output power. The first technique is a frequency domain measurement and the second is a time domain measurement. Both are equivalent and enable extraction of the resonance frequency.

### 7.4.1 Technique 1: Frequency Sweep

In the first technique, a sinusoidal actuation voltage is applied between the cantilever and one of the side electrodes. This causes the cantilever to oscillate in the direction of the arrows in Figure 7. 8, which in turn results in a modulation of the coupled power to the output waveguide. At mechanical resonance, the cantilever will experience maximum displacement. Therefore, mechanical resonance can be measured by monitoring the change in coupled output power as the sinusoidal actuation voltage is swept over a range of frequencies, i.e. $\Delta P = P_{\text{Max.}} - P_{\text{Min.}}$.

A typical measurement is shown in Figure 7. 9 for a cantilever of width, $w = 0.6$ μm and length $L = 50$ μm (CB-3). Measurements were taken "by hand" using a 6 Vp-p sine wave actuation signal. During the measurements, the frequency was manually increased in steps of 1 kHz and the change in coupled power was recorded.

The results are plotted and a Lorentzian lineshape function is fitted to the data using SigmaPlot software [164] in order to obtain the resonant frequency:

$$A(f, f_0, FWHM, a, c) = c + \frac{a}{1 + \left( \frac{f - f_0}{FWHM / 2} \right)^2}, \tag{7.7}$$

where $f_0$ is the center point, *FWHM* is the Lorentzian width, and $c$ and $a$ are constants.

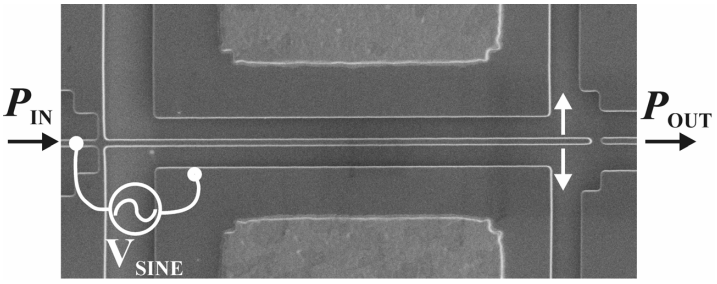


**Figure 7. 8: Frequency sweep with sinusoidal actuation voltage.**

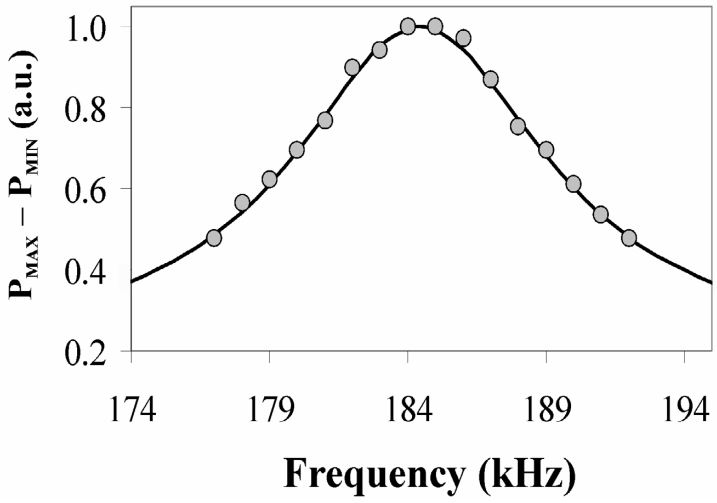


**Figure 7. 9: Frequency sweep with Lorentzian curve fit ($V_{Sine}$ = 6 Vp-p).**

As the cantilever goes through resonance, there is also a distinct 180° phase shift between the sinusoidal actuation signal and the optical output. Figure 7. 10 compares the phase of the sinusoidal actuation voltage with the measured optical output signal. For actuation frequencies much less than the mechanical resonance frequency ($f << f_0$), there is a 180° phase difference between the two (Figure 7. 10a). This is to be expected, since at low frequencies an actuation voltage will cause the cantilever to deflect, thereby decreasing the coupled output power. In other words, there is a π (180°) phase difference between the driving signal and the measured output. For actuation frequencies much greater than the resonance frequency ($f >> f_0$), the cantilever motion undergoes a π-phase shift, so that the driving signal and the optical output are now in phase (e.g. 0° phase difference, Figure 7. 10c). Finally, at resonance ($f \approx f_0$) there is a π/2-phase shift (Figure 7. 10b). This phase shift is characteristic of systems going through a resonance condition and has been utilized to detect changes in resonant frequency [156].

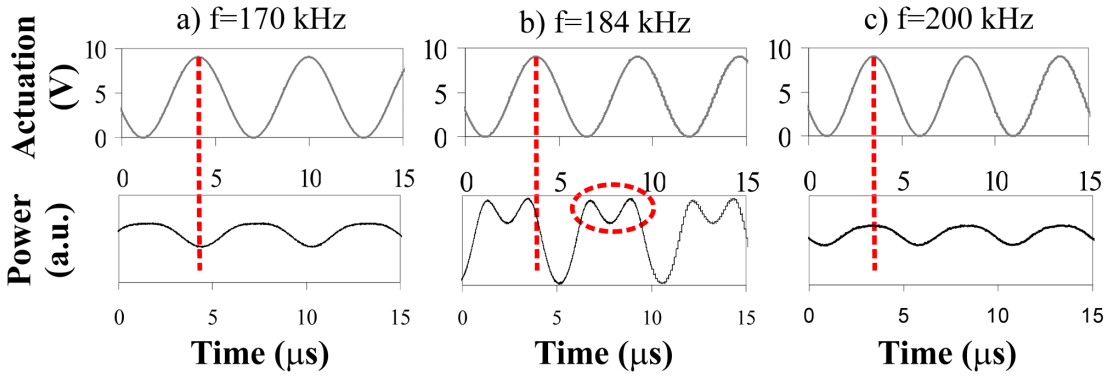


**Figure 7. 10: Cantilever phase shift (vertical dashed lines): a) $f < f_0$, 180° phase shift, $\Delta\phi$, between actuation and optical power, b) $f \approx f_0$, $\Delta\phi$=90°, C) $f > f_0$, $\Delta\phi$=0°.**

One last observation concerning the phase measurement is the "dip" seen in Figure 7. 10b. As the cantilever is excited to resonance, it will undergo maximum displacement. During the return trip, the kinetic energy of the cantilever is large enough that it overshoots its original rest position so that the coupled power reaches a maximum and then decreases slightly as it overshoots, causing the characteristic dip. The larger displacement of the cantilever at resonance can also be ascertained by the large change in optical power (Figure 7. 10b) compared to the off-resonance plots.

### 7.4.2 Technique 2: Unit Step and Impulse Response

The technique of section 7.4.1 is a frequency domain measurement. The frequency response of the sensor can also be obtained by performing a time domain measurement, similar to the temporal measurements performed on the end-coupled switches in Chapter 6. Instead of applying a sinusoidal actuation voltage to the cantilever, a square wave actuation signal is applied (Figure 7. 11). This results in a characteristic 'ringing' in the optical output signal, as shown in Figure 7. 12 ($w$ = 0.6 μm, $L$ = 50 μm). By looking at the ringing period, $T$, and the characteristic decay time constant, τ (Figure 7. 12c), the *damped* resonance frequency is obtained using $f_{\text{Damped}} = 1/T$. The natural resonance frequency and the approximate frequency response are then given by [165], where $Q_{\text{Mechanical}}$ is the mechanical Q-factor:

$$f_{Damped} = f_0 \sqrt{1 - \frac{1}{4Q_{Mechanical}^{\ 2}}} \text{ and} \tag{7.8}$$

$$A \propto 1 \Big/ \sqrt{\left(f_0^{\ 2} - f^2\right)^2 + \left(f/\tau\right)^2} \ . \tag{7.9}$$

Equation (7.8) suggests that even small Q-factors ($Q_{Mech.}$=10) result in almost identical damped and natural resonant frequencies (within 0.13%). Furthermore, in practice it makes little difference which frequency we use for our sensors; measurement of both $f_{Damped}$ and $f_0$ enable resonant sensors based on mass loading to be realized.

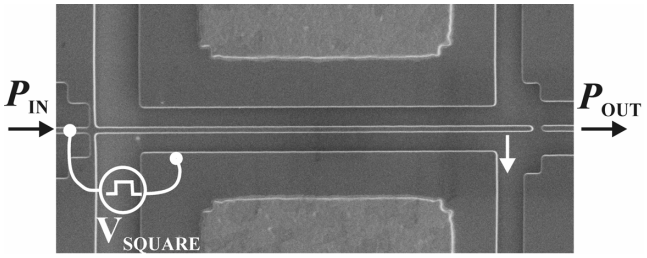


**Figure 7. 11: 'Ringing' measurement with square wave actuation voltage.**

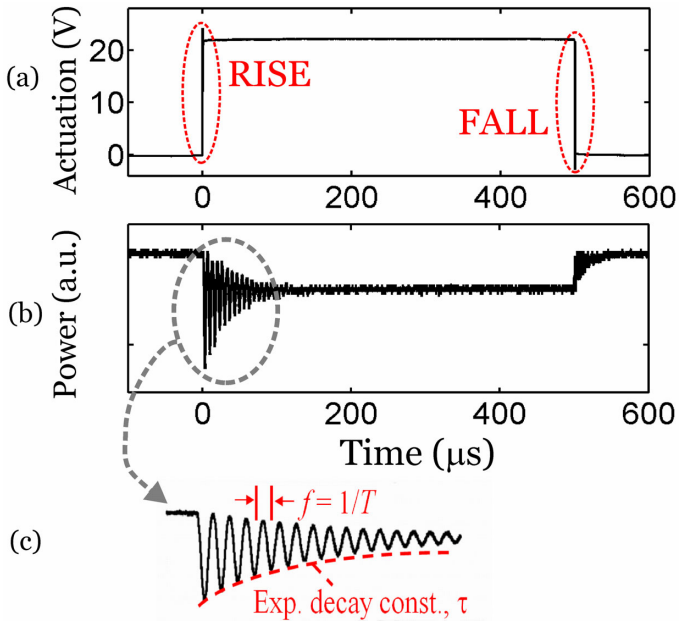


**Figure 7. 12: a) Square wave actuation signal, b) optical output 'ringing,' c) ringing period, *T*, and decay time constant, τ (RISE cycle).**

Alternatively, the ringing data can be processed by performing a Fourier analysis. First, the data is separated into two files: the RISE cycle ($t < 300$ μs in Figure 7. 12) and the FALL cycle ($t > 300$ μs). Next, the Fast-Fourier-Transform (FFT) of each data file is computed using MATLAB software (see Appendix F). This data is the unit step response [166] and gives a good indication of the frequency response of the cantilever beam (Figure 7. 13a). However, it also results in a large DC or low-frequency component. In order to obtain the true frequency response, and hence resonance frequency, the impulse response must be obtained. The impulse response is simply the derivative of the unit step response, which can be computed in the frequency domain by frequency multiplication [166]:

$$\text{FFT (impulse)} = j\omega \cdot \text{FFT (unit step)} \tag{7.10}$$

The resulting impulse response is plotted in Figure 7. 13b, along with a Lorentzian curve fit to obtain the resonance frequency and effective Q-factor (Lorentzian curve fit: Rsq. = 0.998). The impulse response results in $f_0 = 184.969$ kHz (FALL cycle, $V_{Square} = 9.6$ Vp-p). It does not exhibit DC components in the frequency response. The ringing method finds the resonance frequency from the entire spectrum without having to manually narrow down an appropriate frequency range over which to find resonance. This is a significant advantage over the frequency sweep method presented in section 7.4.1, in which an approximate frequency range must be known.

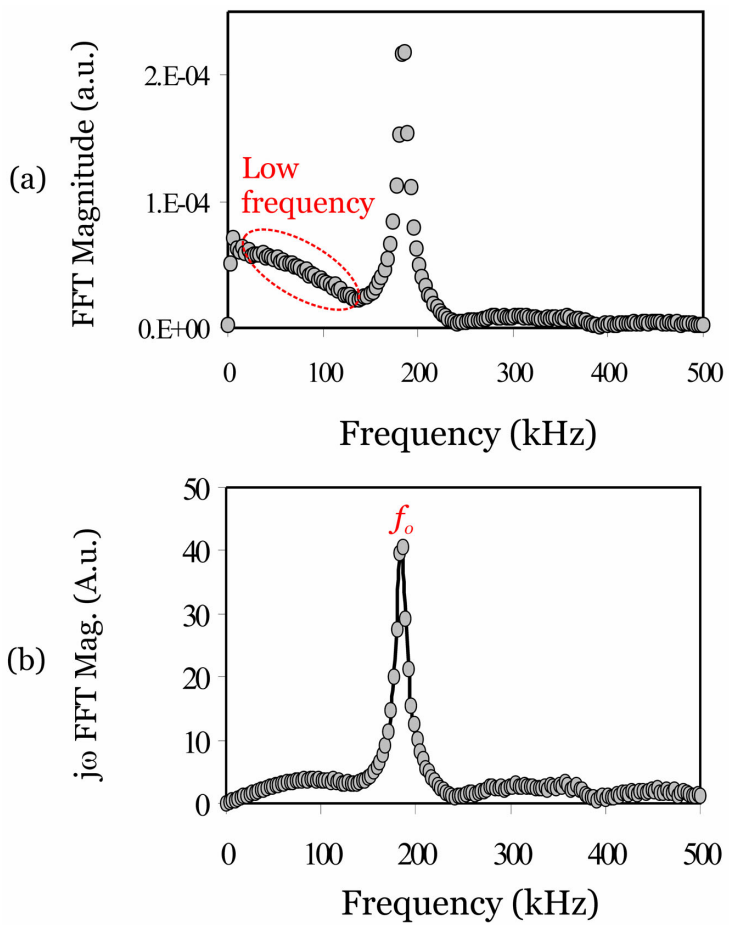


**Figure 7. 13: a) Magnitude FFT, b) Magnitude jω·FFT and Lorentzian curve fit. Data taken from FALL cycle (CB-3, $V_{DC}$ = 10 Vp-p), Lorentzian curve fit for f = 146 – 220 kHz to obtain resonant frequency, $f_0$ (Rsq. = 0.998).**

Finally, a word of caution must be said regarding the Q-factor. The Q-factor is obtained from the FWHM of the Lorentzian curve fit to |jw·FFT|. However, this Q-factor is actually a compound term and incorporates both the mechanical Q-factor (air damping) as well as the optical response to cantilever displacements (as discussed in section 7.3 and Figure 7. 7). It is therefore an *effective* Q-factor for the entire system.

The reader should be aware that the resonant peak obtained from the FFT analysis is a damped resonant frequency. It is related to the natural frequency by the mechanical Q-factor of the cantilever, similar to eqn. (7.8) [167]:

$$f_{FFT,Damped} = f_0 \sqrt{1 - \frac{1}{2Q_{Mechanical}^{\ 2}}} \,. \tag{7.11}$$

However, even for small Q-factors $f_{FFT,Damped}$ and $f_0$ differ by only a small fraction.

### 7.4.3 Proof-of-Concept Experiment: Mass Sensing

In the previous sections, the sensor design and experimental techniques were developed. Next, several devices were tested and their resonant frequencies were extracted. In these early experiments, the resonance frequency was extracted by simply measuring the ringing period, $T$, and the decay time constant, $\tau$ (Figure 7. 12c) and then plotting the resonance spectrum using eqn. (7.9). FFT analysis was used for subsequent experiments for higher accuracy, but does not affect the results of the present experiments significantly. The tested device geometries as well as the calculated and measured resonance frequencies are summarized in Table 7. 4 and the frequency response is plotted in Figure 7. 14 by fitting $T$ and $\tau$ to a Lorentzian lineshape function [168].

**Table 7. 4: Resonance frequencies for three cantilever waveguide sensors.**

| Device | W / L (μm/μm) | Measured $f_0$ (kHz) | Calculated $f_0$ (kHz) |
|---|---|---|---|
| CB-1 | 0.6 / 100 | 41.3 | 39.7 |
| CB-2 | 0.8 / 100 | 54.3 | 53.0 |
| CB-3 | 0.6 / 50 | 168.8 | 159.0 |

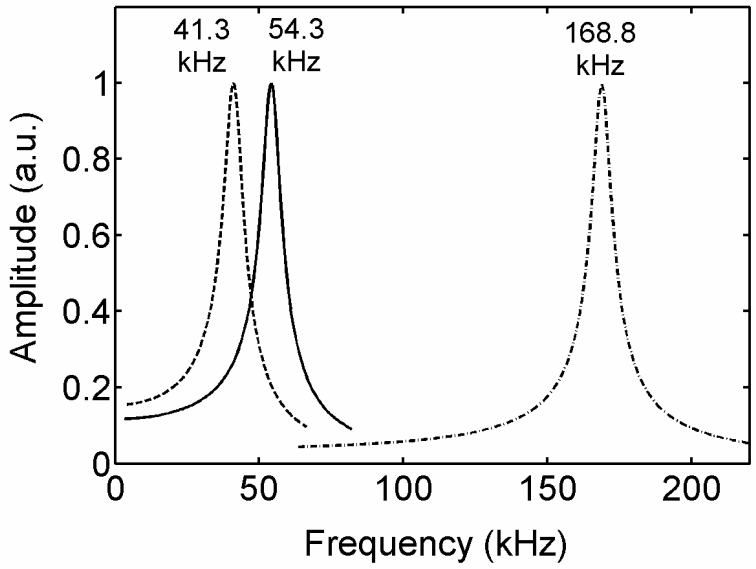


**Figure 7. 14: Measured resonance frequencies for three cantilever sensors from ringing technique and extracted *T* and τ and eqn. (7.9).**

The experiments indicate that the optical ringing technique using end-coupled cantilever waveguides and subsequent FFT analysis are a viable method for obtaining mechanical resonant frequencies. The next step toward developing environmental sensors is to measure resonance frequency shifts in response to changes in cantilever mass. This experiment was performed using device CB-2 ($w$ = 0.8 μm, $L$ = 100 μm). A focused ion beam (FIB) system was used to mill a small mass from the cantilever beam

tip (Figure 7. 15). Care was taken not to mill the waveguide facet so as to minimize any scattering losses. Milling was confined to a 10–15 μm long region at the tip of the 100 μm long cantilever. It should be emphasized that the curvature of the cantilever is the result of an intrinsic strain gradient [7, 8] and not the result of FIB processing. The resonant frequency was re-measured using the ringing technique, resulting in $\Delta f = +4.6$ kHz ($f_0 = 54.3$ kHz and $f_{0,\,\mathrm{FIB}} = 58.9$ kHz, Figure 7. 16).

Several observations concerning the proof-of-concept experiment are now made. In the present experiment the resonance frequency is shifted higher since mass was removed from the cantilever. However, in MEMS resonant sensors mass is typically adsorbed so that there is a downward frequency shift. Second, using eqn. (7.5) the change in mass resulting in $\Delta f = +4.6$ kHz is calculated as $\Delta m = 24.6$ pg ($2.46\times10^{-11}$ g) or 4.27 % of the original cantilever mass, $m_0$. This relatively large mass is much greater than the mass shift commonly encountered in sensing applications. However, the absolute sensitivity can be calculated as $\Delta m/\Delta f = 5.1$ fg/Hz. To place this mass sensitivity in perspective, the mass of a single *E. coli* cell is approximately 600 fg [150], which would result in $\Delta f = 118$ Hz. Such a frequency shift is easily within the measurement sensitivity of the present devices (see section 7.4.6). Therefore, while this proof-of-concept experiment resulted in a large resonance frequency shift due to the large removed mass, the experiment proves the feasibility of mass-based sensors using an on-chip optical measurement technique using end-coupled MEMS-actuated waveguides. Calculations also show that high sensitivity is possible, competitive with previous sensors [150-155].

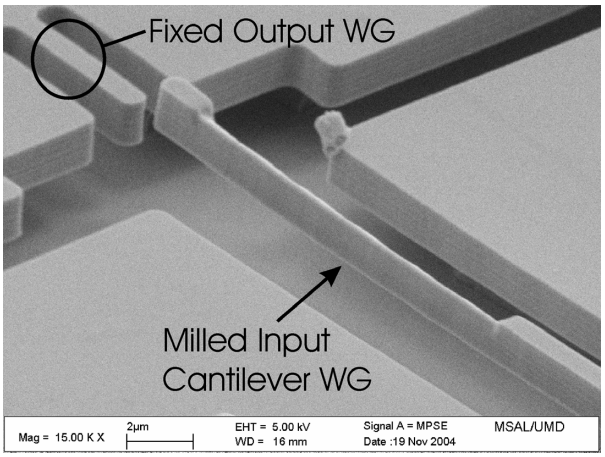


**Figure 7. 15: Detail of FIB milled cantilever sensor.**

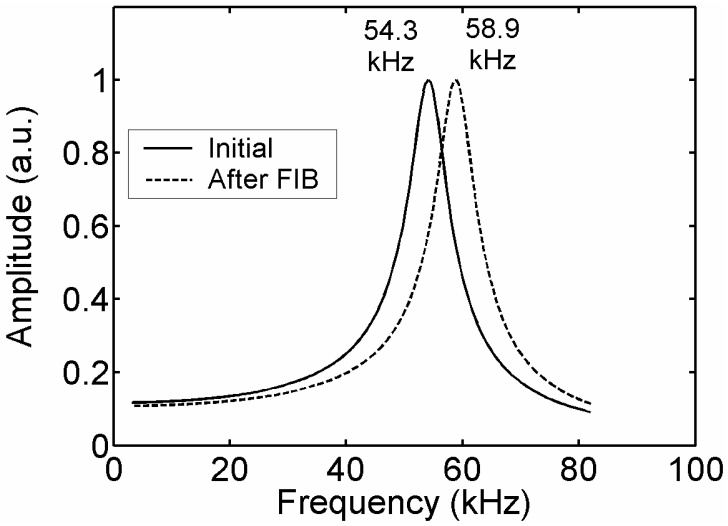


**Figure 7. 16: Measured resonance frequency shift after FIB milling of cantilever.**

### 7.4.4 Electrostatic Tuning

Many previously reported MEMS and NEMS cantilever resonator sensors utilize external excitation mechanisms, including photothermal [151], thermo-mechanical [150], and piezo-actuation [153]. An advantage of the electrostatically-actuated cantilevers in this work is that the actuation mechanism is located on-chip. Furthermore, the

displacements can be increased simply by increasing the actuation voltage. This results in a higher signal-to-noise (SNR) ratio, since thermo-mechanical and ambient noise are no longer a significant source of cantilever motion.

Care must be exercised, however, when using electrostatic actuation to measure resonance frequencies, especially when performing the ringing measurements during the RISE cycle (as in Figure 7. 12). The electrostatic actuator formed by the cantilever and the actuation electrode (Figure 7. 5) forms a parallel-plate capacitor that results in tuning of the resonant frequency. This effect was first reported and modeled by *Nathanson et al.* [169], although others have reported similar effects and models to explain this tuning behavior [170]. The total energy of the capacitor/cantilever resonator system is [170]:

$$E_{total} = E_{Kinetic} + E_{Capacitor}, \text{ or} \tag{7.12a}$$

$$\frac{1}{2}k_0(\Delta x)^2 = \frac{1}{2}k_{Effective}(\Delta x)^2 + \frac{1}{2}CV^2, \tag{7.12b}$$

where $\Delta x$ is the cantilever displacement, $k_0$ is the cantilever spring constant (giving the *calculated* resonance frequency), $k_{\text{Effective}}$ is the effective cantilever spring constant (giving the *measured* resonance frequency), and $C = \varepsilon_0 A/gap$ is the capacitance of the electrostatic actuator ($A$ is the area, $V$ is the applied voltage). The energy in eqn. (7.12) can then be used to give the measured resonance frequency, $f_{\text{Tuned}}$, assuming that the 'ringing' approach is used to excite the cantilever to resonance [171]:

$$f_{Tuned}(V) = f_0\sqrt{1 - \frac{\varepsilon A/(gap - \Delta x)^3}{k_0}V^2}, \tag{7.13}$$

where ε is the free space permittivity, $A$ is the cantilever sidewall area ($A = L \times t$), *gap* is the initial cantilever-electrode separation, $\Delta x$ is the cantilever displacement, $k_0$ is the cantilever spring constant, and $V$ is the applied DC voltage (square wave amplitude).

In order to verify that electrostatic tuning was taking place, the resonance frequency of a cantilever of type CB-3 ($W$ = 0.6 μm, $L$ = 50 μm) was measured for square wave actuation signals ranging from $V$ = 10 $V_{p\text{-}p}$ to 20 $V_{p\text{-}p}$ in steps of 2 V. The resonance frequency was extracted from the damped sinusoid optical ringing data (Figure 7. 12c) by 1) taking the FFT using MATLAB, 2) multiplying the FFT by jω, and then 3) performing a Lorentzian curve fit, as described in section7.4.2. The tuning data is shown in Figure 7. 17ab, including the Lorentzian curve fit (Figure 7. 17a) and the extracted resonance frequency as a function of voltage (Figure 7. 17b). The results clearly illustrate electrostatic tuning, as predicted by eqn. (7.12).

In Figure 7. 17b, the experimental data is compared with the predicted electrostatic tuning using eqn. (7.12). For the theory curve, a calculated spring constant of $k$ = 0.0957 N/m, and estimated values of *gap* = 2.3 μm, and displacement $\Delta x$ = 100 nm were used. The theory is in general agreement with experiment, indicating that electrostatic tuning is indeed the cause of the frequency shift. Some of the discrepancy between the experiment and model is the result of combined tuning and actuation voltage $V_{DC}$. That is, a single DC (square-wave) actuation voltage is used for both tuning and oscillation (ringing). The result of the DC tuning voltage is that the *gap* in eqn. (7.13) is not a constant, but decreases with increasing $V_{DC}$. In contrast, the theory curve in Figure 7. 17b assumes a constant *gap* (and hence capacitance, $C$) and ringing displacement, $\Delta x$, which are not affected by the DC actuation voltage.

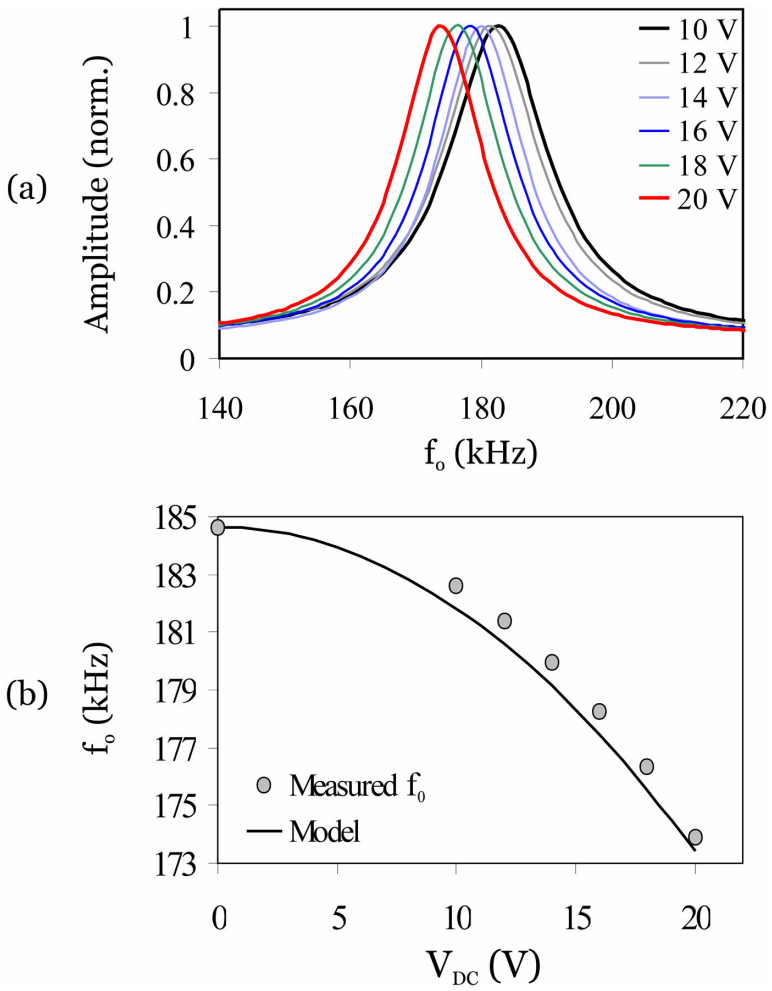


**Figure 7. 17: Electrostatic tuning: a) jω·FFT magnitude, b) resonant frequency.**

### 7.4.5 Frequency Doubling

In the previous section, the resonance frequency when measured during the RISE cycle (Figure 7. 12) was tuned via the energy stored in the electrostatic actuator (capacitor), according to eqn. (7.11) and eqn. (7.13). If the ringing measurement is performed on the FALL cycle, there is no energy stored in the electrostatic actuator ($V = 0$) and the resonant frequency will remain constant. However, there is another consideration and that is frequency doubling.

Frequency doubling is illustrated in Figure 7. 18. A single mechanical oscillation period during a FALL cycle is shown in Figure 7. 18a. The optical coupled power corresponding to a single mechanical oscillation period indicates two optical high-low cycles resulting from the initial alignment of input and output waveguides at zero applied voltage. Therefore, a single mechanical oscillation period results in two points in time at which input and output waveguides are fully aligned so that maximum optical power is coupled. This results in an effective frequency doubling so that $f_{FALL} = f_{DOUBLED} = 1/2T$, where $T$ is the period (Figure 7. 19). The resonance frequency for the RISE cycle is simply $f_{RISE} = 1/T$. For a cantilever sensor (CB-3: $L$ = 50 μm, $w$ = 0.6 μm, $V_{Square}$ = 22.1 $V_{p-p}$) the resonance frequencies are $f_{RISE}$ = 149 kHz ($T_{RISE}$ = 6.70 μs) and $f_{FALL}$ = 168 kHz ($T_{FALL}$ = 2.97 μs). The resonance frequency, $f_{FALL}$, is different from the resonance frequency measured on a cantilever CB-3 on a different chip ($f_0$ = 184 kHz at $V$ = 0 in section 7.4.4) due to lithography and processing variations. For CB-3 with nominal width of $w$ = 600 nm, a 9 % reduction in width (or ~ 55 nm) would account for this resonance frequency discrepancy.

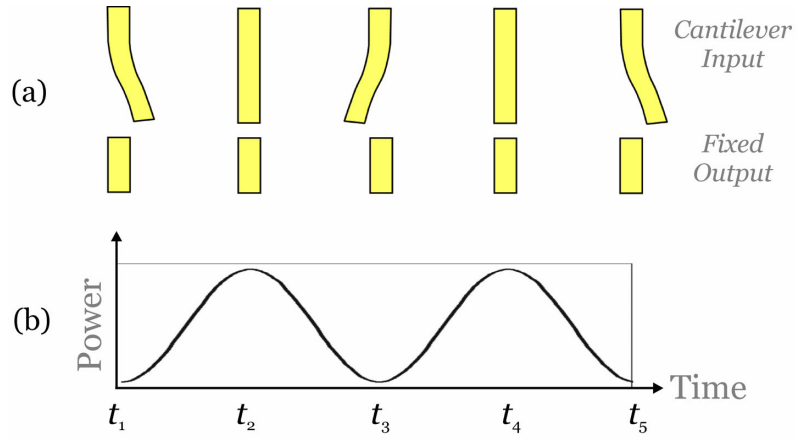


**Figure 7. 18: a) Mechanical oscillation of input cantilever waveguide (one period), b) optical coupled output power (two high-low cycles).**

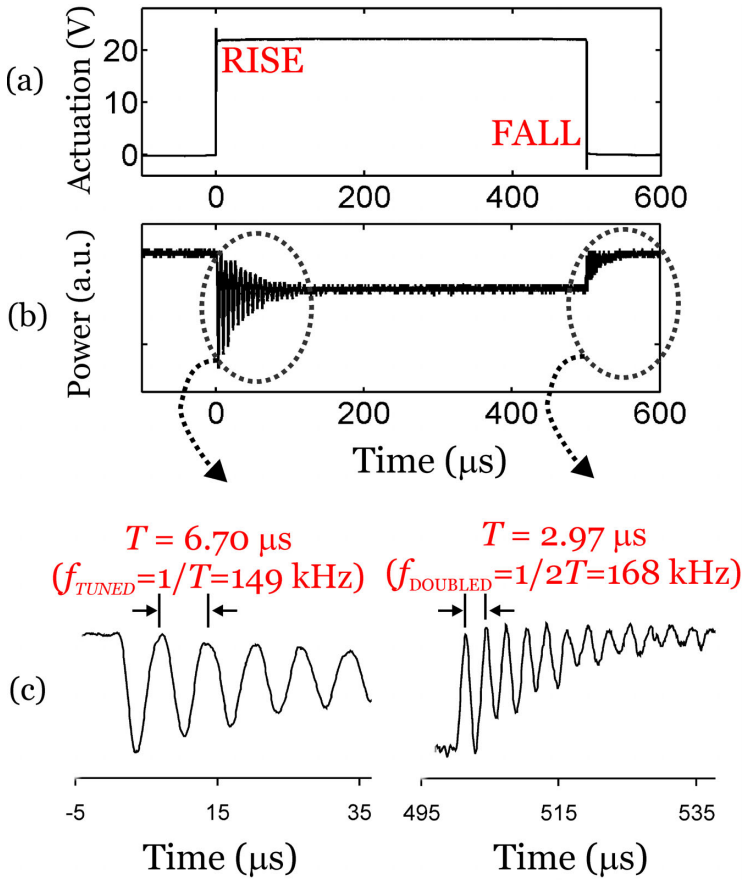


**Figure 7. 19: Frequency doubling: a) actuation, b) optical ringing, c) electrostatic tuning (RISE cycle, left) and frequency doubling (FALL cycle, right).**

A few additional observations can be made regarding the frequency doubling effect. First, frequency doubling will only take place if the cantilever is actuated with large enough displacement that it overshoots its original rest ($V$ = 0) position during oscillation (ringing). For example, Figure 7. 10b shows a characteristic 'dip' in the coupled optical power at resonance ($f$ ~ 184 kHz). This dip results from the cantilever overshooting its rest position during mechanical resonance so that the optical power actually decreases at maximum displacement, similar to Figure 7. 18 at time $t_3$. As the cantilever continues its oscillation, the optical coupled power in Figure 7. 10b initially increases before continuing to decrease, similar to times $t_4$ and $t_5$ in Figure 7. 18.

Another observation is that frequency doubling does not, in general, occur during the RISE cycle. The reason is that the DC actuation voltage causes the cantilever to oscillate about a point offset from the center such that it never overshoots its rest ($V$ = 0) position, i.e. between points $t_2$ and $t_3$ in Figure 7. 18. Therefore, there is generally no dip in the optical output (Figure 7. 10b) nor a frequency doubling effect during the RISE portion of the measurement.

Finally, although frequency doubling is a concern, as long as the doubling is taken into account, the FALL cycle measurements are extremely accurate. That is, there is no electrostatic tuning involved, resulting in very repeatable measurements. Therefore, if sensors based on observing resonance shifts are developed, the FALL cycle represents the more accurate measurement compared to the RISE cycle.

### 7.4.6 Repeatability

Resonance frequencies obtained using the FALL cycle ringing measurement are very repeatable. The FALL cycle does not result in any energy stored in the electrostatic actuator, so the cantilever spring constant and the effective spring constant in eqn. (7.9) are identical. Equivalently, the 'tuned' resonance frequency in eqn. (7.10) is simply $f_0$. The extracted resonance frequency for a cantilever sensor of type CB-3 is shown in Figure 7. 20ab for various actuation voltages (FALL cycle). The average resonance frequency was $f_0$ = 184.633 kHz with a standard deviation $\sigma$ = 55.7 Hz (Figure 7. 20b; Table 7. 5). Therefore, electrostatic tuning is not an issue.

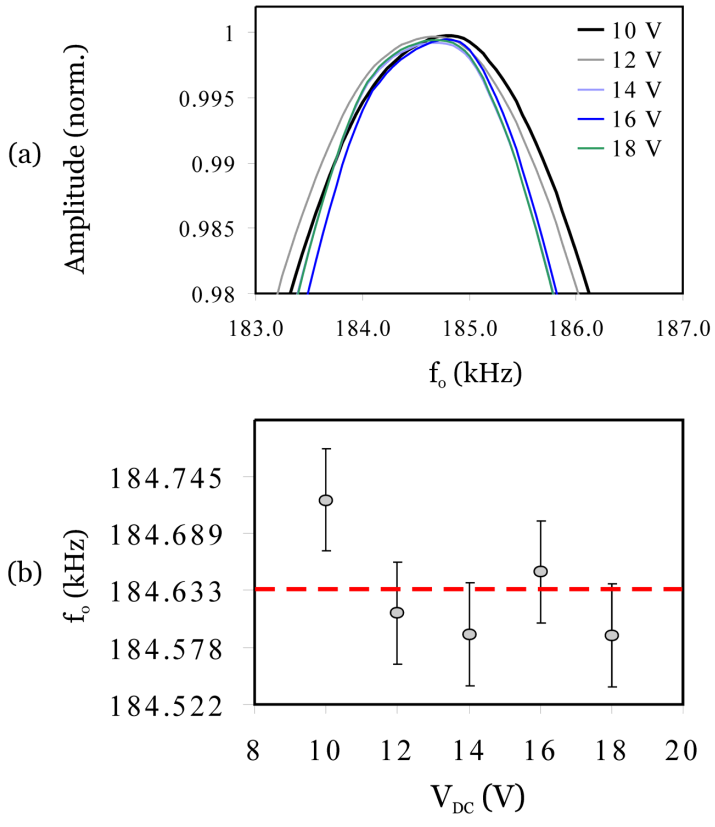


**Figure 7. 20: a) FALL cycle resonance curves for FALL cycle for different $V_{DC}$, b) extracted resonance frequencies as a function of actuation voltage.**

**Table 7. 5: Summary of FALL cycle resonance frequency for CB-3.**

| $V_{DC}$ (V) | $f_0$ (kHz) | $Q_{Effective}$ |
|---|---|---|
| 10 | 184.722 | 9.76 |
| 12 | 184.611 | 9.68 |
| 14 | 184.590 | 11.43 |
| 16 | 184.651 | 11.43 |
| 18 | 184.590 | 11.804 |

The measurements were also repeated multiple times for the same actuation voltage (CB-3, V = 9.6 $V_{p-p}$, FALL cycle). The results are shown in Figure 7. 21 and indicate an average resonance frequency of $f_0$ = 184.969 kHz with a standard deviation of $\sigma$ = 50 Hz over five measurements. If only the first three measurements are considered, then $f_0$ = 184.961 kHz and $\sigma$ = 17 Hz. This shows the high repeatability of the ringing measurements. Finally, comparing the average resonance frequency in Figure 7. 20 (Table 7. 5) with the average in Figure 7. 21, we note a relatively large discrepancy ($f_0$ = 184.633 kHz vs. $f_0$ = 184.969 kHz). The reason is the measurement environment (humidity, temperature, and sample exposure time to environment). The measurements in Figure 7. 21 were taken weeks after those in Figure 7. 20 and the discrepancy between the resonance frequencies is likely a reflection of the different environmental conditions (especially moisture and humidity) and inadvertent mass loading during the experiments. Nonetheless, the results show that for uniform conditions the resonance frequency measurements are repeatable; environmental factors, however, are important in determining the accuracy of resonant sensors.

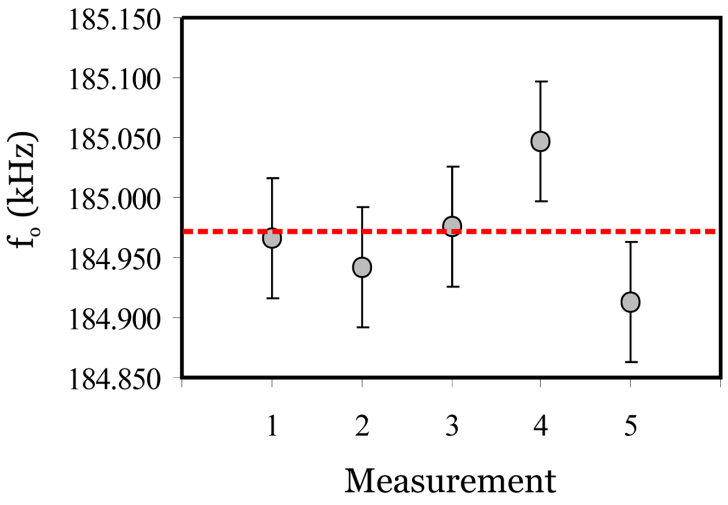


**Figure 7. 21: Repeatability measurements for $V_{DC}$ = 9.6 V (FALL cycle).**

## 7.5 Discussion: Sensitivity Limits

Although the effective Q-factors of the present devices are relatively low, typically $Q$ = 10 – 30 (in air), the minimum detectable frequency shift is significantly smaller than might be expected. For example, $Q$ = 10 and $f_0$ = 184 kHz result in FWHM = $f_0$ / $Q$ = 18.4 kHz (FWHM = "full width at half maximum"). However, the minimum detectable resonance shift is roughly one standard deviation, or $\Delta f_{MIN}$ = 50 Hz, which is significantly smaller than the FWHM. In other words, if many measurements are made, then the average measurement error would be, roughly, one standard deviation. This standard deviation can thus be regarded as the true sensitivity limit of the sensor, which is a little larger than what is calculated (for example, Table 7. 2). Several other considerations in the development of higher-sensitivity resonant sensors will now be discussed, including design as well as fundamental limitations.

### 7.5.1 Displacement Sensitivity of Optical Response

The sensitivity of the resonating cantilever sensors can be improved by considering the optical response in Figure 7. 7. Due to the Gaussian beam shape, the coupled power is a highly nonlinear function of displacement. The maximum displacement sensitivity is the point at which the derivative of Figure 7. 7 with respect to displacement is maximum. The calculated sensitivity for a 0.6 μm wide cantilever sensor is shown in Figure 7. 22, assuming a Gaussian beam waist $w_X = 0.631$ μm at $\lambda = 1550$ nm (TE-polarization) and zero axial gap between the waveguides. The results indicate that the device is most sensitive to cantilever displacement at a partial displacement of $\Delta x_0 \approx 230$ nm (Figure 7. 22b). Therefore, maximum sensitivity is possible for devices with initial axial offset, $\Delta x_0$, and oscillation occurring about $\Delta x_0$.

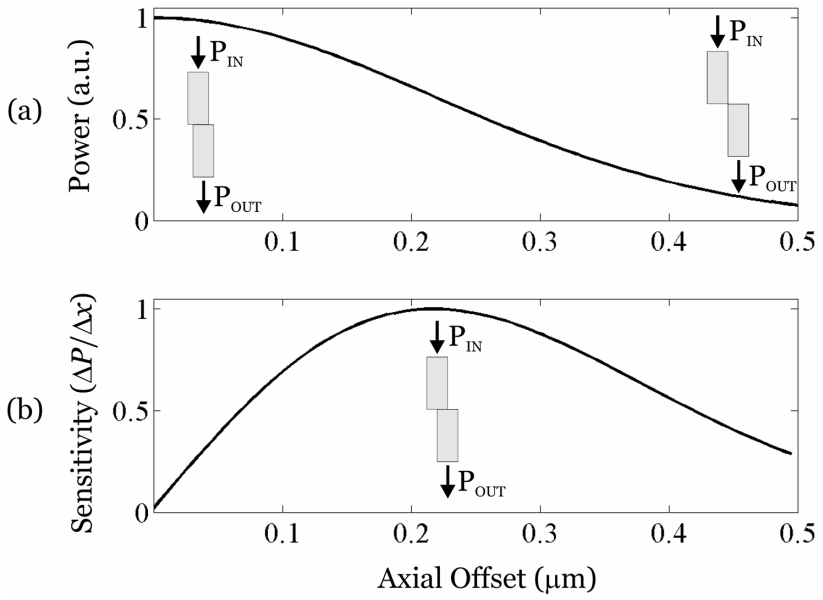


**Figure 7. 22: a) Calculated output power vs. input cantilever displacement, b) sensitivity dP/dx (normalized). Beam waist $w_X = 0.631$ μm, $\lambda = 1550$ nm (TE).**

It should be noted that the results in Figure 7. 22 assume a zero axial gap. In practice, however, a zero axial gap is not possible in real devices, where lithography and etch limitations place a minimum gap limit of a hundred nanometers or more. The sensors had designed gaps of 775 nm, which result in significant beam divergence. This divergence in turn results in a larger Gaussian beam waist $w > w_X$ once the beam traverses the air gap, which reduces the sensitivity compared to Figure 7. 22.

The coupled power as a function of displacement was measured for sensor CB-3 (Figure 7. 23). The waveguide is 0.6 μm wide and has an actuation gap of 2.2 μm. According to Figure 7. 7, a displacement of only 300 nm should result in a drop in coupled power down to 20 %, which is in contrast to the measurements that show a minimum coupled power of 80 %. Although the exact cantilever displacement in Figure 7. 23 is not known, it is certainly greater than 300 nm (the calculated pull-in voltage is $V_{PI,\ Calculated} = 19.7$ V at which the theoretical displacement should be $\Delta x = gap/3 = 733$ nm; note, however, that the device did not pull-in at $V = 22.1$ V). Therefore, the results indicate decreased sensitivity due to beam divergence across the air gap. Maximum sensitivity is obtained for minimum air gap so that beam divergence is avoided. By using other lithographic means, such as electron-beam lithography, smaller air gap definition should be possible, thereby maximizing cantilever displacement measurement sensitivity.

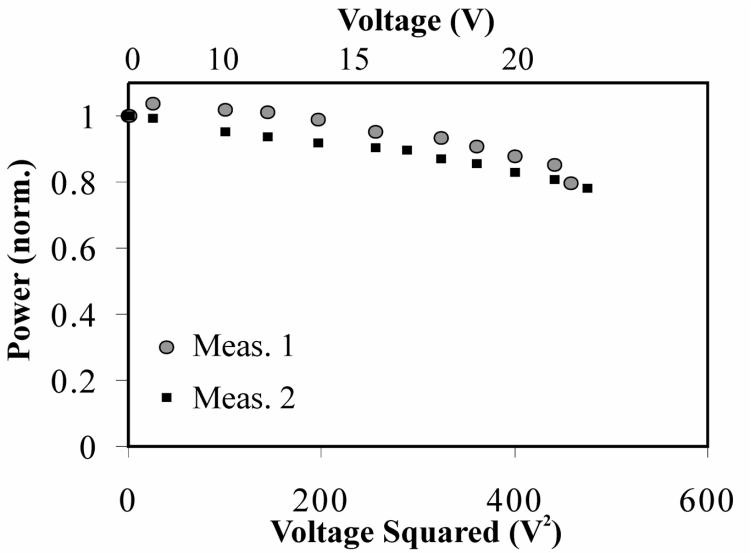


**Figure 7. 23: Measured optical power vs. DC actuation (static measurement). The voltage squared gives the electrostatic force and, roughly, the displacement.**

### 7.5.2 High Optical Q Cavities: Tunable Filters

Another design by which the sensitivity can be increased is to couple the resonating element with a high optical Q-factor resonant cavity. Such a resonant cavity can, for example, be a Fabry-Perot cavity, as is commonly found in vertical cavity MEMS tunable optical filters. Such filters have previously been developed in indium phosphide [74, 75, 81, 128, 172] by creating a vertical cavity filter with fixed bottom Bragg mirror and a movable top Bragg mirror formed on an actuated membrane. Generally, multiple wavelengths $\{\lambda_1, \lambda_2, \lambda_3, \ldots \lambda_N\}$ are sent through the filter and demultiplexed to obtain a single wavelength, say $\lambda_0$, of interest. By actuating the membrane, the optical cavity length is varied and the filtered wavelength can be tuned.

The tunable filter can also be operated in a different manner. A single wavelength, $\lambda_0$, corresponding to the initial cavity length is sent through the filter. The

membrane can then be actuated to bring it to mechanical resonance. If the optical Q-factor is sufficiently large, then even small membrane displacements will result in a large change in transmitted power. In this manner, small vibrations of the membrane (nanometer-scale) can be measured accurately.

Although this proposed technique is very sensitive, there are two potential drawbacks. First, due to the vertical cavity design, single-chip sensors – such as those presented in this work – are not possible without multi-chip designs. Optical sources (lasers or other light sources) and detectors would have to be located on separate chips. Second, the high optical Q cavity can be so sensitive that thermal fluctuations can cause significant noise fluctuations. In fact, such thermal fluctuations can be a dominant source of noise in MEMS structures [157], since they can not be avoided unless measurements are performed at absolute zero (or cryogenic) temperatures. In contrast, the present devices, although quite sensitive, do not approach the sensitivity limits of thermal noise fluctuations. Therefore, the cantilever waveguide design presents a balanced approach with high sensitivity and relative noise immunity.

### 7.5.3 Fundamental Detection Limits

Given the extremely large sensitivity possible with high optical Q-factor measurement techniques, thermal fluctuations can represent significant sources of noise [157]. That is, thermal fluctuations result in small (< 1 nm) vibration amplitude of the top membrane, which results in significant modulation of the optical output. One method to limit the influence of thermal noise fluctuations is to ensure a large mechanical displacement in excess of any displacement due to thermal effects (i.e. displacements >>

1 nm), as is the case for the present cantilever sensors. However, care must be exercised since large displacements can result in nonlinear mechanical behavior that can affect the sensor performance.

Recently, the dynamic range of nano-mechanical systems (NEMS) *doubly-clamped* resonators was examined, specifically in light of the limits imposed by thermal fluctuations (lower detection limit) and nonlinear mechanical resonance behavior (upper displacement limit) [173]. Although thermal-mechanical fluctuations are always a concern that limit the minimum measurable displacement [157], large displacements result in a Duffing spring stiffening that increases the effective resonance frequency; this is especially true for doubly-clamped structures and results in an aspect ratio dependency of the dynamic range (DR): $DR(w, L) \propto w\sqrt{(w/L)^5}$ [173]. While this is a limitation for doubly-clamped structures, it appears to be less of a concern for cantilever-type sensors, in which the onset of nonlinear mechanical behavior occurs at displacements typically much larger than the beam width. This affirms the approach of developing cantilever waveguide resonator sensors.

### 7.5.4 Damping

Many factors affect the Q-factor of the cantilever sensors. The measured Q-factor is given by the weighted average of the individual Q-factors:

$$\frac{1}{Q_{Measured}} = \left( \sum \frac{1}{Q_{Mechanical}} \right) \cdot f_{Optical}, \tag{7.14}$$

where $Q_{\text{Mechanical}}$ refers to various mechanical damping mechanisms, including support losses, air flow damping, and squeeze-film damping. The term $f_{\text{Optical}}$ refers to the non-linear optical response as a function of cantilever displacement, as in Figure 7. 7.

The various mechanical damping mechanisms will now be briefly reviewed; more detailed studies can be found in the literature [174-177]. Structural damping occurs in the form of tether support loss. For very compliant tethers, significant energy will be transmitted from the cantilever to the supports. However, in general the tether support loss is minimal compared to other sources of loss.

A second form of loss results from air-damping. The Q-factor for a vibrational mode *m* due to air flow around the cantilever is given by [176]:

$$Q_{1,m} = \frac{1}{4\pi}\left[\frac{2\rho_b w^2 \omega_m}{3\pi\mu + \frac{3}{4}\pi \cdot t\sqrt{2\rho_a \mu \omega_m}}\right], \tag{7.15}$$

where $\rho_a$ is the mass density of air, $\rho_b$ is the mass density of the beam, $\mu$ is the viscosity of air, $w$ is the beam width, $t$ is the beam thickness or height, and $\omega_m$ is the resonance frequency of the $m^{\text{th}}$ vibrational mode. Equation (7.15) can be simplified to give some insight on the Q-factor and various design choices:

$$Q_{1,m} \propto \frac{1}{4\pi}\left(\frac{w^2 \omega_m}{c_1 + c_2 t\sqrt{\omega_m}}\right). \tag{7.16}$$

The relation in eqn. (7.16) indicates that air damping is independent of the displacement amplitude, $\Delta x$. Wider beams (larger $w$) increase the Q-factor quadratically, whereas thicker beams decrease the Q-factor. Finally, higher-order vibrational modes, $m$, should also result in increased Q-factor. This is an important result, since it means that higher-sensitivity devices can be obtained by exciting the sensors to higher-order modes.

The second effect to be considered is squeeze-film damping, which decreases the Q-factor due to the force of air trapped between the cantilever and actuator sidewalls. The squeeze-film damping Q-factor for a vibrational mode $m$ is [176]:

$$Q_{2,m} = \left(\frac{1}{4\pi}\right)\left[\frac{2\rho_b {g_0}^3 w \omega_m}{\mu \cdot t^2}\right], \tag{7.17}$$

where $g_0$ is the initial cantilever-actuator gap. Equation (7.17) shows a strong (cubic) dependence on $g_0$ and a moderately strong (inverse quadratic) dependence on the cantilever thickness. Thus, designs with large air gaps are preferred. As with the air flow damping, $Q_{1,\mathrm{m}}$, the squeeze-film damping quality factor, $Q_{2,\mathrm{m}}$ will be larger for higher-order vibrational modes, $m$.

### 7.5.5 Higher-Order Vibrational Modes

The discussion on damping mechanisms in section 7.5.4 suggests that it may be possible to increase the sensitivity of resonant sensors by operating them at higher-order vibrational modes. According to eqn. (7.16) and eqn. (7.17), the Q-factor ($Q_{\mathrm{Mechanical}}$) increases as the cantilever is excited to higher-order vibrational modes, $f_{\mathrm{m}}$. This affects

both air damping (viscous damping) as well as squeeze film damping. An increased $Q_{\text{Mechanical}}$ results in a sharper resonant frequency peak so that smaller resonance shifts can be resolved. From eqn. (7.5) we can see that a smaller resonant frequency shift, $\Delta f$, enables the measurement of smaller adsorbed mass, $\Delta m$, which increases the sensitivity.

In addition to the increase in $Q_{\text{Mechanical}}$ with operation at higher-order vibrational modes, $f_{\text{m}}$, the sensitivity is also increased in a second manner. *Dohn et al.* (2005) have studied resonating cantilever sensors and have suggested operation at higher-order vibrational modes [178]. The resonant frequency of the $m^{\text{th}}$ vibrational mode, $f_{\text{m}}$, is [178]:

$$f_m = \frac{1}{2\pi}\sqrt{\frac{k}{m_m^*}}, \tag{7.18}$$

where $k$ is the cantilever spring constant and $m_{\text{m}}^*$ is the effective mass of the $m^{\text{th}}$ vibrational mode. Higher-order modes have smaller effective mass, $m_{\text{m}}^*$, leading to higher resonant frequency, $f_{\text{m}}$ (the spring constant, $k$, remains the same). The smaller effective mass means that smaller adsorbed masses can be detected, leading to a higher sensitivity. In fact, *Dohn et al.* have experimentally shown that the $m = 4$ vibrational mode exhibits a 276-fold increase in sensitivity compared to the $m = 1$ mode for one of their cantilever devices. In their experiments, an external laser/detector system was used for frequency measurements, and the cantilever was excited via an external piezo-actuator. Similar experiments can be carried out with the integrated cantilever waveguide

devices presented in this work, so that enhanced sensitivity is obtained without any change in the devices themselves.

## 7.6 Future Work

### 7.6.1 Functionalization: Cantilever Waveguide Sensors

The first step for developing true environmental sensors is to functionalize the cantilever resonator surface. This is done by coating the cantilever with some receptor coating, which is agent-specific. Examples of such coatings include:

- Evaporated gold films (20 – 50 nm); the gold coating has an affinity for mercury and can be used for mercury vapor detection (*Thundat et al.* [153])
- Poly-(N-vinylpyrrolidinone) and poly-ethyleneglycol as a hydrophyllic coating for humididty sensing (*Ferrari et al.* [36])
- Polyvinylpyridine (PVP), polyurethane (PU), polystyrene (PS), and polymethylmethacrylate (PMMA) coatings to measure various vapors, including alcohols (methanol, ethanol, propanol, etc.) and solvents (acetone, toluene, dichloromethane, etc.) (*Baller et al.* [148])
- Self-assembled monolayer (SAM) of 4-mercaptobenzoic acid; detection of explosives, including pentaerythritol tetranitrate (PETN) and hexahydro-1,3,5-triazine (RDX) (*Pinnaduwage et al.* [152])
- Antibodies for the detection of bacterial cells; specifically, O157:H7 for detection of single *E. coli* cells (*Ilic et al.* [150])

The above examples are only a small set of receptor coatings that have been reported in the literature, although many more exist and/or will be found. A significant challenge with these receptor coatings, however, is their specificity. That is, given a positive response of the sensor to the presence of some unknown agent(s), how can one be sure that the positive response is the result of a single *agent A*? Will a receptor coating result in a positive reading for a different *agent B* in addition to *agent A*? This is probably the single most important and challenging issue facing these types of sensors.

There are two possible solutions. The first is to study receptor coatings in detail so that any single chemical or biological agent of interest corresponds to a *single* unique receptor coating, and vice versa. This approach works for the detection of single cells, if anti-bodies are used as the receptor. Such an approach was taken by *Ilic et al.* for the detection of *E. coli* cells [150]. The second approach is to use an array of sensors operating simultaneously side by side. Each sensor in the array is coated with a different receptor. While a single agent may result in a positive response from two sensors (receptors), it is unlikely that it will affect all sensors (receptors). An example is shown in Table 7. 6. A single receptor can result in a positive response for several agents; suppose agents *A1* and *A2* give a positive reading for receptor *R1*. However, a positive reading for both *R1* and *R2* uniquely identifies *A1*. Similar responses enable the unique identification of all agents. Therefore, the group response of all sensors (receptors) enables high specificity, even if an individual receptor by itself does not give complete specificity.

**Table 7. 6: Example of four sensor detector.**

| Receptor / Agent | A1 | A2 | A3 | A4 |
|---|---|---|---|---|
| **R1** | *Positive* | *Positive* | -- | -- |
| **R2** | *Positive* | *Positive* | *Positive* | -- |
| **R3** | -- | *Positive* | -- | -- |
| **R4** | -- | -- | *Positive* | *Positive* |

### 7.6.2 Single-Chip Sensors

Once receptor coatings suitable for a specific agent of interest are found, true InP-based single-chip sensors can be developed. First, a photodetector needs to be incorporated at the output waveguide. Second, an optical source must be integrated at the input.

The detector can be realized by making use of the InGaAs sacrificial layer already found in the present sensors. A p-i-n photodetector would consist of an n-type waveguide layer, an intrinsic $In_{0.53}Ga_{0.47}As$ absorption layer, and a p-type substrate. The larger index of $In_{0.53}Ga_{0.47}As$ ($n \sim 3.5$) compared to InP ($n = 3.173$) ensures that any optical power in the waveguide will eventually be absorbed by the InGaAs layer resulting in a measurable photocurrent. The only design changes necessary are 1) to create a region at the output waveguide in which the InGaAs layer is not removed during sacrificial etching, and 2) deposit metal electrodes for applying a reverse bias to the p-i-n junction.

Optical sources can be integrated with passive waveguides using resonant coupling between optical modes. For example, it has been demonstrated that active waveguides (incorporating optical gain) can be fabricated on top of passive waveguides. Coupling between the active and passive regions is accomplished by creating resonant vertical couplers such that the optical mode can travel between the active and passive waveguides in a controlled way [18, 179]. In this manner, devices have been reported in which lasers (top layer) were coupled to passive waveguides (middle layer) and finally to a large core passive waveguide (bottom layer) for efficient coupling to standard optical fibers [18].

## 7.7 Summary

In this chapter, MEMS resonating cantilever sensors with end-coupled integrated optical waveguides were demonstrated. Experiments to characterize the mass-sensitivity of the devices were performed, indicating that fg/Hz sensitivity is possible. A ringing measurement and signal processing technique was developed, by which the complete mechanical resonance spectrum can be extracted from a single time domain measurement. Finally, the prospect of developing single-chip sensors was explored.

Page intentionally left blank.

# CHAPTER 8

# CONCLUSION

## 8.1 Introduction

This chapter reviews the accomplishments of this PhD dissertation research and places the results in perspective. Other applications of the MEMS-actuated optical waveguide technology are also briefly reviewed. Finally, an outlook for future work on indium phosphide based optical waveguide MEMS is given.

## 8.2 Summary of Accomplishments

This PhD dissertation research has studied in detail and demonstrated the feasibility of indium phosphide based optical waveguide MEMS. Although MEMS-actuated waveguide devices have previously been demonstrated in various material systems [43, 50, 51, 54, 136, 137, 158], none have utilized InP. Currently, there is great interest in utilizing InP as a substrate material for InP-based (InGaAsP) devices incorporating optical gain (e.g. lasers, optical amplifiers) at the 1550 nm telecommunications wavelength. Compared to silicon, however, the micromechanical properties of InP have been insufficiently studied, especially for MEMS applications. Previous demonstrations of InP-based optical MEMS have focused on vertical cavity tunable optical filters [68-75, 81, 128, 129, 180], with small actuation displacements of 100 nm. These filters utilize a free-space approach as opposed to the integrated approach

of this work. To the best of my knowledge, there have been no previous demonstrations of InP-based integrated optical waveguide MEMS reported to date.

The specific accomplishments of this PhD research are as follows:

1. **Mechanical characterization of thin-film InP-based micromechanical films and structures:** Initial work focused on developing a suitable layer structure and fabrication platform for InP-based optical waveguide MEMS. The micro-mechanical properties of InP were then measured using nanoindentation, micro-beam bending, profile measurements, and electrostatic actuation to ascertain its applicability as a MEMS material [7]; this work was performed for my Master's thesis [8].
2. **Platform technology for MEMS-actuated InP optical waveguides:** The suspended waveguide technology was developed to enable *movable* InP-based waveguides that can be electrostatically actuated. I extended the initial work on passive (fixed) suspended waveguides [9] to create movable waveguides with electrostatic actuation.
3. **MEMS-actuated evanescent coupler:** In this device, two parallel suspended waveguides are optically coupled. The amount of power transfer between the waveguides is controlled by varying the waveguide spacing via electrostatic pull-in actuation. Both optical switches and variable optical couplers were demonstrated. Although MEMS-actuated evanescent devices were recently demonstrated with silicon-on-insulator (SOI) disk-resonator filters [124, 125], InP-based MEMS-actuated directional couplers as demonstrated in this work have never been previously demonstrated.

4. **MEMS-actuated end-coupled switch:** Rather than using two parallel waveguides, a single movable input waveguide was actuated to align axially with one of two fixed output waveguides. Optical power transfer proceeds via end-coupling (also referred to as butt- or end-fire coupling). Instead of pull-in actuation, comb-drive actuators with serpentine suspensions were used to ensure low-voltage operation with larger actuation displacements compared to the MEMS couplers. This is the first demonstration of end-coupled MEMS optical switches in InP.
5. **Cantilever waveguide resonant sensor:** End-coupled switches are modified for environmental sensing applications. A single movable cantilever input waveguide is end-coupled to a single fixed output waveguide. The cantilever can be made to resonate at its natural frequency via electrostatic actuation. By measuring the modulated coupled optical power at the output, the resonant frequency is obtained. Mass adsorption, due to the presence of chemical or biological agents, results in a measurable shift in the resonant frequency. This resonant frequency shift can therefore be used to measure changes in the environment due to chemical or biological agents. Although end-coupled waveguides have been previously used for vibration sensing [158], the sensors presented in this PhD research are the smallest reported MEMS-actuated end-coupled waveguides reported to date (as small as $L = 50$ μm, $w = 0.6$ μm, $h = 1.5$ μm), which enables increased sensitivity for mass-based sensors. The present devices are also the first to apply end-coupling for on-chip displacement measurement in resonant environmental sensors.

## 8.3 Other MEMS-Actuated Waveguide Device Applications

Various devices such as optical waveguide switches and sensors have been demonstrated in this PhD research. In addition, various other devices can be realized, including in-plane tunable Fabry-Perot filters for wavelength demultiplexing, micro-ring and micro-disk resonator filters for switching, optical logic, and dispersion compensation, and wavelength division multiplexed (WDM) transmitters/receivers; all of which are described briefly below.

### 8.3.1 In-Plane MEMS-Tunable Fabry-Perot Filters

InP-based tunable optical filters were demonstrated by my colleague, Dr. Madhumita Datta (MEMS Sensors and Actuators Lab), during the course of this PhD research [181]. The devices differ from previous MEMS tunable Fabry-Perot filters in that the optical cavity is in-plane rather than out-of-plane. This enables ease of integration with optical waveguides and components. While the majority of the design, fabrication, and testing was carried out by Dr. Datta (with help from me), the concept and idea are my own [182].

A fabricated filter with in-plane Fabry-Perot optical cavity and InP/air Bragg mirrors is shown in Figure 8. 1. The devices were tested in a manner similar to the other devices in this PhD research, although a tunable laser was used to sweep the input wavelength from $\lambda$ = 1496 – 1610 nm to obtain the filter spectral characteristics during actuation. The results indicate $\Delta\lambda$ = 12 nm tuning for 7 V actuation and demonstrate the feasibility of developing in-plane MEMS-tunable Fabry-Perot filters with integrated optical waveguides (Figure 8. 2).

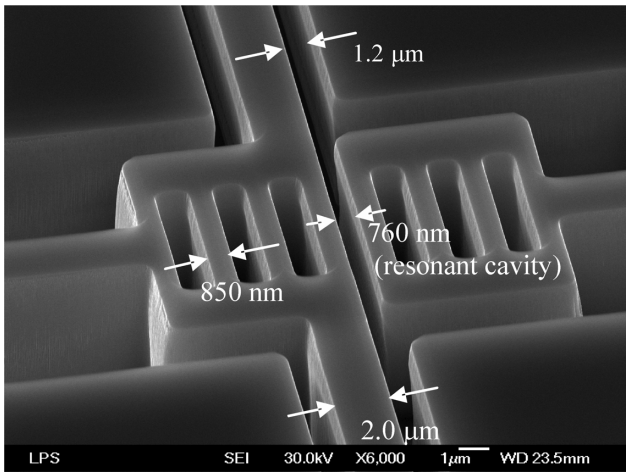


**Figure 8. 1: InP-based in-plane MEMS-tunable Fabry-Perot filter [181].**

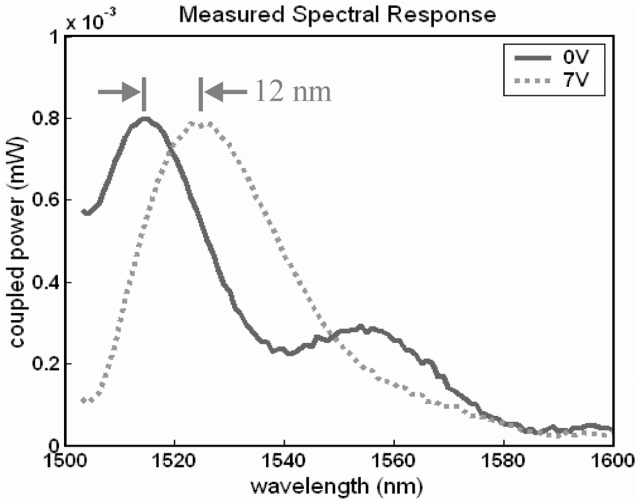


**Figure 8. 2: Measured filter spectral response (adapted from [181]).**

### 8.3.2 Micro-Ring and Micro-Disk Resonator Filters

Another application of MEMS-actuated waveguide devices is in photonic logic. Photonic logic aims to create all-optical circuits; that is, circuits similar to electronic IC's implementing switching and logic functions, but using optical rather than electrical

signals. In electronics, transistors are used as fundamental building blocks to create logic gates, for example NAND gates. In photonics, micro-ring (Figure 8. 3) and micro-disk resonators can form fundamental building blocks enabling all-optical logic gates to be realized, including NAND gates [183].

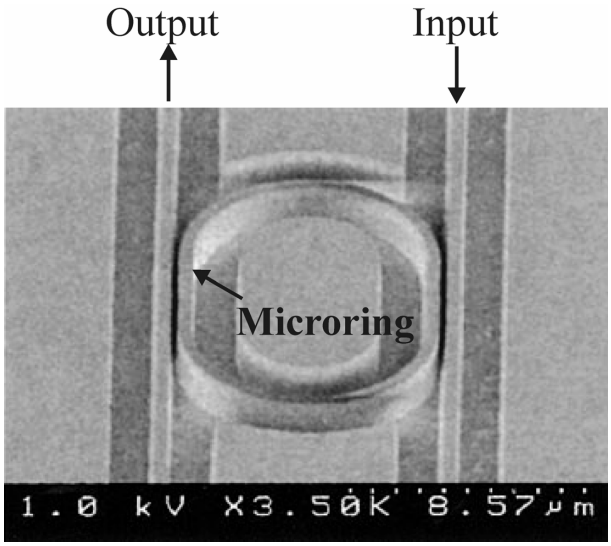


**Figure 8. 3: Micro-ring resonator optical filter with bus input and output waveguides coupled evanescently to the ring (adapted from [27]).**

Micro-ring and micro-disk resonators are similar to Fabry-Perot resonators, but with circular optical cavities. This increases the field intensity compared to Fabry-Perot resonators and enables non-linear optical effects to be observed. Coupling between a waveguide and a ring-resonator generally occurs via an evanescent coupler. There is considerable interest in creating ring-resonators with coupling waveguides in which the amount of coupling can be continuously varied. Such devices enable wavelength-selective switching, logic, and dispersion compensation. The MEMS coupler presented

in Chapter 5 is ideally suited for this purpose. In addition to enabling variable optical coupling, fabrication tolerances are eased compared to fixed-ratio couplers since the coupling gap can be fabricated to be relatively large (> 1 μm compared to <500 nm for fixed couplers), and MEMS actuation can bring the coupling waveguide close to the micro-ring as needed.

MEMS-actuated variable coupling to micro-disks has recently been achieved in silicon-on-insulator devices. Both side-coupling, as in Figure 8. 3, and vertical coupling, in which the input and output waveguides are coupled vertically to the ring, have been demonstrated using silicon-on-insulator (SOI) [124, 125]. InP-based micro-ring devices [97, 183] can be readily integrated with the MEMS couplers described in Chapter 5 and would enable on-chip active optical functionality (e.g. optical amplifiers and lasers). This is a significant advantage compared to the SOI devices [124, 125], in which no optical gain is possible on-chip.

### 8.3.3 WDM Transmitters and Receivers

A tunable p-i-n photodiode was recently demonstrated by bonding two chips together, one with a p-i-n photodiode and the other with an electro-thermally actuated Fabry-Perot filter [184]. Such a device enables tunable wavelength-selective detection of individual channels in a wavelength-division multiplexed (WDM) communications system. A similar device can also be used as a tunable vertical cavity surface emitting laser (VCSEL) [185]. This enables the generation of many different wavelengths (channels) using a single laser source. The tunable pin-photodiode and tunable VCSEL form a low-cost WDM receiver and transmitter pair, whose performance will be similar

to fixed wavelength devices but with significantly smaller required inventory and minimal expense.

In both examples above, the tunable devices require bonding of two separate chips: 1) the active chip (source or detector) and 2) the tunable Fabry-Perot "passive" chip. The tunable Fabry-Perot filter presented in Figure 8. 1 and Figure 8. 2 [181] enables the monolithic integration of tunable devices with passive waveguides. By adding an additional active layer and using lateral tapers to vertically couple between the top active layer and the bottom passive waveguide layer, tunable sources and tunable detectors can be envisioned. A platform for vertically coupling between active and passive device layers was discussed in Chapter 7 [18, 186]. Such devices would achieve the same function as the two-chip devices above [184, 185], but with significantly lower fabrication cost since all required layers (active gain layers, passive waveguide layers) can be grown in a single MBE process run.

## 8.4 Comments and Future Work

A wide variety of devices have been developed for this PhD research. While the devices have operated well and within the design limits (voltage, power, speed, efficiency, and sensitivity), reliability is a concern if any of the devices are to be made into products. The fundamental limitation concerning long-term operation is stiction [104], or permanent adhesion between two micro-mechanical components. It is well known that stiction occurs more frequently in devices with smooth surfaces in close contact. On the other hand, the devices in this work require optical quality surfaces

(waveguide sidewalls and facets) with roughness of $\sigma < 50$ nm. Therefore, stiction is a serious reliability issue.

The most reliable devices in this research were those that did not utilize pull-in actuation. For example, the resonant cantilever waveguide sensors in Chapter 7 were actuated to excite the cantilever to resonance but never up to pull-in. These sensors proved very reliable since no physical contact occurs during operation. The end-coupled switches in Chapter 6 could be operated reliably as long as the specific device did not have two contact surfaces (e.g. comb-drive actuated switch instead of pull-in actuated switch). Finally, the MEMS couplers in Chapter 5 could be operated reliably if pull-in was not used, for example, by using a comb-drive coupler. In fact, even pull-in couplers could be operated reliably in excess of 10 million switching cycles, provided that the mechanical restoring force was large enough (i.e. short devices with large spring constant).

In addition to the designs presented in this research, there are other methods to improving device reliability. If the switches (MEMS couplers and end-coupled switches) are vacuum sealed, then stiction will be less prevalent since stiction is known to increase with humidity due to surface tension effects. Alternatively, surface coatings such as self-assembled monolayers (SAM's) can be used to create hydrophobic surfaces, thereby reducing or eliminating stiction [142]. Other surface coatings include dielectrics, such as $SiO_2$ or $SiN_X$ (see Chapter 5) that will prevent current flow during pull-in and will also prevent stiction. Finally, it should be noted that none of these issues are insurmountable, and much like the successful Texas Instruments DMD micro-mirror display technology

[30], the reliability issues for InP-based waveguide MEMS can be solved with sufficient research effort.

## 8.5 Summary

This PhD dissertation research has definitively shown that InP is suitable as a micro-opto-mechanical material and that a wide variety of waveguide-based optical microsystems ranging from communications to sensing components can be realized with this material. It is my hope that work in this area will continue to the point of true monolithic integration of waveguides, MEMS actuators, and active optical components (optical sources, p-i-n photodetectors, optical amplifiers, etc.) on a single chip. This will enable a wide variety of opto-electro-mechanical components with almost limitless applications.

# APPENDIX A

# MATLAB SCRIPT FOR CALCULATION OF InGaAsP PROPERTIES

## A.1 Introduction

In this appendix, the MATLAB script for calculating the InGaAsP waveguide layer structure properties is reviewed. The MATLAB code is listed, a typical output window is shown, and comments and useful references [91, 93, 187-189] are given.

## A.2 MATLAB Source Code

```
% In(1-x)Ga(x)As(y)P(1-y) Parameter Calculator
%
% This script calculates for a given mole fraction x and y: 1) the refractive
% index as a function of wavelength, 2) the bandgap and 3) the strain of the
% In(1-x)Ga(x)As(y)P(1-y) layer when grown on InP.
%
% Note that this is effective for near-lattice-matched and lattice-matched
% GaInAsP semiconductors only.
%
% REFERENCES:
%
% Refractive index and bandgap:
% [1] B. Broberg and S. Lindgren, Refractive index of In(1-x)Ga(x)As(y)P(1-y) layers and InP in the
% transparent wavelength region, J. Appl. Phys. 55 (9) (1984) 3376-3381.
% [2] S. Adachi, Refractive indices of III-V compounds: key properties of InGaAsP relevant to % device
design, J. Appl. Phys. 53 (8) (1982) 5863-5869.
%
% Strain:
% [3] F. G. Johnson, GaInAsP parameter calculator, Excel file. See also: Paul H. Holloway and % Gary E.
McGuire, "Handbook of Compound Semiconductors : Growth, Processing, Characterization, % and
Devices," Norwich, NY: Noyes Publications, 914 pages, 1996.
%
% Single-mode operation:
% [4] G. P. Agrawal and N. K. Dutta, Semiconductor Lasers 2nd Edition, Van Nostrand % Reinhold:
% New York (1993).
%
% Rohit Grover (rgrover@lps.umd.edu) wrote script for calculating the refractive index and % bandgap.
% Marcel Pruessner (marcelp@glue.umd.edu) wrote everything else.
```

```
%
% Marcel Pruessner
% January 17, 2003
%
% Added output plots.
%
% Marcel Pruessner
% January 20, 2003
%
% Added waveguide width for single-mode operation, assuming air-cladding on sides of waveguide.
%
% Marcel Pruessner
% January 12, 2004
%

clear;
disp(' ')
disp(' ')
disp('InGaAsP Parameter Calculator')
disp(' ')
disp('Note: lattice-matched for x=0.47*y.  Calculations are accurate only for lattice-matched')
disp('or near lattice-matched.')
disp(' ')

x1=input('CORE: Input mole fraction x for Gallium (0 < x < 1): ');
y_lattice_matched=4176.*x1/(125.*x1+1896.)          % lattice-matched: x=0.1896y/(0.4176-0.0125y)
disp('Note: for tensile strain, y < y_lattice_matched.')
disp(' ')
y1=input('CORE: Input mole fraction y for Arsenic (0 < y < 1): ');
disp(' ')
x2=input('CLADDING: Input mole fraction x for Gallium (0 < x < 1): ');
y_lattice_matched=4176.*x2/(125.*x2+1896.)          % lattice-matched: x=0.1896y/(0.4176-0.0125y)
disp('Note: for tensile strain, y < y_lattice_matched.')
disp(' ')
y2=input('CLADDING: Input mole fraction y for Arsenic (0 < y < 1): ');
disp(' ')
lambdastart=input('Enter starting wavelength (in nm): ');
lambdastop=input('Enter end wavelength (in nm): ');
lambdares=input('Enter wavelength resolution (in nm): ');
disp(' ')
p=input('Plot output (1=yes, 0=no)? ');

lambda=lambdastart:lambdares:lambdastop;
tdatasize = size(lambda);
datasize = tdatasize(2);

% CORE
Eg1 = ones(1,datasize)*(1.35 - 0.728*y1 + 0.12*y1^2);
Ed1 = ones(1,datasize)*((12.36*x1 - 12.71)*y1 + 7.54*x1 + 28.91);
E01 = ones(1,datasize)*(0.595*x1^2*(1-y1) + 1.62*x1*y1 - 1.891*y1 + 0.524*x1 + 3.391);
eta1 = (pi*Ed1./(2*E01.^3.*(E01.^2 - Eg1.^2)));
E1 = 1240*(1./lambda);
%size(E)
n_CORE = (ones(1,datasize) + Ed1./E01 + Ed1.*E1.^2./E01.^3 + eta1.*E1.^4/pi.*log((2*E01.^2-Eg1.^2-
E1.^2)./(Eg1.^2 - E1.^2))).^(0.5);
% CLADDING
```

```
Eg2 = ones(1,datasize)*(1.35 - 0.728*y2 + 0.12*y2^2);
Ed2 = ones(1,datasize)*((12.36*x2 - 12.71)*y2 + 7.54*x2 + 28.91);
E02 = ones(1,datasize)*(0.595*x2^2*(1-y2) + 1.62*x2*y2 - 1.891*y2 + 0.524*x2 + 3.391);
eta2 = (pi*Ed2./(2*E02.^3.*(E02.^2 - Eg2.^2)));
E2 = 1240*(1./lambda);
%size(E)
n_CLADDING = (ones(1,datasize) + Ed2./E02 + Ed2.*E2.^2./E02.^3 + eta1.*E2.^4/pi.*log((2*E02.^2-
Eg2.^2-E2.^2)./(Eg2.^2 - E2.^2))).^(0.5);

% Index Contrast
dn=n_CORE-n_CLADDING;

% Mean CORE and CLADDING Refractive Index
n_CORE_mean=mean(real(n_CORE));
n_CLADDING_mean=mean(real(n_CLADDING));
dn_mean=mean(real(dn));

% CORE and CLADDING Bandgap
Eg1=1.24/mean(Eg1);        % bandgap in um wavelength
Eg2=1.24/mean(Eg2);        % bandgap in um wavelength

% Strain
lattice_constant_CORE=5.86875 - 0.4175*x1 + 0.18965*y1 + 0.0128*x1*y1;
                                                    % CORE lattice constant in Angstroms
strain_CORE=((5.86875 - lattice_constant_CORE)/lattice_constant_CORE)*100;  % strain in %
lattice_constant_CLADDING=5.86875 - 0.4175*x2 + 0.18965*y2 + 0.0128*x2*y2;
                                                    % CLADDING lattice constant in Angstroms
strain_CLADDING=((5.86875 - lattice_constant_CLADDING)/lattice_constant_CLADDING)*100;  %
strain in %

% Maximum waveguide thickness for single-mode operation at specified wavelength
t=(10^-3)*(lambda/2)./sqrt(n_CORE.^2 - n_CLADDING.^2);   % thickness in um
t_mean=mean(real(t));
width=(10^-3)*(lambda/2)./sqrt(n_CORE.^2 - 1^2);   % width in um
width_mean=mean(real(width));

% Display properties
disp(' ')
disp(' ')
disp(' ')
disp(' ')
disp(' ')
disp('In(1-x)Ga(x)As(y)P(1-y) Quaternary Layer Properties (Mean Values)')
disp(' ')
disp('LEGEND: ')
disp('     x, y   = Mole fraction of Ga and As, respectively')
disp('     n      = Average refractive index over specified wavelength range')
disp('     dn     = Average refractive index contrast over specified wavelength range')
disp('     Eg(um) = Bandgap in um.  Require Eg < 1.45 um for 1.55 um wavelength')
disp('     e(%)   = Strain in (%).  Tensile: e > 0.  The strain should be less than 0.1%')
disp('     t(um)  = Maximum waveguide core thickness for single-mode operation')
disp(' ')
FORMAT=['      x        y        n        dn       Eg(um)    e(%)      t(um)']
CORE=[x1, y1, n_CORE_mean, dn_mean, Eg1, strain_CORE, t_mean]
CLADDING=[x2, y2, n_CLADDING_mean, dn_mean, Eg2, strain_CLADDING, t_mean]
```

```
% Plot CORE and CLADDING Refractive Index
if p==1
   subplot(2,1,1), plot(lambda, real(n_CORE), lambda, real(n_CLADDING), 'LineWidth', 2)
   title('REFRACTIVE INDICES vs. WAVELENGTH','FontName','CM','FontSize',12)
   xlabel('Wavelength (nm)', 'FontName','CM','FontSize',12);
   ylabel('Refractive Index','FontName','CM','FontSize',12);
   h = gca;
   set(h,'FontName','CM','FontSize',12);
   grid on;
   zoom on;
   %paramarray=[lambda;n];
%%paramarray=[lambda;n];
   legend('Core','Cladding')
   subplot(2,1,2);
   axis([0 1 0 1]);
   axis off

% Output window
% Convert values to strings
   x1_text={x1};   % CORE
   y1_text={y1};
   n_CORE_text={(round(n_CORE_mean*1000)/1000)};
   Eg1_text={(round(Eg1*1000))/1000};
   strain_CORE_text={(round(strain_CORE*10000)/10000)};
   t_text={(round(t_mean*1000)/1000)};
   width_text={(round(width_mean*1000)/1000)};
   x2_text={x2};   % CLADDING
   y2_text={y2};
   n_CLADDING_text={(round(n_CLADDING_mean*1000)/1000)};
   Eg2_text={(round(Eg2*1000))/1000};
   strain_CLADDING_text={(round(strain_CLADDING*10000)/10000)};
   t_text={(round(t_mean*1000)/1000)};
% Plot figure and enter values
   text(0.05, 0.8, 'In(1-X)Ga(X)As(Y)P(1-Y) WAVEGUIDE
PROPERTIES','FontName','CM','FontSize',12)
   text(0, 0.1, 'CORE','FontName','CM','FontSize',12)
   text(0, 0.3, 'CLAD','FontName','CM','FontSize',12)
   text(0.15, 0.5, 'X','FontName','CM','FontSize',12)
   text(0.24, 0.5, 'Y','FontName','CM','FontSize',12)
   text(0.34, 0.5, 'n_m_e_a_n','FontName','CM','FontSize',12)
   text(0.46, 0.5, 'E_g(um)','FontName','CM','FontSize',12)
   text(0.6, 0.5, 'e(%)','FontName','CM','FontSize',12)
   text(0.73, 0.5, 't(um)','FontName','CM','FontSize',12)
   text(0.86, 0.5, 'w(um)','FontName','CM','FontSize',12)
   axis off;
   text(0.15, 0.1, x1_text)
   text(0.24, 0.1, y1_text)
   text(0.34, 0.1, n_CORE_text)
   text(0.46, 0.1, Eg1_text)
   text(0.6, 0.1, strain_CORE_text)
   text(0.73, 0.1, t_text)
   text(0.86, 0.1, width_text)
   text(0.15, 0.3, x2_text)
   text(0.24, 0.3, y2_text)
   text(0.34, 0.3, n_CLADDING_text)
   text(0.46, 0.3, Eg2_text)
```

```
    text(0.6, 0.3, strain_CLADDING_text)
    text(0.73, 0.3, '--')
    text(0.86, 0.3, '--')
end
```

## A.3 Typical Output Window

When the InGaAsP ($In_{1-X}Ga_XAs_YP_{1-Y}$) script is run, the following parameters are queried and the user inputs values as desired: mole fraction $x_{Ga}$ (core and cladding), mole fraction $y_{As}$ (core and cladding), and desired wavelength range (in nm). The program then computes and plots the core and cladding refractive index as a function of wavelength. Core and cladding bandgap wavelength ($E_g$ or $\lambda_g$), strain relative to pure InP, and single mode waveguide width and thickness are calculated as well. A typical output window is shown in Figure A. 1.

## A.4 Summary

This MATLAB script computes the refractive index and bandgap for InGaAsP as a function of mole fractions $x_{Ga}$ and $y_{As}$. The calculations are based on a method by *Broberg et al.* [93], and their method agrees well with experimental data contained in the reference. The strain is computed from the lattice constant of the InGaAsP layer compared to pure InP [188, 189], and the single-mode dimensions are computed from the mode cutoff condition discussed by *Agrawal* [187].

(a)

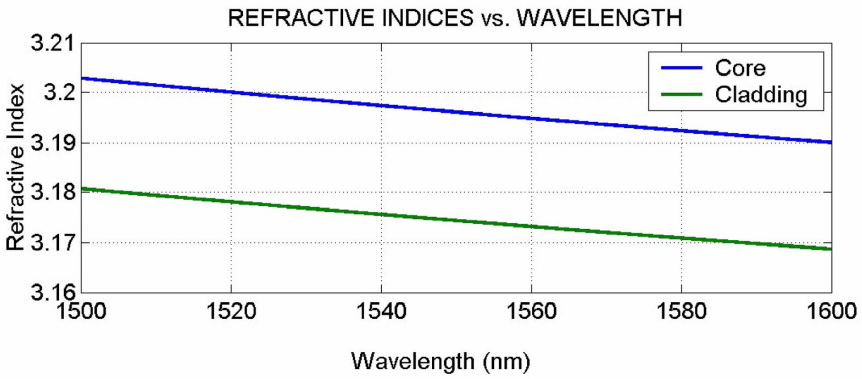


(b)

In(1-X)Ga(X)As(Y)P(1-Y) WAVEGUIDE PROPERTIES

| | X | Y | $n_{mean}$ | $E_g$(um) | e(%) | t(um) | w(um) |
|---|---|---|---|---|---|---|---|
| CLAD | 0.01 | 0.01 | 3.174 | 0.923 | 0.0388 | -- | -- |
| CORE | 0.04 | 0.08 | 3.196 | 0.959 | 0.0253 | 2.083 | 0.255 |

**Figure A. 1: Output window: a) core and cladding refractive index vs. Wavelength, b) summary of core and cladding properties.**

# APPENDIX B

# BASIC THEORY OF DIELECTRIC OPTICAL WAVEGUIDES

## B.1 Introduction

In this appendix, the basic theory of thin-film, integrated optical waveguides is reviewed. The approach of *Saleh and Teich* [86] will be followed and all equations are from their text unless otherwise stated. Similar treatments, however, can be found in the literature [15, 56, 107]. In this appendix, only guided modes will be considered; i.e. those that are supported by the dielectric waveguide. Other non-guided modes include radiation modes and substrate modes [15]. Both of these modes can not, in general, be used to transmit information and are considered sources of loss.

## B.2 Theory: Mirror Waveguides

Integrated optical waveguides are small conductors of light fabricated using integrated circuit technology. Light is guided by pathways fabricated from etched thin films, which form regions of different (effective) refractive indices. The propagation of light is described by Maxwell's wave equation, which can be derived from Maxwell's equations. For a locally homogeneous medium with slowly-varying electric permittivity, $\varepsilon$, and magnetic permeability $\mu = \mu_0$ the wave equation is:

$$\nabla^2 E - \frac{1}{\left(c_0/n\right)^2}\frac{\partial^2 E}{\partial t^2} = 0, \tag{B.1}$$

where $E$ is the electric field, $c_0 = 1/\sqrt{\varepsilon_0 \mu_0}$ is the speed of light in vacuum, and $n$ is the slowly-varying refractive index of the medium. The refractive index of a medium is related to the electric permittivity by:

$$n = \sqrt{\varepsilon(\mathbf{r})}\,, \tag{B.2}$$

where $\varepsilon(\mathbf{r})$ is a function of position $\mathbf{r}$. This wave equation has the general solution:

$$E(\mathbf{r}) = A(\mathbf{r}) \exp[j2\pi\nu t] \exp[j\phi(\mathbf{r})], \tag{B.3}$$

where $A(\mathbf{r})$ is the amplitude, $\nu$ is the frequency, and $\phi(\mathbf{r})$ is the phase. It should be noted that if two electric fields $E_1(\mathbf{r})$ and $E_2(\mathbf{r})$ are solutions to the wave equation, then the *linear superposition* of the two electric fields also satisfies the wave equation.

Now consider a waveguide made of two planar mirrors with perfect reflectivity ($R$ = 100%), as in Figure B. 1. A simple ray-optics approach yields the picture depicted in Figure B. 1a-b, in which a ray incident at angle $\theta$ is reflected with the same angle $\theta$ so that every other reflected ray is a duplicate of the original ray, but shifted in $z$. While this ray optics approach is usually not sufficient for describing real waveguides (mirrors with perfect reflectivity are difficult to realize), it is instructive for the concept of *optical modes* in waveguides, as will be shown.

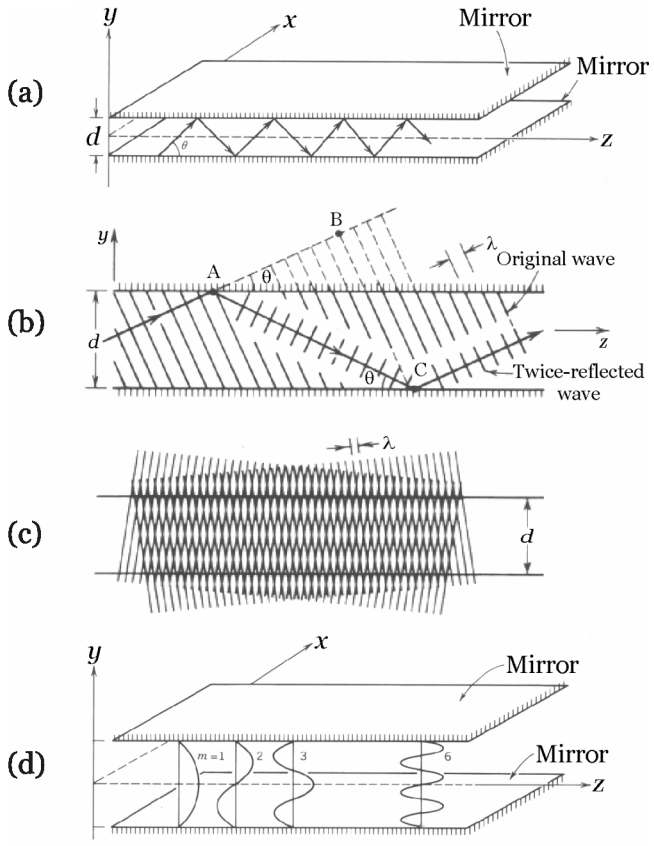


**Figure B. 1: Waveguide with confinement in the y-direction using perfect mirrors and wave propagation in the z-direction: a) ray-optics, b) TEM plane waves, c) interference pattern of TEM plane waves is invariant along the *z*-direction, d) electric field distribution for modes *m* = 1, 2, 3, and 6 (adapted from [86]).**

The ray-optics approach is now modified by replacing each ray with a transverse electromagnetic (TEM) *plane wave*, as in Figure B. 1b. The TEM plane wave is assumed to be polarized in the x-direction (TE-polarization: *E*-field in the *x*-direction) with the wave traveling in the *yz*-plane (i.e. the wavevector **k** is in the *yz*-plane). Each time the TEM plane wave is reflected by the mirror, it undergoes a π-phase shift. The amplitude and polarization, however, are unchanged. *Saleh and Teich* [86] now impose a *self-*

*consistency condition*, which states that every second mirror reflection results in a plane wave identical to the original TEM plane wave. It turns out that only certain angles $\theta$ satisfy this self-consistency condition. The angles $\theta_m$ that meet this requirement are termed eigenmodes (in accordance with a linear system), or simply *modes*. One unique property of these modes is that the original TEM plane wave and its reflection interfere to form an invariant pattern with respect to the propagation direction, *z* (Figure B. 1c). That is, *the amplitude (of the electric and magnetic field) and the polarization of a TEM mode do not change with propagation along the waveguide axis, z*. The angles $\theta_m$ that result in waveguide modes are given by:

$$\sin \theta_m = m\lambda/(2d), \tag{B.4}$$

where *m* is the mode number, $\lambda$ is the wavelength, and *d* is the distance between the waveguide mirrors (Figure B. 1a).

Various TEM waveguide modes (*m* = 1, 2, 3, and 6) are shown in Figure B. 1d. Each mode *m* propagates in the *z*-direction with a characteristic propagation constant $\beta_m$:

$$\beta_m^2 = k^2 - k_{y,m}^2, \tag{B.5}$$

where $k = 2\pi/\lambda$ is the wavevector and $k_{y,m} = m\pi/d$ is the transverse component of the wavevector. The electric field *E* for a mode *m*, assuming $E = E_x$ (and $E_y = E_z = 0$ due to the choice of TE-polarization), is:

$$E_x(y, z) = 2\, A_m \cos(k_{y,m} y) \exp(-j\beta_m z), \text{ for } m=1, 3, 5, \ldots \text{ (odd)} \quad \text{(B.6a)}$$

$$E_x(y, z) = 2j\, A_m \sin(k_{y,m} y) \exp(-j\beta_m z), \text{ for } m=2, 4, 6, \ldots \text{ (even)} \quad \text{(B.6b)}$$

## B.2 Theory: Planar Integrated Dielectric Waveguides

Now consider a planar slab waveguide as in Figure B. 2. Instead of mirrors with perfect reflectivity ($R$ = 100 %), there are three slabs, where the center slab of thickness, $d$, has a refractive index $n_1 > n_2$; that is, the center *core* refractive index ($n_1$) is greater than that of the top and bottom *cladding* ($n_2$). Similar to the mirror waveguide, the plane TEM waves undergo total internal reflection at the $n_1/n_2$ interfaces. Instead of undergoing a π-phase shift as in the mirrors, however, the phase shift is now $\phi_r$ due to total internal reflection.

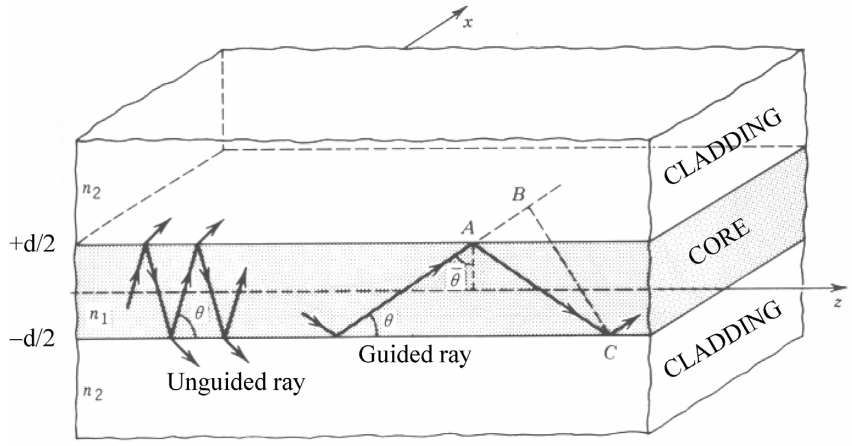


**Figure B. 2: Dielectric slab waveguide (adapted from [86]).**

As before, every other reflected wave is identical to the original wave, but with a phase shift defined by the relation:

$$\frac{2\pi}{\lambda} 2d \sin\theta - 2\phi_r = 2\pi m, \tag{B.7}$$

where $m$ is an integer. The phase shift $\phi_r$ for a TE-wave undergoing total internal reflection is:

$$\tan\left(\frac{\phi_r}{2}\right) = \frac{\left(\sin^2\theta_1 - \sin^2\theta_C\right)^{1/2}}{\cos\theta_1}, \tag{B.8}$$

where $\theta_1$ is the angle of the input wavevector **k** with respect to the *y*-axis and $\theta_C$ is the critical angle for total internal reflection given by *Snell's Law*. For the TE case, $\theta_1 = \pi/2 - \theta$ and $\theta_C = \pi/2 - \overline{\theta}_C$ so that eqn. (B.8) becomes:

$$\tan\frac{\phi_r}{2} = \left(\frac{\sin^2\overline{\theta}_C}{\sin^2\theta} - 1\right)^{1/2}. \tag{B.9}$$

From eqn. (B.7) and eqn. (B.9) the transcendental equation for the "bounce angles," $\theta_m$, for a given mode $m$ is obtained:

$$\boxed{\tan\left(\pi\frac{d}{\lambda}\sin\theta - m\frac{\pi}{2}\right) = \left(\frac{\sin^2\overline{\theta}_C}{\sin^2\theta} - 1\right)^{1/2}}. \tag{B.10}$$

The LHS and RHS of eqn. (B.10) are plotted separately in Figure B. 3, and the intersection of the two curves gives the sin $\theta_m$ from which the angle $\theta_m$ is obtained. *Saleh and Teich* refer to eqn. (B.10) as the *self-consistency condition* for TE-modes, since this equation ensures that the original and every second reflected TEM-plane wave (Figure B. 2) are identical except for a phase shift.

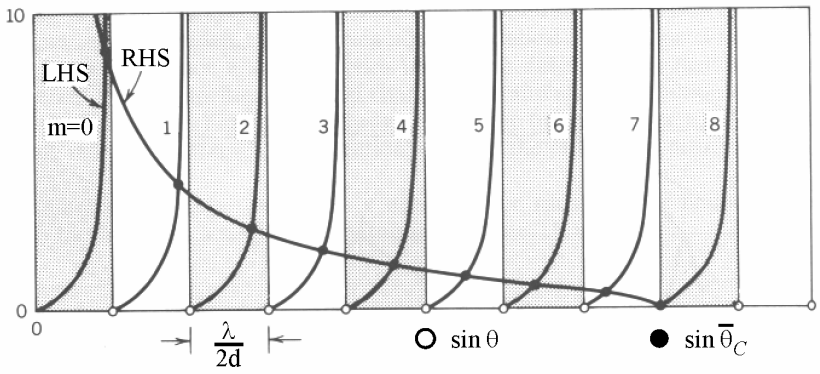


**Figure B. 3: Plot of transcendental eqn. (B.10) for extracting the bounce angle $\theta_m$ for a mode *m* (adapted from [86]).**

Once the bounce angle, $\theta_m$, is known, the propagation constant $\beta_m$ for a mode *m* with free-space wavelength $\lambda_0$ in a planar dielectric waveguide is:

$$\beta_m = n_1 k_0 \cos \theta_m, \tag{B.11}$$

where $k_0 = 2\pi/\lambda$ is the wavevector. The bounce angle, $\theta_m$, can not be greater than the complement of the critical angle, i.e. $\theta_m < \bar{\theta}_C$ for all modes *m*; that is, $\theta_m < \pi/2 - \theta_C$.

For a TM-wave, the electric field is in the *y*-direction (for the previous TE-case, the electric field was in the *x*-direction). The reflection for a TM-wave at a dielectric interface is:

$$\tan\left(\frac{\phi_r}{2}\right)=\frac{\left(\sin^2\theta_1-\sin^2\theta_C\right)^{1/2}}{\cos\theta_1\sin^2\theta_C}. \tag{B.12}$$

By using eqn. (B.12) and eqn. (B.7), it is possible to obtain the transcendental equation for TM-modes.

## B.3 Multimode Waveguides and the Cutoff Condition

The above analysis holds for all modes *m* such that $\theta_m<\overline{\theta}_C=\pi/2-\theta_C$; that is, the bounce angle $\theta_m$ of mode *m* is smaller than $\overline{\theta}_C$, where $\theta_C$ is the critical angle. Because of the limiting constraint placed on $\theta_m$, a waveguide can not guide infinitely many modes. Consequently, there is a cutoff condition for the largest mode *M* that a waveguide can support. This is shown graphically in Figure B. 4. Each mode is separated by $\lambda/2d$ (dashed lines crossing the $k_y$-axis) from the previous one, and the maximum mode is reached when $\sin\theta=\sin\overline{\theta}_C$. Therefore, the maximum number *M* of TE-modes is $M=\sin\overline{\theta}_C/\left(\lambda/2d\right)$, or equivalently:

$$M=\frac{2d}{\lambda_0}NA=\frac{2d}{\lambda_0}\sqrt{n_1{}^2-n_2{}^2}, \tag{B.13}$$

where *NA* is the numerical aperture and the relation cos $\bar{\theta}_C = n_2/n_1$ was used. The first three such modes, $m = 1, 2$, and 3, are shown in Figure B. 5.

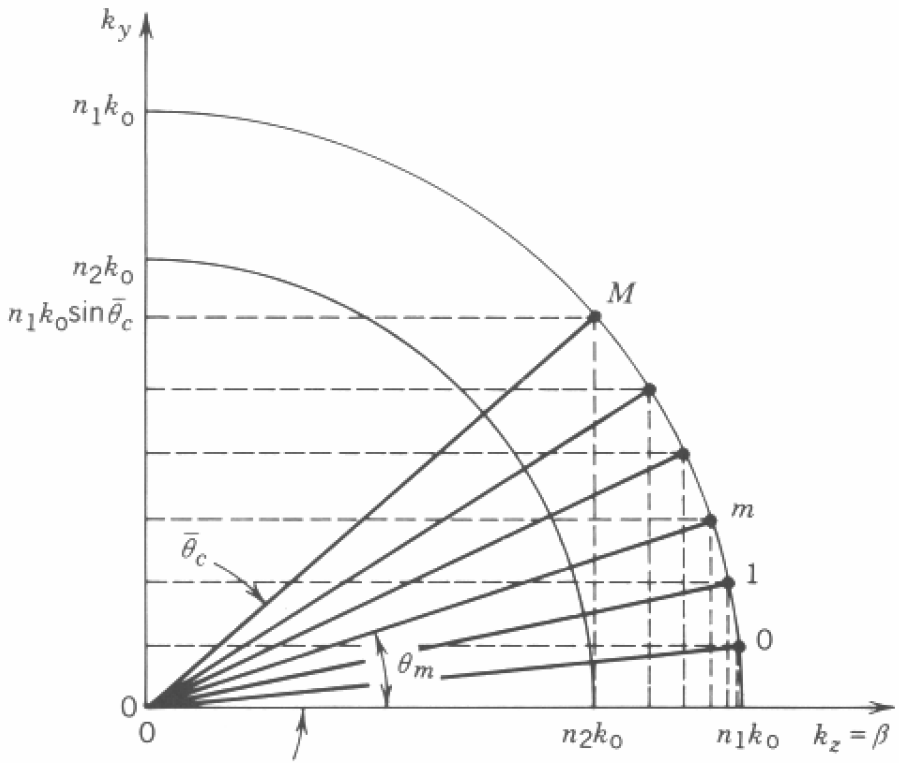


**Figure B. 4: Graphical illustration of the maximum modes in a slab waveguide [86].**

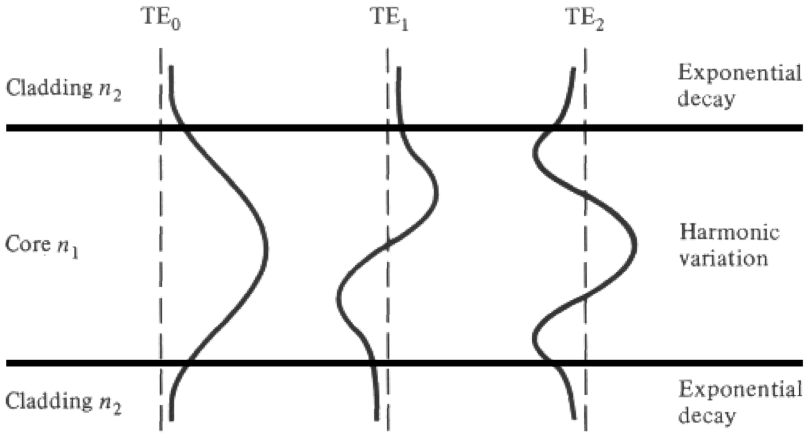


**Figure B. 5: Modes *m* = 1, 2, and 3 in a multi-mode waveguide [56].**

Looking at Figure B. 5, all guided modes consist of a harmonic field (sinusoidal solutions) in the core and an exponentially-decaying field in the cladding. This exponentially-decaying field is called the evanescent field and it can be used to couple power from a mode in one waveguide to a mode in an adjacent waveguide. This is the basis of evanescent coupling. The smaller the index contrast between core and cladding, $\Delta n = n_{\text{CORE}} - n_{\text{CLADDING}} = n_1 - n_2$, the greater the evanescent field will extend into the cladding and the stronger the coupling between the first waveguide to an adjacent one. Therefore, the amount of coupling can be controlled by careful design of the waveguides. It is also interesting to note that higher order modes ($m > 0$) have a larger "bounce angle" $\theta_m$ (Figure B. 4). This increased bounce angle results in a larger evanescent field (extreme case: unguided ray in Figure B. 2) and results in stronger evanescent coupling for higher order modes compared to the fundamental mode, as discussed in Appendix C.

## B.4 Summary

In this appendix, the basics of thin-film integrated optical waveguides have been reviewed. First, wave propagation by reflection from perfect mirrors was described and the concept of *modes* was presented. Next, planar dielectric waveguides were discussed. Cutoff conditions and the maximum number of guided modes in a waveguide were presented. Finally, the concept of an evanescent field was described.

# APPENDIX C

# EVANESCENT COUPLING BETWEEN NON-IDENTICAL WAVEGUIDES AND MULTI-MODE WAVEGUIDES

## C.1 Introduction

In general, evanescent coupling occurs between two identical and single-mode waveguides. That is, two coupled waveguides have the same core and cladding refractive indices, respectively, as well as the same propagation constant, $\beta$. However, coupling can occur between two single-mode waveguides with different propagation constants, $\beta_1$ and $\beta_2$. In addition, coupling can also occur between higher-order modes, so that single-mode waveguides are not necessary. This appendix reviews the two above cases and discusses how coupling occurs in a) non-identical waveguides, and b) multi-mode waveguides.

## C.2 Coupling Between Non-Identical Waveguides

Consider two single-mode waveguides with two different propagation constants, $\beta_1$ and $\beta_2$. For both waveguides the cladding has index $n$, and the core indices are $n_1$ and $n_2$ for *waveguide 1* and *waveguide 2*, respectively (Figure C. 1). Coupling can be described using the coupled-mode equations [108]. The coupling coefficient $\kappa$, however, will be different for *waveguide 1* and *waveguide 2*, so that two coefficients are now required to accurately describe coupling [86]:

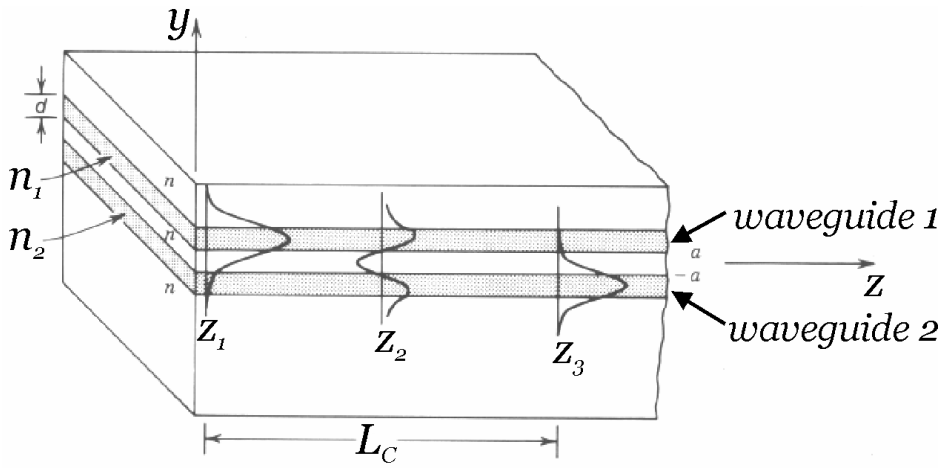


**Figure C. 1: Coupling between two slab waveguides. Mode *m* = 0 is initially in the *BAR* waveguide ($z = z_1$), but eventually couples to the *CROSS* waveguide ($z = z_2$). It resides completely in the *CROSS* waveguide after traveling length $L_C$ ($z = z_3$) (adapted from [86]).**

$$\kappa_{2,1} = \frac{1}{2}\left(n_2^{\,2} - n^2\right)\frac{k_0^{\,2}}{\beta_1}\int_a^{a+d} A_1(y)A_2(y)dy \tag{C.1a}$$

$$\kappa_{1,2} = \frac{1}{2}\left(n_2^{\,2} - n^2\right)\frac{k_0^{\,2}}{\beta_2}\int_{-a-d}^{-a} A_2(y)A_1(y)dy \tag{C.1b}$$

The coupled power in *waveguide 1* and *waveguide 2* is [86]:

$$P_1 = P_1(0)\left[\cos^2\gamma z + \left(\frac{\Delta\beta}{2\gamma}\right)\sin^2\gamma z\right] \text{ and} \tag{C.2a}$$

$$P_2 = P_2(0)\left(\frac{\left|\kappa_{1,2}\right|^2}{\gamma^2}\right)\sin^2\gamma z \text{ , where} \tag{C.2b}$$

$$\gamma^2 = \left(\frac{\Delta\beta}{2}\right)^2 + \mathrm{K}^2 \text{ and} \tag{C.3}$$

$$K = \sqrt{\kappa_{1,2}\kappa_{2,1}} \,. \tag{C.4}$$

From eqns. (C.1–C.4) it is clear that any phase mismatch, $\Delta\beta = \beta_1 - \beta_2$, results in a modulation of the coupling strength between the two waveguides. This in turn shortens the coupling length, $L_C$, compared to the case for two identical waveguides [86, 109]:

$$L_C^{\Delta\beta} = \frac{\pi}{2\sqrt{K^2 + \left(\Delta\beta/2\right)^2}} \,. \tag{C.5}$$

As a comparison, the coupling length for two identical waveguides is:

$$L_C = \frac{\pi}{2\kappa} > L_C^{\Delta\beta} \,. \tag{C.6}$$

The phase mismatch, $\Delta\beta$, in eqn. (C.5) can be used for switching applications. The induced phase mismatch will alter the coupled power according to [86]:

$$\frac{P_2\left(z = L_C\right)}{P_1\left(z = 0\right)} = \left(\frac{\pi}{2}\right)^2 \operatorname{sinc}\left\{\frac{1}{2}\left[1 + \left(\frac{\Delta\beta L_C}{\pi}\right)^2\right]^{1/2}\right\} . \tag{C.7}$$

In practice, the phase mismatch, $\Delta\beta$, can be varied using various techniques, including, for example, the thermo-optic effect [11] or the electro-optic effect [111].

## C.3 Coupling Between Multi-Mode Waveguides

Now, two multi-mode waveguides with propagation constants $\beta_l$ and $\beta_m$ for the $l^{\text{th}}$ mode in *waveguide 1* and the $m^{\text{th}}$ mode in *waveguide 2* are considered. Again, the coupled-mode equations can be used. However, every mode needs to be treated individually and the contribution of each mode to the total field amplitude is obtained by summing all modes using the superposition principle:

$$A(y) = \sum_{l} \sum_{m} A_{l,m}(y). \tag{C.8}$$

The coupling coefficients are obtained by modifying eqn. (C.1) for arbitrary modes $m$ and $l$:

$$\kappa_{l,m} = \frac{1}{2}\left(n_2^{\,2} - n_1^{\,2}\right)\frac{k_0^{\,2}}{\beta_m}\int_a^{a+d} A_m(y)A_l(y)dy, \tag{C.9a}$$

$$\kappa_{m,l} = \frac{1}{2}\left(n_2^{\,2} - n_1^{\,2}\right)\frac{k_0^{\,2}}{\beta_l}\int_{-a-d}^{-a} A_l(y)A_m(y)dy, \tag{C.9b}$$

where the coupling coefficient $\kappa_{l,m}$ refers to the coupling strength between the $l^{\text{th}}$ mode of *waveguide 1* to the $m^{\text{th}}$ mode of *waveguide 2*. Recall that all modes are orthogonal, in accordance with the eigenmodes in a linear system. The overlap integral in eqn. (C.9) between the $l_{\text{Even}}$ and $m_{\text{Odd}}$ modes (coupling coefficient, $\kappa_{l,m}$ or $\kappa_{m,l}$) is zero for all even/odd mode pairs, as is illustrated in Figure C. 2. That is, the integral over symmetric/anti-symmetric function pairs is zero when taken over all (waveguide) space.

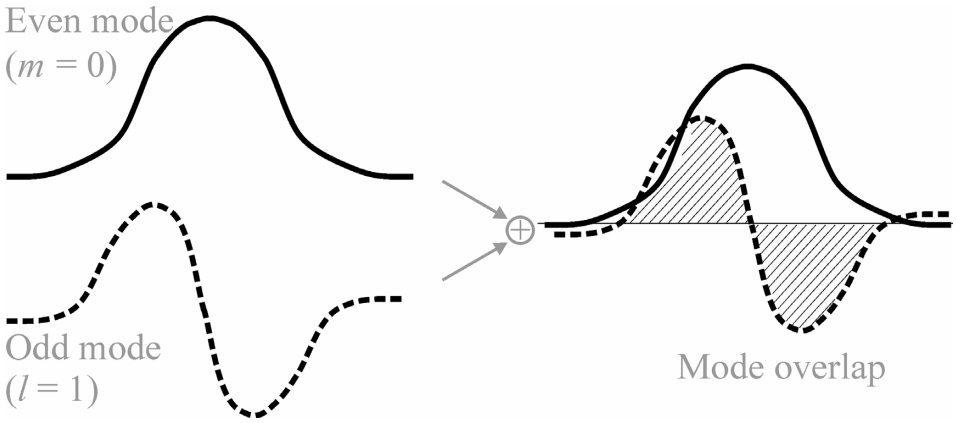


**Figure C. 2: Even (*m* =0) and odd (*l* = 1) modes (left), b) mode overlap resulting in zero overlap integral (right).**

Furthermore, the overlap integral between two modes with larger difference in order (e.g. mode $m = 0$ and $l = 2, 4, 6, \ldots$) has a low probability and a small overlap integral. In other words, without some external perturbation, it is unlikely for significant power to be transferred from a lower order mode $m$ to a higher order mode $l$ and vice versa over the short distances (a few mm) in the present devices.

What about power transfer between the $l = m$ modes for $m > 0$? The overlap integral in eqn. (C.8) can still be evaluated with $l = m$, but the propagation constant $\beta_l = \beta_m$ for modes $m > 0$ is modified according [86]:

$$\beta_m = n_{\text{Core}}\, k_0 \cos \theta_m, \tag{C.10}$$

where $\theta_m$ is the bounce angle obtained from the transcendental equation for the modes in a slab dielectric waveguide (see Appendix B). Also note that $\theta_m < \pi/2 - \theta_C$, where $\theta_C$ is the critical angle for total internal reflection as given by *Snell's law*.

So for higher-order modes $m > 0$, the propagation constant, $\beta_m$, decreases leading to an increase in the coupling coefficient, $\kappa_{l,m}$, according to eqn. (C.8) and a resulting decrease in the period, or characteristic coupling length, $L_C$, according to eqn. (C.6). In other words, higher-order modes will couple faster from *waveguide 1* to *waveguide 2* over shorter distances $L_C$.

Physically, the stronger coupling can be explained by looking at the bounce angle, $\theta_m$, of guided modes as they propagate through a waveguide (see Appendix B). Higher-order modes have larger bounce angles than the fundamental mode ($m = 0$). An extreme case is shown in Figure C. 3 where a higher-order mode is no longer guided (unguided mode). From Figure C. 3, it is clear that the unguided mode is not confined to the waveguide, but light leaks out into the cladding. Conceptually, this indicates that higher-order modes (including *guided* and unguided modes) are not as tightly confined to the core, which results in a larger evanescent field and hence stronger coupling.

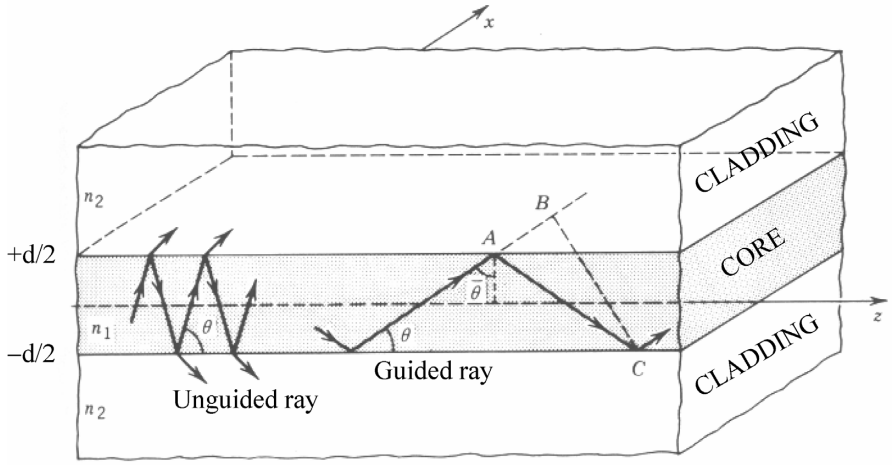


**Figure C. 3: Dielectric slab waveguide with guided ray (lower-order mode) and unguided mode (extreme case of higher-order mode).**

## C.4 Comments

Several observations regarding coupling between two non-identical and/or two multimode waveguides can be made. First, a small phase mismatch, $\Delta\beta$, between two waveguides will reduce the total coupled power according to eqn. (C.2). Second, the phase mismatch also increases the coupling coefficient so that complete coupling occurs over shorter characteristic coupling lengths, $L_C$, according to eqn. (C.5) compared to the phase-matched case.

Regarding multi-mode coupling, the following observations are made: 1) coupling between two modes $m_{Even}$ and $l_{Odd}$ can not occur (zero overlap integral), 2) without an external perturbation, coupling between two modes $m \neq l$ has a low probability of occurring, and 3) coupling between higher-order modes $m = l > 0$ can occur in special cases. Coupled-mode theory predicts 'stronger' coupling over shorter distances, $L_C$, due to the decreased $\beta_m$ for higher order modes according to eqn. (C.9). However, only a fraction of optical power is typically guided by higher-order modes in integrated optical waveguides due to the small size of these waveguides. Most higher-order modes are not guided due to the cut-off condition (see Appendix B). Therefore, coupling due to the higher-order modes is inefficient compared to the fundamental mode and results in smaller coupled-power, as indicated by the mode-coupling simulation in Figure C. 4. The simulation shows coupling between the $m = l$ modes for $m = 0$, 1, and 2 with the result that higher-order modes each contribute only one percent of the total power compared to the $m = 0$ mode.

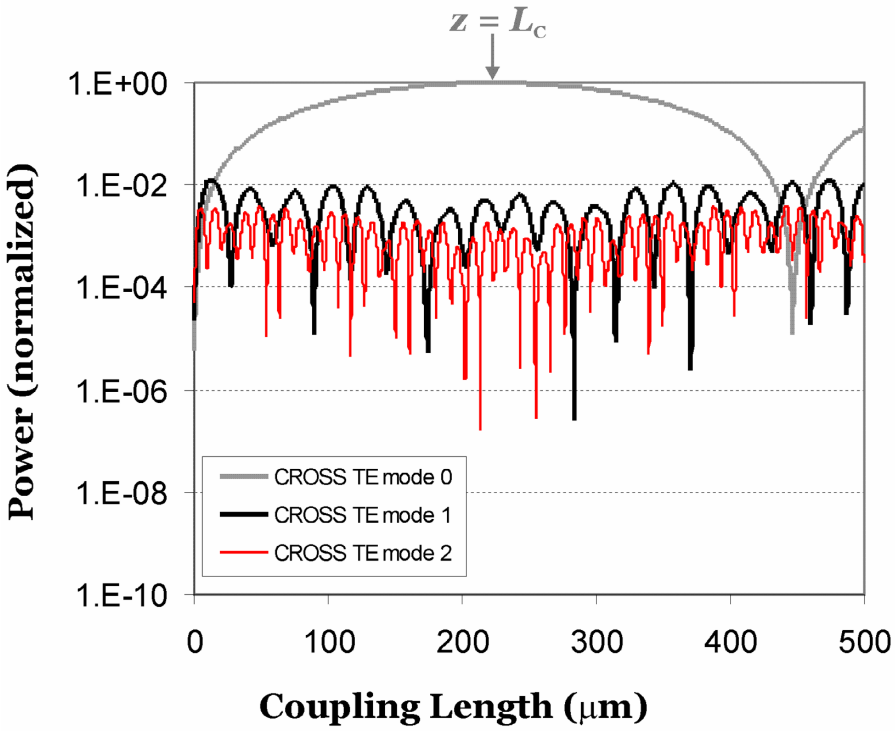


**Figure C. 4: BeamPROP simulation of coupled power for modes $m = 0, 1, 2$. The $m = 0$ mode exhibits the longest characteristic coupling length, $L_C$. However, it also contains most of the coupled power, with the $m = 1, 2$ modes only representing 1 % or less of the power in the $m = 0$ mode. Parameters: waveguide refractive index $n = 3.17$, width $w = 2$ μm, $gap = 60$ nm, $\lambda = 1550$ nm, TE-polarization.**

## C.4 Summary

In this appendix, evanescent coupling for two special cases was discussed: 1) waveguides with different propagation constant, $\beta_1$ and $\beta_2$, and 2) multi-mode waveguides. For both cases, coupling is enhanced in the sense that the characteristic coupling length, $L_C$ is reduced. However, in both cases the total coupled power is also reduced. Therefore, the MEMS coupler in this PhD research considers only single-mode coupling. The reader

should be aware, however, that it is possible to construct devices that couple specifically via multiple modes. These devices are called multi-mode interference couplers, or MMI couplers [110], and they typically have very short coupling lengths with a wide coupling region.

Page intentionally left blank.

# APPENDIX D

# DERIVATION OF CLASSICAL PULL-IN LIMIT AND PULL-IN VOLTAGE

## D.1 Introduction

In this appendix, the classical pull-in limit and pull-in voltage are derived. Similar treatments can be found in other texts [61]. Consider a parallel-plate capacitive actuator consisting of a movable top electrode with spring constant $k_{\text{Mechanical}}$ and a fixed bottom electrode (Figure D. 1). Application of a voltage between the two electrodes will result in an attractive electrostatic force, $F_{\text{Electrostatic}}$, between the two electrodes. As long as the mechanical restoring force, $F_{\text{Mechanical}}$, is large enough, the movable electrode will eventually reach a stable equilibrium point. However, if the applied voltage, $V$, is large enough so that $F_{\text{Electrostatic}} > F_{\text{Mechanical}}$, then "pull-in" occurs and the movable electrode will be pulled-in to the fixed electrode (i.e. *gap* goes to zero). The following analysis solves for the maximum displacement, $\Delta y$, that the movable electrode can be displaced before pull-in occurs. The maximum voltage, $V_{\text{PI}}$, which can be applied to this actuator before pull-in occurs, is also derived.

Consider the parallel-plate actuator in Figure D. 1. The normal force resulting from a voltage potential, $V$, placed across the two electrodes can be derived from the change in energy stored in the capacitor with respect to displacement, $\Delta y$:

$$F_{Electrostatic} = \frac{dW}{dy} = \frac{d}{dy}\left(\frac{1}{2}CV^2\right) = \frac{1}{2}\frac{\varepsilon_0 A}{\left(g_0 - \Delta y\right)^2}V^2 \tag{D.1}$$

where $\varepsilon_0$ is the free-space permittivity, $A$ is the area of the parallel plate capacitor, $g_0$ is the initial gap, and $V$ is the applied voltage. Note that this electrostatic force is the *normal* electrostatic force along the y-direction; tangential forces may also exist in other types of electrostatic actuators (i.e. comb-drive actuators), but these are not considered here. The mechanical restoring force is assumed to obey Hooke's law: $F_{\text{Mechanical}} = k_{\text{Mechanical}}\,\Delta y$.

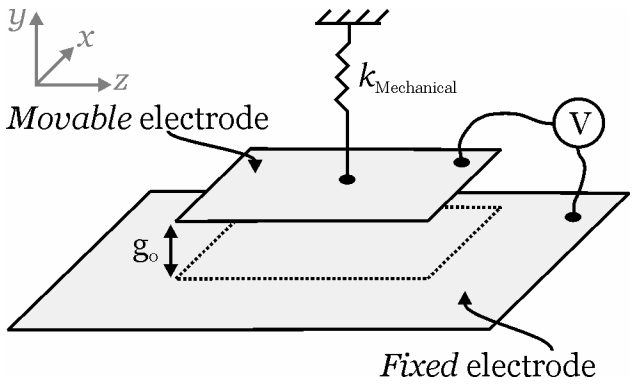


**Figure D. 1: Schematic of pull-in actuator with movable ($k_{\text{Mechanical}}$) and fixed electrode.**

## D.2 Pull-In Limit

The net force on the movable electrode is given by $F_{\text{Total}} = F_{\text{Electrostatic}} - F_{\text{Mechanical}}$. Substituting the electrostatic and mechanical force and expanding our terms, we obtain the 3rd-order polynomial:

$$F_{Total} = \left[ \frac{\varepsilon_0 A}{2\left( g_0{}^2 - 2g_0\Delta y + \Delta y^2 \right)} V^2 \right] - \left[ k\Delta y \right] \tag{D.2}$$

At equilibrium, $F_{\text{Electrostatic}} = F_{\text{Mechanical}}$ and eqn. (D.2) is set to zero:

$$\left[ \Delta y^3 - 2g_0\Delta y^2 + g_0{}^2\Delta y \right] - \left[ \frac{\varepsilon_0 A}{2k_{Mechanical}} V^2 \right] = 0 \tag{D.3}$$

To find the pull-in limit or instability, the *small incremental* displacement $\Delta y$ that yields a net force $F_{\text{Total}} > 0$ needs to be found. To do this, we take the derivative with respect to $\Delta y$ and solve for $\Delta y$ in terms of known parameters:

$$\frac{dF_{Total}}{d(\Delta y)} = 3\Delta y^2 - 4g_0\Delta y + g_0{}^2 = 0 \text{, with solution} \tag{D.4}$$

$$\Delta y = \left\{ g_0, \frac{1}{3} g_0 \right\} \tag{D.5}$$

Of the two solutions, only $\Delta y = g_0/3$ is a physical solution since the original gap is $g_0$ and $\Delta y = g_0$ implies that pull-in has already occurred. Therefore, the pull-in instability or maximum displacement before pull-in occurs is:

$$\boxed{\Delta y_{Pull-In} = \frac{1}{3} g_0} \tag{D.6}$$

## D.3 Pull-In Voltage

We are now interested in finding the voltage, $V$, that results in $F_{\text{Electrostatic}} > F_{\text{Mechanical}}$, or pull-in. As before, the approach is to equate the two forces, $F_{\text{Electrostatic}} = F_{\text{Mechanical}}$. However, we now solve for $V$ instead of $\Delta y$:

$$F_{Electrostatic} = F_{Mechanical} \tag{D.7}$$

$$\frac{1}{2}\frac{\varepsilon_0 A}{\left(g_0 - \Delta y\right)^2} V^2 = k_{Mechanical}\Delta y \tag{D.8}$$

$$V^2 = \frac{2k_{Mechanical}\Delta y}{\varepsilon_0 A}\left(g_0 - \Delta y\right)^2 \tag{D.9}$$

By substituting $\Delta y = g_0/3$, which is the previously derived pull-in limit, we can solve for the corresponding pull-in voltage:

$$\boxed{V_{PI} = \sqrt{\frac{8k_{Mechanical}g_0^{\,3}}{27\varepsilon_0 A}}} \tag{D.10}$$

## D.4 Comments and Summary

The above expressions for the pull-in limit, eqn. (D.6), and the pull-in voltage, eqn. (D.10) are approximations. The equations assume a parallel-plate capacitor with uniform gap at all times as well as a spring constant that does not change with displacement (no non-linear terms). Furthermore, the analysis neglects electrostatic

fringing fields in the parallel-plate capacitor. Nonetheless, eqns. (D.6) and (D.10) are useful for device design and enable fairly accurate device behavior to be extracted. If very high accuracy is required, it is best to use finite-element modeling.

Page intentionally left blank.

# APPENDIX E

# DERIVATION OF ELECTROSTATIC COMB-DRIVE FORCE

## E.1 Introduction

In this appendix, the comb-drive actuator electrostatic force is derived. Basic properties are highlighted based on the force-voltage-displacement relationships. Finally, some non-linear characteristics of comb-drive actuators in the large-displacement region are briefly discussed.

## E.2 Comb-Drive Force

A typical comb-drive actuator is shown in Figure E. 1. At zero applied voltage (Figure E. 1a), the comb-finger overlap is $x_0$. When a voltage is applied between the two sets of comb-fingers, the comb-fingers experience an attractive electrostatic force along the $x$-direction so as to maximize the capacitance.

The behavior of the comb-drive actuator can be analyzed by considering a single pair of comb-fingers, as in Figure E. 2. While each comb-finger will experience a normal force in the $z$-direction (Figure E. 2a), due to symmetry each finger will experience a zero net normal force. The reason for the zero net normal force comes from the fact that each comb-finger has two neighboring comb-fingers which exert equal and opposite normal forces. Consequently, the total normal force (in the $z$-direction) that each comb-finger experiences is zero. Therefore, unlike pull-in actuators that are dominated by the normal

force (Appendix D), comb-drives are dominated by the tangential force along the *x*-direction.

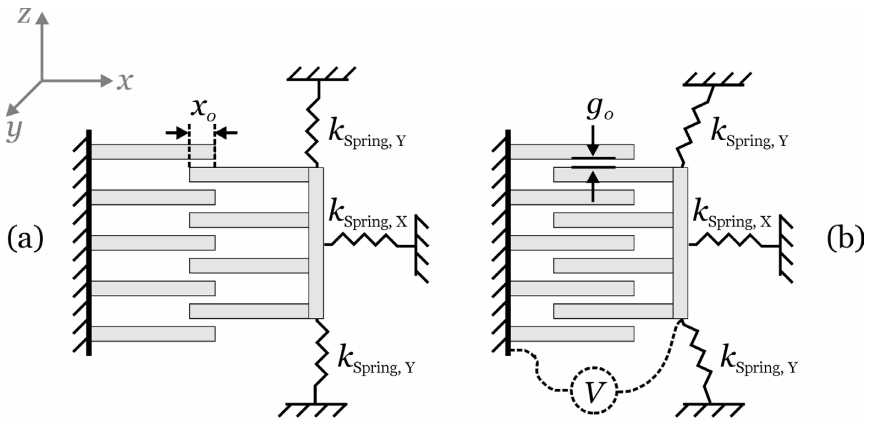


**Figure E. 1: Comb-drive actuator: a) V=0 (rest), b) V > 0 (actuation).**

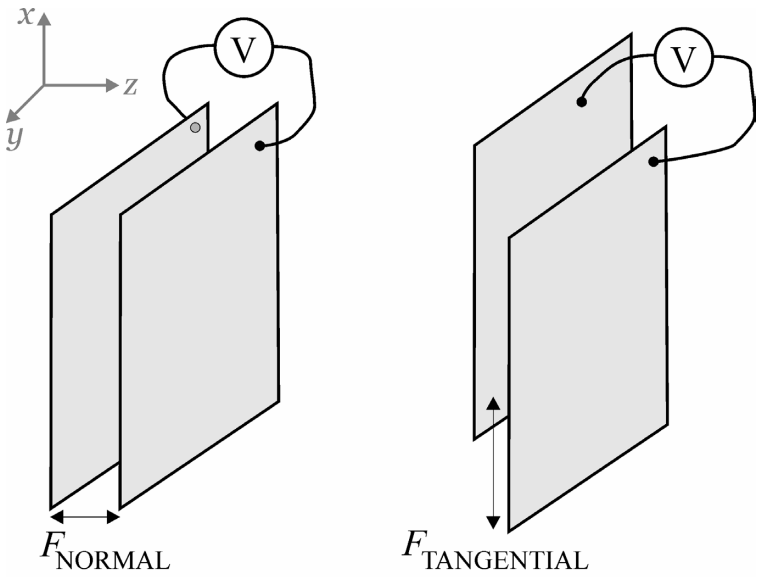


**Figure E. 2: Simplified schematic using two parallel-plate electrodes: a) normal force (left), b) tangential force (right). Comb-drive actuators take advantage of tangential forces.**

Much like the derivation of the pull-in actuator force (Appendix D), the comb-drive force is obtained by considering the energy stored in the comb-drive. The capacitance between two parallel plates (Figure E. 2) is given by:

$$C = \frac{\varepsilon_0 A}{gap} = \frac{\varepsilon_0 h x_0}{gap}, \tag{E.1}$$

where $\varepsilon_0$ is the free-space permittivity, $h$ is the finger height, $x_0$ is the initial finger overlap (Figure E. 1a), and *gap* is the finger separation along the $z$-direction.

The tangential force is found from the change in energy stored in the comb-drive capacitor with respect to displacement along the $x$-direction (Figure E. 1):

$$F_{Electrostatic} = F_{Tangential} = \frac{dW}{dx} = \frac{d}{dx}\left(\frac{1}{2}CV^2\right) = \frac{1}{2}\frac{\varepsilon_0 h}{g_0}V^2. \tag{E.2}$$

The total force for a comb-drive actuator with $N$ combs is given by:

$$\boxed{F_{Comb-drive} = 2N \times F_{Tangential} = N\frac{\varepsilon_0 h}{g_0}V^2}, \tag{E.3}$$

where the factor $2N$ accounts for the tangential force of the two neighboring comb-fingers (fixed combs) with respect to each of the $N$ fingers (movable combs). This can be visualized by considering the two additive normal forces, $F_{N1}$ and $F_{N2}$, as illustrated in Figure E. 3.

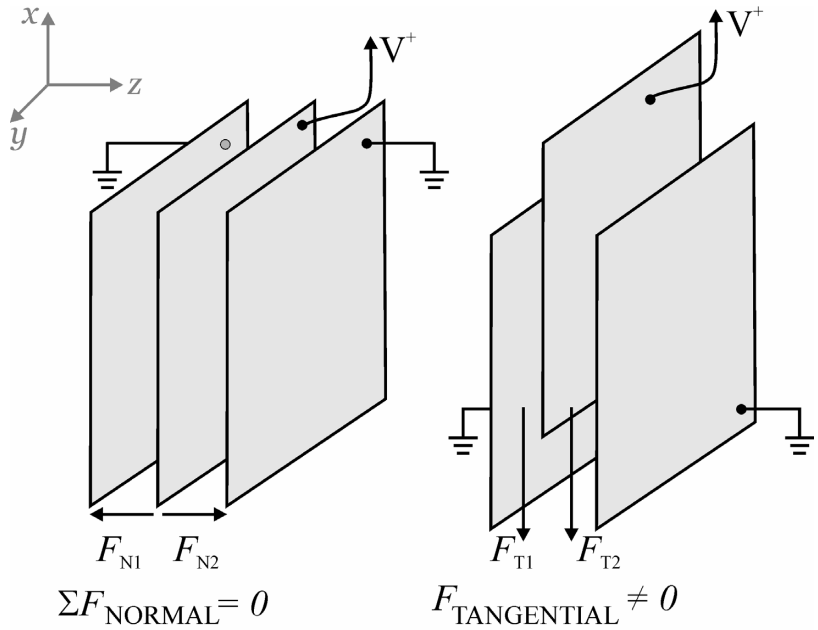


**Figure E. 3: Comb-drive actuator schematic illustrating zero net normal force and non-zero net tangential force.**

From eqn. (E.3), the comb-drive force is independent of displacement (*x*-direction) – assuming constant height and gap for the comb-dingers. Therefore, comb-drive actuators provide a constant electrostatic force and do not suffer from force-singularities as pull-in actuators do (Appendix D). Similar to pull-in actuators, the electrostatic force in comb-drive actuators increases with the square of the applied voltage. The final actuator displacement is determined by the mechanical restoring force of the spring ($k_{\text{Spring, X}}$) in Figure E. 1.

## E.3 Comments and Summary

The comb-drive force in eqn. (E.3) is an approximation since it does not take into account the electrostatic fringe fields. Also, eqn. (E.3) predicts a constant force with

respect to displacement, regardless of the magnitude of displacement. However, in reality, any small non-linear behavior of the suspensions along the *y*-direction ($k_{\text{Spring, y}}$ in Figure E. 1) or a spring compliance in the *z*-direction (small $k_{\text{Spring, Z}}$) will result in the comb no longer being centered and hence movement other than the *x*-direction for large displacements, $\Delta x$. This results in a non-zero normal electrostatic force so that the combs will snap-in (pull-in) [147, 190]. Therefore, the travel range, $\Delta x$, in real electrostatic comb-drive actuators will be limited. Nonetheless, eqn. (E3) presents a reasonably accurate analytical equation for predicting the available electrostatic force in comb-drive actuators and can be used for basic device design. For high-accuracy results, finite-element method (FEM) simulations can be used.

Page intentionally left blank.

# APPENDIX F

# MATLAB SCRIPT FOR CALCULATION OF FAST FOURIER TRANSFORM

## F.1 Introduction

This appendix shows the MATLAB script for calculating the frequency response from optical ringing data. The ringing data represents a damped sinusoid (Figure F. 1). The Fast Fourier Transform (FFT) is computed in MATLAB to obtain the resonance peak and spectral width (Figure F. 2). The script is based on a source code freely available [191].

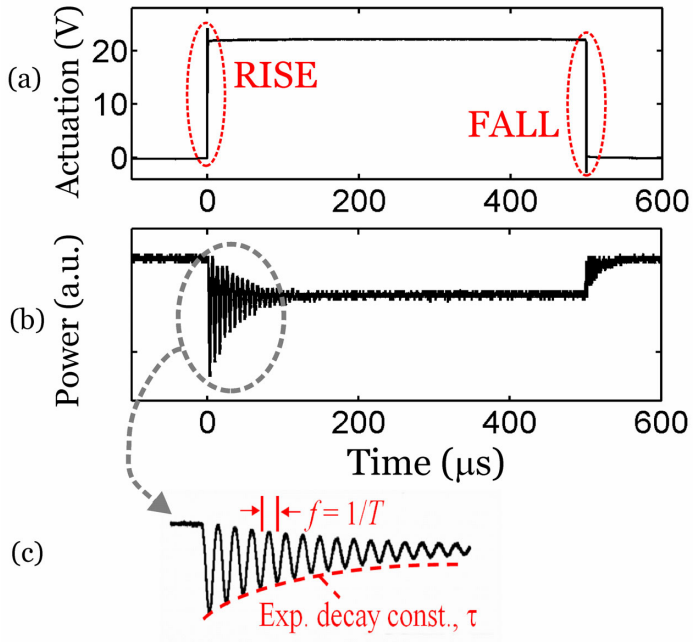


**Figure F. 1: Ringing Data: a) actuation, b) optical rining, c) detail of RISE data.**

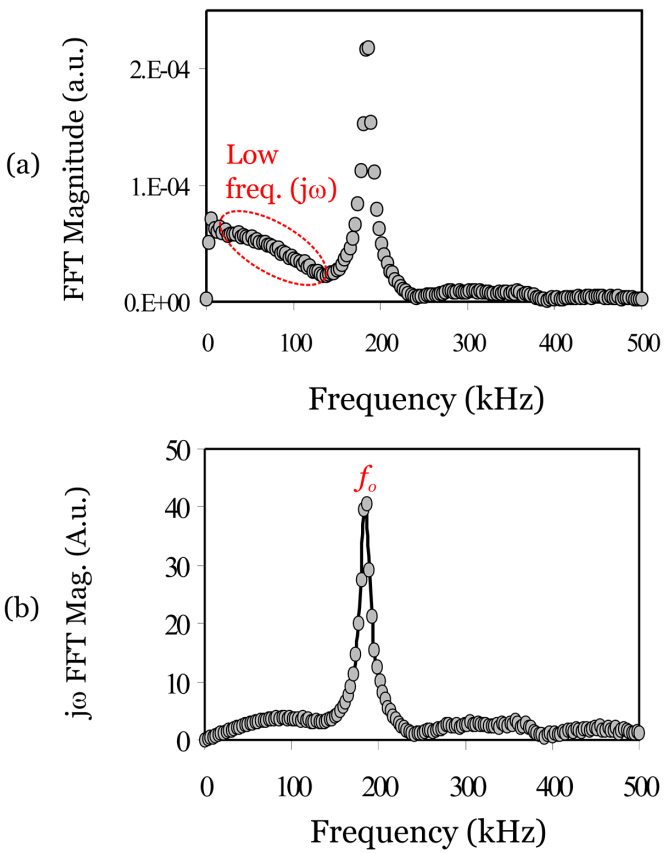


**Figure F. 2: a) Extracted FFT data, b) jω·FFT data.**

## F.2 MATLAB Source Code

```
% This script takes a 2-D matrix (column 1: time, column 2: data)
% and plots the frequency spectrum of the signal by computing the
% FFT.
%
% This program is based on a MATLAB script available at:
% Reference: http://www.utexas.edu/math/Matlab/Manual/tec6.2.html
%
% Marcel Pruessner
% April 3, 2005
%

data=dlmread('TEK00001_FALL.CSV')      % data filename: TEK00001_RISE.CSV
points=size(data);;                    % number of data points
   points=points(1,1);
time=max(data(:,1))-min(data(:,1));    % total sampling time
Fs=points/time;                        % sampling frequency: points/sampling_time
Fn=Fs/2;                               % Nyquist frequency
```

```
t=data(:,1);                          % time vector sampled at Fs Hz
x = data(:,2)-0.99*data(points,2);    % Pout: optical ringing data vector
NFFT=2.^(ceil(log(length(x))/log(2))); % Next highest power of 2 greater than length(x)
FFTX=fft(x,NFFT);                     % Take FFT, padding with zeros
                                      % length(FFTX)==NFFT

NumUniquePts = ceil((NFFT+1)/2);
FFTX=FFTX(1:NumUniquePts);            % FFT is symmetric, throw away second half
MX=abs(FFTX);                         % Take magnitude of X
MX=MX*2;                              % Multiply by 2 to take into account the fact that we
                                      % threw out second half of FFTX above

MX(1)=MX(1)/2;                        % Account for endpoint uniqueness
MX(length(MX))=MX(length(MX))/2;      % We know NFFT is even
MX=MX/length(x);                      % Scale the FFT so it is not a function of the length of x.
f=(0:NumUniquePts-1)*2*Fn/NFFT;       % plot frequency vs. fft
f1=f;
MX1=MX;

% Plot FFT vs. frequency: Unit Step Response
figure
plot(f1/1000, MX1, 'o-');
xlabel('Frequency (kHz)')

% Plot f*FFT ("jw*FFT") vs. frequency: Quasi Impulse Response
figure
plot(f1/1000, f1.*rot90(MX1), 'o-');
xlabel('Frequency (kHz)')

% Write out FFT data
f=rot90(rot90(rot90(f1)));
meas=[f, MX1];
csvwrite('FFT_FALL.CSV', meas)      % FFT_FALL.CSV = filename
```

## F.3 Summary

This script reads in a data file (e.g. optical ringing data) and computes and plots the FFT and spectral response. This represents the unit step response. The approximate impulse response is computed by frequency multiplication, e.g. jω•FFT.

Page intentionally left blank.

# BIBLIOGRAPHY


[1] E. Pennings, G. Khoe, -D., M. K. Smit, and T. Staring, "Integrated-optic versus microoptic devices for fiber-optic telecommunication systems: a comparison," *IEEE Journal of Selected Topics in Quantum Electronics*, vol. 2, pp. 151-164, 1996.

[2] E. Ollier, "Optical MEMS devices based on moving waveguides," *IEEE J. Sel. Top. In Quantum Electronics*, vol. 8, pp. 155-162, 2002.

[3] A. Neukermans and R. Ramaswami, "MEMS technology for optical networking applications," *IEEE Comm. Mag.*, pp. 62-69, 2001.

[4] H. Fujita and H. Toshiyoshi, "Optical MEMS," *IEICE Trans. Elec.*, vol. E83, pp. 1427-1430, 2000.

[5] J. A. Walker, "The future of MEMS in telecommunications networks," *J. Micromech. Microeng.*, vol. 10, pp. R1-R7, 2000.

[6] S. Greek, K. Hjort, J.-A. Schweitz, C. Seassal, J. L. Leclercq, M. Gendry, M. P. Besland, P. Viktorovitch, C. Figuet, V. Souliere, and Y. Monteil, "The strength of indium phosphide based microstructures," *SPIE*, vol. 3008, pp. 251-257, 1997.

[7] M. W. Pruessner, T. King, D. Kelly, R. Grover, L. C. Calhoun, and R. Ghodssi, "Mechanical Property Measurement of InP-based MEMS for Optical Communications," *Sensors and Actuators*, vol. A105, pp. 190-200, 2003.

[8] M. W. Pruessner, "Toward III-V optical MEMS: mechanical property measurement of indium phosphide using nanoindentation, beam bending, and electrostatic testing methods (M. S. Thesis)," in *Department of Electrical and Computer Engineering*. College Park: University of Maryland, 2002, pp. 135.

[9] D. Kelly, M. W. Pruessner, K. Amarnath, M. Datta, S. Kanakaraju, L. C. Calhoun, and R. Ghodssi, "Monolithic Suspended Optical Waveguides for InP MEMS," *IEEE Photonics Technology Letters*, vol. 16, pp. 1298-1300, 2004.

[10] T. Mizuno, H. Takahashi, T. Kitoh, M. Oguma, T. Kominato, and T. Shibata, "Mach–Zehnder interferometer switch with a high extinction ratio over a wide wavelength range," *Optics Letters*, vol. 30, pp. 251-253, 2005.

[11] Q. Lai, W. Hunziker, and H. Melchior, "Low-power compact 2 x 2 thermooptic silica-on-silicon waveguide switch with fast response," *IEEE Photonics Technology Letters*, vol. 10, pp. 681-683, 1998.

[12] T. Goh, M. Yasu, K. Hattori, A. Himeno, M. Okuno, and Y. Ohmori, "Low-loss and high extinction ratio silica-based strictly non-blocking 16 x 16 thermooptic matrix switch," *IEEE Photonics Technology Letters*, vol. 10, pp. 810-811, 1998.

[13] M.-H. Lee, Y. H. Min, S. Park, J. J. Ju, J. Y. Do, and S. K. Park, "Fully Packaged Polymeric Four Arrayed 2x2 Digital Optical Switch," *IEEE Photonics Technology Letters*, vol. 14, pp. 615-617, 2002.

[14] H. Y. Wong, M. Sorel, A. C. Bryce, J. H. Marsh, and J. M. Arnold, "Monolithically integrated InGaAs–AlGaInAs Mach–Zehnder interferometer optical switch using quantum-well intermixing," *IEEE Photonics Technology Letters*, vol. 17, pp. 783-785, 2005.

[15] R. G. Hunsperger, *Integrated Optics: Theory and Technology*, Fifth ed. Berlin: Springer, 2002.

[16] T. C. Huang, G. J. Simonis, M. Stead, and R. P. Leavitt, "A Y-Junction Optical Switch Based On Field-Induced Control of Refractive Index," *IEEE Photonics Technology Letters*, vol. 5, pp. 712-715, 1993.
[17] M. N. Khan, R. Monnard, B. I. Miller, E. C. Burrows, and B. A., "A Novel High-Speed and Wavelength Insensitive Y-Branch Modulator with Reduced and Controllable Chirp," *IEEE Photonics Technology Letters*, vol. 11, pp. 1247-1249, 1999.
[18] S. S. Saini, F. G. Johnson, D. R. Stone, W. Zhou, H. Shen, and M. Dagenais, "A 2 x 2 crosspoint switch fabricated on the passive active resonant coupler (PARC) platform," *IEEE Photonics Technology Letters*, vol. 13, pp. 203-205, 2001.
[19] R. W. Boyd, *Nonlinear Optics*, 2nd ed. Amsterdam: Academic Press, 2003.
[20] D. O. Culverhouse, T. A. Birks, S. G. Farwell, and P. S. J. Russell, "3x3 All-Fiber Routing Switch," *IEEE Photonics Technology Letters*, vol. 9, pp. 333-335, 1997.
[21] S. G. Farwell, M. N. Zervas, and R. I. Laming, "2x2 Fused Fiber Null Couplers with Asymmetric Waist Cross Sections for Polarization Independent (0.01 dB) Switching," *Journal of Lightwave Technology*, vol. 16, pp. 1671-1679, 1998.
[22] S. Krishnamurthya and P. V. Santos, "High-contrast optical modulation by surface acoustic waves," *Applied Physics Letters*, vol. 83, pp. 2548-2550, 2003.
[23] G. Aubin, J. Sapriel, V. Y. Molchanov, R. Gabet, P. Grosso, S. Gosselin, and Y. Jaouen, "Multichannel acousto-optic cells for fast optical crossconnect," *Electronics Letters*, vol. 40, pp. 448-449, 2004.
[24] V. R. Almeida and M. Lipson, "Optical bistability on a silicon chip," *Optics Letters*, vol. 29, pp. 2387-2389, 2004.
[25] A. Hache and M. Bourgeois, "Ultrafast all-optical switching in a silicon-based photonic crystal," *Applied Physics Letters*, vol. 77, pp. 4089-4091, 2000.
[26] A. Sharkawy, S. Shi, and D. W. Prather, "Electro-optical switching using coupled photonic crystal waveguides," *Optics Express*, vol. 10, pp. 1048-1059, 2002.
[27] T. A. Ibrahim, W. Cao, Y. Kim, J. Li, J. Goldhar, P.-T. Ho, and C. H. Lee, "All-Optical Switching in a Laterally Coupled Microring Resonator by Carrier Injection," *IEEE Photonics Technology Letters*, vol. 15, pp. 36-38, 2003.
[28] L. Eldada, "Advances in telecom and datacom optical components," *Optics Engineering*, vol. 40, pp. 1165–1178, 2001.
[29] http://www.analog.com/, "Analog Devices: iMEMS," September 13, 2004.
[30] http://www.dlp.com/dlp_technology, "Texas Instruments' DLP Technology: Digital Light Processing for DLP Projection," December 1, 2003.
[31] H. X. M. Huang, C. A. Zorman, M. Mehregany, and M. L. Roukes, "Nanodevice motion at microwave frequencies," *Nature*, vol. 421, pp. 496-497, 2003.
[32] G. T. A. Kovacs, N. I. Maluf, and K. E. Petersen, "Bulk Micromachining of Silicon," *Proceedings of the IEEE*, vol. 86, pp. 1536-1551, 1998.
[33] J. M. Bustillo, R. T. Howe, and R. S. Muller, "Surface Micromachining for Microelectromechanical Systems," *Proceedings of the IEEE*, vol. 86, pp. 1552-1574, 1998.
[34] K. Ikeda, H. Kuwayama, T. Kobayashi, T. Watanabe, T. Nishikawa, T. Yoshida, and K. Harada, "Silicon pressure sensor integrates resonant strain gauge on diaphragm," *Sensors and Actuators*, vol. A21-23, pp. 146-150, 1990.

[35] http://www.freescale.com/webapp/sps/site/overview.jsp?nodeId=01126944421818, "Freescale Semiconductor: MEMS Overview," September 14, 2004.
[36] N. V. Lavrik, M. J. Sepaniak, and P. G. Datskosa, "Cantilever transducers as a platform for chemical and biological sensors," *Review of Scientific Instruments*, vol. 75, pp. 2229-2253, 2004.
[37] P. L. Chapman and P. T. Krein, "Smaller is better: Perspectives on micromotors and electric drives," in *IEEE Industry Applications Magazine*, 2003, pp. 62-67.
[38] C. Livermore, A. R. Forte, T. Lyszczarz, S. D. Umans, A. A. Ayon, and J. H. Lang, "A High-Power MEMS Electric Induction Motor," *Journal of Microelectromechanical Systems*, vol. 13, pp. 465-471, 2004.
[39] M. Barbic, J. J. Mock, A. P. Gray, and S. Schultz, "Electromagnetic micromotor for microfluidics applications," *Applied Physics Letters*, vol. 79, pp. 1399-1401, 2001.
[40] M. Parameswaran, A. M. Robinson, D. L. Blackburn, M. Gaitan, and J. Geist, "Micromachined thermal radiation emitter from a commercial CMOS process," *IEEE Electron Device Letters*, vol. 12, pp. 57-59, 1991.
[41] S. C. Koa, Y. C. Kimb, S. S. Leeb, S. H. Choic, and S. R. Kim, "Micromachined piezoelectric membrane acoustic device," *Sensors and Actuators*, vol. A103, pp. 130-134, 2003.
[42] V. Lien, Y. Berdichevsky, and Y.-H. Lo, "A prealigned process of integrating optical waveguides with microfluidic devices," *IEEE Photonics Technology Letters*, vol. 16, pp. 1525-1527, 2004.
[43] E. Ollier, "Optical MEMS devices based on moving waveguides," *IEEE Journal on Selected Topics in Quantum Electronics*, vol. 8, pp. 155-162, 2002.
[44] T. G. McDonald and L. A. Yoder, "Digital micromirror devices make projection displays," *Laser Focus World*, vol. 33, pp. SUPL5-8, 1997.
[45] L. Y. Lin, E. L. Goldstein, and R. W. Tkach, "Free-space micromachined optical switches for optical networking," *IEEE Journal of Selected Topics in Quantum Electronics*, vol. 5, pp. 4-9, 1999.
[46] P. B. Chu, I. Brener, C. Pu, S.-S. Lee, J. I. Dadap, S. Park, K. Bergman, N. H. Bonadeo, T. Chau, M. Chou, R. A. Doran, R. Gibson, R. Harel, J. J. Johnson, C. D. Lee, D. R. Peale, B. Tang, D. T. K. Tong, M.-J. Tsai, Q. Wu, W. Zhong, E. L. Goldstein, L. Y. Lin, and J. A. Walker, "Design and Nonlinear Servo Control of MEMS Mirrors and Their Performance in a Large Port-Count Optical Switch," *Journal of Microelectromechanical Systems*, vol. 14, pp. 261-273, 2005.
[47] D. T. Neilson, R. Frahm, P. Kolodner, C. A. Bolle, R. Ryf, J. Kim, A. R. Papazian, C. J. Nuzman, A. Gasparyan, N. R. Basavanhally, V. A. Aksyuk, and J. V. Gates, "256 256 Port Optical Cross-Connect Subsystem," *Journal of Lightwave Technology*, vol. 22, pp. 1499-1509, 2004.
[48] "Small wonder: MEMS will power optical Internet. Lucent Technologies' WaveStar LambdaRouter," in *Computer*, vol. 33, 2000, pp. 23-.
[49] R. T. Chen, H. Nguyen, and M. C. Wu, "A High-Speed Low-Voltage Stress-Induced Micromachined 2x2 Optical Switch," *IEEE Photonics Technology Letters*, vol. 11, pp. 1396-1398, 1999.

[50] E. Ollier, P. Labeye, and F. Revol, "Micro-opto mechanical switch integrated on silicon," *Electronics Letters*, vol. 31, pp. 2003-2005, 1995.
[51] T. Bakke, C. P. Tigges, J. J. Lean, C. T. Sullivan, and O. B. Spahn, "Planar microoptomechanical waveguide switches," *IEEE Journal of Selected Topics in Quantum Electronics*, vol. 8, pp. 64-72, 2002.
[52] L. Dellmann, W. Noell, C. Marxer, K. Weible, M. Hoffmann, and N. F. de Rooij, "4x4 matrix switch based on MEMS switches and integrated waveguides," presented at Proceedings 11th International Conference on Solid-State Sensors and Actuators, Munich, Germany, pp., 2001.
[53] M. Makihara, "Microelectromechanical intersecting waveguide optical switch based on thermo-capillarity," presented at 2000 IEEE/LEOS Conference on Optical MEMS, pp. 33-34, 2000.
[54] D. T. Fuchs, H. B. Chan, H. R. Stuart, F. Baumann, D. Greywall, M. E. Simon, and A. Wong-Foy, "Monolithic integration of MEMS-based phase shifters and optical waveguides in silicon-on-insulator," *Electronics Letters*, vol. 40, pp. 142-143, 2004.
[55] M. C. M. Lee and M. C. Wu, "A MEMS-Actuated Tunable Microdisk Resonator," presented at IEEE Optical MEMS Conference, pp. 28-29, 2003.
[56] G. Keiser, *Optical fiber communications*, Third ed. Boston: McGraw Hill, 2000.
[57] Y. Miyamoto, M. Yoneyama, and T. Otsuiji, "40-Gbit/s TDM transmission technologies based on ultra-high-speed IC's," *IEEE Journal of Solid-State Circuits*, vol. 34, pp. 1246-1253, 1999.
[58] *Semiconductors: Group IV Elements and III-V Compounds*. New York: Springer Verlag, 1991.
[59] S. M. Sze, *Semiconductor Devices: Physics and Technology*. New York: John Wiley and Sons, 1985.
[60] S. Adachi, *Physical properties of III-V semiconductor compounds*. New York: Wiley and Sons, 1992.
[61] S. D. Senturia, *Microsystem Design*. Boston, MA: Kluwer Academic, 2000.
[62] V. Swaminathan and A. T. Macrander, *Materials aspects of GaAs and InP based structures*. Englewood Cliffs, New Jersey: Prentice Hall, 1991.
[63] M. J. A. de Dooda, A. Polman, T. Zijlstra, and E. W. J. M. van der Drift, "Amorphous silicon waveguides for microphotonics," *Journal of Applied Physics*, vol. 92, pp. 649-653, 2002.
[64] B. Bhushan and V. N. Koinkar, "Microtribological studies of doped single-crystal silicon and polysilicon films for MEMS devices," *Sensors and Actuators*, vol. A57, pp. 91-102, 1996.
[65] Y. G. Gogotsi, V. Domnich, S. N. Dub, A. Kailer, and K. G. Nickel, "Cyclic nanoindentation and Raman microspectroscopy of phase transformation in semiconductors," *Journal of Materials Research*, vol. 15, pp. 871-879, 2000.
[66] K. Hjort, "Sacrificial etching of III–V compounds for micromechanical devices," *Journal of Micrmechanics and Microengineering*, vol. 6, pp. 370-375, 1996.
[67] C. Seassal, J.-L. Leclercq, and P. Viktorovitch, "Fabrication of InP-based freestanding microstructures by selective surface micromachining," *Journal of Micromechanics and Microengineering*, vol. 6, pp. 261-265, 1996.

[68] J. L. Leclercq, M. Garrigues, X. Letartre, C. Seassal, and P. Viktorovitch, "InP-based MOEMS and related topics," *Journal of Micromechanics and Microenginering*, vol. 10, pp. 287-292, 2000.

[69] A. Spisser, R. Ledantec, C. Seassal, J.-L. Leclercq, T. Benyattou, D. Rondi, R. Blondeau, G. Guillot, and P. Viktorovitch, "Highly selective and widely tunable 1.55 um InP/air-gap micromachined Fabry–Perot filter for optical communications," *IEEE Photonics Technology Letters*, vol. 10, pp. 1259-1261, 1998.

[70] R. Ledantec, T. Benyattou, G. Guillot, A. Spisser, C. Seassal, J. L. Leclercq, P. Viktorovitch, D. Rondi, and R. Blondeau, "Tunable microcavity based on InP–air Bragg mirrors," *IEEE Journal of Selected Topics in Quantum Electronics*, vol. 5, pp. 111-114, 1999.

[71] P. Bondavalli, R. LeDantec, and T. Benyattou, "Influence of the involuntary underetching on the mechanical properties of tunable Fabry–Pérot filters for optical communications," *Journal of Microelectromechanical Systems*, vol. 10, pp. 298-301, 2001.

[72] P. Bondavalli, T. Benyattou, M. Garrigues, J. L. Leclercq, S. Jourba, C. Pautet, and X. Hugon, "Opto-mechanical design of tuneable InP-based Fabry-Perot filter for gas analysis," *Sensors and Actuators*, vol. A94, pp. 136-141, 2001.

[73] J. Daleiden, N. Chitica, and M. Strassner, "Tunable InP-based microcavity devices for optical communication systems," *Sensors and Materials*, vol. 14, pp. 35-44, 2002.

[74] S. Irmer, J. Daleiden, V. Rangelov, C. Prott, F. Römer, M. Strassner, A. Tarraf, and H. Hillmer, "Ultralow Biased Widely Continuously Tunable Fabry–Pérot Filter," *IEEE Photonics Technology Letters*, vol. 15, pp. 434-436, 2003.

[75] M. Strassner, J. C. Esnault, L. Leroy, J.-L. Leclercq, M. Garrigues, and I. Sagnes, "Fabrication of ultrathin and highly flexible InP-based membranes for microoptoelectromechanical systems at 1.55 um," *IEEE Photonics Technology Letters*, vol. 17, pp. 804-806, 2005.

[76] D. P. Kelly, "Monolithic suspended optical waveguides for InP MOEMS," in *Electrical and Computer Engineering*. College Park: University of Maryland, 2005.

[77] W. S. N. Trimmer and K. J. Gabriel, "Design Considerations for a Practical Electrostatic Micro-Motor," *Sensors and Actuators*, vol. 11, pp. 189-206, 1987.

[78] M. W. Pruessner, T. King, D. Kelly, and R. Ghodssi, "Micro-Mechanical Characterization of Indium Phosphide (InP) for Active Optical MEMS Applications," presented at American Vacuum Society 49th International Symposium, Denver, CO, pp., 2002.

[79] K. Fricke, E. Peiner, M. Chahoud, and A. Schlachetzki, "Fractures properties of InP microcantilevers by hetero-micromachining," *Sensors and Actuators*, vol. A76, pp. 395-402, 1999.

[80] N. Chitica, M. Strassner, and J. Daleiden, "Quantitative evaluation of growth-induced residual stress in InP epitaxial micromechanical structures," *Applied Physics Letters*, vol. 77, pp. 202-204, 2000.

[81] M. Strassner, J. Daleiden, N. Chitica, D. Keiper, D. Stalnacke, S. Greek, and K. Hjort, "III-V semiconductor material for tunable Fabry-Perot filters for coarse and dense WDM systems," *Sensors and Actuators*, vol. A85, pp. 249-255, 2000.

[82] D. Arivouli, R. Fornari, and J. Kumar, "Microhardness studies of doped and undoped InP crystals," *Journal of Material Science Letters*, vol. 10, pp. 559-561, 1991.

[83] K. E. Petersen, "Silicon as a mechanical material," *Proceedings of the IEEE*, vol. 70, pp. 420-457, 1982.

[84] P. M. Osterberg and S. D. Senturia, "M-Test: a test chip for MEMS material property measurement using electrostatically actuated test structures," *Journal of Microelectromechanical Systems*, vol. 6, pp. 107-118, 1997.

[85] R. Grover, T. A. Ibrahim, S. Kanakaraju, L. Lucas, L. C. Calhoun, and P.-T. Ho, "A tunable GaInAsP-InP optical microring notch filter," *IEEE Photonics Technology Letters*, vol. 16, pp. 467-469, 2004.

[86] B. E. A. Saleh and M. C. Teich, *Fundamentals of Photonics*, 1st ed. New York: Wiley and Sons, 1991.

[87] R. J. Deri and E. Kapon, "Low-loss III-V semiconductor optical waveguides," *IEEE Journal of Quantum Electronics*, vol. 27, pp. 626-40, 1991.

[88] D. Garbuzov, L. Xu, S. R. Forrest, R. Menna, R. Martinelli, and J. C. Connolly, "1.5 um wavelength SCH-MQW InGaAsP/InP broadenedwaveguide laser diodes with low internal loss and high output power," *Electronics Letters*, vol. 32, pp. 1717-1719, 1996.

[89] D. Heo, I. K. Han, J. I. Lee, and J. Jeong, "Study on InGaAsP–InGaAs MQW-LD With Symmetric and Asymmetric Separate Confinement Heterostructure," *IEEE Photonics Technology Letters*, vol. 16, pp. 1801-1803, 2004.

[90] R. E. Nahory, M. A. Pollack, W. D. J. Johnston, and R. L. Barns, "Band gap versus composition and demonstration of Vegard's law for In(1-x)Ga(x)As(y)P(1-y) lattice matched to InP," *Applied Physics Letters*, vol. 33, pp. 659-661, 1978.

[91] S. Adachi, "Refractive indices of III-V compounds: key properties of InGaAsP relevant to device design," *Journal of Applied Physics*, vol. 53, pp. 5863-5869, 1982.

[92] C. L. Chiang, S. Wagner, and A. A. Ballman, "Optical absorption tail in InP:Mn from surface photovoltage measurements," *Applied Physics Letters*, vol. 43, pp. 1113-1115, 1983.

[93] B. Broberg and S. Lindgren, "Refractive index of In(1-x)Ga(x)As(y)P(1-y) layers and InP in the transparent wavelength region," *Journal of Applied Physics*, vol. 55, pp. 3376-3381, 1984.

[94] H. Burkhard, "Effective phase and group indices for In(1-x)Ga(x)P(1-y)As(y) / InP waveguide structures," *Journal of Applied Physics*, vol. 55, pp. 503-508, 1984.

[95] E. Gini and H. Melchior, "Thermal dependence of the refractive index of InP measured with integrated optical demultiplexer," *Journal of Applied Physics*, vol. 79, pp. 4335-4337, 1996.

[96] P. H. Holloway and G. E. McGuire, *Handbook of compound semiconductors: growth, processing, characterization, and devices*. Park Ridge, NJ: Noyes Publications, 1995.

[97] R. Grover, T. A. Ibrahim, T. N. Ding, Y. Leng, L.-C. Kuo, S. Kanakaraju, K. Amarnath, L. C. Calhoun, and P.-T. Ho, "Laterally coupled InP-based single-mode microracetrack notch filter," *IEEE Photonics Technology Letters*, vol. 15, pp. 1082-1084, 2003.
[98] H. Lapierre, T. Okada, B. J. Robinson, D. A. Thompson, and G. C. Weatherly, "Spinodal-like decomposition of InGaAsP/(100) InP grown by gas source molecular beam epitaxy," *Journal of Crystal Growth*, vol. 155, pp. 1-15, 1995.
[99] ArchChemicals, "Oir906 Series Photoresists, http://www.archmicro.com/products/oir906.PDF," July 22, 2004.
[100] J. Kaindl, S. Sotier, and G. Franz, "Dry etching of III/V semiconductors: fine tuning of pattern transfer and process control," *Journal of the Electrochemical Society*, vol. 142, pp. 2418-2424, 1995.
[101] S. J. Pearton, U. K. Chakrabarti, A. Katz, A. P. Perley, W. S. Hobson, and C. Constantine, "Comparison of CH4/H2/Ar reactive ion etching and electron cyclotron resonance plasma etching of In-based III-V alloys," *Journal of Vacuum Science and Technology*, vol. B9, pp. 1421-1432, 1991.
[102] R. Grover, J. H. Hryniewicz, O. S. King, and V. Van, "Process development of methane–hydrogen–argon-based deep dry etching of InP for high aspect-ratio structures with vertical facet-quality sidewalls," *Journal of Vacuum Science and Technology*, vol. B19, pp. 1071-1023, 2001.
[103] A. G. Baca, F. Ren, J. C. Zolper, R. D. Briggs, and S. J. Pearton, "A Survery of Ohmic Contacts to III-V Compound Semiconductors," *Thin Solid Films*, vol. 308-309, pp. 599-606, 1997.
[104] R. Maboudian and R. Howe, "Critical Review: Adhesion in surface micromechanical structures," *Journal of Vacuum Science and Technology*, vol. B15, pp. 1-20, 1997.
[105] D. M. Tanner, "Reliability of Surface Micromachined MicroElectroMechanical Systems," presented at 22nd International Conference on Microelectronics (MIEL2000), Nis, Serbia, pp. 97-104, 2000.
[106] K. Okamoto, *Fundamentals of Optical Waveguides*, 1st ed. San Diego: Academic Press, 2000.
[107] C. R. Pollock, *Fundamentals of Optoelectronics*. Chicago: Irwin, 1995.
[108] A. Yariv, "Coupled-mode theory for guided-wave optics," *IEEE Journal of Quantum Electronics*, vol. QE-9, pp. 919-933, 1973.
[109] F. Chollet, M. d. Labacherie, and H. Fujita, "Compact evanescent optical switch and attenuator with electromechanical actuation," *IEEE Journal of Selected Topics in Quantum Electronics*, vol. 5, pp. 52-59, 1999.
[110] L. B. Soldano and E. C. M. Pennings, "Optical Multi-Mode Interference Devices Based On Self-Imaging: Principles and Applications," *Journal of Lightwave Technology*, vol. 13, pp. 615-626, 1995.
[111] V. R. Chinni, T. C. Huang, P. K. A. Wai, C. R. Menyuk, and G. J. Simonis, "Performance of field-induced directional coupler switches," *IEEE Journal of Quantum Electronics*, vol. 31, pp. 2068-2074, 1995.
[112] M. Asobe, H. Itoh, T. Miyazawa, and T. Kanamori, "Efficient and ultrafast all-optical switching using high An, small core chalcogenide glass fibre," *Electronics Letters*, vol. 29, pp. 1966-1968, 1993.

[113] A. E. Attard, "Analysis of an optically controlled photonic switch," *Applied Optics*, vol. 38, pp. 3239-3248, 1999.
[114] N. Takato, J. Kaname, Y. Mitsuho, H. Toba, and M. Kawachi, "Silica-Based Single-Mode Waveguides on Silicon and their Application to Guided-Wave Optical Interferometers," *Journal of Lightwave Technology*, vol. 6, pp. 1003-1010, 1988.
[115] M. Thorhauge, L. H. Frandsen, and P. I. Borel, "Efficient photonic crystal directional couplers," *Optics Letters*, vol. 28, pp. 1525-1527, 2003.
[116] B. Liu, A. Shakouri, P. Abraham, B.-G. Kim, A. W. Jackson, and J. E. Bowers, "Fused vertical couplers," *Applied Physics Letters*, vol. 72, pp. 2637-2638, 1998.
[117] D. An, Z. Shi, L. Sun, J. M. Taboada, Q. Zhou, X. Lu, R. T. Chena, S. Tang, H. Zhang, W. H. Steier, A. Ren, and L. R. Dalton, "Polymeric electro-optic modulator based on 1Ã2 Y-fed directional coupler," *Applied Physics Letters*, vol. 76, pp. 1972-1974, 2000.
[118] F. Chollet, M. d. Labalecherie, and H. Fujita, "Electromechanically actuated evanescent optical switch and polarization independent attenuator," presented at IEEE Conference on Microelectromechanical Systems, pp. 476-481, 1998.
[119] G. J. Veldhuis, C. Gui, T. Nauta, T. M. Koster, J. W. Berenschot, P. V. Lambeck, J. G. E. Gardeniers, and M. Elwenspoek, "Mechano-optical waveguide on–off intensity modulator," *Optics Letters*, vol. 23, pp. 1532-1534, 1998.
[120] K. Hane, J.-H. Song, M. Sasaki, Y. Taguchi, and H. Shimoda, "Photolithography on optical fiber and micro-fabrication of fiber-optic devices controlling evanescent field," presented at 12th International Conference on Solid-State Sensors, Actuators, and Microsystems (Transducers '05), Boston, MA, pp. 198-201, 2003.
[121] M. L. Povinelli, R. E. Bryant, S. Assefa, S. G. Johnson, S. Fan, A. A. Erchak, G. S. Petrich, E. Lidorikis, J. D. Joannopoulos, L. A. Kolodziejski, and E. P. Ippen, "Design of a nanoelectromechanical high-index-contrast guided wave optical switch for single-mode operation at 1.55 um," *IEEE Photonics Technology Letters*, vol. 15, pp. 1207-1209, 2003.
[122] T. Oguchi, S. Tanaka, M. Hayase, and T. Hatsuzawa, "An electro-statically driven displlay device using evanescent coupling between a sheet waveguide and multi-cantilevers," *Transactions of the Institute of Electrical Engineers of Japan*, vol. 124-E, pp. 87-92, 2004.
[123] M.-C. M. Lee, S. Mathai, and M. C. Wu, "Dynamic Dispersion Compensator Using MEMS-Actuated Microdisk Resonators," presented at Conference on Lasers and Electrooptics, pp. 736-738, 2004.
[124] M.-C. M. Lee and M. C. Wu, "MEMS-Actuated Microdisk Resonators With Variable Power Coupling Ratios," *IEEE Photonics Technology Letters*, vol. 17, pp. 1034-1036, 2005.
[125] M.-C. M. Lee and M. C. Wu, "Vertically-Coupled MEMS Microdisks for Tunable Optical Delays and Dynamic Dispersion Compensation," presented at Conference on Lasers and Electro-Optics (CLEO), Baltimore, MD, pp., 2005.
[126] G. N. Nielson, D. Seneviratne, F. Lopez-Royo, P. T. Rakich, Y. Avrahami, M. R. Watts, H. A. Haus, H. L. Tuller, and G. Barbastathis, "Integrated Wavelength-

Selective Optical MEMS Switching Using Ring Resonator Filters," *IEEE Photonics Technology Letters*, vol. 17, pp. 1190-1192, 2005.
[127] G. N. Nielson, D. Seneviratne, F. Lopez-Royo, P. T. Rakich, F. Giacometti, H. L. Tuller, and G. Barbastathis, "MEMS based wavelength selective optical switching for integrated photonic circuits," presented at Conference on Lasers and Electro-Optics (CLEO), San Francisco, CA, pp., 2004.
[128] J. Daleiden, V. Rangelov, S. Irmer, F. Romer, M. Strassner, C. Prott, A. Tarraf, and H. Hillmer, "Record tuning range of InP-based multiple air-gap MOEMS filter," *Electronics Letters*, vol. 38, 2002.
[129] J. L. Leclercq, C. Seassal, and P. Viktorovitch, "InP-based micro-opto-electro-mechanical systems (MOEMS)," presented at Journees Nationales de Microelectronique et Optoelectronique III-V, Chantilly, France, pp. Pr2 123-131, 1999.
[130] R. Ledantec, T. Benyattou, G. Guillot, C. Seassal, J. L. Leclercq, X. Letartre, A. Gagnaire, M. Gendry, P. Viktorovitch, R. Benferhat, D. Rondi, and R. Blondeau, "Optical characterization methods of InP-based micro-opto-electro-mechanical systems," *SPIE*, vol. 3008, pp. 258-264, 1997.
[131] OWMS, "Apollo Photonics, Optical Waveguide Mode Solver V1.21." Waterloo, Canada.
[132] BeamPROP, "RSoft Design Group." Ossining, NY.
[133] C. H. Kwan and K. S. Chiang, "Study of Polarization-Dependent Coupling in Optical Waveguide Directional Couplers by the Effective-Index Method With Built-in Perturbation Correction," *Journal of Lightwave Technology*, vol. 20, pp. 1018-1026, 2002.
[134] M. K. Chin, "Polarization dependence in waveguide-coupled micro-resonators," *Optics Express*, vol. 11, pp. 1724-1730, 2003.
[135] M. W. Pruessner, K. Amarnath, M. Datta, D. P. Kelly, S. Kanakaraju, P.-T. Ho, and R. Ghodssi, "Optical and Mechanical Characterization of an Evanescent Coupler Optical Switch," presented at Solid-State Sensor, Actuator and Microsystems Workshop, Hilton Head, S.C., pp. 238-241, 2004.
[136] T. Bakke, C. P. Tigges, and C. T. Sullivan, "1x2 MOEMS switch based on silicon-on-insulator and polymeric waveguides," *Electronics Letters*, vol. 38, pp. 177-178, 2002.
[137] I. Shubin and P. L. K. Wa, "Electrostatically actuated 1x2 micromechanical optic switch," *Electronics Letters*, vol. 37, pp. 451-452, 2001.
[138] E. M. Garmire and K. Honda, "Depolarization in channel glass waveguides," *Journal of Lightwave Technology*, vol. LT-4, pp. 220-227, 1986.
[139] B. E. Little and T. Murphy, "Design rules for maximally flat wavelength-insensitive optical power dividers using Mach–Zehnder structures," *IEEE Photonics Technology Letters*, vol. 9, pp. 1607-1609, 1997.
[140] T. E. Murphy, B. E. Little, and H. I. Smith, "Wavelength- and polarization-insensitive integrated directional couplers," presented at Integrated Photonics Research Conference, Santa Barbara, CA, pp., 1999.
[141] K. Okamoto, *Fundamentals of Optical Waveguides*. San Diego: Academic Press, 2000.

[142] H. Lim, C. Carraro, R. Maboudian, M. W. Pruessner, and R. Ghodssi, "Chemical and thermal stability of alkanethiol and sulfur passivated InP(100)," *Langmuir*, vol. 20, pp. 743-747, 2004.
[143] D. Marcuse, "Tilt, Offset, and End-Separation Loss of Lowest-Order Slab Waveguide Mode," *Journal of Lightwave Technology*, vol. LT-4, pp. 1647-1650, 1986.
[144] MemCAD. Cary: North Carolina, 2003.
[145] D. Marcuse, "Loss analysis of single-mode fiber splices," *Bell System Technical Journal*, vol. 56, pp. 703-718, 1977.
[146] P. Beckmann and A. Spizzichino, *The scattering of electromagnetic waves from rough surfaces*. Norwood, MA: Artech House, Inc., 1987.
[147] G. Zhou and P. Dowd, "Tilted folded-beam suspension for extending the stable travel range of comb-drive actuators," *Journal of Micromechanics and Microengineering*, vol. 13, pp. 178-183, 2003.
[148] M. K. Baller, H. P. Lang, J. Fritz, C. Gerber, J. K. Gimzewski, U. Drechsler, H. Rothuizen, M. Despont, P. Vettiger, F. M. Battiston, J. P. Ramseyer, P. Fornaro, E. Meyer, and H.-J. Guntherodt, "A cantilever array-based artificial nose," *Ultramicroscopy*, vol. 82, pp. 1-9, 2000.
[149] P. G. Datskos, T. Thundat, and N. V. Lavrik, "Micro and Nanocantilever Sensors," in *Encyclopedia of Nanoscience and Nanotechnology*, vol. 5, H. S. Nalwa, Ed. Stevenson Ranch, California: American Scientific Publishers, 2004, pp. 551-560.
[150] B. Ilic, D. Czaplewski, M. Zalalutdinov, H. G. Craighead, P. Neuzil, C. Campagnolo, and C. Batt, "Single cell detection with micromechanical oscillators," *Journal of Vacuum Science and Technology*, vol. B19, pp. 2825-2828, 2001.
[151] N. V. Lavrik and P. G. Datskosa, "Femtogram mass detection using photothermally actuated nanomechanical resonators," *Applied Physics Letters*, vol. 82, pp. 2697-2699, 2003.
[152] L. A. Pinnaduwage, V. Boiadjiev, J. E. Hawk, and T. Thundat, "Sensitive detection of plastic explosives with self-assembled monolayer-coated microcantilevers," *Applied Physics Letters*, vol. 83, pp. 1471-1473, 2003.
[153] T. Thundat, E. A. Wachter, S. L. Sharp, and R. J. Warmack, "Detection of mercury vapor using resonating microcantilevers," *Applied Physics Letters*, vol. 66, pp. 1695-1697, 1995.
[154] M. K. Baller, H. P. Lang, J. Fritz, C. Gerber, J. K. Gimzewski, U. Drechsler, H. Rothuizen, M. Despont, P. Vettiger, F. M. Battiston, J. P. Ramseyer, P. Fornaro, E. Meyer, and H.-J. Guntherodt, "A cantilever array-based arti"cial nose," *Ultramicroscopy*, vol. 82, pp. 1-9, 2000.
[155] P. G. Datskos, T. Thundat, and N. V. Lavrik, "Micro and Nanocantilever Sensors," in *Encyclopedia of Nanoscience and Nanotechnology*, vol. 5, H. S. Nalwa, Ed. Stevenson Ranch, California: American Scientific Publishers, 2004, pp. 551-560.
[156] R. T. Howe and R. S. Muller, "Resonant microbridge vapor sensor," *IEEE Transactions on Electron Devices*, vol. ED-33, pp. 499-506, 1986.

[157] T. H. Stievater, W. S. Rabinovich, H. S. Newman, R. Mahon, P. G. Goetz, J. L. Ebel, and D. J. McGee, "Measurement of thermal-mechanical noise in microelectromechanical systems," *Applied Physics Letters*, vol. 81, pp. 1779-1781, 2002.
[158] E. Ollier, P. Philippe, C. Chabrol, and P. Mottier, "Micro-Opto-Mechanical Vibration Sensor Integrated on Silicon," *Journal of Lightwave Technology*, vol. 17, pp. 26-29, 1999.
[159] X. Wang, I. Kartadjodjaja, V. Almeida, M. Lipson, B. Ilic, and R. Panepucci, "Silicon cantilever-waveguide displacement sensors," presented at 49th International Electron, Ion, and Photon Beam Technology and Nanofabrication Conference (EIPBN), Orlando, FL, pp. 329-330, 2005.
[160] M. W. Pruessner, W.-H. Chuang, K. Amarnath, S. Kanakaraju, and R. Ghodssi, "Micromechanical Resonators with Integrated Optical Waveguides for Sensing Applications," presented at Conference on Lasers and Electro-Optics, Baltimore, MD, pp., 2005.
[161] M. W. Pruessner, M. Datta, K. Amarnath, S. Kanakaraju, and R. Ghodssi, "Indium Phosphide Based MEMS End-Coupled Optical Waveguide Switches," presented at 17th International Indium Phosphide and Related Materials Conference, Glasgow, Scotland, pp., 2005.
[162] W.-H. Chuang, T. Luger, R. K. Fettig, and R. Ghodssi, "Mechanical Property Characterization of LPCVD Silicon Nitride Thin Films at Cryogenic Temperatures," *Journal of Microelectromechanical Systems*, vol. 13, pp. 870-879, 2004.
[163] Femlab. Version 3.0, Burlington, MA: Comsol, Inc., 2005.
[164] SigmaPlot. Version 9, Point Richmond, CA: Systat Software, 2005.
[165] P. A. Tipler, *Physics For Scientists And Engineers*, vol. 1, 3rd ed. New York, NY: Worth Publishers, 1991.
[166] A. V. Oppenheim, A. S. Willsky, and S. H. Nawab, *Signals & Systems*, 2nd ed. Upper Saddle River, NJ: Prentice Hall, 1997.
[167] A. V. Oppenheim, A. S. Willsky, and H. S. Nawab, *Signals and Systems*, Second ed. Upper Saddle River, NJ: Prentice Hall, Inc., 1997.
[168] P. A. Tipler, *Physics for Scientists and Engineers*, vol. 1-2. New York, NY: Worth Publishers, 1991.
[169] H. C. Nathanson, W. E. Newell, R. A. Wickstrom, and R. J. J. Davis, "The resonant gate transistor," *IEEE Transactions on Electron Devices*, vol. ED-14, pp. 117-133, 1967.
[170] J. J. Yao and N. C. MacDonald, "A Micromachined, Single-Crystal Silicon Tunable Resonator," *Journal of Micromechanics and Microenegineering*, vol. 6, pp. 257-264, 1996.
[171] J. J. Yao and N. C. MacDonald, "A micromachinged, single-crystal silicon, tunable resonator," *Journal of Micromechanics and Microengineering*, vol. 6, pp. 257-264, 1996.
[172] F. Romer, C. Prott, S. Irmer, J. Daleiden, A. Tarraf, H. Hillmer, and M. Strassner, "Tuning efficiency and linewidth of electrostatically actuated multiple air-gap filters," *Applied Physics Letters*, vol. 82, pp. 176-178, 2003.

[173] H. W. C. Postma, I. Kozinsky, A. Husain, and M. L. Roukes, "Dynamic range of nanotube- and nanowire-based electromechanical systems," *Applied Physics Letters*, vol. 86, pp. 223105, 2005.
[174] D. S. Greywall, P. A. Busch, and J. A. Walker, "Phenomenological model for gas-damping of micromechanical structures," *Sensors and Actuators A*, vol. 72, pp. 49-70, 1999.
[175] J. Hietanen, J. Bomer, J. Jonsmann, W. Olthuis, P. Bergveld, and K. Kaski, "Damping of a vibrating beam," *Sensors and Actuators A*, vol. 86, pp. 39-44, 2000.
[176] H. Hosaka, K. Itao, and S. Kuroda, "Damping characteristics of beam-shaped micro-oscillators," *Sensors and Actuators A*, vol. 49, pp. 87-95, 1995.
[177] J.-M. Huang, K. M. Liew, C. H. Wong, S. Rajendran, M. J. Tan, and A. Q. Liu, "Mechanical design and optimization of a capacitive micromachined shunt switch," *Sensors and Actuators A*, vol. 93, pp. 273-285, 2001.
[178] S. Dohn, R. Sandberg, W. Svendsen, and A. Boisen, "Enhanced functionality of cantilever based mass sensors using higher modes and functionalized particles," presented at The 13th International Conference on Solid-State Sensors, Actuators and Microsystems (Transducers), Seoul, South Korea, pp. 636-639, 2005.
[179] S. S. Saini, V. Vusirikala, R. Whaley, F. G. Johnson, D. Stone, and M. Dagenais, "Compact Mode Expanded Lasers Using Resonant Coupling Between a 1.55um InGaAsP Tapered Active Region and an Underlying Coupling Waveguide," *IEEE Photonics Technology Letters*, vol. 10, pp. 1232-1234, 1998.
[180] S. Greek, R. Gupta, and K. Hjort, "Mechanical considerations in the design of a micromechanical tuneable InP-based WDM filter," *Journal of Microelectromechanical Systems*, vol. 8, pp. 328-334, 1999.
[181] M. Datta, M. W. Pruessner, K. Amarnath, J. McGee, S. Kanakaraju, and R. Ghodssi, "Wavelength-Selective Integrated Optical MEMS Filter in InP," presented at 18th International Conference on Micro Electro Mechanical Systems, Miami Beach, FL, pp. 88-91, 2005.
[182] M. W. Pruessner, "In-Plane Tunable Fabry Perot Filter." Personal communication, MSAL Group Meeting, University of Maryland, 2201 J.M. Patterson Bldg., January 14, 2003.
[183] T. A. Ibrahim, R. Grover, L.-C. Kuo, S. Kanakaraju, L. C. Calhoun, and P.-T. Ho, "All-Optical AND/NAND Logic Gates Using Semiconductor Microresonators," *IEEE Photonics Technology Letters*, vol. 15, pp. 1422-1424, 2003.
[184] H. Halbritter, F. Riemenschneider, S. Syguda, C. Dhanavantri, M. Strassner, A. Tarraf, B. R. Singh, I. Sagnes, and P. Meissner, "Tunable and wavelength selective pin photodiode," *Electronics Letters*, vol. 40, pp. 20040275, 2004.
[185] H. Halbritter, F. Riemenschneider, J. Jacquet, J.-G. Provost, I. Sagnes, and P. Meissner, "AM and RIN of a Tunable Optically Pumped 1.6 um VCSEL," *IEEE Photonics Technology Letters*, vol. 16, pp. 723-725, 2004.
[186] S. S. Saini, V. Vusirikala, R. Whaley, F. G. Johnson, D. Stone, and M. Dagenais, "Compact Mode Expanded Lasers Using Resonant Coupling Between a 1.55um InGaAsP Tapered Active Region and an Underlying Coupling Waveguide," *IEEE Photonics Technology Letters*, vol. 10, pp. 1232-1234, 1998.

[187] G. P. Agrawal and N. K. Dutta, *Semiconductor lasers*. New York: Van Norstrand, 1993.
[188] P. H. Holloway and G. E. McGuire, *Handbook of Compound Semiconductors: Growth, Processing, Characterization, and Devices*. Norwich, NY: Noyes Publications, 1996.
[189] F. G. Johnson, "InGaAsP parameter calculator." Excel file.
[190] R. Legtenberg, A. W. Groeneveld, and M. Elwenspoek, "Comb-drive actuators for large displacements," *Journal of Micromechanics and Microengineering*, vol. 6, pp. 320-329, 1996.
[191] http://www.utexas.edu/math/Matlab/Manual/tec6.2.html, 2005.

Page intentionally left blank.

# LIST OF PUBLICATIONS

## Journal Papers


[6] M. W. Pruessner, K. Amarnath, M. Datta, D. Kelly, S. Kanakaraju, P-T. Ho and R. Ghodssi, "InP-Based Optical Waveguide MEMS Switches with Evanescent Coupling Mechanism," *Journal of Microelectromechanical Systems* (In Press).

[5] M. Datta, M. W. Pruessner, D. P. Kelly, and R. Ghodssi, "Design of MEMS-tunable novel monolithic optical filters in InP with horizontal Bragg mirrors," *Solid-State Electronics*, Vol. 48, pp. 1959-1963, 2004.

[4] D. P. Kelly, M. W. Pruessner, K. Amarnath, M. Datta, S. Kanakaraju, L. C. Calhoun, and R. Ghodssi, "Monolithic Suspended Optical Waveguides for InP MEMS," *IEEE Photonics Technology Letters*, Vol. 16 (5), pp. 1298-1300, 2004.

[3] H. Lim, C. Carraro, R. Maboudian, M. W. Pruessner, and R. Ghodssi, "Chemical and Thermal Stability of Alkanethiol and Sulfur Passivated InP(100)," *Langmuir*, Vol. 20, pp. 743-747, 2004.

[2] M. W. Pruessner, T. King, D. Kelly, R. Grover, L. Calhoun, and R. Ghodssi, "Mechanical Property Measurement of InP-based MEMS for Optical Communications," *Sensors and Actuators A: Physical*, Vol. 105 (2), pp. 190-200, 2003.

[1] P.G. O'Shea, M. Reiser, R.A. Kishek, S. Bernal, H. Li, M. Pruessner, V. Yun, Y. Cui, W. Zhang, Y. Zou, T. Godlove, D. Kehne, P. Haldemann, I. Haber, "The University of Maryland Electron Ring (UMER)," *Nuclear Instruments & Methods in Physics Research A*, Vol. 464, pp. 646-652, 2001.


## Conference Paper & Poster Presentations


[15] M. W. Pruessner, W.-H. Chuang, K. Amarnath, S. Kanakaraju, and Reza Ghodssi, "Micromechanical Resonators with Integrated Optical Waveguides for Sensing Applications," *Conference on Lasers and Electro-Optics* (CLEO 2005), Baltimore, MD, May 22-27.

[14] M. Datta, J. McGee, M. W. Pruessner, K. Amarnath, S. Kanakaraju, and R. Ghodssi, "Tunable optical filters for in-plane integration on InP MEMS platform," *SPIE Microtechnologies for the New Millennium Conference* (EMT 2005), Sevilla, Spain, May 9-11, 2005.

[13] M. W. Pruessner, M. Datta, K. Amarnath, S. Kanakaraju, and R. Ghodssi, "Indium Phosphide Based MEMS End-Coupled Optical Waveguide Switches," *17th Indium Phosphide and Related Materials Conference* (IPRM 2005), Glasgow, Scotland, U.K., May 8-12, 2005. (**Best Student Paper Award**)

[12] M. Datta, M. W. Pruessner, K. Amarnath, J. McGee, S. Kanakaraju, and R.Ghodssi, "Wavelength-Selective Integrated Optical MEMS Filter in InP," *Proc. 18th International Conference on Micro Electro Mechanical Systems* (MEMS 2005), pp. 88-91, Miami, FL, January 30-February 3, 2005.

[11] M. Datta, M. W. Pruessner, D. P. Kelly, and R. Ghodssi, "Suspended Waveguide-Based Tunable Integrated Optical Filters on Indium Phosphide MEMS Platform," *American Vacuum Society 51st International Symposium*, Anaheim, CA, November 14-19, 2004.

[10] M. W. Pruessner, K. Amarnath, M. Datta, D. P. Kelly, S. Kanakaraju, P.-T. Ho and R. Ghodssi, "Optical and Mechanical Characterization of an Evanescent Coupler Optical Switch," *Proc. 2004 Solid-State Sensor, Actuator and Microsystems Workshop* (Hilton Head 2004), pp. 238-241, Hilton Head Island, S. C., June 6-10, 2004.

[9] M. Datta, M. W. Pruessner, D. Kelly and R. Ghodssi, "MEMS-Tunable Novel Monolithic Optical Filters in InP with Horizontal Bragg Mirrors," *Proc. 2003 International Semiconductor Device Research Symposium* (ISDRS), Washington, DC, December 10-12, 2003.

[8] D. Kelly, M. W. Pruessner, M. Datta and R. Ghodssi, "Suspended Waveguides for InP Optical MEMS," *Proc. 2003 International Semiconductor Device Research Symposium* (ISDRS), Washington, DC, December 10-12, 2003.

[7] M. W. Pruessner, D. Kelly, M. Datta, H.Lim, R. Maboudian and R. Ghodssi, "Design and fabrication of an InP-based Moving Waveguide 1x2 Optical MEMS Switch," *Proc. 2003 International Semiconductor Device Research Symposium* (ISDRS), Washington, DC, December 10-12, 2003.

[6] M. W. Pruessner, T. King, D. Kelly, and R. Ghodssi, "Micro-Mechanical Characterization of Indium Phosphide (InP) for Active Optical MEMS Applications," *AVS 49th International Symposium* (49th AVS), Denver, CO, November 3-8, 2002.

[5] M. W. Pruessner, T. King, D. Kelly, and R. Ghodssi, "Towards III-V Optical MEMS: Mechanical Property Measurement of Indium Phosphide," *2002 Solid-State Sensor, Actuator and Microsystems Workshop* (Hilton Head 2002), *Open Poster Session*, Hilton Head, SC, June 2-6, 2002.

[4] M. W. Pruessner, R. Grover, L. Calhoun, R. Ghodssi, "Development of InP-based Test Structures for Optical MEMS Applications," *Proc. 2001 International Semiconductor Device Research Symposium* (ISDRS), Washington, DC, December 5-7, 2001.

[3] J. Harris, B. Quinn, M. Pruessner, V. Yun, M. Reiser, S. Bernal, P. G. O'Shea, "A Fast Beam Position Monitor for UMER," *Proc. 2001 Particle Accelerator Conference* (PAC 2001), pp. 1387-1389, Chicago, IL, June 18-22, 2001.

[2] P.G. O'Shea, M. Reiser, R.A. Kishek, S. Bernal, H. Li, M. Pruessner, M. Virgo, V. Yun, W. Zhang, T. Godlove, D. Kehne, P. Haldemann, I. Haber, "UMER: The University Maryland Electron Ring," *Advanced Accelerator Concepts: Ninth Workshop* (AAC 2000), AIP Conference Proceedings, no.569, p. 405-14, 2001.

[1] M. Reiser, P.G. O'Shea, R.A. Kishek, S. Bernal, P. Chin, S. Guharay, Y. Li, M. Venturini, J.G. Wang, V. Yun, W. Zhang, Y. Zou, M. Pruessner, T. Godlove, D. Kehne, P. Haldemann, R. York, D. Lawton, L. G. Vorobiev, I. Haber, H. Nishimura, "The Maryland Electron Ring for Investigating Space-Charge Dominated Beams in a Circular FODO System," *Proc. 1999 Particle Accelerator Conference* (PAC 1999), vol. 1, pp. 234-6, New York City, NY, March 29-April 2, 1999.

**Other Meetings**

[1] M. W. Pruessner, K. Amarnath, M. Datta, D. P. Kelly, S. Kanakaraju, and R. Ghodssi, "Indium Phosphide Based Optical Waveguide MEMS for Communications and Sensing," *MEMS Alliance Spring 2005 Workshop on The Post Telecommunication Boom*, Johns Hopkins Applied Physics Laboratory, Laurel, Maryland, April 18-19, 2005. (**Best Poster Award**)

**Thesis/Dissertation**

[2] M. W. Pruessner, "Indium Phosphide Based Optical Waveguide MEMS for Communications and Sensing," *PhD Dissertation*, University of Maryland, College Park, MD (*This document*, July, 2005).

[1] M. W. Pruessner, "Toward III-V Optical MEMS: Mechanical Property Measurement of Indium Phosphide Using Nanoindentation, Beam Bending, and Electrostatic Testing Methods," *Master's Thesis*, University of Maryland, College Park, MD, October, 2002.